Charged Kaon and ϕ Reconstruction in Au+Au Collisions at 1.23 AGeV

Dissertation
zur Erlangung des Doktorgrades
der Naturwissenschaften

vorgelegt beim Fachbereich Physik
der Johann Wolfgang Goethe-Universität
in Frankfurt am Main

von
Heidi Schuldes
aus Bad Pyrmont

Frankfurt 2016
(D30)

vom Fachbereich Physik der Johann Wolfgang Goethe-Universität als Dissertation angenommen.

Dekan:

Prof. Dr. Rene Reifarth

Gutachter:

Prof. Dr. Joachim Stroth

Prof. Dr. Christoph Blume

Datum der Disputation:

10.11.2016

Abstract

In this thesis, the production of charged kaons and ϕ mesons in Au+Au collisions at $\sqrt{s_{AuAu}}$ = 2.4 GeV is studied. At this energy, all particles carrying open and hidden strangeness are produced below their respective free nucleon-nucleon threshold with the corresponding so-called excess energies: $\sqrt{s_{exc}^{K^+}}$ = -0.15 GeV, $\sqrt{s_{exc}^{K^-}}$ = -0.46 GeV, $\sqrt{s_{exc}^{\phi}}$ = -0.49 GeV. As a consequence, the production cross sections are very sensitive to medium effects like momentum distributions, two- or multistep collisions, and modification of the in-medium spectral distribution of the produced states [1]. K^+ and K^- mesons exhibit different properties in baryon dominated matter, since only K^- can be resonantly absorbed by nucleons. Although strangeness exchange reactions have been proposed to be the dominant channel for K^- production in the analyzed energy regime, the production yield and kinematic distributions could also be explained in smaller systems based on statistical hadronization model fits to the measured particle yields, including a canonical strangeness suppression radius R_C, and taking the ϕ feed-down to kaons into account [2, 3]. For the first time in central Au+Au collisions at such low energies, it is possible to reconstruct and do a multi differential analysis of K^- and ϕ mesons. In principle, this should be the ideal environment for strangeness exchange reactions to occur, as the particles are produced deeply sub-threshold in a large and long-living system. Therefore, it is the ultimate test to differentiate between the different sources for K^- production in HIC.

In total 7.3x10^9 of the 40% most central Au(1.23 GeV per nucleon)+Au collisions are analyzed. The data has been recorded with the High Acceptance DiElectron Spectrometer HADES located at Helmholtzzentrum für Schwerionenforschung GSI in April/May 2012. A substantially improved reconstruction method has been employed to reconstruct the hadrons with high purity in a wide phase space region.

The estimated particle multiplicities follow a clear hierarchy of the excess energy: $41.5 \pm 2.1|_{sys}$ protons at mid-rapidity per unit in rapidity, $11.1 \pm 0.6|_{sys} \pm 0.4|_{extrapol}$ π^-, $(3.01 \pm 0.03|_{stat} \pm 0.15|_{sys} \pm 0.30|_{extrapol})x10^{-2}$ K^+, $(1.94 \pm 0.09|_{stat} \pm 0.10|_{sys} \pm 0.10|_{extrapol})x10^{-4}$ K^- and $(0.99 \pm 0.24|_{stat} \pm 0.10|_{sys} \pm 0.05|_{extrapol})x10^{-4}$ ϕ per event. The multiplicities of the strange hadrons increase more than linear with the mean number of participating nucleons $\langle A_{part} \rangle$, supporting the assumption that the necessary energy to overcome the elementary production threshold is accumulated in multi-particle interactions. Transport models predict such an increase, but are overestimating the measured particle yield and are not able to describe the kinematic distributions of K^+ mesons perfectly. However, the best description is given by the IQMD model with a density dependent kaon-nucleon potential of 40 MeV at nuclear ground state density.

The K^-/K^+ multiplicity ratio is constant as a function of centrality and follows with (6.45 ± 0.77)x10^{-3} the trend of increasing with beam energy indicated from previous experiments [4]. The effective temperature of K^- $T_{eff}^{K^-}$ = (84 $\pm$ 6) MeV is found to be systematically lower than the one of K^+ $T_{eff}^{K^+}$ = (104 $\pm$ 1) MeV, which has also been observed by the other experiments.

The ϕ/K^- ratio is with a value of 0.52 $\pm$ 0.16 higher than the one obtained at higher center-of-mass energies and smaller systems. This behavior is predicted from a tuned version of the UrQMD transport model [5], when including higher mass baryonic resonances which can decay into ϕ mesons and from statistical hadronization models when suppressing open strangeness canonically. The found ratio is constant as a function of centrality and results with a branching ratio of 48.9%, that $\approx$ 25% of all measured K^- originate from ϕ feed-down decays. A two component PLUTO simulation, consisting of a pure thermal and a K^- contribution originating from ϕ decays, can fully explain the

observed lower effective temperature in comparison to K^+ and the shape of the measured rapidity distribution of K^-. As a result, we find no indication for strangeness exchange reactions being the dominant mechanism for K^- production in the SIS18 energy regime, if taking the contribution from ϕ feed-down decays into account.

The hadron yields for the 20% most central collisions can be described by a statistical hadronization model fit with the chemical freeze-out temperature of T_{chem} = (68 $\pm$ 2) MeV and baryochemical potential of μ_B = (883 $\pm$ 25) MeV, which is higher than expected from previous parameterizations. The analysis of the transverse mass spectra of protons indicate a kinetic freeze-out temperature of T_{kin} = (70 $\pm$ 4) MeV and radial flow velocity of β_r = 0.43 $\pm$ 0.01, which is in agreement with the parameters obtained from the linear dependence of the effective temperatures on the particle mass T_{kin} = (71.5 $\pm$ 4.2) MeV and β_r = 0.28 $\pm$ 0.09.

Inhaltsangabe

In dieser Arbeit wird die Produktion von geladenen Kaonen und ϕ Mesonen in Au+Au Kollisionen bei einer Schwerpunktsenergie von $\sqrt{s}$ = 2,4 GeV studiert. Bei dieser Energie werden alle Teilchen mit Seltsamkeitsinhalt unterhalb ihrer jeweiligen freien Nukleon-Nukleon Schwellenenergie produziert (Exzess-Energien: $\sqrt{s^{K^+}_{exc}}$ = -0.15 GeV, $\sqrt{s^{K^-}_{exc}}$ = -0.46 GeV, $\sqrt{s^{\phi}_{exc}}$ = -0.49 GeV). Dies bedingt, dass die Wirkungsquerschnitte dieser Teilchen sehr sensitiv auf Mediumeffekte, wie Impulsverteilungen, zwei- oder mehrstufige Kollisionen und die Modifikation der in-Medium Spektralfunktionen der produzierten Zustände sind [1]. In baryondominierter Materie unterliegen K^+ und K^- unterschiedlichen Eigenschaften, da nur K^- resonant von Nukleonen absorbiert werden kann. Obwohl die sogenannten Seltsamkeitsaustauschreaktionen als dominanter Kanal für die K^- Produktion im analysierten Energiebereich vorgeschlagen wurden, konnte die Produktionsrate und kinematischen Verteilungen in kleineren Reaktionssystemen auch mithilfe statistischer Hadronisationsmodelle, in denen Seltsamkeit durch einen kanonischen Radius R_C unterdrückt ist, und der Berücksichtigung von ϕ-Zerfällen in Kaonen beschrieben werden [2, 3]. Zum ersten Mal ist es möglich K^- und ϕ Mesonen in zentralen Au+Au Kollisionen zu rekonstruieren und eine multidifferentiale Analyse durchzuführen. Im Prinzip sollten in diesem grossen und langlebigen System die idealen Bedingungen für das Auftreten von Seltsamkeitsaustauschreaktionen vorliegen, da die Teilchen weit unterhalb ihrer NN-Schwellenenergie produziert werden. Somit ist dies der ultimative Test um zwischen den unterschiedlichen Quellen für die K^- Produktion in Schwerionenstößen zu unterscheiden.

Insgesamt werden 7,3x10^9 der 40% zentralsten Au(1,23 GeV pro Nukleon)+Au Kollisionen ausgewertet. Die Daten wurden mit dem High Acceptance DiElectron Spectrometer HADES an dem Helmholtzzentrum für Schwerionenforschung GSI im April und Mai 2012 aufgenommen. Es wurde eine erheblich verbesserte Rekonstruktionsmethode angewendet um die Hadronen mit hoher Reinheit in einer weiten Phasenraumregion zu identifizieren.

Die erhaltenen Teilchenmultiplizitäten folgen einer eindeutigen Hierarchie ihrer Exzess-Energien: $41.5 \pm 2.1|_{sys}$ Protonen bei Schwerpunktsrapidität pro Einheit in Rapidität, $11{,}1 \pm 0{,}6|_{sys} \pm 0{,}4|_{extrapol}$ π^-, $(3{,}01 \pm 0{,}03|_{stat} \pm 0{,}15|_{sys} \pm 0{,}30|_{extrapol})x10^{-2}$ K^+, $(1{,}94 \pm 0{,}09|_{stat} \pm 0{,}10|_{sys} \pm 0{,}10|_{extrapol})x10^{-4}$ K^- and $(0{,}99 \pm 0{,}24|_{stat} \pm 0{,}10|_{sys} \pm 0{,}05|_{extrapol})x10^{-4}$ ϕ pro Reaktion. Die Multiplizitäten der seltsamen Hadronen steigen stärker als linear mit der mittleren Anzahl der an der Reaktion teilnehmenden Nukleonen $\langle A_{part} \rangle$ an. Dies unterstützt die Annahme, dass die benötigte Energie um die elementare Produktionsschwelle zu überwinden in Multi-Teilchen-Interaktionen akkumuliert wird. Transport-Modelle sagen solch eine Proportionalität vorher, sie überschätzen jedoch die Teilchenproduktionsraten und sind nicht in der Lage die kinematischen Verteilungen zufriedenstellend zu beschreiben. Die beste Beschreibung der Kaonenspektren ist von dem IQMD Modell, mit einem dichteabhängigen Kaon-Nukleon-Potential von 40 MeV bei nuklearer Grundzustandsdichte, gegeben.

Das K^-/K^+-Verhältnis is konstant als Funktion der Zentralität und folgt mit $(6{,}45 \pm 0{,}77)$x10^{-3} dem Trend vorhergegangener Experimente [4] linear mit der Schwerpunktsenergie anzusteigen. Die effektive Temperatur von K^- $T^{K^-}_{eff}$ = (84 $\pm$ 6) MeV ist, wie bereits von vorhergegangen Experimenten beobachtet, systematisch niedriger als die von K^+ $T^{K^+}_{eff}$ = (104 $\pm$ 1) MeV.

Das ϕ/K^--Verhältnis ist mit einem Wert von 0,52 $\pm$ 0,16 höher als das bei höheren Schwerpunktsenergien und kleineren Systemen. Dieses Verhalten ist von einer modifizierten Version des UrQMD-Transportmodelles [5], in dem zusätzliche schwere Baryonenresonanzen, die in ϕ Mesonen zerfallen können implementiert wurden und von statistischen Hadronisationsmodellen, in denen Selt-

samkeit kanonisch unterdrückt wird, vorhergesagt. Das Verhältnis ist konstant als Funktion der Zentralität und bedingt mit einer Zerfallswahrscheinlichkeit von 48,9%, dass $\approx$ 25% aller gemessenen K^- aus ϕ-Zerfällen resultieren. Eine Zweikomponenten PLUTO-Simulation, bestehend aus einem rein thermischen und einem K^--Beitrag aus ϕ Zerfällen, kann die beobachtete niedrigere effektive Temperatur im Vergleich zu K^+ und die Form der gemessenen Rapiditätsverteilung von K^- erklären. Somit finden wir keine Anzeichen für die Dominanz der Seltsamkeitsaustauschreaktionen für K^--Produktion im SIS18-Energiebereich, wenn der Beitrag aus ϕ-Zerfällen berücksichtigt wird.

Die gemessenen Hadronenraten der 20% zentralsten Reaktionen können mithilfe eines statistischen Hadronisationsmodells mit der chemischen Ausfriertemperatur T_{chem} = (68 $\pm$ 2) MeV und dem baryochemischen Potential μ_B = (883 $\pm$ 25) MeV, welches etwas höher ist als von vorhergegangen Parameterisierungen erwartet, beschrieben werden. Die Analyse der transversalen Massenspektren von Protonen deutet eine kinetische Ausfriertemperatur von T_{kin} = (70 $\pm$ 4) MeV und eine radiale Flussgeschwindigkeit von β_r = 0,43 $\pm$ 0,01 an. Diese Parameter stimmen mit den Werten T_{kin} = (71,5 $\pm$ 4,2) MeV und β_r = 0,28 $\pm$ 0,09 überein, die aufgrund der linearen Abhängigkeit der effektiven Temperaturen von der Teilchenmasse extrahiert wurden.

Contents

Chapter 1

Introduction and Motivation

By the current state of scientific knowledge, the origin of the universe is the simultaneous formation of matter, space and time about 13.8 billion years ago, the so-called *big bang*. The newly formed primordial matter was composed of extremely dense, compressed and hot (T $\approx 10^{28}$ K) elementary constituents of matter, the *quark-gluon-plasma* [6]. This matter expanded rapidly and cooled down. Already after $\approx 10^{-5}$ s the early universe cooled down to a temperature of $\approx 10^{12}$ K and the quarks were confined into light hadrons (mesons and baryons), which formed after around three minutes the first atomic nuclei at a temperature of $\approx 10^{9}$ K. Electrons were captured in orbits around the nuclei and atoms were formed. The atoms formed galaxies and after $\approx$10 billion years our earth developed. Figure 1.1 shows a sketch of the evolution of the universe.

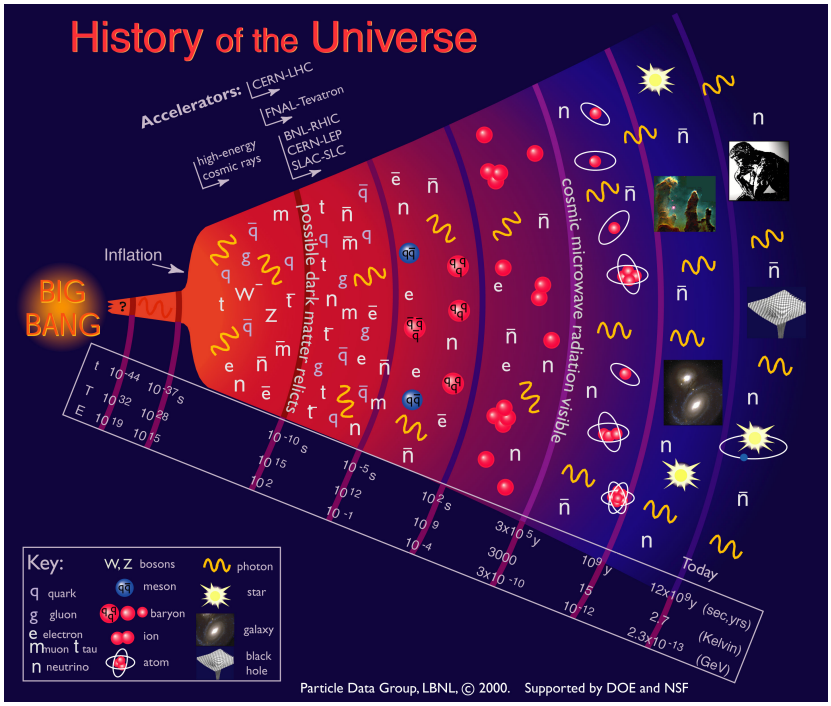

Figure 1.1: Sketch of the time evolution of the universe. Shortly after the big bang, the quarks and gluons formed the hot and dense quark-gluon plasma. The universe expanded and cooled down, until the quarks were confined into light hadrons, after around three minutes atomic nuclei, then the galaxies and finally, after $\approx$10 billion years our earth were formed. [7]

The elementary particles (fermions) which form all visible matter in the universe and the forces between them, respectively the particles transmitting the forces (bosons), are summarized in the *standard model of particle physics* (see Fig.1.2). Fermions are carrying spin $\frac{1}{2}$ and are split into two groups: quarks and leptons. There are six different types of quarks, namely up- (u), down- (d), strange- (s),

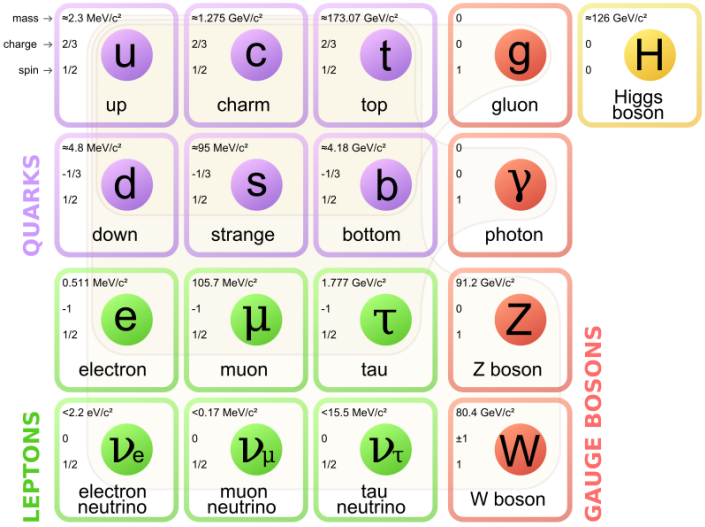

Figure 1.2: The standard model of particle physics summarizes the elementary particles, the forces, respectively the particles transmitting the forces, and the Higgs-boson. The particles are grouped into three different families. [8]

charm- (c), bottom- (b) and top-quark (t). The electric charge of the quarks is a multiple of one third. Based on their masses and charge, the quarks can be classified into three different families. All stable matter on earth is build out of up- and down-quarks from the first family. A proton, for example, is composed of two up- and one down-quark, which leads to charge = +1. Leptons can be divided into charged positrons/electrons (e^+/e^-), (anti-)muons (μ^+/μ^-) and (anti-)tauons (τ^+/τ^-) with charge ± 1 and corresponding neutral (anti-)neutrinos ($\bar{\nu}/\nu$). As in the case of the quarks, they can be classified into three families.

We know four fundamental forces: the electromagnetic, strong, weak and gravitational force. In the standard model, the forces, except the gravitational force, can be described by quantum field theories and are transmitted via (virtual) exchange bosons with spin = 1. The range of the forces depends on the mass of the exchange boson and can be estimated with help of the uncertainty principle formulated in the energy and time space. Every charged particle is interacting via the electromagnetic force, which is transmitted by the photon. Because the photon is massless, the range of the electromagnetic force is infinite. Quantum Electro Dynamics (QED) is the underlying quantum field theory. It was mainly established by Richard P. Feynman, Julian Schwinger and Shinchiro Tomonaga in the 1940s [9, 10, 11]. All particles which carry a property called color are feeling the strong force (see section 1.3). Each (anti-)quark is carrying one of the colors (anti-)blue, (anti-)green or (anti-)red. The three colors or a color with its anti-color are combined to color neutrality. In nature only color neutral objects are existing, due to the so-called *confinement*. Objects formed out of three quarks, e.g. the proton ($|uud\rangle$), are called *baryons*, and objects formed out of an quark-antiquark-pair, e.g. the pions ($|u\bar{d}\rangle$, $|d\bar{u}\rangle$, $|u\bar{u}/d\bar{d}\rangle$), are called *mesons*. The strong force is the reason why quarks form nucleons and those nucleons are forming atomic nuclei. The exchanged bosons are the eight different gluons. Gluons are massless, but as they carry color (a color and an anti-color) they are interacting also among themselves. Therefore, the strong force has a range in the order of $\sim 10^{-15}$ m, which corresponds to the radius of a proton (1 fm). As was QED for the electromagnetic force, a quantum field theory, Quantum Chromo Dynamics (QCD), was developed to describe the strong force (see section

1.3). The weak force is acting on all particles[1] of the standard model and is e.g. responsible for the β-decay. The corresponding exchange particles are the W^+, W^- and Z^0 bosons with a mass of $m \approx$ 80 MeV/c^2. The high mass of these exchange bosons is leading to a small range of the weak force. The theoretical description of the weak and the electromagnetic force was unified to the electroweak force, mainly by Sheldon Glashow, Abdus Salam and Steven Weinberg, who were awarded with the Nobel Prize in 1979 [12, 13, 14].

The last ingredient of the standard model is the famous Higgs-boson, which was recently detected at CERN[2] [15]. According to the Higgs-mechanism, the Higgs-field is generating mainly the different masses of the $W^{\pm}$ and Z^0 bosons, whereas the quantum mechanic excitation of the field results in the massive Higgs-boson ($m \approx 125$ GeV/c^2) [16, 17, 18].

The main goal of relativistic and ultra-relativistic heavy-ion experiments is to study nuclear matter far away from its ground state. Heavy-ion collisions at high energies are used to recreate conditions in the laboratory similar to those in the early universe. There are several facilities existing at which experiments are studying heavy-ion collisions (see section 1.1) at different beam energies to probe the phase diagram of nuclear matter (see section 1.4). One of them is the GSI Helmholtzzentrum für Schwerionenforschung GmbH in Darmstadt, Germany, with the HADES experiment (see chapter 2). HADES is investigating elementary and heavy-ion collisions in the energy regime between 1 - 2 AGeV, by looking mainly at rarely produced and penetrating probes like dilepton pairs from the decay of light vector mesons or hadrons carrying strangeness. As strangeness is produced close to or below its elementary nucleon-nucleon threshold in this energy regime, charged kaons and ϕ mesons are indeed sensitive observables to investigate the properties of hot and dense nuclear matter in heavy-ion collisions. Since the discovery of strange particles, their production at energies close to the elementary production threshold is one of the main topics in heavy-ion physics at intermediate energies. Strangeness production might help to understand fundamental questions of QCD and astrophysics. The first experiments on strangeness production in light systems have been performed at the Lawrence Berkeley Laboratory (LBL) [19, 20]. With the advent of the SIS18 accelerator at GSI, two major experiments, KaoS [21] and FOPI [22], started detailed investigations on kaon production also in heavier systems in the energy regime between 1 - 2 GeV per nucleon (see section 1.7.1 and 1.7.3). The experimental field was supplemented by different theoretical approaches. Especially chiral models, mean field approaches and transport calculations started to deal with the puzzling experimental findings on strangeness production in the late 80s and 90s, which will be addressed in sections 1.3.1 and 1.5.

1.1 Heavy-ion collisions

Heavy-ion collisions are the only possibility to create in the laboratory matter under conditions similar to those which appeared a few microseconds after the big bang, or which are supposed to still exist in compact stellar objects, like neutron stars. By varying the collision system and the energy, the phase diagram of nuclear matter (see section 1.4) and the nuclear equation of state (see section 1.6) can be systematically probed. The initial energy of the colliding nucleons is transformed into thermal energy of the matter in the reaction zone, compressional energy and resonances. As a result, new particles are produced, which will be explained in section 1.1.1 and collective effects of the reaction zone, like directed flow of the matter (see section 1.1.2) are built up.

[1] except the gluons and photons

[2] **C**onseil **E**uropéen pour la **R**echerche **N**ucléaire

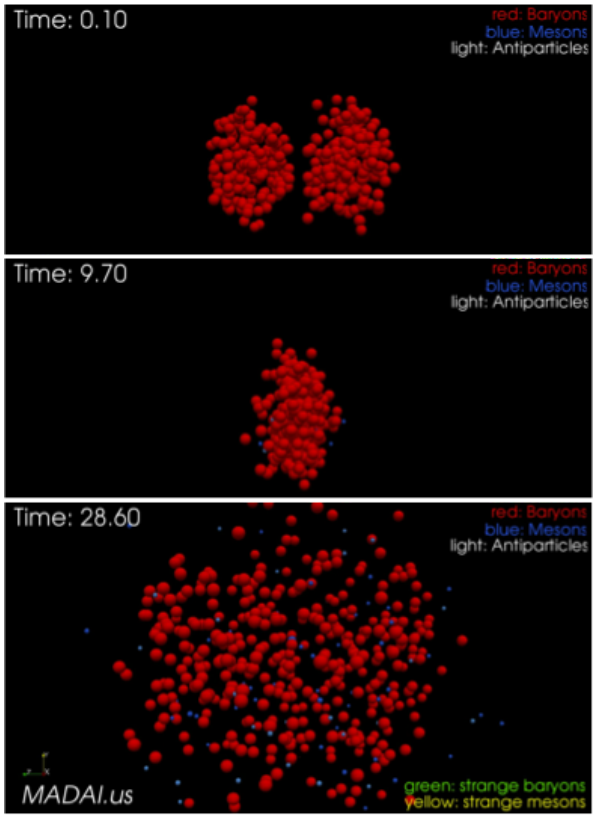

Figure 1.3: Illustration of the time evolution of a heavy-ion collision at 2 AGeV. Baryons are represented by red bullets. In the high density stage after ≈10 fm/c, the most abundantly produced Δ resonances and mesons (blue bullets) are created. The system expands and cools down in the freeze-out stage. [23]

A heavy-ion collision can be divided into three stages: first-chance nucleon-nucleon (NN) collisions, the high density and the freeze-out stage. Figure 1.3 illustrates these three stages. For nuclear matter studies, the high density stage is the most interesting phase of heavy-ion collisions. At SIS18 energies the matter is assumed to be compressed up to $\rho \approx 3 \cdot \rho_0$, with the nuclear ground state density $\rho_0 \approx 0.16 \frac{nucl}{fm^3}$, and heated up to T = 80 - 100 GeV. The so-called *fireball* is created. The lifetime of the fireball is with $\sim 10^{-22}$ s extremely short, which makes it necessary to search for sensitive observables for the understanding of the created matter (see section 1.1.3). The compressed matter is expanding and cools down until no further inelastic processes take place (so-called *chemical freeze-out*). After this point the number of produced stable particles stays constant[3]. The particles are however still interacting elastically until the so-called *kinetic freeze-out*. After this point, the momenta of the particles stay constant.

The outcome of a heavy-ion collision depends strongly on the collision geometry. The centrality of a collision is characterized by the impact parameter b, which is defined as the distance between the two centers of the colliding nucleons. The smaller the impact parameter, the more central the collision is. Collisions with large b are called peripheral collisions. Nucleons which are participating in the collision are called *participants*, while nucleons which pass the reaction zone without interaction are

[3]Weekly decaying or particles whose decays are suppressed by the OZI rule may live longer than the time of the chemical freeze-out.

called *spectators*. There is no direct observation of the impact parameter possible in the experiment, but it can be estimated based on the total number of emitted particles, the so-called *multiplicity*.

1.1.1 Particle production

The kinetic energy of colliding nucleons is partially transformed into production of new particles in inelastic processes. The center-of-mass energy available for particle production in fixed target experiments can be calculated with:

$$\sqrt{s} = \sqrt{2E_{kin,Beam} \cdot m_{Target}c^2 + (m_{Beam}^2 + m_{Target}^2)c^4}, \tag{1.1}$$

with the kinetic energy and mass of the beam particle $E_{kin,Beam}, m_{Beam}$ and m_{Target} the mass of the target particle. For example, this results in a threshold energy of $E_{kin,Beam} \geq 280$ MeV for π^0 production (m_{π^0} = 134.977 MeV/c^2) in proton-proton-collisions. Heavier particles have even higher nucleon-nucleon threshold energies.

Strangeness production

The lightest particles carrying strangeness are kaons, namely the $|\bar{s}u\rangle$-state K^+ and the $|s\bar{u}\rangle$-state K^- with a mass of $m_{K^\pm}$ = 493.677 MeV/c^2. The neutral kaons K_0 ($|K^0\rangle = |\bar{s}d\rangle$ and $|\bar{K^0}\rangle = |\bar{d}s\rangle$) have a mass of m_{K^0} = 497.614 MeV/c^2. The ϕ meson is the lightest $|s\bar{s}\rangle$-state with a mass of m_ϕ = 1019.455 MeV/c^2. Baryons carrying strangeness are called hyperons. The lightest hyperon is the $|uds\rangle$-state Λ with a mass of m_Λ = 1115.683 MeV/c^2. By definition strange quarks carry the quantum number S = -1 and anti-strange quarks S = +1. As strangeness is a conserved quantity in processes of the strong force, only associated production of strange and anti-strange quarks is possible. Therefore, positive kaons can only be produced together with a hyperon or a negative kaon. This leads to relatively high elementary production threshold energies and steep excitation functions. Figure 1.4 summarizes the multiplicities measured in central Au+Au (Pb+Pb) collisions at various accelerators (AGS, SPS and RHIC) compiled in the review [24]. Up to now, almost no data points from the multiplicities of strange particles, except charged kaons, for Au+Au collisions at low energies have been measured, therefore in the plot only data points from Ar+KCl reactions at 1.76 AGeV (see section 1.7.2) are included. One goal of this thesis is to include also data points from central Au+Au collisions. In table 1.1 the energetically cheapest elementary production channels for charged kaons and ϕ are listed. The complete strangeness production in Au+Au-collisions at 1.23 AGeV ($\sqrt{s_{AuAu}}$ = 2.41 GeV) is below the free nucleon-nucleon threshold.

Production channel	$E_{Beam,thr}$ [GeV]	$E_{Beam,AuAu} - E_{Beam,thr}$ [GeV]
$NN \rightarrow NK^+\Lambda$	1.58	-0.35
$NN \rightarrow NNK^+K^-$	2.49	-1.26
$NN \rightarrow NN\phi$	2.59	-1.36

Table 1.1: Elementary production channels for charged kaons and ϕ with the corresponding threshold energy and the energy the particles are produced below their elementary production threshold in Au+Au collisions at 1.23 AGeV.

Nevertheless, in heavy-ion collisions particles have been also observed below their free nucleon-nucleon threshold. The Fermi motion $p_F \approx 0.25$ GeV/c can provide additional energy in the center-of-mass system to create particles below their threshold. If the two Fermi momenta of the colliding

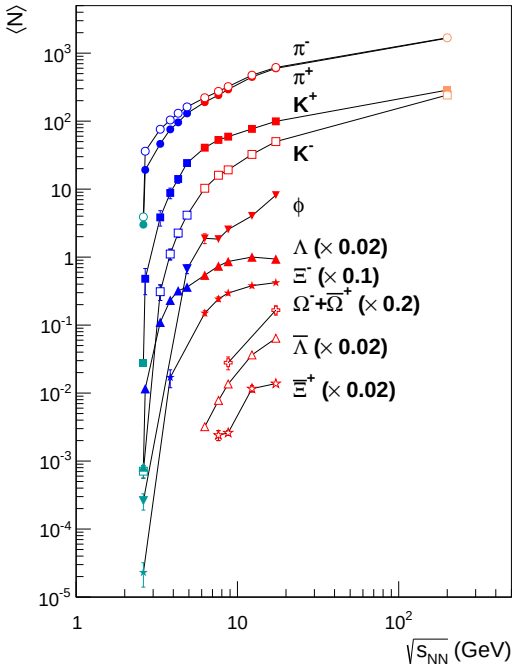

Figure 1.4: Excitation function of particles produced in central Au+Au (Pb+Pb) collisions ranging from AGS (blue) and SPS (red) to RHIC (orange), compiled in the review [24], data taken from [25, 26, 27, 28, 29, 30, 31, 32, 33, 34, 35, 36]. As there are almost no published data on strangeness production for central Au+Au collisions in the SIS18 energy regime, only data from Ar+KCl collisions are included [37, 38, 2, 39].

nucleons are exactly directed in the opposite direction, the production threshold can be maximally reduced. The probability for this is very small though, which makes additional particle production mechanisms more favorable to be the dominant channel for production below threshold. The most dominant mechanism is the accumulation of energy in multi-particle interactions. Which could be for example the production of a positive kaon and a Λ hyperon via a Δ resonance, as it is used in transport models (compare section 1.5):

$$\begin{aligned} NN &\rightarrow N\Delta \\ N\Delta &\rightarrow NK^{+}\Lambda. \end{aligned} \tag{1.2}$$

Furthermore, the particles can be produced off-shell in a first collision and then gain the necessary energy in a second collision.

1.1.2 Collective flow

As soon as the hot and dense system which was created in the collision of two heavy nuclei expands and cools down so-called flow patterns are developed. Those effects cause non-isotropic particle emission and a correlation between the momenta of the particles and their emission angles. One distinguishes various types of flow: radial, elliptic and directed flow. In a purely thermal scenario according to the fireball-model, the hot and dense medium created in a heavy-ion collision emits particles isotropically after its formation. The resulting particle spectra can be described by Boltzmann functions according to:

$$\frac{\mathrm{d}^3N}{\mathrm{d}p^3} \propto \exp(-E/T). \tag{1.3}$$

In a heavy-ion collision, strong pressure is built up in the reaction zone. This leads to an expansion of the created fireball. The particles acquire a Lorentz-Boost in radial direction, with radial flow velocity β_r, which leads to an additional mass dependent term to the inverse slope parameter T_{eff} of

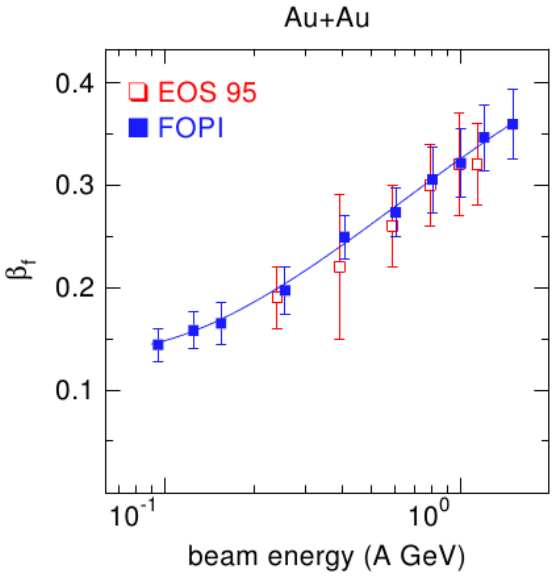

Figure 1.5: Measured radial flow velocities β_r as a function of the beam energy in Au+Au collisions [40].

the transverse particle spectra:

$$T_{eff} = \frac{1}{2} \cdot m \cdot \beta_r^2 + T_{kin}. \tag{1.4}$$

The shape of the spectra develop a kind of shoulder instead of showing a linear behavior in a semi-logarithmic scale and can be described with the blast wave model developed by P. J. Siemens and J. O. Rasmussen [41]:

$$\frac{\mathrm{d}^2N}{2\pi p_t \mathrm{d}p_t y_0} = C \cdot E \cdot \exp\left(-\gamma_r \frac{E}{T}\right)\left[\left(\gamma_r + \frac{T}{E}\right) \cdot \frac{\sinh\alpha}{\alpha} - \frac{T}{E} \cdot \cosh\alpha\right], \tag{1.5}$$

with $\alpha = (\gamma_r \beta_r p)/T$, $\gamma_r = \frac{1}{\sqrt{1-\beta_r^2}}$, a normalization constant C, the radial flow velocity β_r, the freeze-out temperature T, the energy E and the momentum p of the particle in the center-of-mass system. Figure 1.5 shows measured radial flow velocities β_r as a function of the beam energy in Au+Au collisions [40]. For Au+Au collisions at a center-of-mass energy of $\sqrt{s}$ = 2.41 GeV, a radial flow velocity of β_r = 0.3 - 0.4 is expected.

The elliptic and directed flow can be quantitatively described in terms of anisotropies of the azimuthal emission pattern with respect to the reaction plane, expressed by a Fourier series:

$$\frac{\mathrm{d}N}{\mathrm{d}\phi} \propto (1 + 2v_1\cos(\phi) + 2v_2\cos(2\phi) + ...). \tag{1.6}$$

The first order Fourier coefficient v_1 describes the directed flow, which corresponds to the collective sideward deflection of the particles in the reaction plane. v_2, the second order Fourier coefficient, quantities the elliptic flow, which describes the emission pattern in, respectively out, of the reaction plane. The reaction plane can be estimated in HADES with help of the forward-wall installed at the end of the setup (see section 2.5).

1.1.3 Observables

As already mentioned, a direct measurement of the conditions inside the fireball is not possible because of its short lifetime. In detectors, only reaction products and their kinetic distributions can be

measured. Different observables which allow to draw conclusions on the early stage of the hot and dense reaction zone are:

- **Particle multiplicities**. The comparison of the chemical composition of the heavy-ion collision with a statistical hadronization model allows to draw conclusions about thermodynamical properties like temperature T and baryochemical potential μ_B of the reaction zone (see section 1.4.1).

- **Transverse momentum distributions**. The inverse slope parameters of transverse momentum spectra of the particles can be interpreted as a superposition of radial expansion and the kinetic freeze-out temperature of the system.

- **Anisotropies in polar or azimuthal angular distributions**. Anisotropies in the angular distributions allow to draw conclusions about, for example, attractive or repulsive potentials between participants. HADES can measure the angular distributions of identified particles with respect to the bulk matter by estimating the event-plane with the recently installed forward-wall. Especially the elliptic flow of kaons and antikaons allows to draw conclusions on a possible kaon-nucleon potential and the equation of state for nuclear matter (compare section 1.6).

1.2 The generation of hadron masses

All our stable visible matter is built from nuclei, which are formed from protons and neutrons. The strong force is the reason for the binding of the constituents in the nucleus. The mass of the nucleus is given by the sum of the masses M of its constituents minus their binding energy B:

$$M(A,Z) = ZM_p + (A-Z)M_n - B(Z,A), \tag{1.7}$$

with A being the number of nucleons and Z being the number of protons in the nucleus. The binding energy per nucleon has a weak dependence on the number of constituents A and has a value of around 7 - 9 MeV for most nuclei. In lepton scattering experiments it was found that the nucleons consist mainly out of three valence quarks, which define the quantum numbers of the object. In contrast to the nucleus, the mass of the nucleon is with 938 MeV/c^2 $\approx$ 50 times larger than the sum of the masses of its valence quarks, which has been extracted to be smaller than 10 MeV/c^2 for up- and down-quarks. The strong force between the quarks is generating some additional mass instead of reducing it. An explanation for the generation of additional mass can be given on a phenomenological level by the usage of Heisenberg's uncertainty relation:

$$\Delta x \Delta p \geq \hbar \tag{1.8}$$

and Einstein's relation between energy and momentum:

$$E = \sqrt{p^2c^2 + m^2c^4}. \tag{1.9}$$

As a result of the small radius of a nucleon of around 1 fm, the uncertainty on the momentum Δp is at least 200 MeV/c (with $\hbar c$ = 200 MeV fm). By using formula 1.9, the total energy of the nucleon can be estimated to be $\approx$ 999 MeV. This explains the hadron mass by dynamical generation.

1.3 Quantum Chromo Dynamics and chiral symmetry

The interaction between quarks and gluons inside a hadron can be described by the relativistic quantum field theory QCD (**Q**uantum **C**hromo **D**ynamics). It is a non-abelian gauge theory with the symmetry group SU(3). The analogue to the electric charge in QED is a property called color, which gives the theory the name chromo dynamics. QCD shows two peculiar properties: confinement and asymptotic freedom. Confinement describes the phenomenon that single quarks have never been observed in nature, as they are always bound inside color-neutral objects like mesons and baryons [42]. The strong force between two quarks stays constant when the distance between the quarks increases, unlike in case of QED. Once the energy in the gluon field is high enough, another quark anti-quark pair is created. Asymptotic freedom describes the fact that the bonds between quarks and gluons becomes asymptotically weaker as the energy increases and distances decrease. The coupling constant decreases with momentum transfers, α_S is therefore called *running coupling constant*. If the coupling constant is small, calculations can be done perturbatively. This is not possible in case α_S is close to one, therefore phenomenological models are needed in this regime.

Each field theory is based on local and global symmetries. Local symmetry means that the symmetry acts independently at each point in spacetime and requires the introduction of gauge bosons. In QCD the degrees of freedom of the SU(3) symmetry define a local symmetry. To define a global symmetry, all symmetry transformations must be simultaneously applied to all points of spacetime. One global symmetry of QCD is the chiral symmetry if quarks are massless. For massless particles, chirality is identical to the helicity of a particle. If the spin of a moving particle points into the same direction as its momentum (positive helicity), the particle is right-handed and if the spin points into the opposite direction (negative helicity), the particle is left-handed. An observer of a massive particle can move into a reference frame in which he can overtake the particle. In this frame, the particle is moving into the other direction and as a consequence the helicity changes. Chiral symmetry describes the independent transformations of left- and right-handed particles. These transformations can be divided into vector symmetry $V = L + R$ and axial symmetry $A = L - R$.

The Higgs field leads to an explicit breaking of the chiral symmetry, as it generates the small current quark masses. As the masses of the light quarks are below 10 MeV/c^2 and even the mass of the strange quark ($m_S \approx 150$ MeV/c^2) [43] is small compared to the chiral symmetry breaking scale $\Lambda_\chi \cong 4\pi f_\pi \approx 1$ GeV, with the weak pion decay constant $f_\pi \cong 93$ MeV, chiral symmetry is still an approximate symmetry. In addition, the chiral symmetry of QCD is spontaneously broken due to a non-vanishing expectation value of the quark-antiquark-condensate $\langle \bar{q}q \rangle$. This breaks the degeneracy of chiral partners like the π and the σ meson and leads to the generation of hadron masses. Figure 1.6 illustrates the spontaneous symmetry breaking by using a mechanical example. The spontaneous symmetry breaking implies the existence of massless Goldstone bosons, the pions (which would be massless if chiral symmetry is not explicitly broken).

If the QCD vacuum becomes thermally excited, the condensate is melting and as a consequence, chiral symmetry gets restored ($\langle \bar{q}q \rangle \rightarrow 0$). In case of an environment of high baryonic densities, the chiral condensate can be literally squeezed out and is predicted to be reduced. This should be reflected in the modification of the spectral properties of the particles. Both situations can be achieved with heavy-ion collisions (see section 1.1). For a nice review about perspectives and controlled realizations of confinement and chiral symmetry breaking we recommend [44], [46] and [47]. Figure 1.7 shows the expectation value of the quark-antiquark condensate as a function of temperature and density within a Nambu-Jona-Lasinio model [45]. The area in this figure indicates the experimentally accessible region for the experiments at the SIS18 accelerator. According to these calculations, the expectation value of the chiral condensate already decreases by 30 - 50% at the reached densities and

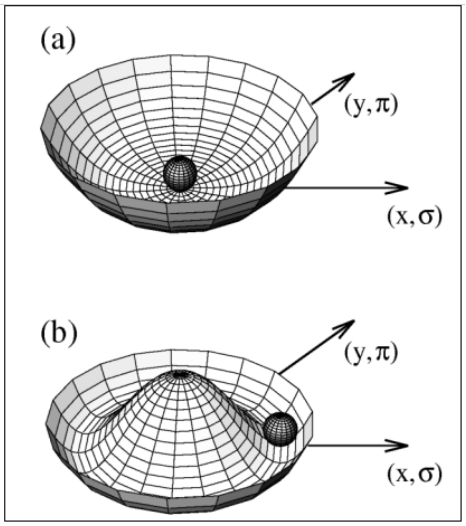

Figure 1.6: Illustration of spontaneous chiral symmetry breaking. (a) The ground state is in the center, the potential and the ground state are invariant under rotations. (b) The center is an unstable local maximum, the ground state is at the bottom of the valley. A ball would roll from the maximum into the ground state somewhere in the valley. This breaks the rotational symmetry of the ground state. [44]

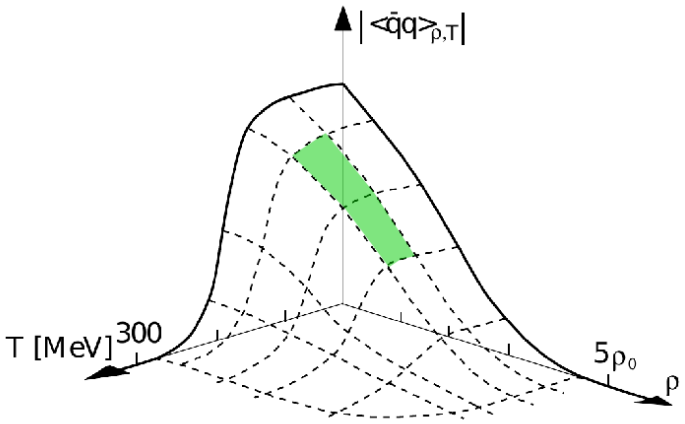

Figure 1.7: Expectation value of the quark-antiquark condensate as a function of temperature and density in a Nambu-Jona-Lasinio model [45]. The green area shows the region where the SIS18 is operating. According to these calculations, the expectation value of the chiral condensate already decreases by 30 - 50% at the reached densities and temperatures.

temperatures. However, it is not possible to study the chiral condensate directly. QCD sum rules provide a connection between the expectation value of the condensate and hadronic properties, using spectral functions [48, 49]. Since spectral functions are integrated (with an energy weight), QCD sum rules can only give constraints where the condensate is expected to change appreciably and do not give exact predictions for masses and widths of hadrons. The following section will give a more detailed overview on chiral models and their application to charged kaon production.

1.3.1 Strangeness production in chiral models

Chiral models are phenomenological models describing effective interactions of hadrons with the help of Lagrangians. In field theories, the symmetries of the Lagrangian lead to conserved quantities, respectively currents. The Lagrangian of massless fermions for example is invariant under axial and vector transformations which means that the left- and right-handed parts of Dirac-fields may transform independent. When one introduces a mass term, the axial vector symmetry gets explicitly broken. But as the masses of the light quarks u and d with 5 - 10 MeV/c^2, and even of s with 150 MeV/c^2, are small compared to the relevant scale, the symmetry is approximately realized. The spontaneous breaking of the chiral symmetry can be nicely described in case of the pion. The vector transformation of a pion is for example the rotation in isospin space which is conserved in strong interactions. The axial vector transformation rotates the chiral partners into each other. The chiral partner of the pion is the σ meson. If chiral symmetry holds, these partners should have the same mass, which is clearly not the case ($M_\pi \approx 135$ MeV/c^2 $\neq M_\sigma \approx 600$ MeV/c^2), the chiral symmetry is thus spontaneously broken. However, comparisons to experiments showed that it is still a good approximation, as the calculations for the weak π decay constant and for the π-nucleon coupling constant are in nice agreement with experimental data.

One simple chiral model is the linear sigma model involving pions and nucleons, which was introduced by Gell-Mann and Levy already in 1960 [50]. The Lagrangian includes π-nucleon interactions, the nucleon mass term, the $\pi - \sigma$ potential ("Mexican Hat-potential") and kinetic energy terms. In this model, the explicit symmetry breaking is introduced by a pion mass $\neq 0$ and for nucleons by the so-called pion-nucleon sigma term $\Sigma_{\pi N} \cong q_\pi f_\pi \frac{m_\pi^2}{m_\sigma^2}$. With help of the Gell-Mann-Oakes-Renner equation [51], it is possible to relate f_π to the quark-antiquark condensate:

$$m_\pi^2 f_\pi^2 \cong -\frac{1}{2}(m_u + m_d)\langle \bar{u}u + \bar{d}d \rangle. \tag{1.10}$$

Chiral Perturbation Theory (ChPT) offers a way to tell what terms have to be included in the Lagrangian of the model [52]. For example, it describes S-matrix elements for scattering amplitudes with the help of an effective Lagrangian. It is not a perturbation theory in the classical sense, as the power counting of terms contributing to the Lagrangian is not formulated in terms of the coupling constant of QCD, but in pion momenta and masses. The validity scale is given by renormalization arguments to be below $4\pi f_\pi \cong 1GeV$ or below the mass of the lowest lying resonance, the σ meson, as it corresponds to a singularity of the S-matrix. The mass of the included nucleons is in the same order of the relevant scale. To make sure that the model is still valid, an additional expansion in terms of the velocity of the nucleons is included, as their kinetic energy is low compared to the one of pions at same momenta ($\sim \frac{p^2}{2M_N}$).

Kaplan and Nelson were the first who applied the chiral Lagrangian to kaons [53, 54]. The extension to the full SU(3) flavour sector turned out to be very complicated. While the πN and KN interaction can be treated perturbatively, the $\bar{K}N$ interaction is already around threshold dominated by resonances. As a consequence, non-perturbative approaches in chiral dynamics have been developed.

The treatment of the Lagrangian in the full SU(3) sector leads to a coupled-channel problem, which could be in a first attempt avoided by switching to an effective chiral Lagrangian on the mean field level:

$$\mathcal{L} = \bar{N}(i\gamma^\mu\partial_\mu - m_N)N + \partial^\mu\bar{K}\partial_\mu K - (m_K^2 - \frac{\Sigma_{KN}}{f_\pi^2}\bar{N}N)\bar{K}K - \frac{3i}{8f_\pi^2}\bar{N}\gamma^\mu N\bar{K}\overleftrightarrow{\partial_\mu}K, \quad (1.11)$$

with the kaon fields $K = (K^+\ K^0)$ and $\bar{K} = (K^-\ \bar{K}^0)$, the nucleon fields $N = (p\ n)$ and $\bar{N} = (\bar{p}\ \bar{n})$ and the kaon-nucleon sigma term Σ_{KN} [55]. It contains kinematic, mass and kaon-nucleon interaction terms. The third term corresponds to the attractive scalar kaon-nucleon interaction term from Kaplan and Nelson. This term depends on the magnitude of the kaon-nucleon sigma term. Whereas the pion-nucleon sigma term is well known from pion-nucleon scattering ($\Sigma_{\pi N} \approx 45$ MeV), the kaon-nucleon sigma term is an uncertain quantity, but predicted to be around $\Sigma_{KN} \approx 400$ MeV. The last term is the so-called Weinberg-Tomozawa term, which corresponds to vector interactions [56]. This term is repulsive for kaons and attractive for antikaons. The Gell-Mann-Oakes-Renner equation can again be used to relate the kaon mass to the quark condensates:

$$m_K^2 f_K^2 \cong -\frac{1}{2}(m_u + m_s)\langle\bar{u}u + \bar{s}s\rangle. \quad (1.12)$$

The nucleon expectation value of this equation defines the kaon-nucleon sigma term:

$$\Sigma_{KN} = \frac{1}{2}(m_u + m_s)\langle N|\bar{u}u + \bar{s}s|N\rangle. \quad (1.13)$$

ChPT calculations predict a repulsive s-wave scattering length for K^+N and an attractive one for K^-N. As a consequence, kaon condensation in dense matter becomes possible. This would have a strong impact on the stability of neutron stars. K^- condensation would lead to additional negative charge and therefore to an increase of the proton fraction in the neutron stars. The consequence is a softening of the equation of state (see section 1.6). At nuclear densities of around 4 - 5 times nuclear saturation density, the onset of K^- condensation can be reached, as the electron chemical potential starts to exceed the one of the kaons. As a consequence, the maximal neutron star mass possible before it collapses into a black hole reduces to 1.5 solar masses. However, experimentally there are no signs for a resulting large number of black holes in the universe and neutron stars with masses higher than 1.5 solar mass have been observed[4]. The results for the repulsive potential for positive kaons of $V\approx$+(20 - 30) MeV are in a nice agreement with results for the K^+N scattering length and other theoretical estimates. However, in case of the K^- potential the models strongly differ from experimental observations in the investigation of kaonic atoms. The reason for this difference was found to be the presence of the $\Lambda(1405)$ resonance, which is located just below the free KN threshold. ChPT is not able to generate resonances directly, but it predicts strong interactions between protons and K^-, which can generate the $\Lambda(1405)$ resonance. The depth of the antikaon-nucleon potential ranges from $V\approx$-(50 - 100) MeV within chiral coupled-channel dynamics to $V\approx$-(100 - 200) MeV predicted by mean-field approaches. The first mean-field calculations were carried out using the Nambu-Jona-Lasinio (NJL) model [45]. With such models, kaon mass shifts in nuclear matter and kaon dynamics in heavy-ion collisions can be investigated. Figure 1.8 shows the density dependence of the in-medium mass in nuclear matter calculated from mean-field models. Inputs are taken from experimental measurements of the K^+N scattering length, and the isospin-averaged K^-N scattering

[4]PSR J1614-2230 with 1.97 $\pm$ 0.04$M_\odot$ (Demorest et al.) and PSR J0348+0432 with 2.01 $\pm$ 0.04$M_\odot$ (Antoniadis et al.)

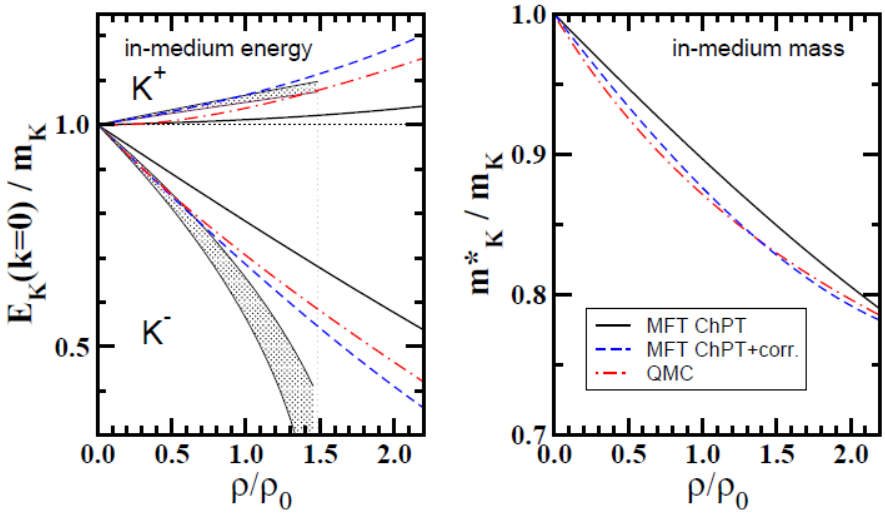

Figure 1.8: In-medium kaon energy (left) and quasi-particle mass (right) as a function of density in the chiral mean-field theory (MFT ChPT) and after including higher order corrections (MFT ChPT+corr) [57]. The bands correspond to experimentally observed results from experimental K^+N scattering and K^- atoms. [58].

length from kaonic atom data [58]. Due to the different sign of the vector potential of kaons and antikaons, their behavior as a function of density is different. Whereas the K^+ mass is increasing, the K^- mass decreases with density. As a result, the production of antikaons becomes energetically easier, which would lead to an enhanced yield. The K^+ yield on the contrary is predicted to be reduced, as it becomes energetically more expensive. However, as their production is coupled, the overall yield of particles carrying strangeness is expected to change, if at all, only slightly.

And what about chiral symmetry restoration?

It is not easy to combine the obtained medium properties from chiral dynamics and connect them to the restoration of chiral symmetry. The pseudoscalar meson masses are directly proportional to the scalar condensates via the GOR relation (Equation 1.12). When chiral symmetry is restored, the scalar quark condensate vanishes. Therefore, in the mean-field picture, the effect of the dropping mass from the Kaplan-Nelson term can be interpreted in terms of a partial restoration of the chiral symmetry.

1.4 Phase diagram of nuclear matter

Phase diagrams summarize thermodynamical information about the conditions of matter. Analogously to the well known phase diagram of water, which displays the different phases water (liquid), ice (solid) and vapor (gaseous) with their phase boundary lines, the triple and the critical point, results from heavy-ion experiments and theory have been put together in the phase diagram of nuclear matter. Figure 1.9 shows one version of this diagram as a function of temperature T and baryochemical potential[5] μ_B. At zero temperature and nuclear ground state density ρ_0 = 0.16 fm^{-3}, the quarks are bound to nucleons with a volume[6] of around 6 fm^3. At higher temperatures, the system can

[5]The baryochemical potential equates the energy which is needed to add or remove a baryon in a baryonic system.
[6]Note that the nucleon does not have a well defined volume as the charge distribution drops exponentially.

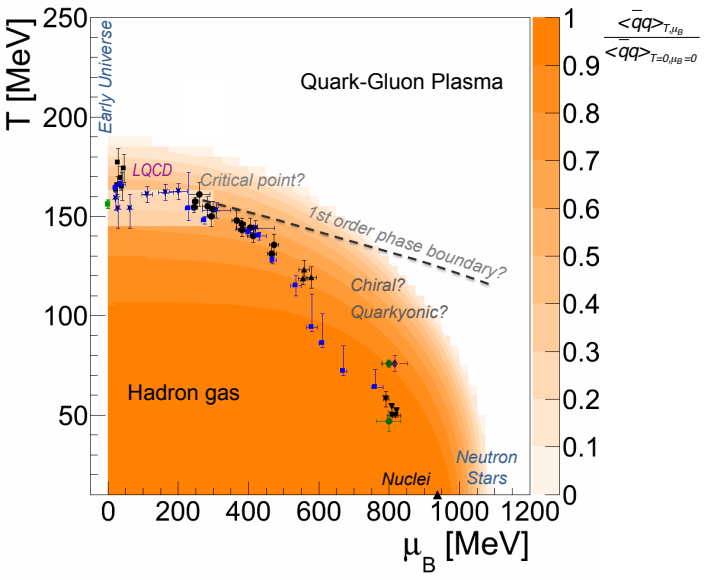

Figure 1.9: Phase diagram of nuclear matter in the temperature T and baryochemical potential μ_B representation. The data points are estimated from a statistical model fit to particle yields measured at SIS, AGS, SPS and RHIC energies. The color code corresponds to the quark-antiquark-condensate ratio $\langle\bar{q}q\rangle_{T,\mu_B}/\langle\bar{q}q\rangle_{T=0,\mu_B=0}$ [59].

be described as a hadron gas. If the system is heated up to a critical temperature, a crossover to the quark-gluon plasma (QGP) can be achieved. In this stage the quarks and gluons are supposed to be deconfined and chiral symmetry is predicted to be restored ($\langle\bar{q}q\rangle \rightarrow 0$). The crossover to the deconfined state can be imagined as follows: due to an increase of the energy in the system, more pions are produced, as a result, the hadron density and frequency of their interactions is so high, that an allocation of the quarks and gluons to a hadron is not possible anymore. At these low μ_B, the phase transition happens smoothly without discontinuities [60, 61]. For higher baryochemical potentials a phase transition of first order is expected [62]. If the system is compressed, it can be imagined, that the nucleons start to overlap and the quarks and gluons seem to be free. The changing of the order of the phase transition from a cross over to first order leads to the prediction of a critical end point (CEP) [63, 64, 65, 66]. At densities towards values above this critical point it is not clear if the transition to the quark-gluon plasma is different from the one to chiral symmetry restoration. The predicted state in this region is called quarkyonic matter [67, 68, 69]. In the region of even higher densities and zero temperatures neutron stars are located.

Lattice QCD solves the QCD equations on a discrete space-time lattice. A critical temperature T_C for the phase transition at low baryochemical potentials into a quark-gluon plasma around 154 MeV has been derived [70, 71]. An advantage of lattice calculations is that there is no input from effective models needed, as the exact QCD Lagrangian is subjected to Monte-Carlo simulations. But drawbacks are time consuming calculations and systematic uncertainties, which arise mainly due to the finite lattice spacing. The region of finite baryochemical potentials cause additional problems for lattice QCD calculations, as a result phenomenological models become more important here and the exact location of the CEP can not be predicted.

Heavy-ion collisions provide the unique opportunity to heat and compress nuclear matter. The different facilities reach different bombarding energies resulting in different thermodynamical properties of the produced fireball, so that different areas in the phase diagram can be explored. The

experiments at LHC[7] [72] are probing the region of high temperatures and low densities. The RHIC[8] [73] beam energy scan (BES) has the main goal to search for the critical point. It is operating over a broad range of center-of-mass energies between $\sqrt{s_{NN}}$ = 7.7 - 200 GeV. One proposed observable are higher moments of the event-by-event net baryon number distribution [74]. The experiments at GSI, for example HADES, are exploring the region of rather low temperatures but high μ_B. In the future, the CBM[9] experiment at FAIR[10] [75] will perform measurements at high baryochemical potential and moderate temperatures.

1.4.1 Strangeness production within statistical hadronization models

Statistical **H**adronization **M**odels (SHM) have been used to successfully describe particle yields in heavy-ion collisions for various collision systems and beam energies [76]. The basic assumption is that the particles are emitted from a homogenous source, whereas the particle number densities of type i for an infinite volume are proportional to the integrals over the particle momentum p

$$\rho_{i,q} \propto \int_0^\infty p^2 \mathrm{d}p \exp \frac{-E_i + \bar{\mu}\bar{q}_i}{kT}, \tag{1.14}$$

which is in thermal equilibrium and can therefore be described as a grand canonical ensemble. The quantum numbers baryon number B, strangeness S and charge Q are conserved on average by using chemical potentials μ_B, μ_S, and μ_Q. μ_S and μ_B are usually constrained by the initial state. The parameters to describe the system are the temperature T, the chemical potential μ_B, and the volume V, respectively the radius of the system R_V. In the SIS18 energy regime, strangeness is produced rarely. Therefore, strangeness conservation is explicitly treated by the model in a canonical approach. In the SHM this is realized by introducing a smaller volume with radius R_C inside the fireball, in which strangeness is calculated canonically and exactly conserved. The ϕ meson has no open strangeness by definition and is therefore not suppressed by R_C. As a result, the thermal model predicts a rise of the ϕ to K^- ratio towards low energies. The smaller the radius R_C, the more pronounced the rise. To estimate the parameters T, μ_B, R_V and R_C, the measured particle yields are fitted with the model. In the strangeness canonical ensemble, the parameter T is usually constrained by the ratio of strange to non-strange particles, for example K/π, ϕ/K, or p/Λ, and μ_B by the ratio of mesons to baryons, for example π/p or K/Λ. The resulting parameters correspond to the chemical freeze-out point of the system, and can be placed into the phasediagram of strongly interacting matter (see figure 1.10). Surprisingly, all estimated parameters from various experiments at different $\sqrt{s}$ seem to line up on one universal freeze-out curve with $E/N \approx 1$ GeV, even at low energies, where no thermal equilibrium is expected [77].

[7] **L**arge **H**adron **C**ollider at CERN
[8] **R**elativistic **H**eavy-**I**on **C**ollider at Brookhaven National Lab
[9] **C**ompressed **B**aryonic **M**atter experiment
[10] **F**acility for **A**nti-proton and **I**on **R**esearch

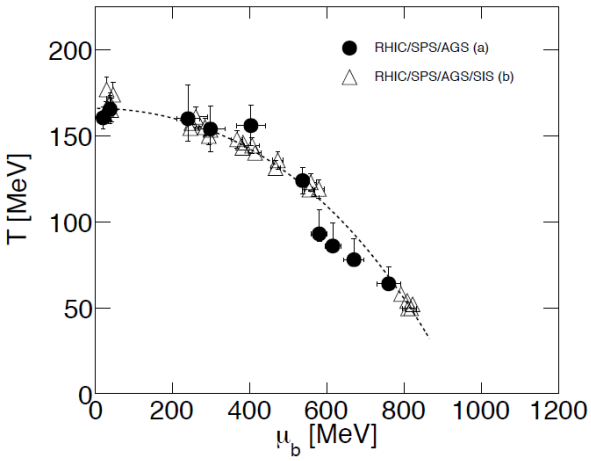

Figure 1.10: Chemical freeze-out points estimated from fits with statistical hadronization models to measured particle yields. The dashed line corresponds to $E/N \approx 1$ GeV. (Data from [76, 78])

1.5 Strangeness production in transport models

A tool to obtain a deeper understanding of the dynamics of a heavy-ion collision are transport model calculations. Those microscopic models simulate the whole reaction, starting from first-chance collisions, until the formation of the finally observed particles. The input to the models are particle properties (e.g. pole masses, life times in vacuum, etc.), elementary cross sections and interactions among the different particles. Unknown cross sections are usually constructed with the additive quark model. To get a consistent description of the dynamics of heavy-ion collisions over the whole energy range, one has to deal with a lot of different production mechanisms of particles, e.g. compound nucleus formation, deep inelastic scattering at the Coulomb barrier, string excitation and fragmentation, and parton scattering. At low energies, it is convenient to use hadronic degrees of freedom, whereas at higher energies the direct contributions from quarks and gluons have to be taken into account. In the SIS18 energy regime, resonances are treated as quasi-particles which propagate and scatter in the medium. After a certain lifetime they decay into other resonances or stable hadrons. At higher energies, the resonances are dominated by continuous string excitations.

The first microscopic transport models were cascade-models, in which nucleons are treated as point-like particles. A reaction takes place when two particles come closer to each other than a certain distance (*cross section*). Wether a reaction is elastic or inelastic and the distribution of momenta and angles is based on probabilistic decisions. To take into account also the influence of nuclear potentials, extensions of these models, for example the Boltzmann-Uehling-Uhlenbeck (BUU) model [79] and its relativistic extension (RBUU) [80], or the GiBUU model [81], have been developed. The degrees of freedom of these models are baryons and mesons. From phenomenological effective Lagrangians, solvable equations of motion are derived. In those models the particles feel an average potential of the surrounding particles between the collisions. The effective potential usually used in these models are Skyrme-like [82] and depend on the baryon density ρ:

$$U(\rho(\vec{q}_i)) = \alpha \left(\frac{\rho}{\rho_0}\right) + \beta \left(\frac{\rho}{\rho_0}\right)^{\gamma}. \tag{1.15}$$

A test particle method is used to solve the Boltzmann equation with so-called parallel ensembles. The baryon density $\rho(\vec{q}_i)$ is averaged after each time step over all parallel ensembles, estimated by counting the point-like particles in a defined volume around the position $\vec{q}_i$. While the collisions are worked out in each ensemble separately. In Quantum Molecular Dynamics (QMD) [83], its relativistic versions RQMD [84] and UrQMD [85], and the isospin quantum molecular dynamics approach IQMD [86], the

K^+	K^-	type
$BB \rightarrow BYK^+$	$BB \rightarrow BBK^+K^-$	strangeness production (primary/secondary)
$\pi B \rightarrow YK^+$	$\pi B \rightarrow BK^+K^-$	strangeness production (secondary)
	$BY \rightarrow BBK^-$	strangeness exchange
	$\pi Y \leftrightarrow BK^-$	strangeness exchange
$YK^+ \rightarrow \pi B$		strangeness absorption
$BK^{+/0} \leftrightarrow BK^{0/+}$	$BK^- \leftrightarrow BK^-(K^0)$	elastic/charge exchange
$\pi K^{+/0} \leftrightarrow \pi K^{0/+}$	$\pi K^- \leftrightarrow \pi K^-(K^0)$	elastic/charge exchange

Table 1.2: Elementary hadronic reaction channels for K^+ and K^- as used in transport models. B stands for nucleons and nucleon resonances (N, Δ, N^*) and Y for hyperons (Λ, Σ). [47]

particles are not treated as point-like, but as Gaussian wave packages in position and momentum space. A reaction takes place, if the positions of two particles are close enough. The elementary reaction channels for kaons included in these models are summarized in table 1.2. The cross sections for the different channels are, whenever possible, taken from experimental data. The unknown channels are usually parametrized.

The sub-threshold particle production is realized in multi-step processes by first exciting a resonance which interacts further with the medium and where the resonance acts as an energy reservoir (compare equation 1.2). Due to the rare appearance of strange particles in the SIS18 energy regime, the K^+ absorption on hyperons is strongly suppressed. The mean free path of K^+ mesons is therefore only influenced by scattering processes and thus rather long, for example λ_{mean} = 5 - 7 fm for nuclear ground state density. As a result, the positive kaons leave the reaction zone relatively undisturbed and carry the information from the hot and dense stage[11]. On the contrary, negative kaons show an attractive kaon-nucleon potential and can be reabsorbed in the so-called strangeness exchange reaction

$$K^- N \rightleftharpoons \pi Y, \tag{1.16}$$

with a nucleon N (proton or neutron) and a hyperon Y, for example Λ. As a result, the K^- couple over a much longer time to the system compared to the K^+. With the predicted in-medium mass shifts of kaons (see section 1.3.1), the strangeness exchange reaction becomes energetically exothermal for the K^- final state and is therefore predicted from transport models to be the most dominant production channel of K^- at SIS18 energies. Those predictions seemed to be confirmed by measurements of the KaoS collaboration (see section 1.7.1). However, the strong sub-threshold ϕ meson production and its influence on the observed kaon spectra, measured by the FOPI and HADES collaborations (see section 1.7.2 and 1.7.3), was not taken into account in those models, which therefore missed one of the important channels.

The ϕ meson is decaying with a branching ratio of BR = 48.9% into K^+K^-. Its mean decay length in the vacuum is $c\tau \approx 46$ fm, which is larger than the size of the fireball created in a collision. As a result, the decay occurs predominantly in the vacuum. This has a strong impact on the observed kinematic and thermodynamical observables of negatively charged kaons, as they are produced 30 - 50 times less abundantly then positive kaons. The ϕ meson is in transport models typically produced via string fragmentation at higher energies and in $BB \rightarrow BB\phi$ and $\pi B \rightarrow \phi B$ ($B = N, \Delta$) reactions, with the dominant contribution from pion-nucleon reactions in the low energy regime. To account for the large observed yield of ϕ mesons in heavy-ion collisions below 2 AGeV, the different models

[11] Note that charge exchange reactions can change this picture.

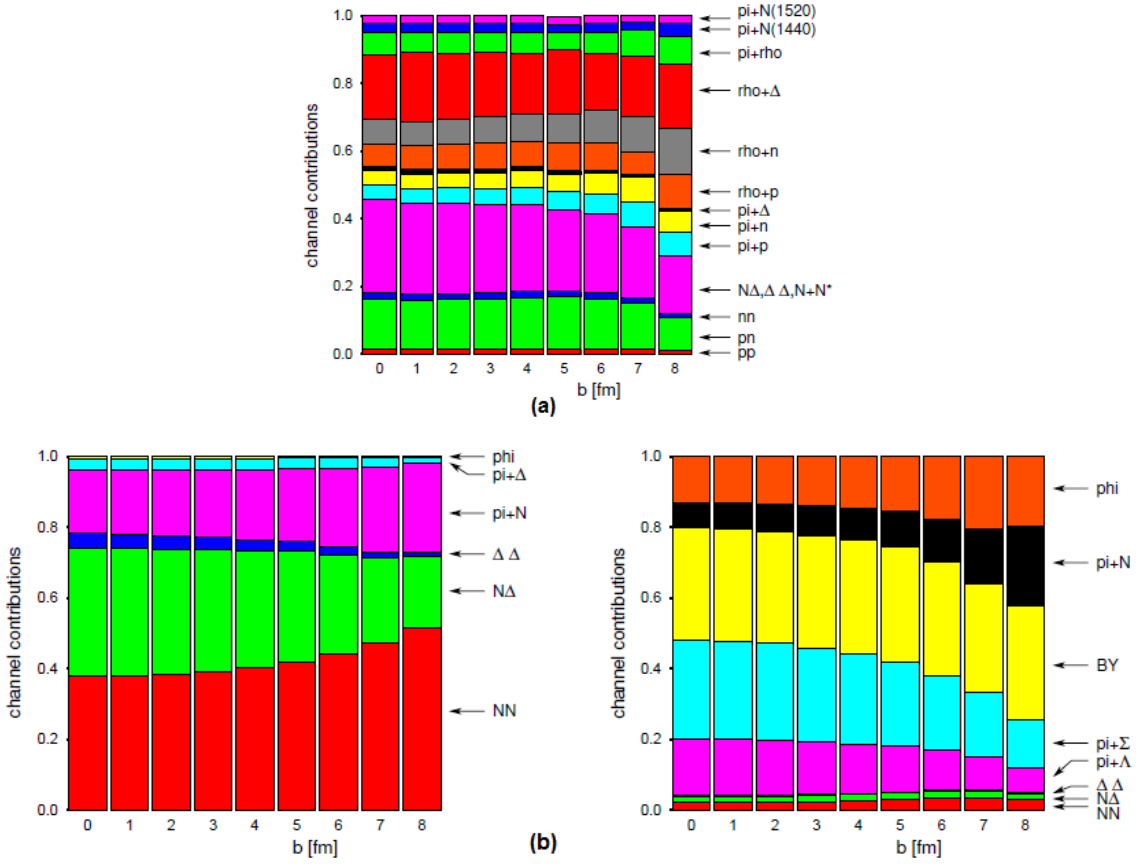

Figure 1.11: Contribution of individual channels for ϕ (a), K^+ (left side of (b)) and K^- (right side of (b)) production for various impact parameters b calculated with the Dresden-Rossendorf BUU model [87].

tuned their individual input channels for its production. For example the Dresden-Rossendorf-BUU model found a huge contribution from the $\rho B \rightarrow N\phi$ and $\rho\phi \rightarrow \phi$ channels. Figure 1.11 shows the contributing channels for ϕ production for various impact parameters and the different channels for kaon production in this model [87]. The UrQMD model, on the other hand, explored new resonance decays of the sort $N^* \rightarrow N + \phi$, with N^* being $N^*(1990)$, $N^*(2080)$, $N^*(2190)$, $N^*(2220)$ and $N^*(2250)$ [5]. The decay probabilities for these resonances are experimentally not well constrained. However, the decay probability of a heavy resonance into ϕN final states is extracted using data from proton-proton collisions at different energies near threshold from the ANKE collaboration, which is found to be $\Gamma_{N\phi} = 0.2\%\ \Gamma_{tot}$. With this improvement, the model is able to describe the measured ϕ/K^- ratio near the threshold energy, whereas it under-predicts the ratio for higher energies (compare figure 1.12). Another attempt are so-called *catalytic reactions* $\pi Y \rightarrow \phi Y$ and $\bar{K}N \rightarrow \phi Y$, with $Y = \Lambda, \Sigma$, which could contribute to the ϕ production [92]. The cross sections for such reactions are also not well known, which makes predictions strongly model dependent. These reactions are allowed by the OZI-rule [93, 94, 95], but suppressed due to the rare appearance of hyperons Y at low energies.

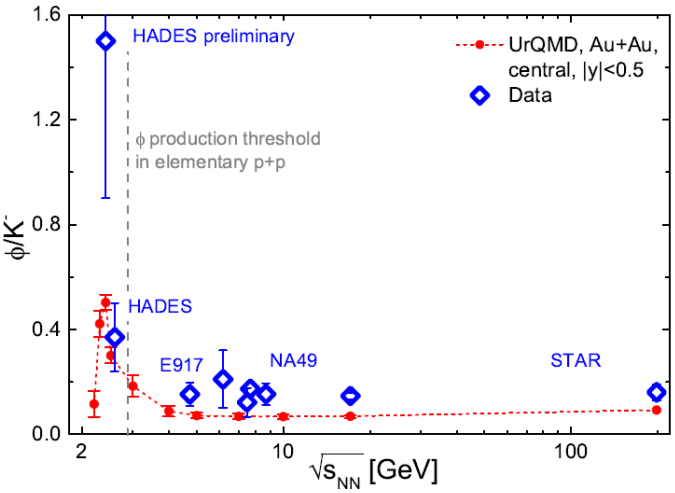

Figure 1.12: Measured ϕ/K^- ratio as a function of beam energy from various experiments [2, 88, 89, 90, 91] (Blue points) and calculation for central Au+Au collisions with the UrQMD model including the new N^* decays (red line) [5].

1.6 Nuclear equation of state

Equations **O**f **S**tate (EOS) describe correlations of thermodynamical variables like temperature T, pressure p, density ρ and number of particles N in equilibrium. In heavy-ion collisions, when nuclear matter is compressed and heated up, a thermodynamical equilibrium can be reached for short timescales. In this phase, the total center-of-mass energy per nucleon $\epsilon = \frac{E}{A}$ of the system can be divided into thermal energy ϵ_{th} and compressional energy ϵ_C:

$$\epsilon(\rho, T) = \epsilon_{th}(\rho, T) + \epsilon_C(\rho, T = 0) + \epsilon_0, \tag{1.17}$$

with the binding energy in the ground state $\epsilon_0 \approx$ -16 MeV/nucleon. The compressional energy depends strongly on the compressibility of nuclear matter:

$$\kappa = -V\frac{\mathrm{d}p}{\mathrm{d}V} = \left(9\rho^2\frac{\partial^2\epsilon_C(\rho, T = 0)}{\partial\rho^2}\right)_{\rho=\rho_0}. \tag{1.18}$$

When the matter expands, the compressional energy is released into collective motion or creation of particles which are mainly pions. Experimental results on the compressibility of nuclear matter in the region around the ground state density have been obtained by studying the iso-scalar giant monopole resonance in heavy nuclei [96, 97]. This resonance is excited by inelastic scattering of α particles on the nucleus. The measured energy spectrum depends on the resonance frequency (E=hω_0), which is a measure for the reset force. This reset force is proportional to the compressibility, which was estimated to be κ = 231 $\pm$ 14 MeV [98].

Already in the beginning of the 80ties, one of the primary goals of the first relativistic heavy-ion experiments and theory was to determine the equation of state of nuclear matter at higher energies [99]. The nuclear matter densities reached in heavy-ion collisions at SIS18/100 energies are believed to be almost of the same order as the one in neutron stars and as the temporarily formed densities during the core-collapse phase of supernova explosions. One parameter of the different theoretical models is the compressibility κ. One distinguishes between a stiff/hard ($\kappa \approx$ 380 MeV) and a soft EOS ($\kappa \approx$ 200 MeV). Figure 1.13 sketches the equation of state at T = 0 MeV for the two different values of κ. To draw conclusions on the real value of κ, different experimental observables have been compared to results from transport models. As suitable observables to extract information about

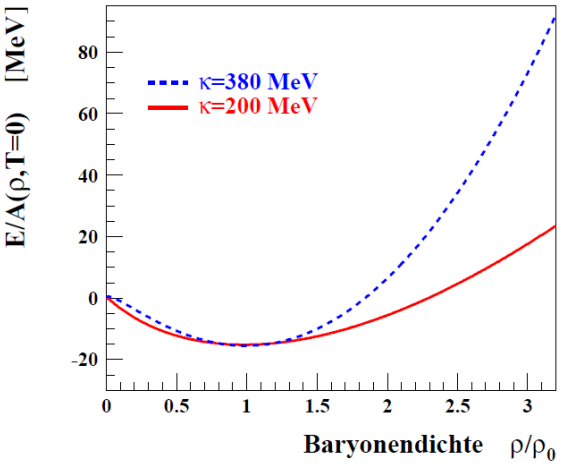

Figure 1.13: Skyrme equation of state at T = 0 MeV with two different values of the compressibility of nuclear matter κ = 380 MeV and κ = 200 MeV. Figure taken from [100].

the EOS and its stiffness in heavy-ion collisions meson production and collective flow of particles have been proposed. Hydrodynamic models suggested that the flow of nucleons transverse to the reaction plane is a measure for the pressure build up in the reaction zone [101, 102]. Measurements of the elliptic flow of protons in semi-central Au+Au collisions at 0.6 AGeV show a clear preference for a soft equation of state [103] [104]. The conclusions on pion production turned out to be not as sensitive on the stiffness of the equation of state as expected, as they undergo several absorption cycles through nucleon resonances till the final freeze-out. Figure 1.14 shows the total pion multiplicities per mass number in Au+Au over C+C reactions from the KaoS collaboration in comparison to theoretical predictions with a soft and a hard EOS. In addition to the observation that one can not distinguish between the two EOS with this observable, one can see that theory is not able to reproduce pion data in Au+Au collisions perfectly, as their production and/or absorption mechanisms are not fully understood.

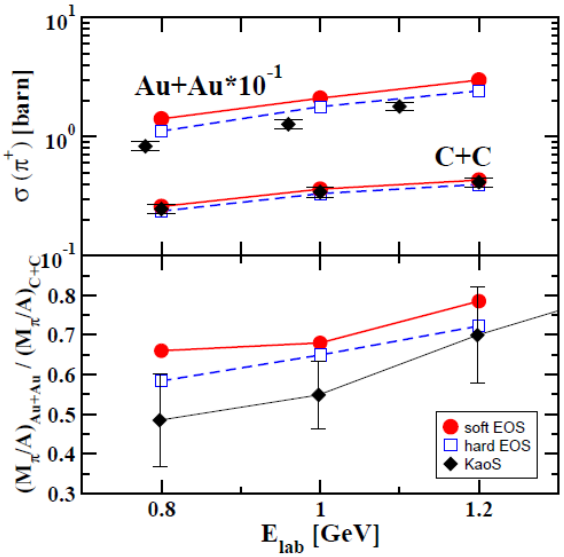

Figure 1.14: Top: Excitation function of the π^+ production cross section in Au+Au (scaled by 10^{-1}) and C+C reactions. Bottom: Ratio of the total pion multiplicities in Au+Au over C+C. The calculations were performed with a QMD transport code, using a hard/soft nuclear EOS and compared to data from KaoS. Figure taken from [47].

1.6.1 Probing the equation of state with kaons

As a promising tool to extract information about the equation of state of nuclear matter, kaon production in central heavy-ion collisions close to the elementary production threshold has been proposed [105]. The yield of K^+ strongly depends on the density created in the interaction, therefore it gives access to the stiffness of the EOS. When the equation of state is soft, less energy is needed to compress the matter, and therefore the density created in these collisions is higher. At energies below the threshold, the main production mechanism of K^+ according to transport models is the accumulation of energy in multi-step processes via a Δ resonance (compare section 1.5). If high densities are created, the Δ resonance has a higher probability to interact further with the medium before it decays, resulting in a higher yield of K^+. The most sensitive observable for the stiffness of the equation of state so far is the ratio of the K^+ multiplicity produced in a heavy system divided by the one produced in a light system [100]. The stopping power for the colliding nucleons is not so much pronounced in lighter systems than in heavy systems, as a result, the created density depends only little on the stiffness of the equation of state. The advantage of the ratio between the two systems is, that many uncertainties in the models cancel, because they act in the same way on both systems. Figure 1.15 shows the excitation function of the multiplicities per mass number of K^+ produced in Au+Au over C+C collisions, measured by the KaoS collaboration [100] in comparison to transport model calculations [106, 107] with a soft and a hard equation of state. The observable is most sensitive to the stiffness of the EOS at lower energies. In these models, the data is only compatible with a soft equation of state.

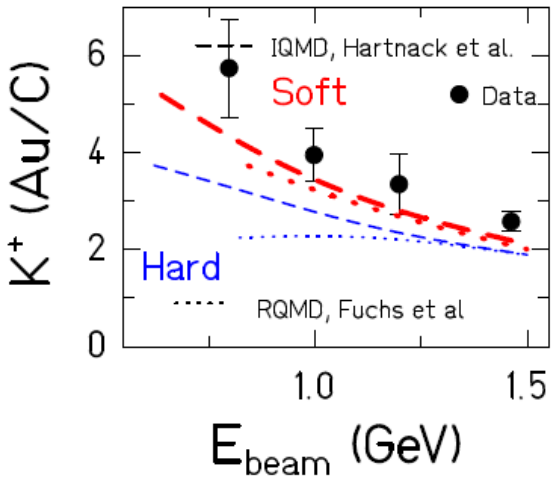

Figure 1.15: Excitation function of the multiplicities per mass number A of K^+ produced in Au+Au over C+C collisions. The experimental data measured by the KaoS collaboration [100] is compared to RQMD (dotted) [106] and IQMD calculations (dashed) [107] with a soft and a hard equation of state.

1.6.2 The equation of state for asymmetric matter

The nuclear composition in neutron stars is not isospin symmetric. To estimate also the response of nuclear matter to isospin asymmetry, the EOS can be expanded in terms of the asymmetry $\delta = \frac{\rho_n - \rho_p}{\rho}$, with ρ_n, ρ_p and ρ representing the neutron, proton and total densities:

$$E/A(\rho, \delta) = E/A(\rho, \delta = 0) + E_{sym}(\rho) \cdot \delta^2 + \mathcal{O}(\delta^4). \tag{1.19}$$

This is called the *asy-EOS*. E_{sym} corresponds to the symmetry energy and describes the difference between the energies of neutron matter (δ = 1) and symmetric matter (δ=0). Whereas E_{sym} at normal

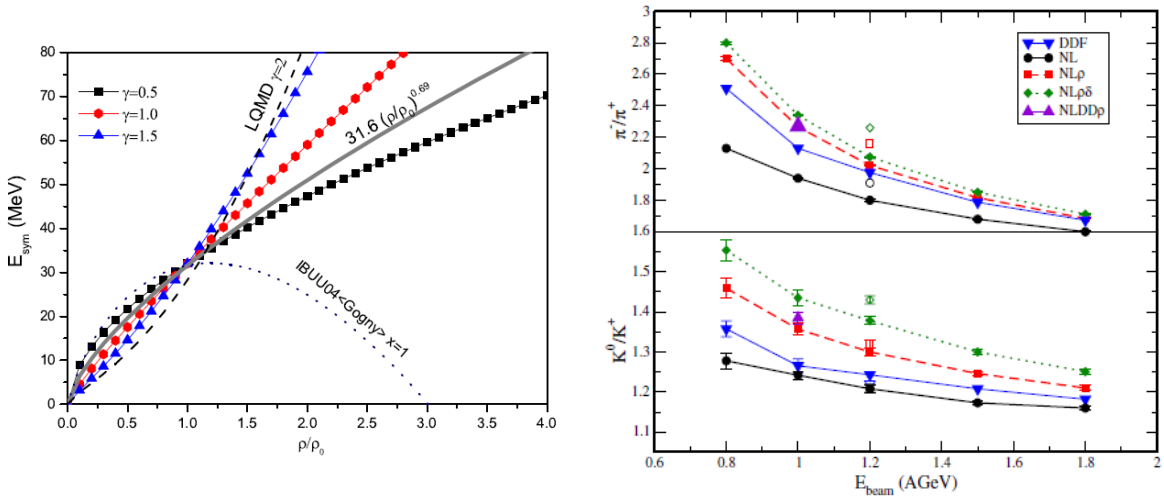

Figure 1.16: Left: Parameterizations of the nuclear symmetry energy as used in transport models. Result from UrQMD [108] for three different values for γ = 0.5, 1.0 and 1.5, result from IBUU with γ = 0.69 [109] and the super-soft and stiff parametrization from IBUU (dotted line [110]) and ImIQMD (labeled LQMD [111]). Figure taken from [112]. Right: Excitation function of the π^-/π^+ (upper) and K^0/K^+ (lower) ratios in Au+Au reactions calculated with a RBUU model for different stiffness of E_{sym}. Figure taken from [113].

nuclear density ρ_0 is basically known from the symmetry term in the Bethe-Weizsäcker mass formula and has a value between 28.1 MeV - 33.2 MeV [114], the theoretical predictions for the behavior of the symmetry energy at higher densities diverge strongly. The symmetry energy can be divided into a kinetic and a potential part. The kinetic contribution can be obtained with the Fermi-gas model and is proportional to $(\rho/\rho_0)^\gamma$, with γ = 2/3. The proportionality factor is approximately 1/3 of the Fermi energy ($\epsilon_F \approx 28$ MeV). The potential term reflects the properties of nuclear forces and dominates the symmetry energy. It is defined as the potential of saturation density 22 MeV times the relative nuclear density to the power of γ.

$$E_{sym} = E_{sym}^{pot} + E_{sym}^{kin} = 22\text{MeV} \cdot (\rho/\rho_0)^\gamma + 12\text{MeV} \cdot (\rho/\rho_0)^{2/3}. \tag{1.20}$$

Left side of figure 1.16 shows the parametrization of the nuclear symmetry energy as used in different transport models with various values for the exponent γ. The particle ratios of isospin partners have been suggested to provide an experimental access to the exponent γ [113]. Right side of figure 1.16 shows the expected ratios of the isospin partners π^-/π^+ and K^+/K_s^0 for different values of stiffness of the asy-EOS. Again, kaons are predicted to be a more sensitive probe than pions. First attempts to compare K^+ and K_S^0 production yields in Au+Au collisions at 1.23 AGeV have been performed in [115]. The results from the phase space dependent analysis of K^+ presented in this thesis will be compared to the ones on K_S^0 analyzed in [116].

1.7 Experimental results in the SIS18 energy regime

1.7.1 Charged kaon production measured with KaoS

Systematic investigations on the production of charged kaons in heavy-ion collisions in the SIS18 energy regime have been performed in the Nineties by the KaoS collaboration. Data for the systems

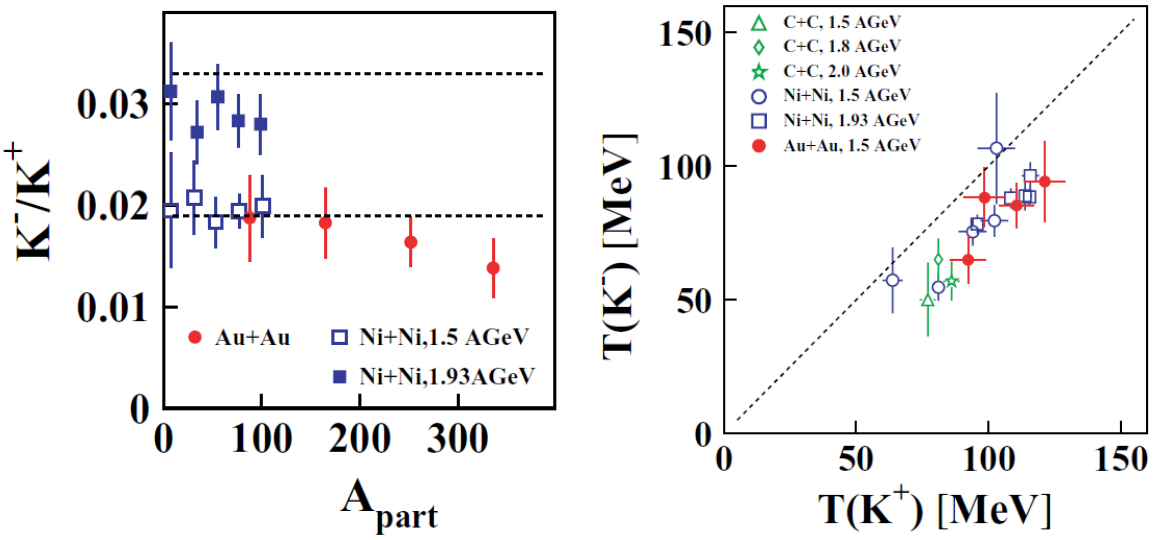

Figure 1.17: Results from the KaoS-collaboration. Left: K^- to K^+ ratio as a function of participating nucleons for different collision systems and energies. Right: Comparison of the inverse slopes of positive and negative kaons for different collision systems and energies. [4]

C+C (0.8, 1.0, 1.2, 1.5, 1.8 and 2.0 AGeV), Ni+Ni (1.1, 1.5 and 1.93 AGeV) and Au+Au (0.6, 0.8, 1.0, 1.135 and 1.5 AGeV) has been collected, a review can be found in [4]. One of the main findings was that the production of K^+ and K^- is linked, as the multiplicities show a very similar centrality dependence, despite their different production thresholds (see left side of figure 1.17). The K^+ and K^- multiplicities rise proportional to A^{α}_{part}, with α_{K^+}(Au) = 1.34 $\pm$ 0.16, α_{K^+}(Ni) = 1.26 $\pm$ 0.06, α_{K^-}(Au) = 1.22 $\pm$ 0.27 and α_{K^-}(Ni) = 1.25 $\pm$ 0.12. This supports the assumption, that the accumulation of energy by multiple collisions inside the reaction zone is the main production mechanism for K^+ production at these low energies, as predicted from transport theory (see section 1.5). The second observation was that there are differences in the energy spectra and polar angle distributions of the two kaon species. KaoS found that the inverse slope parameter of positive kaons is always higher than the one for negative kaons (15 - 25 MeV), which was at these times interpreted as a contradiction to a simultaneous freeze-out of the two particle species (see right side of figure 1.17). Also the polar angle distributions show a small forward-backward preference, which is more pronounced for K^+, whereas the K^- are emitted almost isotropically in central collisions. From this observations and the comparison with theoretical models, for example the IQMD model, it was concluded that the main production mechanism for K^- is the strangeness exchange mechanism (see reaction 1.16). First hyperons are produced together with a K^+, which then interact with a pion from the created system and exchange the strange quark, such that a K^- and a nucleon are produced. This reaction is endothermal in the vacuum, but with theoretical predictions of a dropping in-medium mass of K^- ($\approx$ 100 MeV/c^2), this process becomes exothermal. As a result the K^- are produced later in time at a phase of lower density and temperature. Re-absorption in the medium enhances this effect. Furthermore, from the comparison of the yields of positive kaons in C+C and Au+Au collisions it was found that the data is only compatible with a soft equation of state, which was already mentioned in section 1.6.1.

1.7.2 Hadron production in Ar+KCl at 1.76 AGeV measured with HADES

The HADES collaboration performed a complete measurement of strange particles in the system Ar+KCl at 1.76 AGeV. Results for various particles have been published: K^0_S [37]; K^+, K^-, ϕ [2]; Ξ^- [39] and Λ [38]. Even the not directly measurable $\Sigma^{0\pm}$ yield could be estimated by using the strangeness balance relation:

$$K^+ + K^- = \Sigma^{0\pm} + \Lambda + K^- + \bar{K}^0 + 2\Xi^{0,-}. \tag{1.21}$$

Particle	Multiplicity	T_{eff} [MeV]	Reference
π^-	$3.9 \pm 0.1 \pm 0.1$	$82.4 \pm 0.1\ ^{+9.1}_{-4.6}$	[37]
$\Lambda + \Sigma^0$	$(4.09 \pm 0.1 \pm 0.17\ ^{+0.17}_{-0.37}) \times 10^{-2}$	95.5 ± 0.7 +2.2	[38]
K^+	$(2.8 \pm 0.2 \pm 0.1 \pm 0.1) \times 10^{-2}$	$89 \pm 1 \pm 2$	[2]
K^0_S	$(1.15 \pm 0.05 \pm 0.09) \times 10^{-2}$	92 ± 2	[37]
K^-	$(7.1 \pm 1.5 \pm 0.3 \pm 0.1) \times 10^{-4}$	$69 \pm 2 \pm 4$	[2]
ϕ	$(2.6 \pm 0.7 \pm 0.1$ - $0.3) \times 10^{-4}$	84 ± 8	[2]
Ξ	$(2.3 \pm 0.9) \times 10^{-4}$	-	[39]
$\Sigma^+ + \Sigma^-$	$(0.75 \pm 0.65) \times 10^{-2}$	-	strangeness balance

Table 1.3: Summary of all measured particle multiplicities and inverse slope parameters at mid-rapidity T_{eff} in Ar+KCl reactions at 1.76 AGeV and corresponding publication reference.

In table 1.3 all estimated multiplicities and inverse slope parameters at mid-rapidity T_{eff} are summarized. The measured yields could be nicely described by a thermal model fit (See left side of figure 1.18). The estimated parameters of the fit T = (76 $\pm$ 2) MeV and μ_B = (799 $\pm$ 22) MeV are following the trend of other experiments to be on the universal freeze-out curve (see right side of figure 1.18). Figure 1.19 shows the effective temperatures of the different particle species measured in Ar+KCl with (blue) and without strangeness content (red). The blue line corresponds to the chemical freeze-out temperature estimated with the statistical hadronization model fit. The dashed line corresponds to a linear fit according to equation 1.4. With this fit, the kinetic freeze-out temperature T_{kin} = (74 $\pm$ 5.8) MeV and the radial flow velocity β_r = 0.37 $\pm$ 0.13 could be estimated [118].

For the first time it was possible to measure ϕ mesons and kaons simultaneously in the same experiment at SIS18 energies below threshold with sufficient statistics. About 170 ϕ mesons were measured and a ϕ/K^- ratio of 0.37 $\pm$ 0.13 was found. This ratio means that (18 $\pm$ 7)% of K^- originate from ϕ decays, which has a strong impact on the interpretation of the observed kinematics and in-medium effects. The left side of figure 1.20 shows the measured ratio compared to ratios obtained at higher beam energies. The lines correspond to thermal model calculations with different values for the canonical strangeness suppression radius R_C. To estimate the effect of the observed ϕ production yield on the K^- kinematics, the transverse mass spectrum of K^- has been simulated with a cocktail simulation. The cocktail includes a pure thermal K^- distribution with the measured inverse slope of positive kaons and 18% contribution from K^- resulting from ϕ decays. The inverse slope parameter of the cocktail is significantly lower than the pure thermal one and agrees roughly with the measured inverse slope of K^- in the experiment. In contrast to the conclusions from the KaoS collaboration, the lower effective temperature of K^- compared to K^+ does not have to be only an effect of the strangeness exchange mechanism being the dominant channel for K^- production at sub-threshold energies.

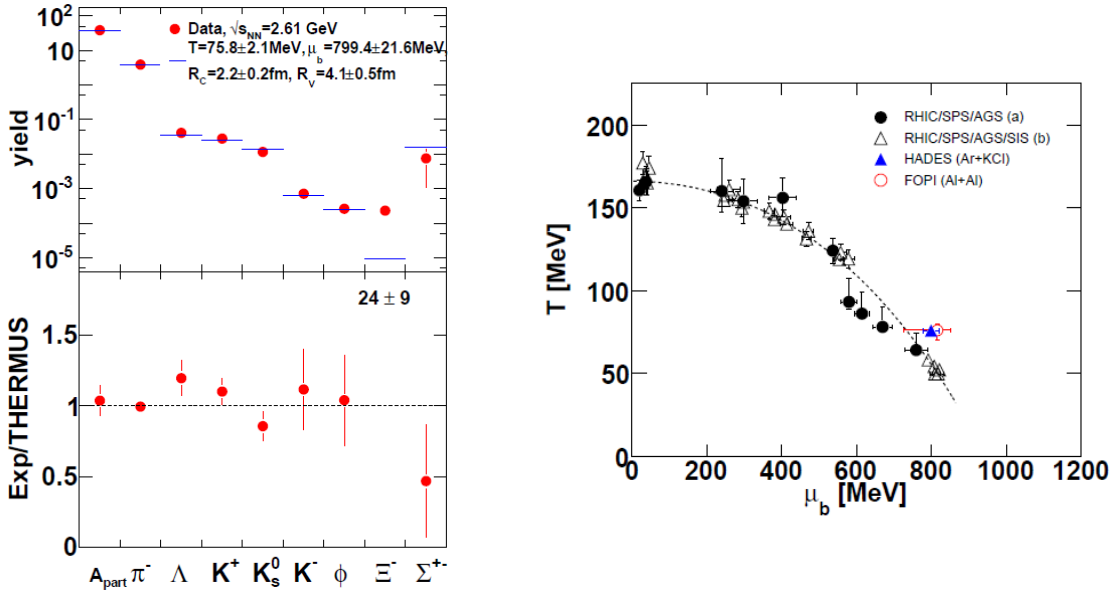

Figure 1.18: Results from a THERMUS [117] fit to measured particle yields in Ar+KCl reactions. Left: Measured yields (red circles) and the corresponding statistical hadronization model fit (blue bars). The lower plot shows the ratio of measurement and fit. Right: Chemical freeze-out points in the T-μ_b-plane. [38]

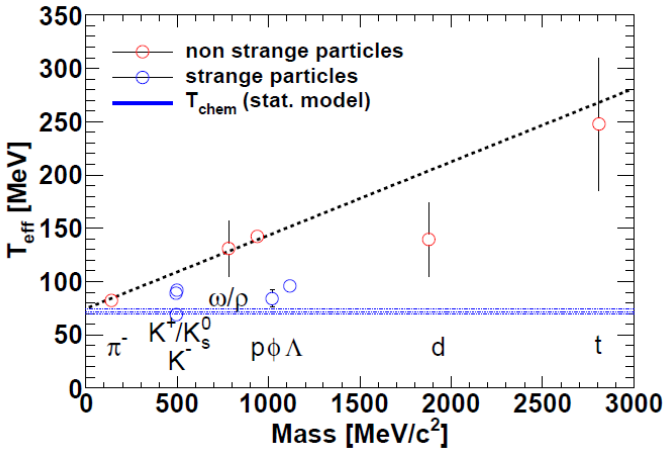

Figure 1.19: Effective temperatures of the different particle species measured in Ar+KCl with (blue) and without strangeness content (red). The blue line corresponds to the chemical freeze-out temperature estimated with a statistical hadronization model fit. The dashed line corresponds to a linear fit according to equation 1.4. With this fit, the kinetic freeze-out temperature T_{kin} = (74 $\pm$ 5.8) MeV and the radial flow velocity β_r = 0.37 $\pm$ 0.13 could be estimated [118].

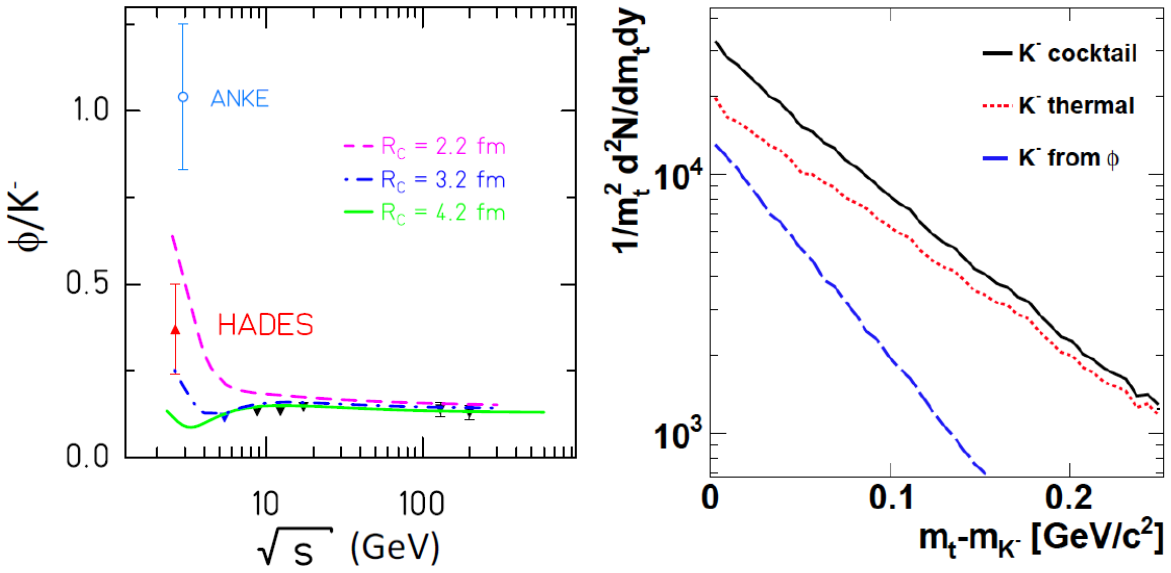

Figure 1.20: Left: Measured ϕ/K^- ratio in heavy-ion collisions as a function of center-of-mass energy $\sqrt{s}$ and in p+p collisions at $\sqrt{s}$ = 2.8 GeV (blue point). The lines correspond to thermal model calculations for different canonical suppression radii R_C [2]. Right: Cocktail simulation of the transverse mass spectrum of negative kaons. The red dashed line corresponds to a pure thermal distribution with the measured T_{eff} of positive kaons. The blue line shows the around 18% additional contribution to the cocktail from ϕ meson feed-down [119].

1.7.3 K^- and ϕ meson production measured with FOPI

The FOPI detector was installed at the SIS18 accelerator of the Helmholtzzentrum für Schwerionenforschung GSI in Darmstadt. The collaboration did systematic investigations on particle production in heavy-ion collisions in the energy regime between a few hundred MeV and 2 GeV. In the collision system Ni+Ni and Al+Al at 1.91 AGeV, simultaneous measurements of charged kaons and ϕ were performed and an earlier observation of a significant ϕ meson production, even at this low energies, was confirmed [120, 121, 3].

In the data set from central and semi-central Ni+Ni collisions corresponding to 51% of the total geometrical cross section, a K^- multiplicity of $(9.84 \pm 0.21\ ^{+0.63}_{-0.57})\text{x}10^{-4}$ was estimated. Furthermore, about 170 ϕ mesons were measured. The inverse slope of the kinetic energy distribution of the ϕ meson was found to be T = $(105 \pm 18\ ^{+19}_{-13})$ MeV. By assuming a thermal production, a multiplicity of $(4.4 \pm 0.7\ ^{+1.7}_{-1.4})\text{x}10^{-4}$ could be extracted. A ϕ/K^- ratio of $0.22 \pm 0.07\ ^{+0.18}_{-0.12}$ was estimated, meaning that $(22 \pm 3\ ^{+9}_{-6})$% of the observed K^- originate from ϕ decays at this energy. The influence of ϕ decays on the kinematic properties of the observed K^- was estimated by generating a K^- spectrum coming from two sources with the PLUTO event generator and was found to be on the same level as already discussed in context of the HADES results.

A very similar amount of statistics with 108 ϕ has been reconstructed in the data set of Al+Al collisions. A ϕ multiplicity of $(3.3 \pm 0.5\ ^{+0.4}_{-0.8})\text{x}10^{-4}$ per event was obtained and the amount of K^- originating from ϕ decays was found to be $(17 \pm 3\ ^{+2}_{-7})$%. Figure 1.21 displays the effect of the ϕ feed-down correction on the K^-/K^+ ratio as a function of center-of-mass kinetic energy. This observable has been proposed by transport models (see section 1.5) to be sensitive on in-medium potentials of the kaons. Without taking the feed-down contribution from ϕ decays into account, only the

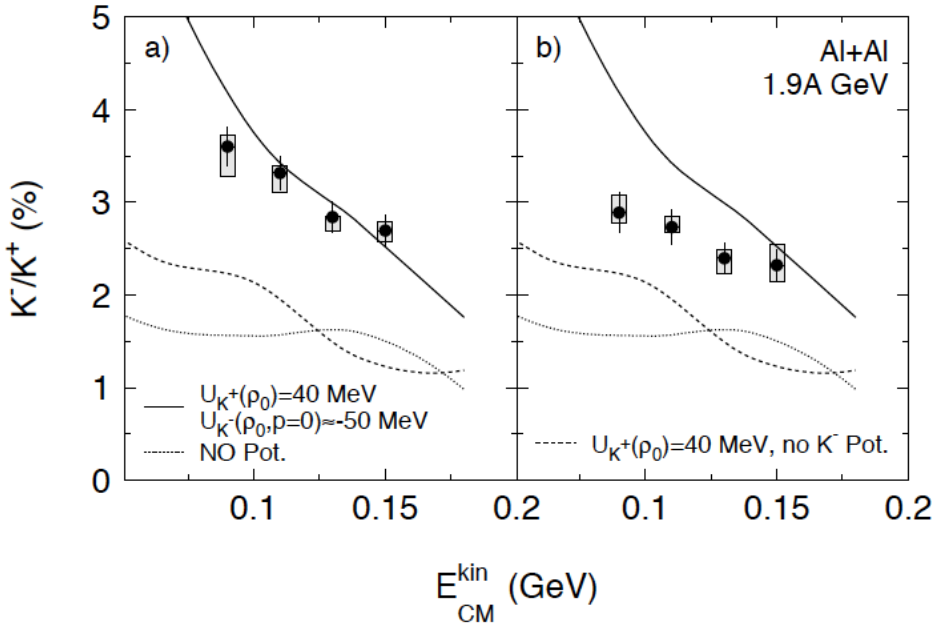

Figure 1.21: K^-/K^+ ratio as a function of center-of-mass kinetic energy in comparison to calculations with different kaon-nucleon potentials from the HSD transport model (lines) without (left) and after (right) correcting the K^- contribution for ϕ feed-down decays [3].

inclusion of both, a repulsive K^+N potential $U_{K+N}(\rho_0)$ = 40 MeV and an attractive K^-N potential of $U_{K^-N}(\rho_0, p = 0) \approx$ -50 MeV, lead to a sufficient description of the measured data (left side of figure 1.21). After correction for the ϕ contribution, the ratio is lowering and flattening and favors as a result a somewhat lower K^-N potential (right side of figure 1.21).

1.8 Structure and goal of this thesis

The particles analyzed in this thesis are protons, π^-, $K^\pm$ and ϕ via its decay into charged kaons. The set is complemented by the measurement of K^0_S and Λ which can be found in [116]. The main goal of the analysis is the reconstruction of a close to complete set of sub-threshold produced strange hadrons in Au+Au collisions at 1.23 AGeV in order to gain a better understanding of the production and propagation of strangeness in HIC below the free NN threshold of the corresponding hadrons. For the first time at such low energies it is possible to study the production of charged kaons and ϕ in central Au+Au collisions. This measurement will help to understand the puzzling findings from previous measurements at higher energies from the KaoS, FOPI and HADES collaboration which was discussed in section 1.7. The production of charged kaons was found to be coupled, as the production rates of both species show a very similar centrality dependence. However, the measured effective temperatures of K^- are systematically below the one of K^+, independently of the energy or system size. Both experimental findings from the KaoS collaboration could be explained from transport theory with strangeness exchange reactions being the dominant production channel for K^- below the elementary threshold energy. That this is not the complete picture to describe sub-threshold kaon production, was already observed from HADES and FOPI as they measured also a sizable ϕ production in the SIS18 energy regime. The measured ϕ/K^- ratio was found to be around 0.4,

meaning with a branching ratio of 48.9% into K^+K^- that almost 20% of all measured K^- are originating from ϕ feed-down decays. The lower observed effective temperatures of K^- compared to K^+ could be explained taking the feed-down contribution into account. The increase of the ϕ/K^- ratio towards lower energies is predicted from statistical hadronization models using the canonical suppression radius R_C instead of γ_s (see section 1.4.1) and can also be described by a tuned version of the UrQMD transport model [5], including additional high mass baryon resonances decaying into ϕ mesons, which is predicting a maximum at our analyzed energy of 1.23 AGeV (see section 1.5).

With the high statistics data sample of Au+Au collisions at 1.23 AGeV we will be able to do a multi-differential simultaneous measurement of $K^\pm$ and ϕ mesons to shine light on the production mechanisms of strange particles far below their elementary production thresholds. In principle the created system is the ideal environment for the mentioned strangeness exchange reactions to occur, as is is rather long living and all strange particles are produced deeply below their free nucleon-nucleon threshold energy. The measured particle spectra and yields will be compared to previous experimental data, transport model calculations and statistical hadronization model fits.

The HADES spectrometer is with its high acceptance and trigger rate the perfect detector to study rare probes and will be explained in section 2. In the following chapter 3 the basic concept of the data analysis in the high multiplicity environment of Au+Au collisions will be explained. This is including the event selection and centrality determination and the description of how the raw data will be processed to physical relevant observables, like masses and momenta of the particles, using a tracking algorithm. As well as the modeling of the heavy-ion collision using a Monte-Carlo simulation and the calibration of the energy loss measurement in the HADES drift chambers performed in the framework of this thesis. Chapter 4 is dedicated to the analysis of the charged particles protons, π^- and $K^\pm$ and the reconstruction of the neutral ϕ via its decay into K^+K^-. After the particle identification, the differential count rates are estimated, which have to be corrected for acceptance of the detector and reconstruction efficiency. Afterwards the experimental results on the effective temperatures and the multiplicities of the analyzed particles are shown in chapter 5 and will be discussed in chapter 6. At the end there will be a summary and an outlook.

Chapter 2

The HADES Experiment

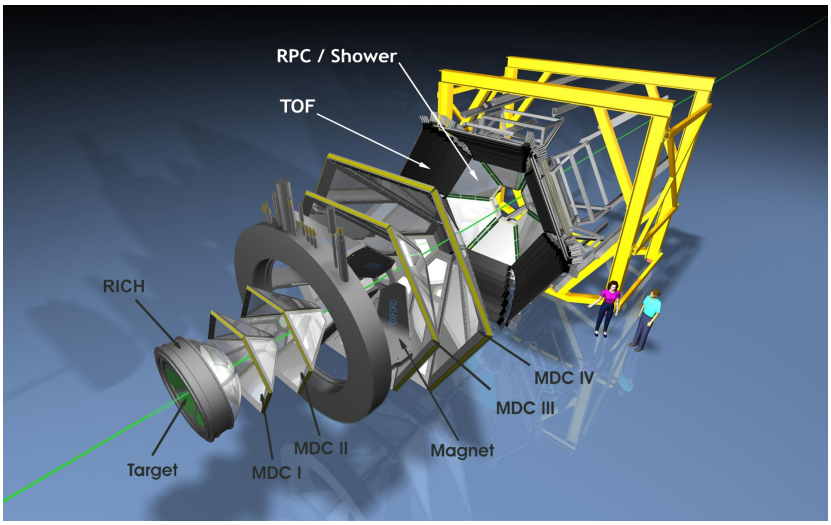

Figure 2.1: Expanded view of the HADES detector with its main components. The green line sketches the beam. [122]

The **H**igh **A**cceptance **Di**-**E**lectron **S**pectrometer (HADES) is a fixed target experiment located at the heavy-ion synchrotron SIS18 of the Helmholtzzentrum für Schwerionenforschung GSI in Darmstadt, Germany. Starting in 2002, the HADES collaboration has successfully recorded data of various collision systems, ranging from heavy-ion collisions to elementary reactions like proton + proton, proton + nucleus and recently pion + nucleus, at different beam energies. Figure 2.2 shows a summary of the collected raw data volume and days of data taking for all beam times. A detector and data acquisition (DAQ) upgrade, focusing on increasing granularity, data bandwidth and DAQ speed, allowed to record 140 TB of data on the heaviest reaction system since the beginning of data taking with the spectrometer: Au+Au at 1.23 AGeV. The new DAQ system features **F**ield **P**rogrammable **G**ate **A**rray (FPGA) based electronic boards and optical data transmission [123]. The main hardware upgrade was the replacement of an old time-of-flight wall (TOFino) by a highly granular Resistive Plate Chamber (RPC) and the drift chamber closest to the interaction point was modernized.

The spectrometer was designed to investigate in-medium modifications of the light vector mesons ω, ρ and ϕ, by measuring e^+e^- pairs originating from their decay. Lepton pairs are promising observables for the high density phase created in a heavy-ion collision, because they are carrying the

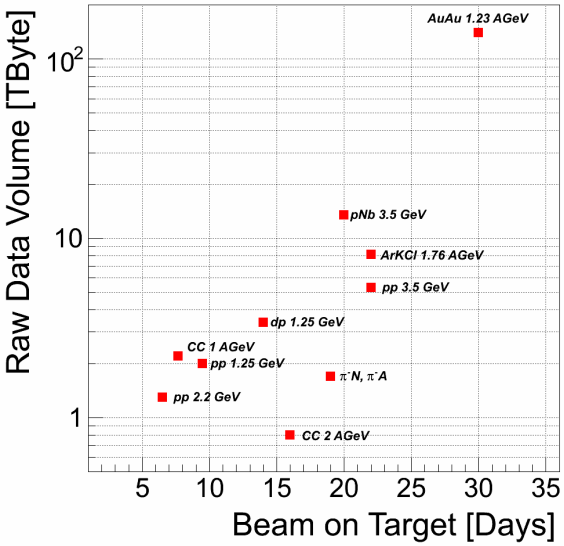

Figure 2.2: Summary of the collected raw data volume and days of data taking for all HADES beam times until 2012. The large increase for the Au+Au beam time became possible due to a detector and data acquisition upgrade, including the replacement of an old time-of-flight wall (TOFino) by a highly granular resistive plate chamber and the new DAQ system based on FPGAs and optical data transmission. [124]

information about the vector mesons and are not affected by the strong interaction. However, they are strongly suppressed compared to other decay products. For this purpose, the spectrometer was build out of fast sub-detectors, in order to record high event rates and accumulate sufficient statistics, as well as with a large geometrical acceptance, covering polar angles from 18° to 85° degrees and almost the full azimuthal angle. To reduce background sources, like dilepton pairs from conversion of real photons, the material budget of the sub-detectors is kept as low as possible. With its high momentum resolution and large geometrical acceptance, the spectrometer provides additionally excellent opportunities to identify hadrons, especially rarely produced mesons carrying strangeness like kaons. The compact detector system is composed of six identical sectors in azimuth, which are symmetrically surrounding the beam axis. In figure 2.1 the spectrometer is shown in an expanded view and figure 2.3 shows its simplified cross section[1]. In direction of the incoming beam, the following detector components can be seen:

- **Target and START/VETO-detector**
  The START-detector is located close to the target and delivers a precise reaction start time determination, whereas the VETO-detector discriminates reactions, where no interaction in the target took place (see section 2.1 and 2.4.1).

- **RICH-detector**
  The **R**ing **I**maging **CH**erenkov detector has the main purpose to discriminate electrons and positrons from pions or other hadrons (see section 2.2).

- **Magnet-spectrometer**
  The detector uses two **M**ini **D**rift **C**hambers (MDC) in front and two behind a superconducting magnet for track and momentum reconstruction and specific energy loss measurements (see section 2.3).

- **Time-of-flight detectors**
  The region of small polar angles (18° - 45°) is covered by a **R**esistive **P**late **C**hamber (RPC) and

[1] Without projection of the coil boxes.

large angles (44° - 85°) by a **T**ime-**O**f-**F**light wall (TOF) composed of scintillators, to measure the flight time of a particle. In the TOF-detector it is also possible to identify particles by making use of the specific energy loss in the scintillator material. Behind the RPC-detector the PRE-SHOWER-detector for additional lepton discrimination is installed (see section 2.4.2).

- **Forward-wall**
  For event-plane reconstruction and centrality determination a forward-wall, covering small polar angles, is installed (see section 2.5).

A detailed description of all detector components can be found in [125].

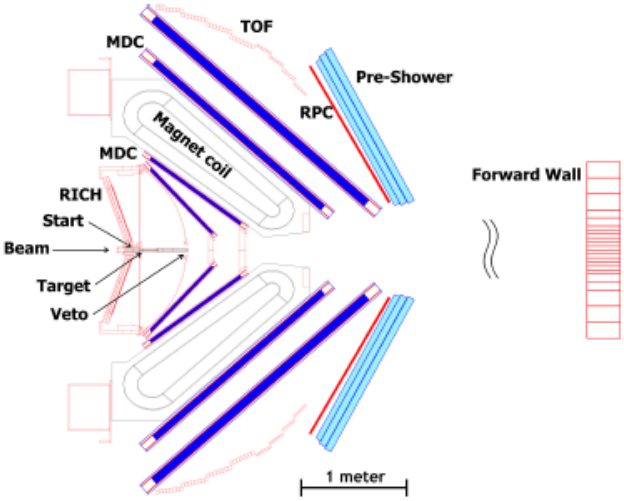

Figure 2.3: Cross section of the HADES detector with its components: START- in front, VETO- behind and RICH-detector surrounding the target; Mini Drift Chambers in front and behind the superconducting magnet; Time-of-flight wall consisting of TOF- and RPC- plus PreSHOWER-detector and at the back of the setup the forward-wall. [122]

2.1 Target

For the analyzed data sample, a segmented Au-target was used (see figure 2.4). Each of the 15 gold foils has a thickness of 3 mm and is glued into the hole of a 7 μm thick Kapton foil with a distance of 4.5 mm to the next foil. The target holder is made out of carbon. The segmentation is necessary to reduce the conversion of photons into lepton pairs. The target interaction probability is 2.0%.

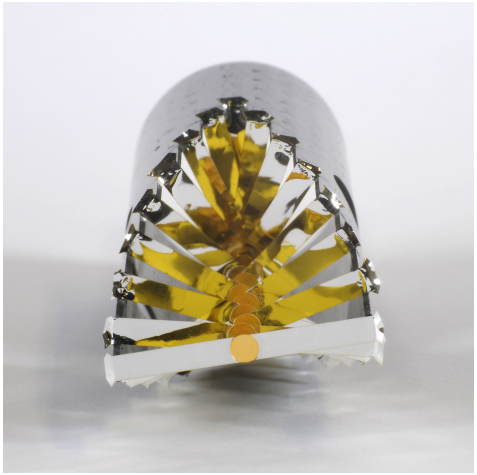

Figure 2.4: Photo of the Au target with its 15 segments before exposure to the beam. Each gold foil is glued into the hole of a Kapton foil, which is bonded to the target holder. [122]

2.2 RICH-detector

The **R**ing **I**magining **CH**erenkov detector (RICH) employs the Cherenkov effect to identify particles. When a particle passes a gas with a velocity v higher than the speed of light inside this medium ($c^{'} = \frac{c}{n}$, n = refractivity of the medium), light is emitted in a cone with a fixed opening angle Θ around the particle track, which is sent out in flight direction:

$$\Theta = \arccos\left(\frac{c}{v \cdot n}\right). \tag{2.1}$$

This cone is reflected by a spherical mirror and registered by a photon detector in the backward hemisphere (see figure 2.5). The mirror panels consist of a glass ceramic made of pure carbon featuring low density ($\rho \sim 1.5$), extreme stiffness and large radiation length ($x/X_0 < 1\%$). The RICH detector in the HADES setup is optimized to identify electrons and positrons in a momentum range of 0.1 to 1.5 GeV/c which is achieved by using the radiator gas C_4F_{10}. The refractivity of this gas is n = 1.00151. At these energies, only electrons and positrons reach the threshold velocities to produce Cherenkov light, which makes the detector hadron-blind and optimizes light lepton identification.

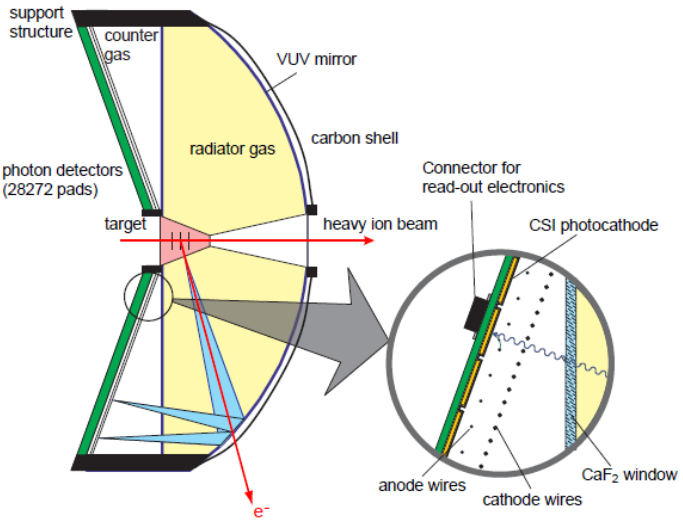

Figure 2.5: Schematic view of the RICH detector. An electron passing the radiator gas generates a light cone, which gets reflected by the mirror and registered by the photon detectors in the backward hemisphere as a ring. [125]

2.3 Magnet spectrometer

The Magnet spectrometer for track reconstruction consists of two **M**ini **D**rift **C**hambers (MDC) in front and two behind a superconducting magnet (see figure 2.6). Charged particles ionize the gas molecules in the drift chambers. The resulting free electrons are drifting to the sense wires. The signal is amplified in an avalanche close to the sense wire as well as from the induced charge by the free ions in this avalanche drifting away from the sense wires to the cathode and field wires. After the first two MDCs, the particles feel the toroidal magnetic field of the magnet, which leads to a deflection due to the Lorentz force. From the bending direction and the radius of the curvature it is possible to determine the charge and the momentum of a particle. For more details on the momentum reconstruction see section 3.6. Combined with the measured time-of-flight charged particle identification is possible (see section 3.7). To improve particle identification, the specific energy loss of the particles in the drift chambers can be used in addition (see section 3.8).

2.3.1 Magnet

The superconducting magnet ILSE[2] consists of six NbTi-coils. It is cooled with liquid He at 2.8 bar pressure down to a temperature of 4.7 K. The toroidal magnetic field strength ranges from 3.6 T inside the coils to 0.8 T in the region of the drift chambers. In a simplified picture one can imagine that the particles, passing the magnetic field, are getting a single transversal "kick". The challenge for the magnet ILSE is that it should "kick" particles with a broad momentum range from 0.1 to 2 GeV/c into the acceptance of the detector. In addition, there should be no material inside the field, to reduce multiple scattering. It is important that the magnetic field is covering the region of the RICH, the drift chambers and the time-of-flight detectors only to a negligible amount, to exclude mis-identification of electrons and distortion of the drift time and time-of-flight measurement.

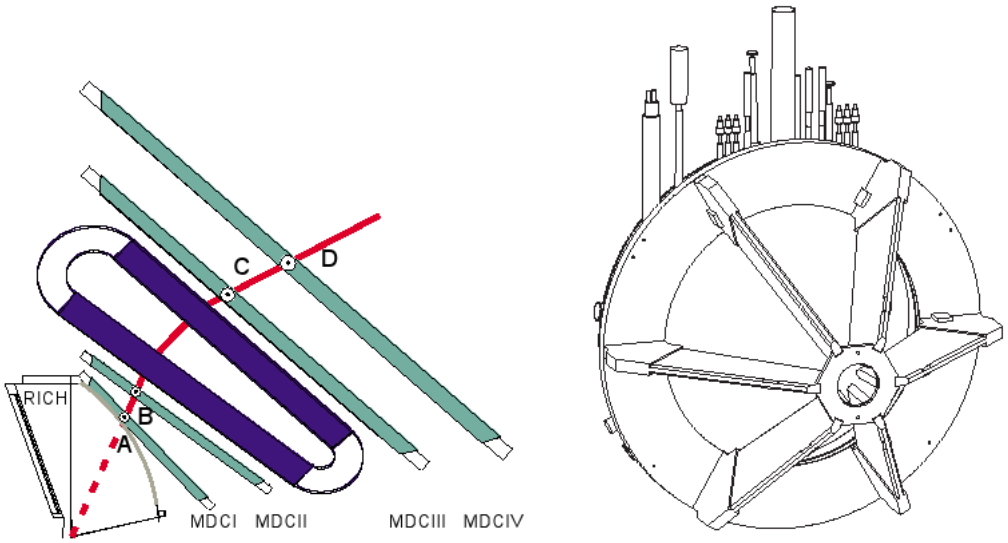

Figure 2.6: Left: Schematic view of the magnet spectrometer for track- and momentum-reconstruction. By measuring the track of the particle before (A,B) and after (C,D) the magnet, it is possible to estimate the bending direction and radius of the curvature and with this the charge and momentum of the particle. Right: The superconducting magnet ILSE. [125]

2.3.2 Mini Drift Chambers

The main purpose of the **M**ini **D**rift **C**hambers (MDCs) is the track reconstruction. The smallest functional unit of a drift chamber, a drift cell, consists of a signal wire which is surrounded by two potential wires (field wires) and several cathode wires (a two dimensional projection of a particle passing one drift cell can be seen in figure 2.7). A particle passing this drift cell is ionizing the gas molecules. The resulting electrons are drifting with almost constant velocity to the signal wire. The HADES drift chambers are operated as proportional counters. As a consequence, the free electrons are ionizing additional gas molecules which create electron avalanches close to the sense wires. The sense wires are read out by one dedicated channel of an Analog Shaper Discriminator chip (ASD8), which amplifies, shapes and discriminates the analogue signal. A Time-to-Digital converter TDC measures the start time t_1 when the incoming signal is high enough to overcome a specific threshold

[2] **I**ron **L**ess **S**uperconducting **E**lectromagnet

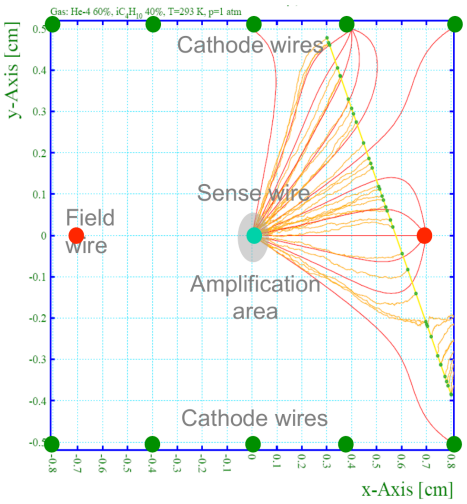

Figure 2.7: Schematic view of a track passing one MDC driftcell. A charged particle passing the cell is ionizing the gas molecules. The electrons (green points) are drifting to the sense wire in the middle of the cell along the field lines (red lines). Figure taken from [126].

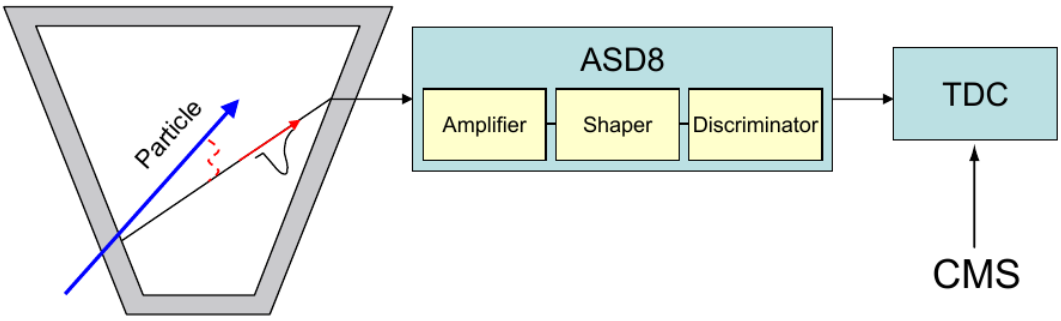

Figure 2.8: Scheme of the electronic read-out chain of the MDCs. The induced signal on the sense wire is propagating to the ASD8 chip, which amplifies, shapes and discriminates the signal. The TDC measures the times with respect to the common stop signal. Figure taken from [126].

(leading edge) and the time t_2 when the signal falls below this threshold again (trailing edge). The difference of the two times is called *time over threshold ToT*. The times are measured with respect to a common stop signal, which stops the read-out a few hundred ns[3] after the reaction start time measured by the START-detector. Figure 2.8 shows a sketch of the electronic read-out chain of the MDCs. The dependence of t_1 on the distance of the track to the sense wire due to the drift time of the electrons is calibrated. For details on the read-out electronics and calibration of the MDCs see [126, 123]. The combination of the measurements from all cells which the particle passed with a tracking algorithm allows to reconstruct the trajectory of the particle (see section 3.6).

The HADES drift chambers are optimized for small area density, which reduces multiple scattering. Therefore, each chamber is only 3 - 6 cm thick and consists of six signal wire planes. This results in a maximum set of 24 measurements per sector, with a cell efficiency of around 95%. If the positions of the chambers are exactly known, the particle trajectory can be precisely obtained. The resolution in the polar angle direction is 60 - 100 μm and in azimuthal direction 120 - 200 μm [126]. The position determination of the chambers was done using the photo alignment method for MDC II. Based on this position (few hundred micrometers accuracy), beam and cosmic tracks were used to further increase the precision in the absolute position of the chambers [127]. Each of the six sectors of the spectrom-

[3]The time has to be long enough to measure the trailing edge of very long $ToTs$ in the outer drift chambers.

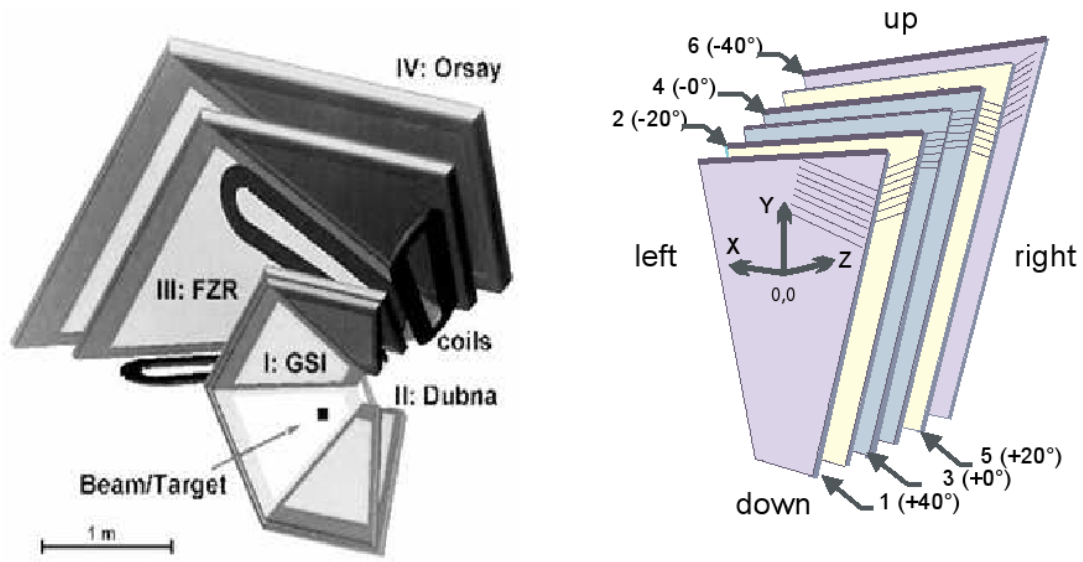

Figure 2.9: Left: Schematic view of the magnet-spectrometer of HADES which illustrates the construction from six identical sectors around the beam axis. The names correspond to the places of construction of the chambers. The GSI built plane I was exchanged by new chambers built in the Helmholtzzentrum Rossendorf. Right: Schematic view of a drift chamber module. Illustrated are the different orientations of the signal wires with respect to the coordinate system of the chamber. [125]

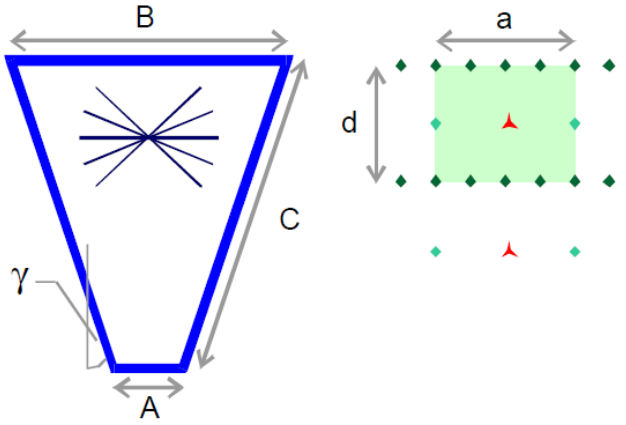

MDC	A [mm]	B [mm]	C [mm]	γ [°]	a [mm]	d [mm]
I	139.21	767.38	839.19	21.98	5	5
II	205.00	905.00	1049.27	19.49	6	5
III	310.43	1804.80	2139.05	20.44	12	8
IV	345.46	2224.05	2689.04	20.44	14	10

Figure 2.10: Geometrical dimensions of the different drift chamber modules (capital letters) and their corresponding drift cells (small letters). [125]

eter is equipped with four planes of drift chambers, which contain around 1100 signal wires. Inside a given plane the cells are grouped in six layers (i.e. wire planes) separated by cathode wire planes, with different sense and field wire orientations. These so-called stereo angles are: +40°, -20°, +0°, +0°, +20° and -40° (see figure 2.9). The drift chambers are trapezoidally formed, the size is rising from MDCI to MDCIV to provide a constant coverage in the solid angle per sector (see figure 2.10). Hence the size of the drift cells is increasing, as well as, providing constant granularity throughout the tracking system. For the Au+Au run in April 2012, the most inner plane was filled with a gas mixture of 70% Argon and 30% CO_2, whereas the gas mixture of the other planes was 84% Argon and 16% Isobutane. To minimize photo-feedback, the Isobutane and CO_2 act as quenching gas, which absorbs the photons from photo emission and transforms the energy into rotation and vibration energy.

2.4 Time-of-flight measurement

The time-of-flight measurement of the particles is done using the reaction start time t_0 determination with a diamond counter in front of the target and the signal in the so called META-detector, consisting of the RPC at low and the TOF scintillator wall at high polar angles, downstream behind the tracking system. The measurement is together with the momentum determination of the magnet spectrometer the most important observable for particle identification in HADES.

2.4.1 START- and VETO-detector

The START-detector is a 4.7 mm broad and 70 μm thick monocrystalline CVD diamond semiconductor, consisting of 16 stripes in x- and y-direction. It is located 2 mm in front of the Au-target and estimates the reaction start time t_0 with a time resolution of around 50 ps. Additionally, it provides an excellent position resolution, which makes it possible to use it also for beam focusing. To avoid efficiency losses due to radiation damage, nine disjunct beam spots can be utilized. The diamond efficiency was found to be above 95% [128]. The 100 μm thick, polycrystalline CVD diamond VETO-detector is located 70 cm behind the target. It is used to exclude reactions where no interaction with the target took place, in order to reduce the dead time of the HADES detector. Figure 2.11 shows a scheme and a picture of the START- and the VETO-detector. For a detailed description of the design, the intrinsic properties and the performance after irradiation with Au ions see [129].

2.4.2 META-detector

The **M**ultiplicity and **E**lectron **T**rigger **A**rray (META)-detector consists of the **R**esisitve **P**late **C**hamber (RPC), the scintillator wall (TOF) and the Pre-SHOWER-detector. Its main tasks are:

- Providing the multiplicity of charged particles for a fast decision of the trigger (see section 2.6).
- Measuring the time-of-flight in combination with the START-detector and in case of the TOF-detector additionally the specific energy loss for particle identification.
- Improve the purity of reconstructed particle tracks. By spatially correlating the tracks in the MDCs with hits in the META-detector, fake tracks can be reduced.

The TOF-detector is covering large polar angles from 44° to 85° in six identical sectors. The sectors are build out of eight modules with eight plastic scintillator rods each. At both ends of each of those 64 stripes per sector are **P**hoto **M**ultiplier **T**ubes (PMT). Particles crossing a scintillator stripe excite

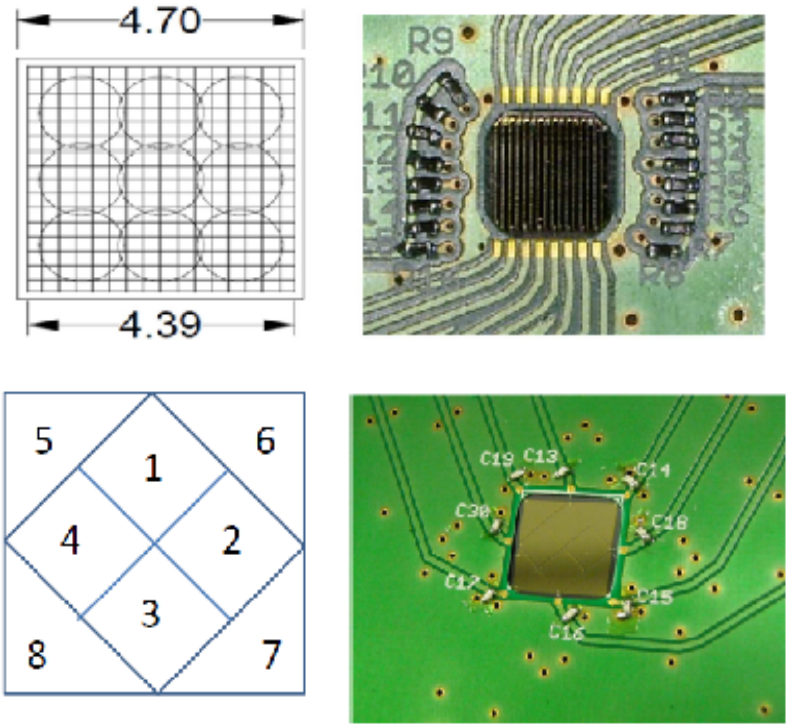

Figure 2.11: Scheme (left) and photo (right) of the START- (top) and VETO-detector (bottom) used during the Au+Au run in April 2012. To avoid efficiency losses of the START-detector due to radiation damage, nine disjunct beam spots can be utilized as depicted upper left. [130]

the material, which will return to its ground state by emitting a photon. This photon will be amplified and transformed into an electrical signal in the PMTs. The position x along the rod can be calculated when the arrival time of the light signals at both ends of the rod t_{left} and t_{right} and the group velocity of light in the scintillator V_g is known:

$$x = \frac{1}{2}(t_{left} - t_{right}) \cdot V_g. \tag{2.2}$$

Using the length of the rod L the time-of-flight of the particle t_{tof} can be calculated:

$$t_{tof} = \frac{1}{2}(t_{left} + t_{right} - \frac{L}{V_g}). \tag{2.3}$$

In addition, the amplitudes of the signals a_{left} and a_{right} are measured in the PMTs, which allows to extract the deposited energy of the particle:

$$\Delta E \propto \sqrt{a_{left} \cdot a_{right} \cdot \exp \frac{L}{\lambda_{at}}}, \tag{2.4}$$

with λ_{at} being the attenuation length of the light in the scintillator. The extracted time signals on both sides of the stripe constrain the polar angle coordinate with a resolution of 2 - 3 cm. The azimuthal angle coordinate is constrained with a resolution of 2.5 cm. With its high granularity the TOF-detector reaches a time resolution of 150 ps.

The low polar angle region between 18° and 45° is covered by the RPC-detector. The six identical sectors are composed of 187 cells. The cells are made alternatively of aluminum and float-glass. Between two parallel electrode plates a strong electric field is applied. The gap between the plates is filled with gas. A charged particle ionizes the gas and triggers an electron avalanche, which leads to a discharge. A scheme of one sector of the RPC-detector is shown on the left side of figure 2.12. The time resolution is below 73 ps and the longitudinal position resolution around 8 mm. The transversal resolution is constrained by the cell width, ranging from 22 mm to 42 mm. The efficiency for single hits of minimum ionizing particles is of about 95% and the double hit probability in central Au+Au collisions is below 10%.

Behind the RPC-detector an additional detector for lepton identification is located, the Pre-SHOWER detector. It is a sandwich of three wire chambers, separated by two lead converter plates (see right side of figure 2.12). Each sector is equipped with one module, consisting of 1024 pads. At these low polar angles, electrons and hadrons have similar momenta and time-of-flight distributions. While electrons passing the material of the detector create electromagnetic showers due to bremsstrahlung ($\propto \gamma^4$), the shower generation of hadrons is strongly suppressed due to the significant lower γ values compared to electrons. By integrating the charge of the electromagnetic shower on the pads surrounding the pad with the highest local charge value, one can distinguish between electrons and hadrons.

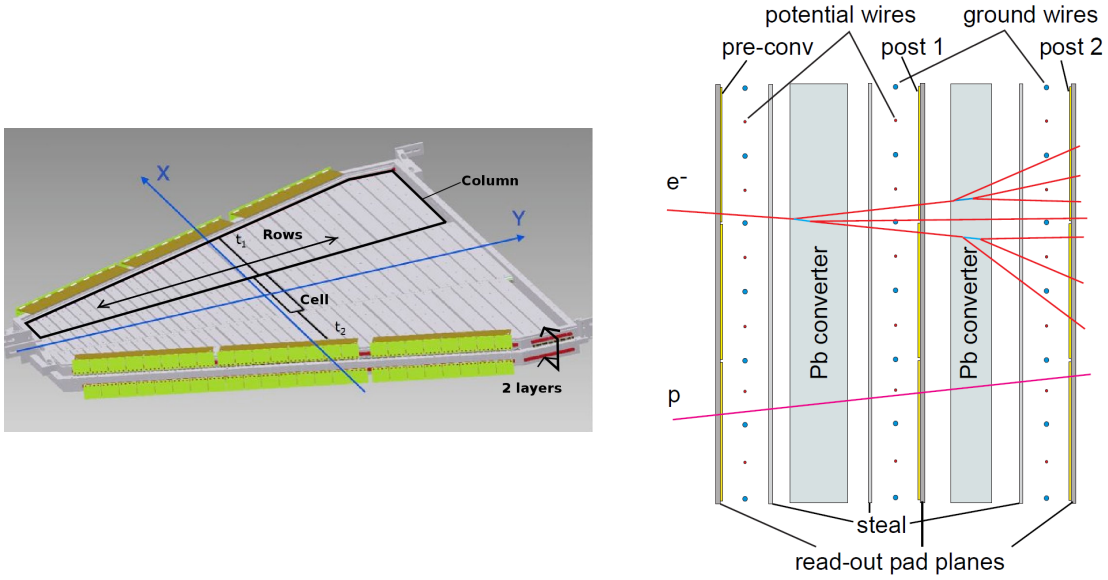

Figure 2.12: Left: Scheme of one sector of the RPC-detector. Right: Cross section of a cell from the Pre-SHOWER detector. Electrons create electromagnetic showers in the two lead converters. [122]

2.5 Forward-wall

In a distance of seven meters from the target, at low polar angles, a forward-wall for event-plane reconstruction is installed. The main purpose of the hodoscope is to determine the reaction plane and centrality on an event-by-event basis by measuring the reaction spectators. The volume between the forward-wall and HADES is filled by a helium-ballon to reduce multiple scattering of the spectators. It consists of 288 scintillators of different sizes. The sizes are increasing with increasing distance to the beam axis. The smallest blocks are 4 x 4 cm^2 and are located around the beam axis. The following blocks are 8 x 8 cm^2 and the ones in the outer region 16 x 16 cm^2 (see figure 2.13). With this

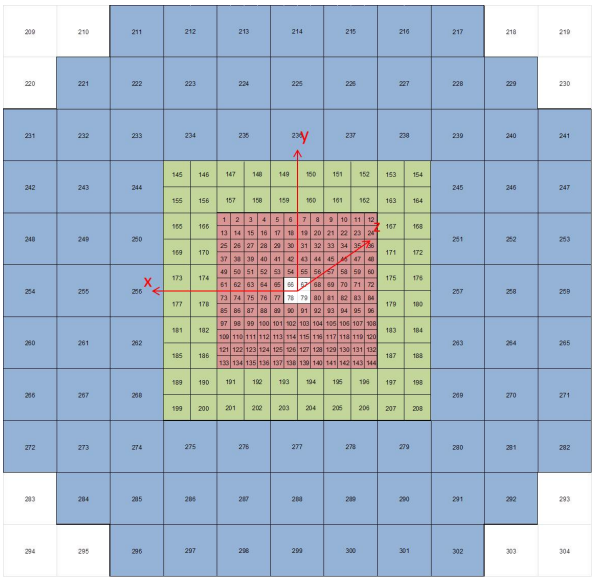

Figure 2.13: Layout of the forward-wall with all scintillator blocks surrounding the beam line (red: 4 x 4 cm^2, green: 8 x 8 cm^2 and blue: 16 x 16 cm^2). [122]

setup the HADES forward-wall reaches a sufficient angle and position determination of the spectators from the collision, whose track density is highest at low polar angles, as well as moderate double hit probability. The particles are identified by measuring the deposited energy in the scintillator modules and the time-of-flight information. Each cell is 2.54 cm thick and read-out by one photo multiplier tube. The total transverse dimensions are 180 x 180 cm^2.

2.6 DAQ and Central-Trigger-System

The Data AcQuisition (DAQ) is based on a multi-purpose electronic device developed at GSI, the Trigger and Read-out Board (TRB). To combine all detector sub-systems and the steps from data read-out, a special network protocol the TrbNet has been developed [123]. The signals from the front-end electronics of the different sub-detectors are collected by means of dedicated and customized end point boards (e.g. MDC: optical endpoints) which are linked to hubs and streamed via the Gigabit Ethernet to the so-called event builders, which combine and prepare the data for a long-term storage and analysis (see figure 2.14). In order to reduce the dead time of the data acquisition, a Central-Trigger-System (CTS) is used in HADES. The first level trigger (LVL1) selects only events with a minimal track multiplicity, which corresponds to a certain centrality range of the collision. The decision time is around 100 ns, which is on average much faster than the time between two collisions. As a result, peripheral collisions or part of the collisions outside the target are efficiently excluded. For the Au+Au beam time a track multiplicity of more than 20 hits in the TOF-detector was selected by the so called PT3-trigger. In addition, minimum bias reactions with more than four tracks were recorded (PT2). The selected events are written from the buffer memory into HLD files (**H**ades **L**ist **D**ata).

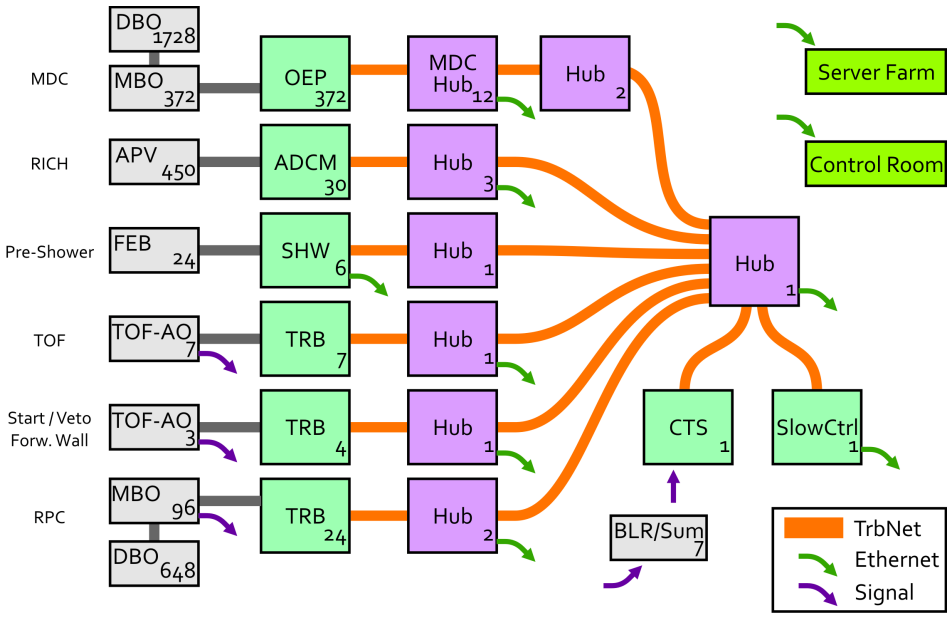

Figure 2.14: Schematic view of the HADES data acquisition system. The signals from the different sub-detectors are processed via the TrbNet network protocol. The data is streamed via Gigabit Ethernet to so-called event builders, where it is combined and saved on disc. The central trigger system (CTS) pre-selects the recorded events in order to reduce the dead time of the data acquisition. [123]

Chapter 3

Event and Track Reconstruction

In April and May 2012 the HADES collaboration took data for the collision system Au+Au. In total 557 hours of data taking, corresponding to 140 TByte, have been recorded. The particle accelerator SIS18 delivered gold ions with an intensity of (1.2 - 1.5)x10^6 ions per second and a kinetic beam energy of 1.23 AGeV. The beam was focused on a 15-fold segmented gold target close to the HADES detector. The events have been registered with a trigger rate of 8 kHz with a 50% duty cycle and recorded to tape with a data rate of 200 MByte/s. In total 7.3x10^9 events have been collected. Table 3.1 summarizes the target and beam properties for the Au+Au measurement.

Beam and target properties	
Beam energy	E_{kin} = 1.23 AGeV
Center-of-mass rapidity	y_{cm} = 0.74
Beam particle	$^{197}_{79}$Au^{69+}
Target	$^{197}_{79}$Au
Target density	19.32 g/cm^3
Target thickness	3 mm
Target diameter	2.2 mm
Target segmentation	15
Target separation	4.5 mm
Cross section	σ_{tot}^{AuAu} = (6833 $\pm$ 430) mb [1]

[1] Total cross section estimated via Glauber Monte Carlo simulation [131]

Table 3.1: Summary of the target and beam properties for the Au+Au beam time.

3.1 Data processing

The raw signals from the different sub-detectors of HADES are recorded with the DAQ[1] system and stored on tape in so-called *HLD*[2] files (see section 2.6). The files get a unique identifier corresponding to the time they were recorded, including the day of the year (96 - 126) and the exact time (hh:mm:ss). The operating parameters of the sub-detectors are stored as a function of time in the Oracle data base

[1] **D**ata **AQ**uisition
[2] **H**ADES **L**ist **D**ata

[132], in order to check detector performance and settings for each file afterwards in the analysis. To access physically relevant information of the particles, like their energies and momenta, the different sub-detectors have to be calibrated and their position has to be known exactly. The position determination of the MDCs for example, is done by using a photo alignment method for MDC II. Based on this exact position (few hundred micrometers accuracy), beam and cosmic tracks are used to estimate the exact position of the other chambers [127]. A tracking algorithm combines the signals from the different sub-detectors to tracks (see section 3.6). Afterwards the momentum can be reconstructed (see section 3.6.1). The event information and particle candidates are saved in DST[3] files.

3.2 Stability of the drift chambers during the time of data taking

During the Au+Au beam time the drift chambers could not be operated at exactly the same constant high voltages. Changes in the high voltage lead to different layer efficiencies and change the mean Time-over-Threshold distributions in the different cells. Furthermore, one sector (sector 2, azimuthal angle coverage $240° \leq \phi \leq 300°$) had to be switched of on most of the days and was only working properly on a few days. This requires a careful validation of files used in the analysis.

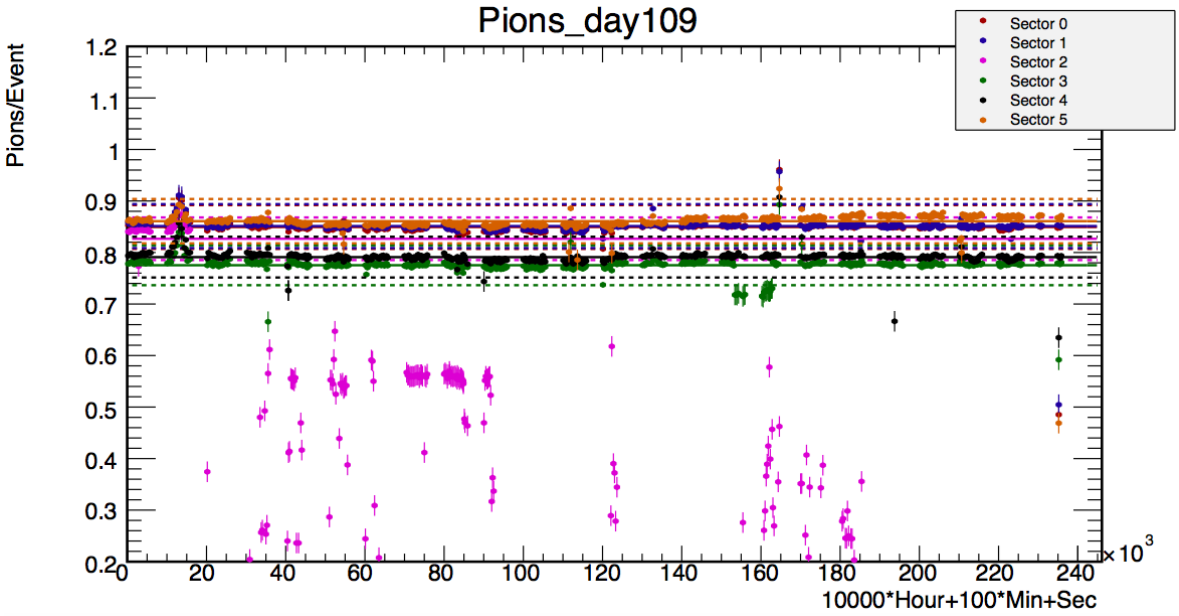

Figure 3.1: Mean number of reconstructed pions for the different sectors (see legend) of the HADES detector as a function of the time of data taking for day 109 of the beam run. Similar pictures are produced for each day of the beam time. Taken from [133].

Figure 3.1 shows the mean number of reconstructed pions for the different sectors as a function of the time of data taking for one day of the beam time. While the number of reconstructed pions stays almost constant for most of the sectors, the number in sector 2 is fluctuating strongly and is on average below the other sectors. Based on a time dependent check of the number of measured pions and protons which should be constant, performed in the framework of [133], only those input DST files have been selected for the analysis of the rarely produced strange particles, where all of the other

[3] **D**ata **S**ummary **T**ape

five sectors were working under stable conditions. The analysis of protons and π^- (section 4.1.1) is done for one particular day (day 108), which showed the best conditions for all six sectors, however, sector 2 is excluded from the analysis.

3.3 Event selection

To guarantee that only Au+Au collisions are included in the analysis, the recorded events have to pass a careful event cleaning procedure, which is done using coincidence measurements between the different sub-detectors and applying constraints on the reconstructed event vertex. Possible background sources are events in which the incident beam ions are reacting with the carbon ions of the START-detector or the holder of the target strips instead of the target material. Furthermore, it may occur that more than one nuclear reaction is registered within the time window of the data acquisition, so-called *pile-up events*, leading to a wrongly estimated reaction start time and therefore to wrongly calculated flight times of the particles and a spoiled centrality determination. Especially the analysis of the ϕ meson (see section 4.2) is strongly affected by the latter ones, because pions with a wrong flight time can be mistaken as kaon candidates. Therefore, these events have to be removed from the analysis. The starting point for the event selection are all events where all five sectors except sector 2 were working at stable conditions (compare section 3.2) and which have been selected by the PT3-trigger[4]. The amount of selected events corresponds to 78% of all recorded events (*PT3*). Furthermore, the following selections are applied:

- The beam particle has to be registered by the START-detector to allow for a proper time-of-flight measurement (*selectStart*).
- Cuts on the reconstructed event vertex are applied. The vertex can be reconstructed using at least one reconstructed track (*GoodClusterVertex*) or at least two identified particles (*GoodCandVertex*). Both criteria work in a similar way and support each other, in both cases the χ^2 of the vertex reconstruction has to be greater than zero. The left side of figure 3.2 shows the reconstructed primary vertex in beam direction before and after event cleaning. The events in which only a collision with the carbon atoms in the START-detector took place can be easily removed by cutting on the z-position of the reconstructed vertex: -65 mm $< z_{vertex} <$ 0 mm. Furthermore, the events have to fulfill the condition of having a transverse primary vertex position defined as $\sqrt{x^2_{vertex} + y^2_{vertex}} \leq 4$ mm. The resolution of the vertex reconstruction in the x-y-direction is displayed on the right side of figure 3.2.
- The multiplicity in the START-detector has to be one in a time interval of -5 to 15 ns around the reaction start time (*StartPileUp*). Possible pile-up events in times very close to the actual start time of the reaction have to be strictly removed for the analysis, as the calculated masses of the particles from the second reaction will be in the same range as the physical masses from the actual triggered event.
- To avoid events in which reactions outside the target region took place, only events are chosen, where no VETO-signal has been registered in a time interval of $\pm$15 ns after or before the interaction signal by the START-detector (*NoVeto*).
- All events with a second START-hit, which have no correlated VETO-signal in a time interval of 15 - 350 ns after the reaction start time, are excluded (*VetoStart*). If a second coincidence

[4]The PT3-trigger requires a minimum number of 20 hits in the TOF-detector

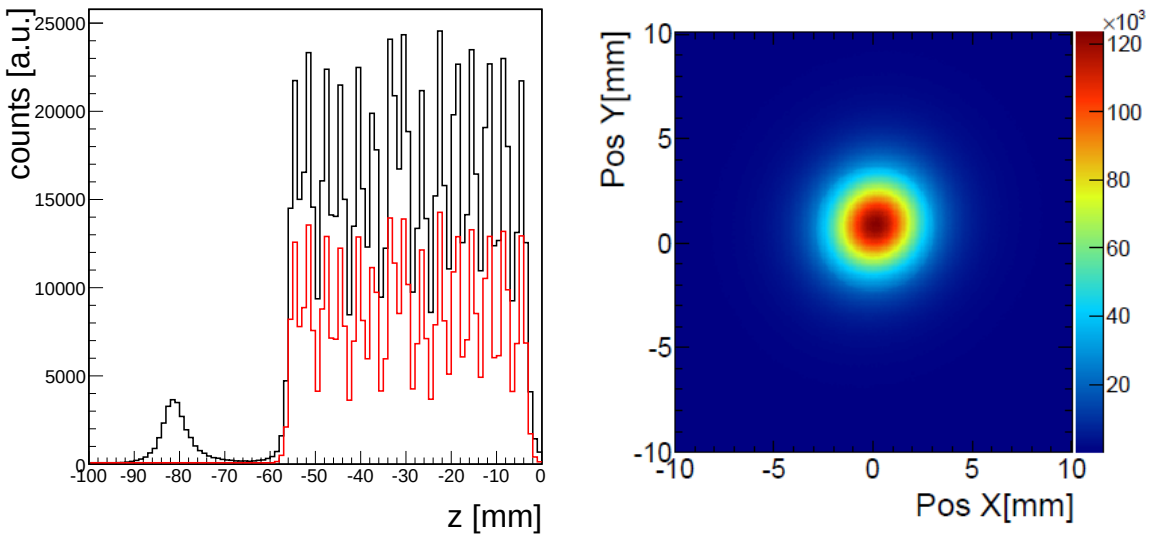

Figure 3.2: Reconstructed primary vertex. Left: Reconstructed primary vertex in direction of the incoming beam before (black) and after event cleaning (red). The different 15 target strips can be clearly separated. Reactions with the carbon ions of the START-detector can be completely removed by cutting on the z-position of the vertex. Right: Reconstructed primary vertex in the x-y-plane. The diameter of the target segments of 2.2 mm is visible.

measurement between the START- and the VETO-detector happens in the time interval between 15 - 350 ns after the reaction start time, it is most likely that a beam ion just passed the target without any reaction. However, if one of the signals is missing, most likely a second reaction in the target occurred.

- Events with a second START-hit in a time interval of 80 - 350 ns after the reaction start time, which show a correlation to the META-detectors, are rejected (*StartMeta*). The flight times of the corresponding particles are not in the physical range of the actual triggered event, but these events lead to higher multiplicities in the META-detectors, which are used for the centrality determination. Therefore, these events should be rejected.

Figure 3.3 shows a sketch of the time line of the different coincidence measurements between the START-, VETO- and META-detectors used for event cleaning. All these selection criteria are limited in efficiency due to the measured 5% inefficiency of the diamond and the META-detectors [128]. Figure 3.4 shows the reduction of the number of events that pass the applied event selection criteria to reduce background, off-target and pile-up events. The final number of $2.38x10^9$ selected events correspond to 58% of all PT3-triggered events.

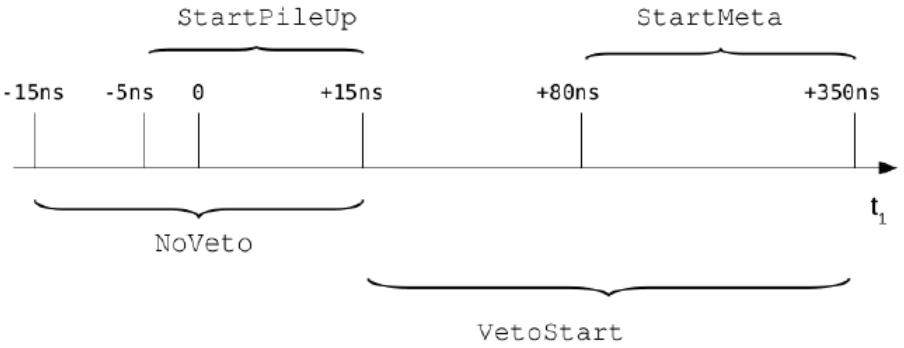

Figure 3.3: Sketch of the time line of the coincidence measurements between the START- , VETO- and META-detectors, which are used as event cleaning criteria.

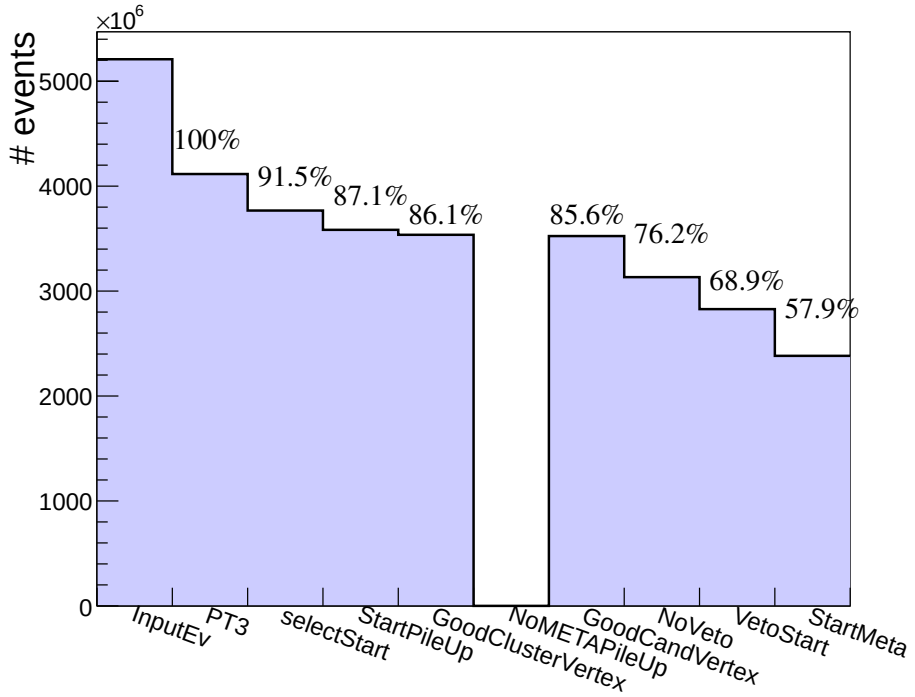

Figure 3.4: Number of events which pass cumulative the event selection criteria. Starting point are all PT3 triggered events (*PT3*). A START-hit is required (*selectStart*) and no further interactions in the START-detector are allowed (*StartPileUp*). The event vertex has to be reconstructed with a good quality (*GoodClusterVertex* and *GoodCandVertex*). Additionally, events in which a VETO-hit is registered in a time window between $\pm$15 ns after and before the hit in the START-detector (*NoVeto*) are discarded. All events with a second START-hit in a time interval of 15 - 350 ns after the reaction start time which have no correlated VETO-signal are excluded (*VetoStart*). Furthermore, events with a second START-hit in a time interval of 80 - 350 ns after the reaction start time which show a correlation to the META-detectors are rejected (*StartMeta*). For more information see text.

3.4 Centrality determination

The centrality of a heavy-ion collision has a strong impact on most physical observables. The centrality is defined by the impact parameter b, which corresponds to the distance between the center of the colliding nuclei (compare section 1.1). The impact parameter can not be measured directly in the experiment. However, e.g. a Glauber model [134] can be used to relate observables which can be measured to the impact parameter. Under the assumption, that the probability to produce particles rises monotonically with the number of participating nucleons A_{part} towards more central collisions, the average charged particle multiplicity N_{ch} or the transverse energy E_t can be used to estimate the impact parameter and A_{part} for simulated events with Glauber Monte-Carlo calculations which has been performed in [131]. From the distribution of b, the total reaction cross section can be determined. N_{ch} can then be calculated by sampling a Gaussian distribution with a mean and sigma of:

$$N_{ch} = \mu \cdot A_{part}, \sigma = k \cdot \sqrt{\mu \cdot A_{part}}, \tag{3.1}$$

whereas the parameters μ and k are determined by a fit with the Glauber model. This fit is a minimization procedure, which compares the measured with various simulated multiplicity distributions. During the beam time, two physics triggers were active, the PT3- and PT2-trigger. The PT2-trigger selects only events with at least five hits in the TOF-detector, those selected events correspond as close as possible to minimum bias reactions without collecting mostly noise. Semi-central and central Au+Au collisions were selected by the PT3-trigger, which requires at least 20 hits in the TOF-detector.

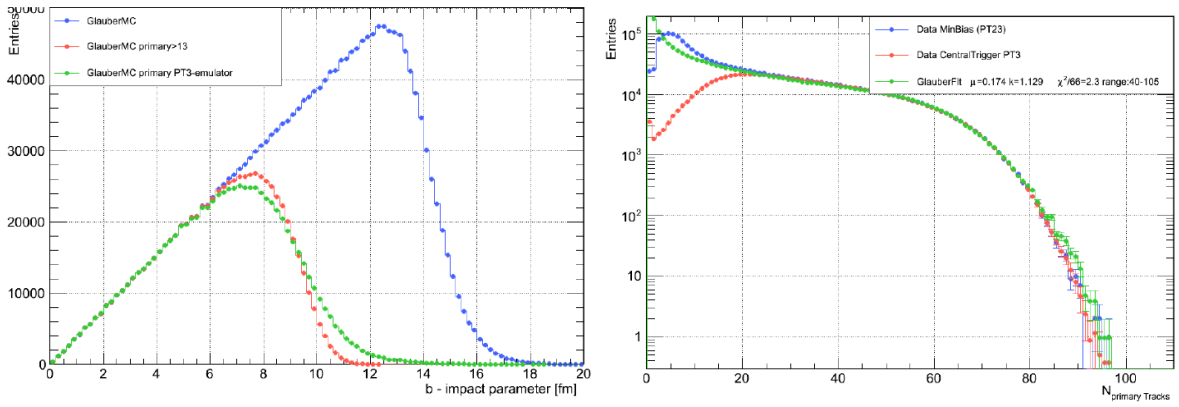

Figure 3.5: Centrality determination with the Glauber Monte-Carlo model. Left: Estimated impact parameter distribution for Au+Au collisions at 1.23 AGeV and the distribution for the PT3-triggered events. The trigger selected events with an impact parameter b < 10 fm, which corresponds to about 38% of the total reaction cross section. Right: Result from the fit with the Glauber model to the measured data. The fit is describing the measured data in the semi-central and central region, but is a bit diverging in the more peripheral part. Figures taken from [131].

The left side of figure 3.5 shows the estimated impact parameter distribution for Au+Au collisions at 1.23 AGeV and the distribution for the PT3-triggered events. The trigger selected events with an impact parameter b < 10 fm, which corresponds to about 38% of the total reaction cross section. On the right side of figure 3.5 the result from the fit with the Glauber model to the measured data can be seen. The fit is describing the measured data in the semi-central and central region, but is a bit diverging in the more peripheral part. To reduce the error on the estimated mean number of participating nucleons $\langle A_{part} \rangle$ only the 40% most central Au+Au collisions with $\langle A_{part} \rangle$ = 191 $\pm$ 7 are used in the analysis.

To get more insight into particle production mechanisms in heavy-ion collisions, the hadron analysis will be later on performed also centrality dependent. The data sample is equally divided into four different centrality classes based on the number of hits in the META-detectors. The corresponding $\langle A_{part} \rangle$ is calculated from the comparison to the fit with the Glauber model. The values are summarized in table 3.2 and the corresponding number of events are displayed in figure 3.6.

Class [%]	$\langle A_{part} \rangle$	b_{max} [fm]	N_{min}	N_{max}	Bin in figure 3.6
0-10	303	4.6	≥ 160	< 250	Mult3
10-20	215	6.5	≥ 121	< 160	Mult2
20-30	150	7.95	≥ 88	< 121	Mult1
30-40	103	9.18	≥ 60	< 88	Mult0

Table 3.2: Summary of the four different centrality classes used in the analysis with corresponding mean number of participating nucleons $\langle A_{part} \rangle$, maximum impact parameter b_{max}, minimum and maximum number of hits in the META-detectors N_{min}, N_{max} and the corresponding bin in figure 3.6

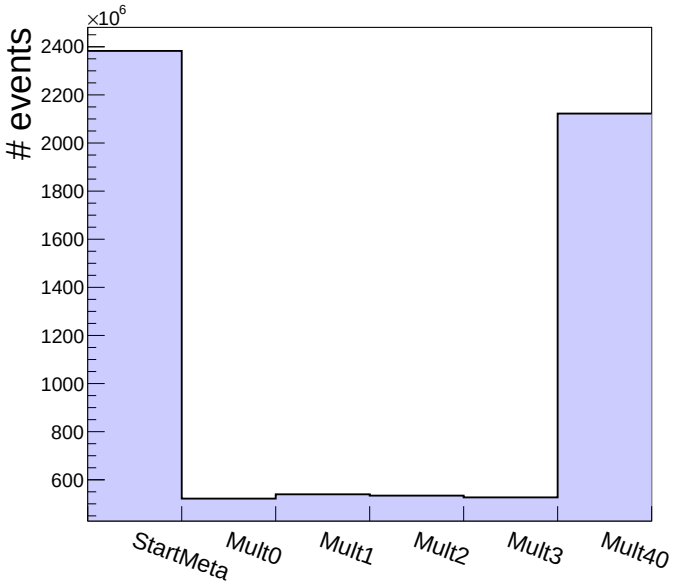

Figure 3.6: Number of events which are contributing to the four different analyzed centrality classes which are summarized in table 3.2.

3.5 Modeling of the heavy-ion collision using a Monte-Carlo simulation

To correct for a limited geometrical acceptance and for the dead times of the HADES sub-detectors which influence the measured particle distributions, the experimental data have to be compared to simulations. A tool to generate a realistic scenario for heavy-ion collisions is the UrQMD transport model [85]. UrQMD simulates the complete heavy-ion collision microscopically from first-chance collisions to the freeze-out stage. The input needed to describe multiplicities and distributions of the produced particles are elementary production cross sections. The produced particles are passing a

(H)GEANT-simulation ((**H**ADES) **GE**ometry **AN**d **T**racking). The HGEANT simulation package is based on the CERN software GEANT 3.21 [135] and is used for the following purposes:

1. Define and represent the detector geometry, i.e. volumes and media.

2. Track particles through these volumes.

3. Generate detector hits based on a realistic modeling of the physical processes occurring along the tracks, like deflection in the magnetic field and the specific energy loss in the detector material.

The detector hits are digitized and analyzed like real data in DST files within the framework of the HYDRA data analysis environment, where the hit reconstruction and their correlation to tracks take place. In figure 3.7 a sketch of the analysis procedure for the experimental and the simulated data is shown. The PLUTO event generator and the extraction of the acceptance and efficiency matrices will be explained in section 4.3. The detector effects are reproduced in the digitization process, which leads to a smearing of the simulated signals. The tuning of the digitizers is based on real data and is one of the most crucial parts of the analysis. Only a correct modeling of all detector signals allows to use the simulation to correct the measured data and interpret the physical results.

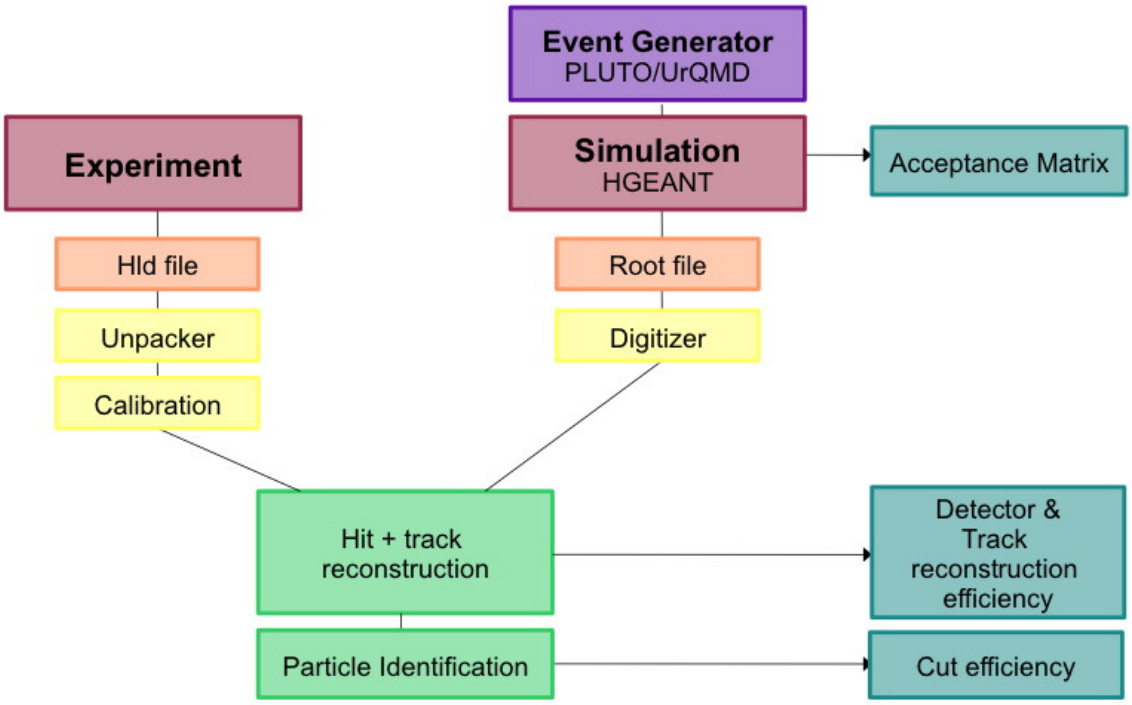

Figure 3.7: Sketch of the analysis procedure for experimental and simulated data. The experimental data is stored on tape in HLD files. The sub-detectors have to be calibrated and their position has to be known exactly to correlate the hits in the detectors with particle tracks. After momentum reconstruction the particles can be identified. The input for the simulation is the UrQMD event generator. The HGEANT package simulates the detector geometry and tracks the particles through the volumes, while taking physical effects like deflection in the magnetic field and energy loss into account. The detector informations are stored in the digitizer. The modeled detector hits are treated in the same way as the real hits.

The calibration of the specific energy loss in the drift chambers has been performed in the framework of this thesis and will be explained in section 3.10. To obtain a realistic description of the occupancy in the HADES drift chambers in the high multiplicity environment of Au+Au collisions, an enhanced δ-electron contribution had to be implemented, which will be explained in the following section.

3.5.1 Enhancement of the δ-electron contribution

A crucial part for the correct implementation of all detector effects into the simulation is the complete understanding of possible background sources. The main background sources are collisions of Au-ions with material outside the Au-target, pile-up events and δ-electrons. Due to these background sources, additional charged particles are produced, resulting in a higher occupancy in the sub-detectors of the spectrometer than expected and therefore to efficiency losses for real particles, which can not be reproduced by the Monte-Carlo simulation generated with UrQMD. Especially the inner MDCs are strongly affected, as the produced δ-electrons are forced on strongly curved trajectories due to the magnetic field and are not reaching the outer chambers. To reduce the background sources, the experimental data has to pass through a careful event cleaning procedure, which is explained in section 3.3. Left side of figure 3.8 shows the correlation between the measured leading t_1 and trailing edge t_2 of the signal in the MDC and the resulting time-over-threshold $ToT = t_2 - t_1$ before event cleaning. On the right side the projection of this distribution on the t_1-axis is displayed (black). The red distribution shows the projection after the event cleaning. In order to compare the reduction of correlated and uncorrelated background, the two distributions are normalized individually on the number of entries. The cleaning procedure helps to reduce (around one order of magnitude), but is not able to completely remove correlations which do not belong to real triggered events. Especially the underlying background, which appears as random correlation to the actual triggered event at low ToT over the complete t_1 range can not be removed by any time cuts and has therefore also to be implemented into the simulation, in order to generate a realistic detector occupancy.

In detailed studies, the source for the underlying uncorrelated background could be traced down to a larger amount of δ-electrons than expected, which are producing a high occupancy in the first two MDC modules. One observation which led to this assumption was the fact, that the sectors 2 and 5 show a lower hit occupancy than the other four sectors (see left side of figure 3.9), which could be correlated to the different material of the mirrors from the RICH-detector in these sectors. The mirrors of sector 2 and 5 are built out of glass instead of the more expensive carbon (see right side of figure 3.9), leading to a higher absorption of δ-electrons and therefore to a lower load in the drift chambers. To reduce the amount of δ-electrons which are reaching the drift chambers, a δ-electron shield was installed in the region of lower theta angles, covering roughly the RPC acceptance. A sketch of the electron shield and the effect from the shield on the hit occupancy in MDC I is shown in figure 3.10. The surviving electrons are on average firing 18 wires per Au-ion, which is causing the mean number of fired wires to be higher in the experimental data than the simulation. The implementation of the correct amount of additional δ-electrons is not a trivial task. Therefore, an iterative procedure is used in which δ-electrons are generated until the number of fired MDC cells in a time window of $t_1 <$ 0, which can not belong to the real triggered event and describes therefore only noise, is equal in simulation and real data and furthermore the distribution of the layer efficiency on the wire level in the simulation reproduces the one from the experimental data (see figure 3.11). For more details on the procedure to obtain the layer efficiencies from experimental and simulated data see [133].

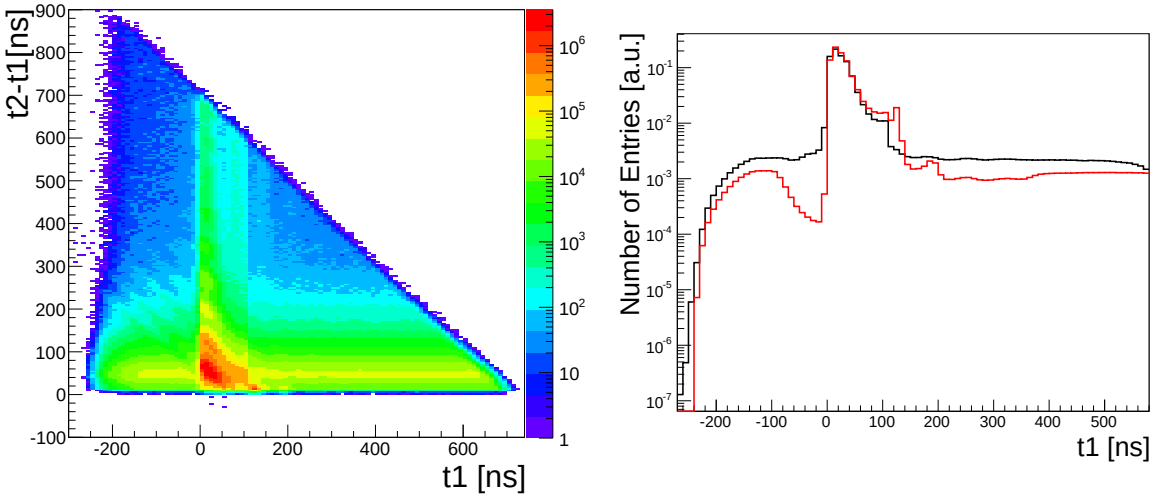

Figure 3.8: Left: Correlation between the time-over-threshold $ToT = t_2 - t_1$ and the leading edge of the signal in the MDC t_1 before event cleaning. Right: Projection of the correlation on the t_1-axis before (black) and after (red) event cleaning. The underlying background from reactions outside the Au-target, pile-up events and δ-electrons, which appears as random correlation to the triggered event ($0 \leq t_1 \leq 200$ ns) can be reduced by the cleaning procedure (around one order of magnitude).

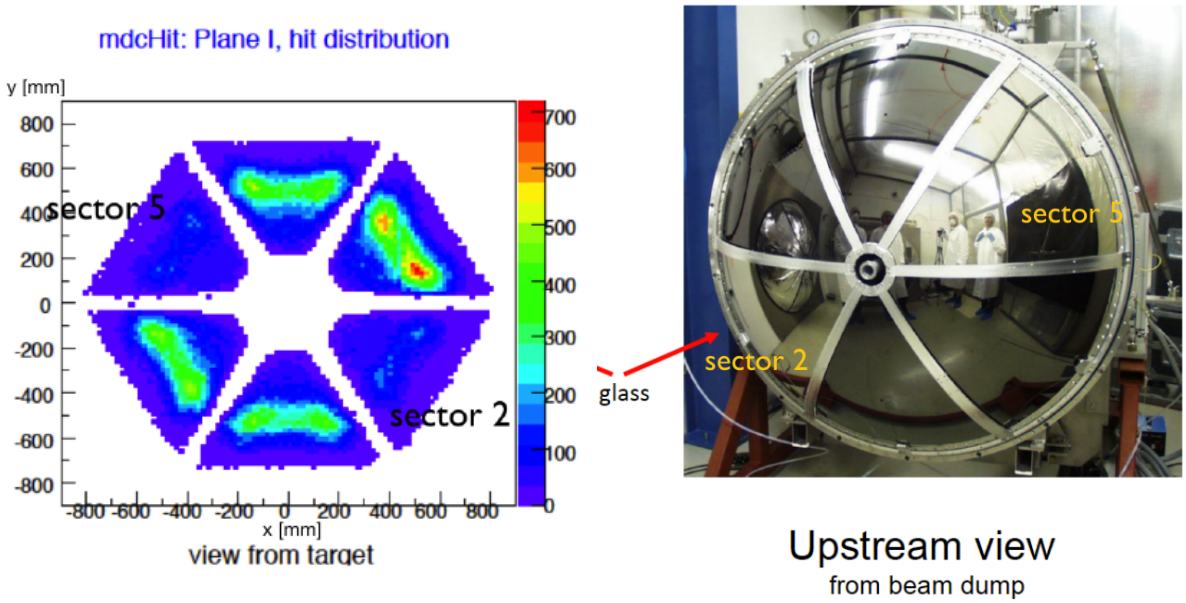

Figure 3.9: Left: Spatial distribution of the hit occupancy in the first plane of the drift chambers. Right: Photograph of the back of the mirrors from the RICH-detector. The mirrors of sector 2 and 5 are built out of glass instead of carbon. Figures taken from [122].

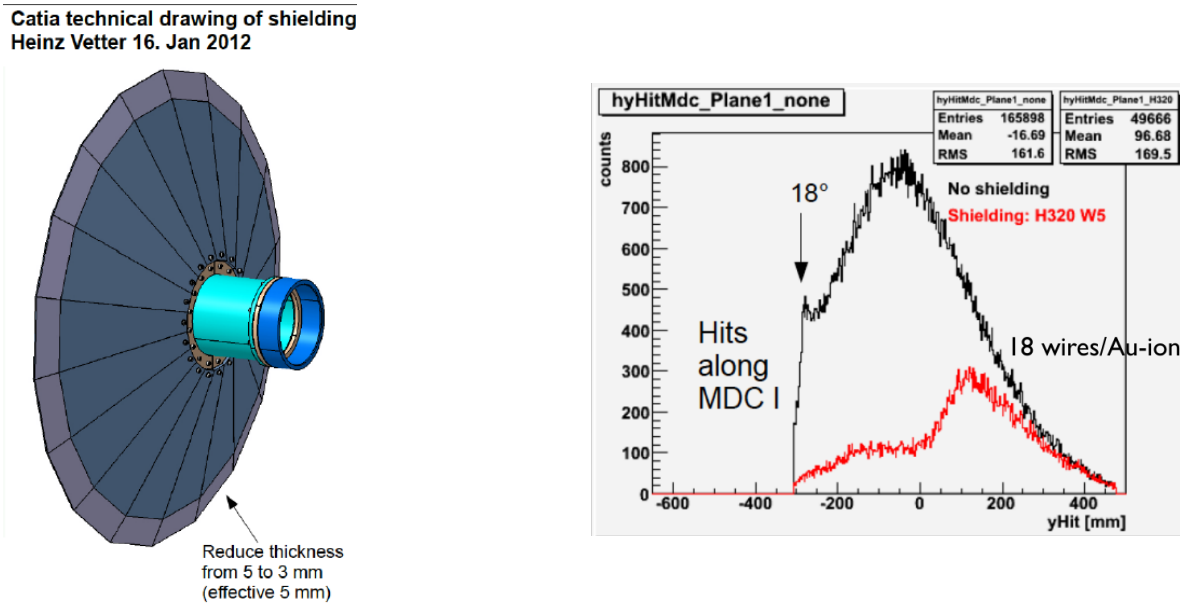

Figure 3.10: Left: Technical drawing of the δ-electron shield which was installed during the beam time. Right: Simulated effect from the shielding on the hit occupancy in MDC I. Figures taken from [122].

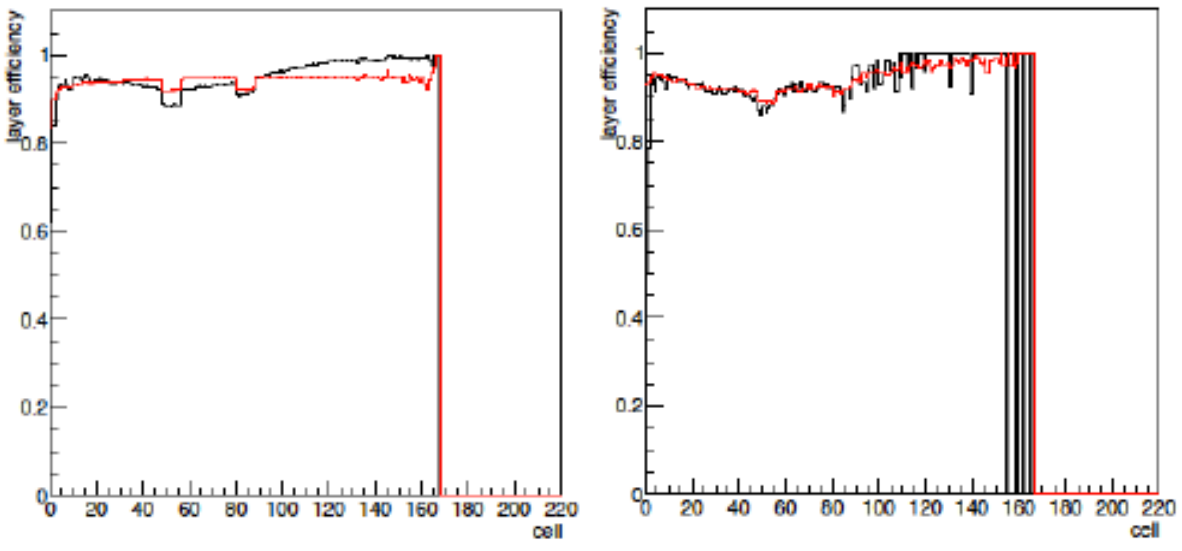

Figure 3.11: Example for the distribution of the wire efficiency (indicated by cell number) as obtained for data (black) and simulation (red) before (left) and after (right) enhancement of the δ-electron contribution in the simulation. [133]

3.6 Track reconstruction

A particle passing the drift cell volumes of the MDCs induces an electrical signal on the sense wires in these volumes (see section 2.3.2). The corresponding cells and wires are called "fired" in the following. A single fired wire in a drift chamber does not give any unambiguous position of the track. Therefore, the measurements in the several layers with different orientation of the stereo angles of the wires have to be combined by the tracking algorithm to obtain the position and direction of the track. The spatial correlation of the fired wires is performed by the so-called *track candidate search* algorithm. The volumes of the fired drift cells are projected along a certain direction onto a projection plane, which is different for the inner and outer MDCs. Overlapping wires are forming maxima on this plane which are called wire clusters. In the Au+Au data the track multiplicity within the acceptance can reach up to 140 charged particles, leading to a high occupancy in the different sub-detectors. The amount of fake and so-called *ghost tracks*, which are the result of long-range correlations between the tracks on the wire level, increases for higher track multiplicities. To improve the tracking in the high multiplicity environment some new features had to be introduced. The track candidate search can be roughly divided into the following steps:

1. **Cluster vertex finder**
   First, all fired wires are used simultaneously to find the target segment where the interaction took place. The found *cluster vertex* is the vanishing point for the projection of the fired cells in the inner MDCs used in the *cluster finder* procedure. To improve the spatial resolution of the projection procedure, the measured drift time of a track in the given cell is used to reduce the sensitive volume of the cell "shadow" on the projection plane. Figure 3.12 sketches the procedure of the cluster vertex finder and the advantage of the smaller projection volume for the track candidate search.

2. **Cluster finder in the inner MDCs**
   As a first step of the cluster finder procedure, the fired cells of the inner MDCs are projected on a common plane between the two drift chambers with respect to the event vertex. In order to improve the spacial resolution, the measured drift time inside the given cell is used to reduce the projection volume. The projection plane is binned. For fired wires the bins corresponding to the projected volume are incremented. The bins where fired wires cross form a local maximum in the common plane. When a certain amount of wires cross, this maximum is accepted as a wire cluster. The threshold for the minimum number of wires is set dynamically for each event according to the amount of fired wires in total. High thresholds reduce the efficiency of the cluster finder, whereas low thresholds increase the amount of fakes due to randomly crossing wires. In the high multiplicity environment of Au+Au collisions, the typical threshold is set to nine fired wires per cluster. The left side of figure 3.13 shows an example for a maximum formed from fired wires in the projection plane. In this example the fired wires overlap in the center of the plane and forming a maximum with 12 incremented bins in the inner drift chambers. As a next step ghost tracks in the inner segment are removed. Ghost tracks show some distinctive features in comparison to real tracks, which can be used to remove those tracks from the track sample:

   - The average amplitude of the projection of the wires is smaller.
   - The average number of unique contributing wires, which do not contribute to other clusters, to the cluster is less.

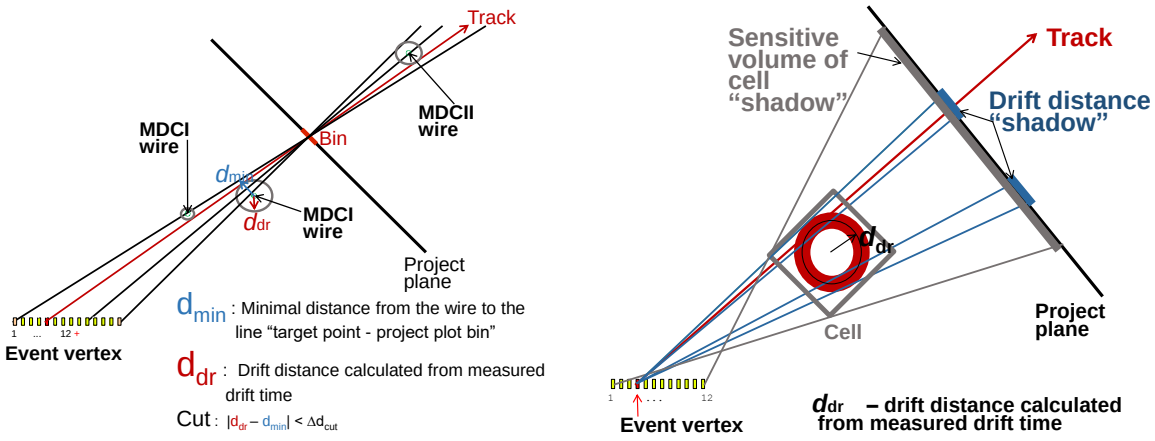

Figure 3.12: Left: Sketch of the cluster vertex finder. Right: Zoom into the region between the target, the fired cell in the first MDC and the projection plane. The drift time of the track is used to reduce the volume of the projected drift cell, which improves the spacial resolution of the cluster vertex finder procedure. Figure taken from [125].

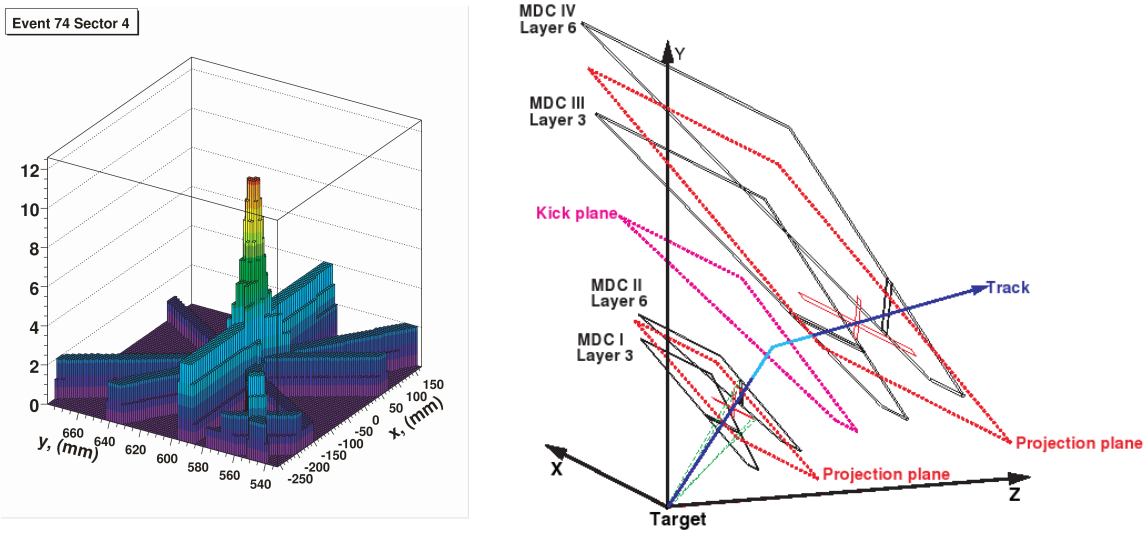

Figure 3.13: Left: Fired wires in the projection plane and the resulting maximum of 12 incremented bins in the center of the plane. Right: Method of searching for track candidates in HADES. The drift chambers are approximated by only one layer (black lines). Red lines show the projection planes between the inner, respectively outer, drift chambers. Blue lines point to the vanishing point of the projection plane. The magenta line sketches the virtual kick plane, where the particle is deflected according to its momentum. Figure taken from [122].

- The average cluster size, respectively the number of bins contributing to the maximum of fired wires in the projection plane, is smaller.

First, the algorithm searches for clusters which are formed by practically the identical set of wires as a real cluster and removes those clusters. In a next step also ghost tracks which are combined from different track wires are removed.

3. **Pre-fit procedure for the inner segment**
   The list of fired wire clusters is used as input for the so-called *pre-fit* procedure. This procedure is simply combining all found wire clusters to preliminary possible inner track segments assuming straight lines. Like in the case of the cluster vertex finder, the volume of the projected cells is reduced using the drift times of the track in the cell. This procedure picks up also previously lost wires, which may contribute to real tracks. The track origin of the pre-fit is not restricted to the primary vertex as obtained by the cluster vertex finder, which allows the reconstruction of off-vertex tracks.

4. **Inner segment fitter**
   The inner segment fitter is a χ^2-minimization procedure assuming a straight line to combine the wire clusters found in the two inner MDCs into a straight track segment. The pre-fit procedure provides improved start values for the minimization procedure of the segment fitter, which are closer to the global minimum than the list of wire clusters. The distance of closest approach of the assumed line to the fired wire is converted into a drift time. The deviation of the hit points to the found inner segment is given by a χ^2_{inner}-value, which can be used in the analysis to select the best track candidates (see section 3.6.3).

5. **Hit point estimation on a virtual kick plane**
   The inner segment intersects a two-dimensional, almost flat virtual kick plane, which approximates the deflection of a charged particle inside the magnetic field by a kick. The strength of the deflection of a particle depends on its momentum (compare also section 3.6.1).The right side of figure 3.13 shows the method of the track candidate search to illustrate the approximation of the simple kick on the kick plane. For each inner segment outer segments are searched in the two following steps.

6. **Cluster finder in the outer MDCs**
   The same procedure of cluster finding as for the inner MDCs is also used for the outer MDCs. The volume of fired wires is projected along a certain direction onto a common plane. The projection is performed with respect to the intersection point of the inner segment on the virtual kick plane. The cluster search in the outer segment is restricted to the range of physical correlations of the momenta and charge of the tracks. Again ghost tracks are reduced by searching for distinctive features of those tracks.

7. **Outer segment fitter**
   The list of found wires from the cluster finder is used to find the outer track segment in a χ^2-minimization procedure. The deviation of the hit points to the found segment is given by a χ^2_{outer}-value, which can be used in the analysis to select the best track candidates (see section 3.6.3).

In a last step, the track segments are roughly matched (5σ deviation) to the hit points in the META-detectors, by interpolating the found outer segment to the META-detector plane assuming a straight

line. For the found combinations of an inner and outer track segment, the momentum can be reconstructed.

3.6.1 Momentum reconstruction

The momentum reconstruction is based on the fact that a charged particle (charge q, velocity $\vec{v}$) is deflected when passing a magnetic field (strength B) due to the Lorentz force $F = q[\vec{v} \times \vec{B}]$. The deflection can be approximated by a simple transverse kick $\Delta\vec{p}_{kick}$:

$$\Delta\vec{p}_{kick} = \vec{p}_{out} - \vec{p}_{in} = \int d\vec{p} = \int \vec{F} dt = \int q[\vec{v} \times \vec{B}]dt = -q \int \vec{B} \times d\vec{s}, \tag{3.2}$$

with incoming and outgoing momentum vector $\vec{p}_{in}$ and $\vec{p}_{out}$ of the particle. The angle of deflection can be estimated with the equation

$$\sin \frac{\Delta\theta}{2} = \frac{|\Delta\vec{p}_{kick}|}{2|\vec{p}|}, \tag{3.3}$$

with $|\vec{p}_{in}| = |\vec{p}_{out}| = |\vec{p}|$. To reconstruct the momentum from the spatial information of the inner and outer track segments found by the segment fit an iterative procedure is used, starting with the assumption that the particle trajectory can be described by a cubic spline. The so-called **spline method** calculates continuous interpolation functions over small intervals, for which supporting points between the inner and outer segments are introduced. Additionally higher order derivations in the intervals and at their borders have to be continuous. To take into account that the region inside the drift chambers is not perfectly field free, the **Runge-Kutta method** is used to obtain the final momentum of the track candidates. The equations of motion are numerically solved. As start parameters the results of the spline method are used, the equations are solved at the starting point and then extrapolated to the next track point. As a next step, the recursively reconstructed trajectory is compared to the measured hit

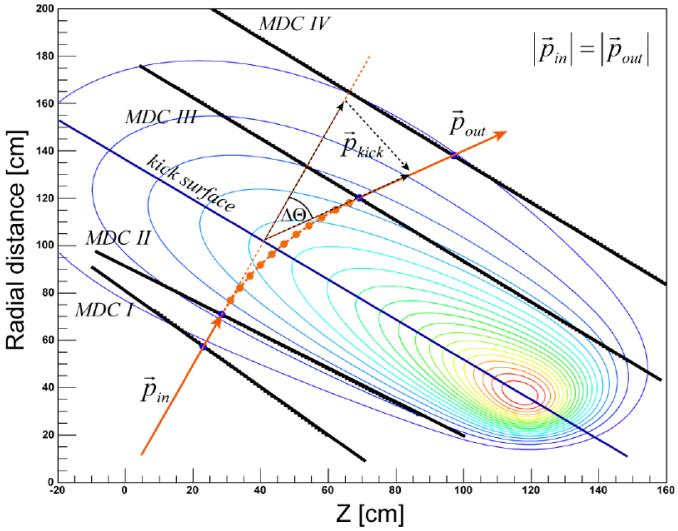

Figure 3.14: Scheme of the momentum reconstruction in HADES. The track is passing the four MDC layers and feels a transverse kick of $\Delta\Theta$ at the kick surface, from which the momentum can be derived by using equation 3.3. The spline method is used to reconstruct the momentum of the particle by solving equations of motion at some supporting points (orange points). The results are used as input parameter for the iterative numerical solution of the equations of motion at several points with the Runge-Kutta method. Figure taken from [125].

points and the procedure is repeated up to 11 times in order to find the optimum trajectory. The quality of the track is estimated by a normalized χ^2_{RK}-value, which can be used in order to select best track candidates (see section 3.6.3). In order to avoid instabilities of the χ^2-minimization for momentum reconstruction, the errors used for normalization are not perfectly calibrated and too small in some cases. Therefore, the χ^2_{RK} can reach high values far above one. Figure 3.14 shows a sketch of the momentum reconstruction in HADES.

3.6.2 META-matching

In order to match a found particle candidate, consisting of an inner and outer track segment, to the corresponding hit in one of the META-detectors, the particle trajectory found by the Runge-Kutta algorithm is extrapolated to the intersection point with the META-detector plane. For the reconstructed position from the extrapolation, a real META-hit is searched in absolute x-y-coordinates in the laboratory system. The deviation to the real hit point is given by dx or dy.

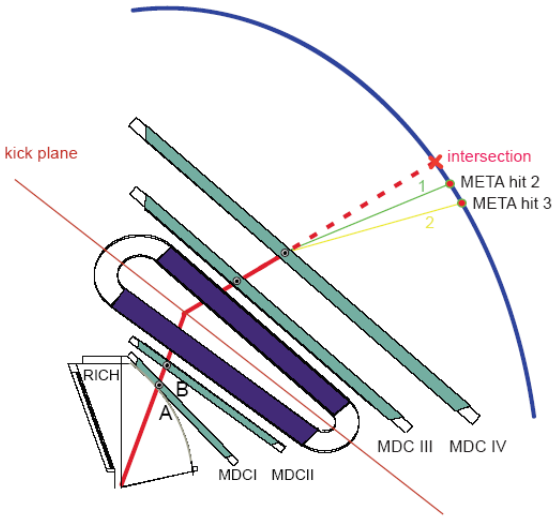

Figure 3.15: Simplified scheme of the matching of tracks to the hits in the META-detector. The track segment from the outer drift chamber is extrapolated as a straight line to the intersection point on the META-detector plane, neglecting the curvature of the track in the magnetic field. From the deviation of the intersection point to the META-hits in the x-coordinate, the quality parameter χ^2_{MM} is calculated. Figure taken from [125].

A simplified scheme of the META-matching, neglecting the curvature of the track, is shown in figure 3.15. The quality of this matching is given in x-direction by a χ^2_{MM}-value:

$$\chi^2_{MM} = \frac{dx}{\sigma_x}, \tag{3.4}$$

with σ_x being the error of the measurement. On the left side of figure 3.16 the dx-distribution from the Runge-Kutta algorithm to the TOF-hits is shown for minimum- (MIPS), medium- (MEPS) and maximum- (MAPS) ionizing particles. The smaller the energy loss, the broader the resulting width of the distribution. In order to apply the same quality cut for all particles, the errors σ_x of the matching are calibrated for the so-called "walk-effect" [136]. The walk-effect describes the dependence of the time measurement inside the scintillator on the induced strength of the signal. High-ionizing particles are inducing a stronger signal than minimum-ionizing particles. Therefore, the errors σ_x are depending on the energy loss. The energy dependence is implemented in the simulation (dashed lines), to correct for efficiency losses when applying a cut on the quality of the META-matching. Furthermore, the amplitude of the signal does also depend on the position at which the particle has passed the scintillator rod, as the signal is attenuated and gets diffused when traveling through the

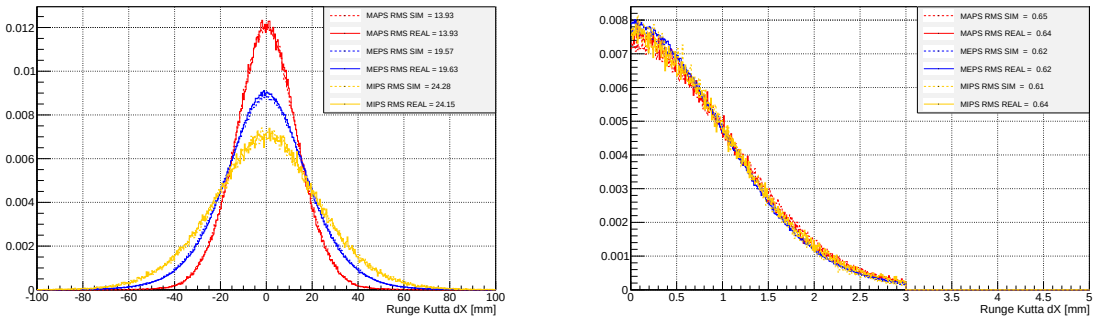

Figure 3.16: Left: Distribution of the deviation of the interpolated hit in the TOF-detector from the Runge-Kutta algorithm to the real hit dx for minimum- (MIPS, yellow), medium- (MEPS, blue) and maximum-ionizing particles (MAPS, red) for data (solid lines) and simulation (dashed lines). Right: Calibrated quality of the META-matching χ^2_{MM} for minimum- (MIPS, yellow), medium- (MEPS, blue) and maximum-ionizing particles (MAPS, red) for data (solid lines) and simulation (dashed lines). Figure taken from [136].

plastic of the scintillator. As a result, the amplitude of the signal is getting smaller, if the particle passes at one edge of the scintillator instead of in the center. In order to calibrate this effect, the deviation of the reconstructed time, which has been explained in section 2.4.2 to the real flight time of the particle is depending on the measured amplitude of the signal. The resulting distribution for the META-matching quality parameter is displayed on the right side of figure 3.16, again for MIPS, MEPS and MAPS in real data and compared to the simulation. The width of the distribution is the same for the different particles after calibration and reproduced by the simulation.

The measurement in the META-detectors in y-direction is just a uniform measurement whether the rod (TOF), respectively cell (RPC), got hit or not, therefore the search in the dy-direction is just based on a boundary condition and restricted for straight lines to the dimensions of the rod or cell of 4 mm. To take into account multiple scattering of the particles a tolerance window is allowed, which scales inverse to the momentum of the particle.

3.6.3 Particle candidate selection

The distributions of the number of found inner and outer track segments in all six sectors of the spectrometer for the selected events (see section 3.3) are shown in the upper row of figure 3.17. On average 74 inner and 78 outer segments are reconstructed by the tracking algorithm, however, the amount of found segments can reach up to $\approx$ 500 for some events. The Monte-Carlo simulation is reproducing the shape of the distributions in the region of most probable values up to $\approx$ 150 found segments. The tails from events with a higher amount of found segments in the real data are not reproduced, leading to a smaller average of 62 inner and 64 outer segments in the simulation. The hit multiplicities in the RPC- and TOF-detector are displayed in the lower row of figure 3.17. The average hit multiplicity is 82 in the RPC and 36 in the TOF and can reach up to 200 hits in the RPC and 100 hits in the TOF. The deviation between the amount of hits in the two detectors is due to their different coverage in polar angles and is also reflected in the amount of fired wires in the drift chambers in the corresponding region. Furthermore, the distributions are reproduced by the Monte-Carlo simulation. The deviation between data and simulation in the low multiplicity region in the TOF is due to the

trigger condition. In the real data this condition is explicitly selecting the minimum amount of 20 hits in the TOF, whereas in simulation a smooth impact parameter distribution with b_{max}<10 based on Glauber Monte-Carlo is modeled.

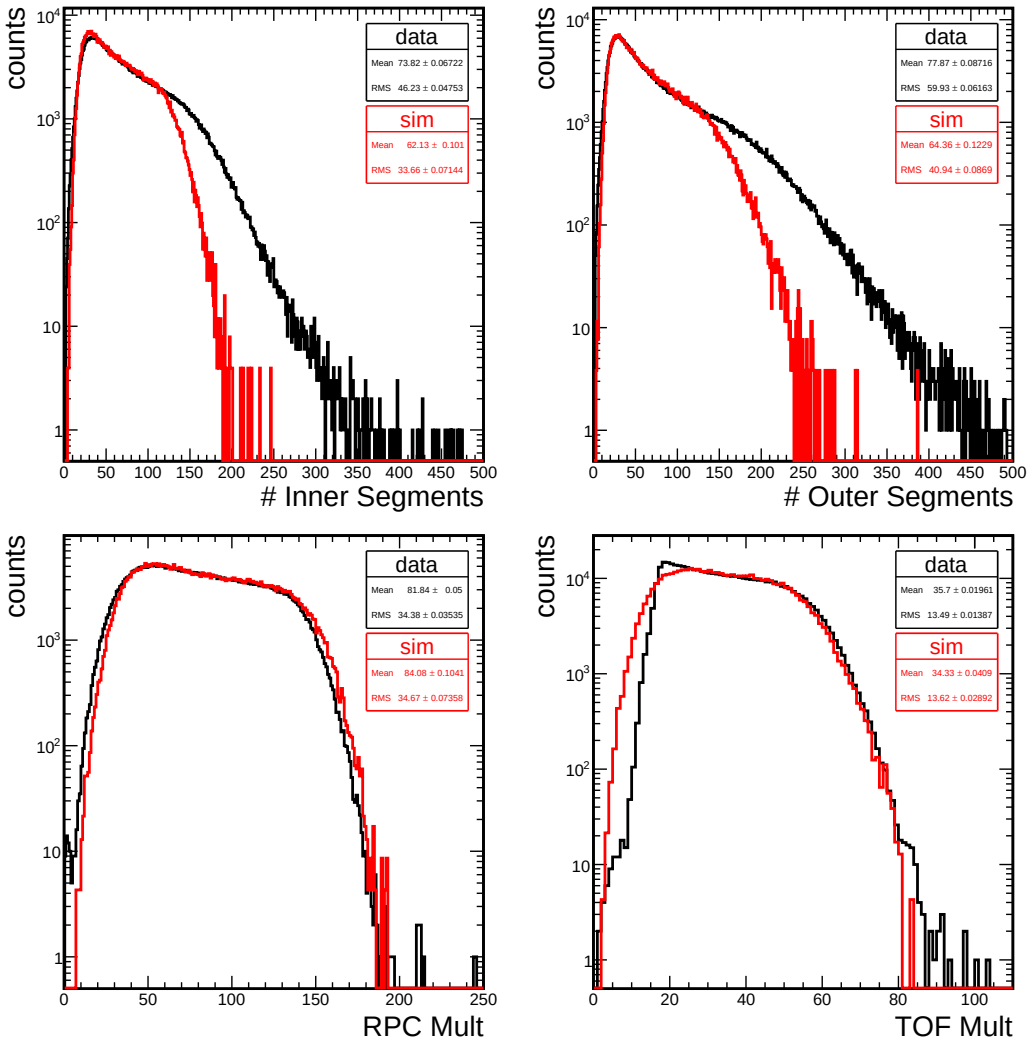

Figure 3.17: Top: Number of inner (left) and outer (right) track segments found by the tracking algorithm in all six sectors of the spectrometer for experimental data (black) and the Monte-Carlo simulation (red). Bottom: Hit multiplicity in the RPC- (left) and TOF-detector (right) from experimental data (black) and the Monte-Carlo simulation (red). In order to compare only the shape the spectra are normalized to each other.

The tracking algorithm combines the found inner and outer segments plus a META-hit to possible track candidates. The distribution of the number of particle track candidates for all six sectors is displayed on the left side of figure 3.18. Like in case of the number of inner and outer segments, the experimental data is reproduced by the Monte-Carlo simulation in the region of most probable values up to $\approx$ 150 track candidates. However, the simulation cannot describe the tails corresponding to those events with a significantly higher amount of possible candidates, leading to a lower average number of possible track candidates of 65 instead of 73. In order to reduce the high amount of possible track candidates the following minimum requirements have to be fulfilled:

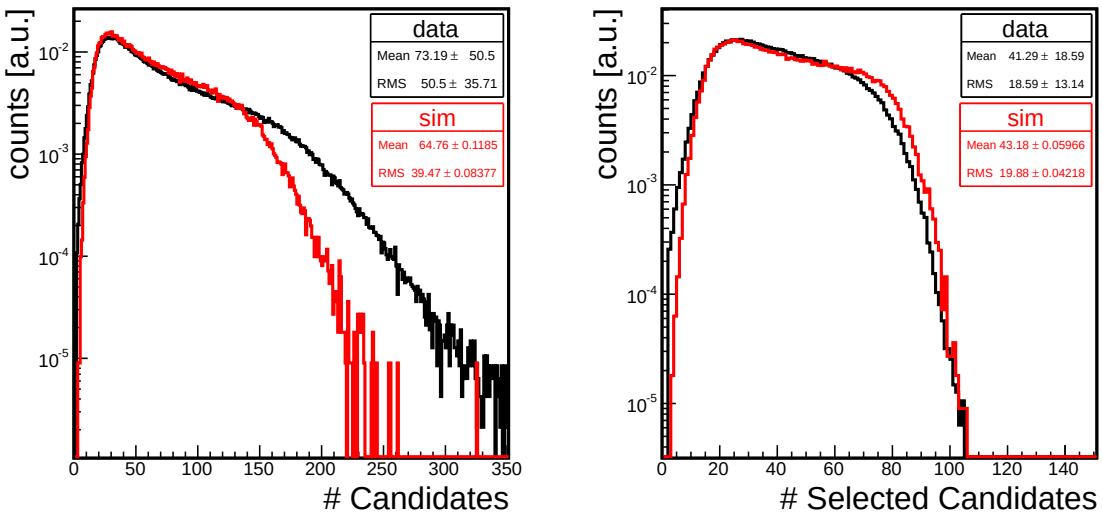

Figure 3.18: Left: Number of track candidates consisting of an inner and outer segment plus a hit in the META-detector in all six sectors of the spectrometer from experimental data (black) and simulation (red). Right: Number of selected particle track candidates after the rejection of tracks which share track segments in all six sectors from experimental data (black) and simulation (red).

1. The track has to have a hit in the inner and outer MDCs plus a hit in the META-detector.
2. The Runge-Kutta momentum reconstruction has to be successful and the reconstructed momentum has to have a value greater than zero.
3. The β measurement of the track has to have a value greater than zero and the time-of-flight should be below 60 ns.
4. The χ^2_{inner} has to be greater than zero and the χ^2_{RK} smaller than 1000[5].
5. The tracks are matched to the META-detectors in absolute dx-dy-coordinates of the rods of the TOF-, respectively cells of the RPC-detector (4 mm in dy and 3σ in dx).

The combination of the different track segments and hits in the META in order to generate particle candidates has not always a single solution in the high multiplicity environment of a Au+Au collision. The possibilities to create track candidates which share the same detector hits is sketched in figure 3.19. For example one found inner segment can be matched to two different combinations of outer segments and to two different (A) or even the same META hit (B). Furthermore, the combination of one inner and outer segment can be matched to two different META hits (C) or two found tracks can be matched to the same META hit (D). The probability distribution for sharing an inner/outer track segment or a hit in the META-detector of a pion or proton candidate is shown in figure 3.20 for central (0 - 10%) and semi-central collisions (30 - 40%). In peripheral collisions 90% of the particle candidates are unique tracks which are not sharing a track segment and 95% without a shared META-hit with other tracks. In most central collisions, for which the occupancy in the sub-detectors is much higher, these numbers are reduced and the probability for tracks sharing the segment increases.

[5]Note that the quality χ^2_{RK} from the momentum reconstruction can reach very high values, because the errors from the single measurements are too small (see section 3.6.1).

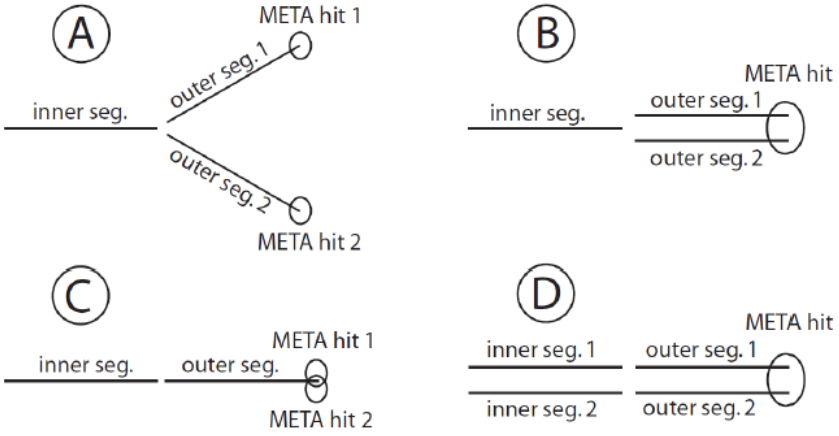

Figure 3.19: Possibilities to create track candidates which share the same detector hits. One found inner segment can be matched to two different combinations of outer segments and to two different (A) or even the same META hit (B). Furthermore, the combination of one inner and outer segment can be matched to two different META hits (C) or two found tracks can be matched to the same META hit (D). Taken from [137].

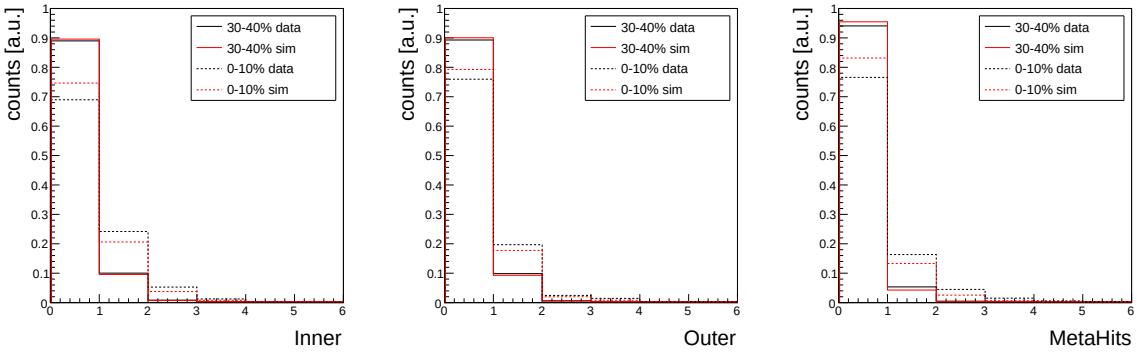

Figure 3.20: Probability distribution of a particle candidate sharing an inner (left) or outer (center) track segment or a META-hit (right) with other track candidates for 0 - 10% (dashed lines) and 30 - 40% (solid lines) most central collisions in experimental data (black) and simulation (red).

30% of the tracks share the inner, 20% the outer segment and 25% the META-hit with other track candidates. The simulation is reproducing the distributions for the semi-central collisions but the tracking algorithm finds more unique tracks in case of the most central collisions. The dependence of the probability of tracks to share segments or hits on the track multiplicity is reflected in the polar angle θ coverage of the spectrometer. In low polar angles the track density and the noise within the detectors is higher compared to high polar angles. The probability distributions for different regions in polar angles can be found in appendix A, figure A.1.

For the analysis it is crucial that only unique tracks which do not share detector segments and hits with other analyzed tracks are used. Furthermore, it is crucial that the track segments are correctly matched, to avoid wrongly determined momenta or flight times of the particles. Especially the wrong combination of fast pion tracks to hits of protons in the META-detector should be avoided, as those matches lead to a wrongly calculated mass (see section 3.7) which is hampering the kaon signal for some momenta. This will be addressed in more detail in section 4.1.2.2. To decide which of the possible track candidates are the correctly reconstructed particles, a careful track sorting routine is applied. The tracks which share track segments or a META-hit are sorted according to the best quality of the Runge-Kutta momentum reconstruction χ^2_{RK}. Only the track with the smallest χ^2_{RK}-value is selected, the other tracks are discarded. On the right side of figure 3.18 the resulting distribution of the selected tracks is displayed. On average 41 track candidates per event in the six sectors of the detector are selected. However, in most central collisions the multiplicity of selected tracks can reach up to $\approx$ 100. The simulation is reproducing the amount of selected tracks. The distributions of the track quality parameters χ^2_{RK} and χ^2_{MM} from the selected and the discarded tracks are shown in figure 3.21. In order to compare the shape of the distributions to the simulation, the spectra have been normalized to the number of entries. It can be clearly seen that the discarded tracks have worse track quality parameters than the selected ones. The simulation is reproducing the trend but shows on average slightly more good quality tracks than the real data.

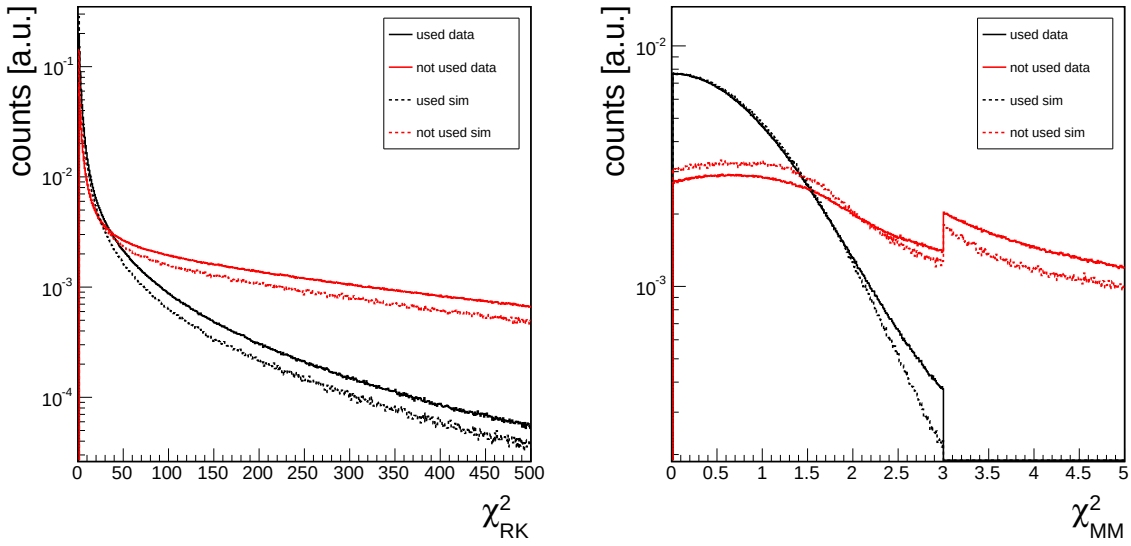

Figure 3.21: Distribution of the track quality parameters χ^2_{RK} (left) and χ^2_{MM} (right) of the selected (black) and discarded tracks after rejection of shared segments and hits in the META-detectors (red) in real data (solid lines) and compared to simulation (dashed lines). The distributions are normalized to the number of entries.

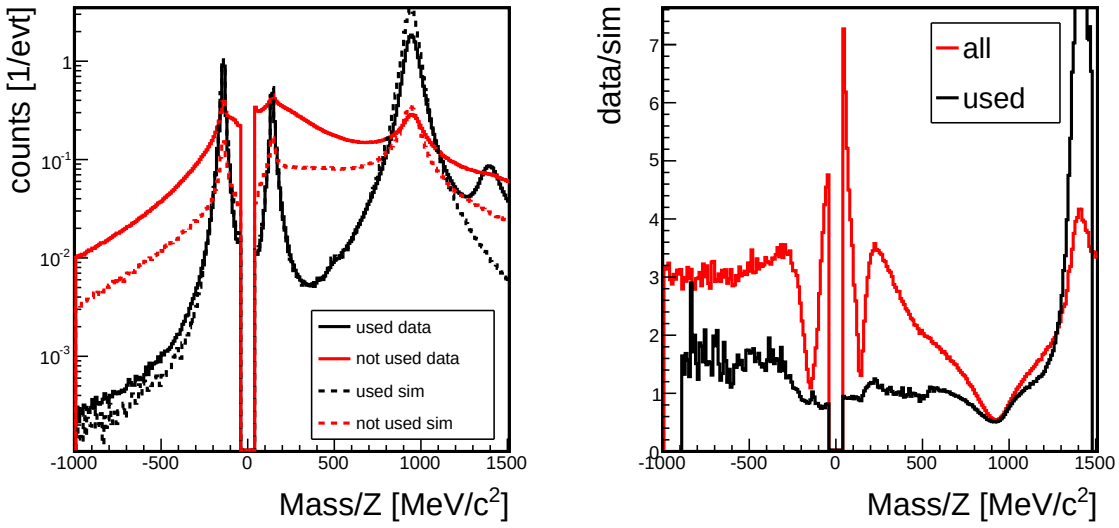

Figure 3.22: Mass distribution of the selected particle candidates (black) and discarded tracks which had shared a track segment with a selected track (red) of data (solid lines) and simulation (dashed lines) normalized to the corresponding number of events. Right: Ratio between data and simulation of the mass distribution of all track candidates (red) and the selected tracks (black).

The result of the rejection of shared track segments can be seen as a function of the calculated mass spectrum of the particles (see section 3.7) on the left side of figure 3.22. The black solid line is the resulting mass distribution of the selected particle candidates and the red solid line the one of the discarded tracks. The selected tracks show clear separated peaks around the physical masses of the particles whereas the discarded tracks are mostly background at unphysical masses. The dashed lines correspond to the result from the Monte-Carlo simulation. Whereas the distribution of the selected tracks is well reproduced[6], the background of wrong tracks is underestimated in the simulation. Nevertheless, the purity of the track selection is high which can be indirectly estimated when comparing the ratio between data and simulation of the mass distribution of all track candidates to the ratio of the one from selected tracks shown on the right side of figure 3.22. In the region of the physical masses of the protons and pions those two ratios are giving the same values whereas they diverge in the region of the background. Therefore, the simulation can be used to estimate track reconstruction efficiencies of identified particles like pions and protons, although there are small deviations to the real data. However, for a realistic description of the background, which influences the track quality parameters, further correction factors have to be used in the analysis. The track reconstruction efficiency of negative pions is in the order of 83% and 89% for protons, which is displayed as a function of momentum in figure 3.23 for the analyzed 40% most central collisions. The correlation between the number of expected primary particles inside the HADES acceptance and all selected tracks after the rejection of tracks which share track segments or a hit in the META-detectors from the Monte-Carlo simulation is displayed in figure 3.24. The slight deviation from the linear correlation illustrates the expected track reconstruction efficiency which is in the order of 90%. The track reconstruction efficiency shows a small centrality dependence, as the efficiency is lower for more central collisions in which more primary particles are produced. The deviation of the track reconstruction between data and simulation is

[6] except the exact production cross section of the particles and the the high mass region, due to missing fragments in the simulation

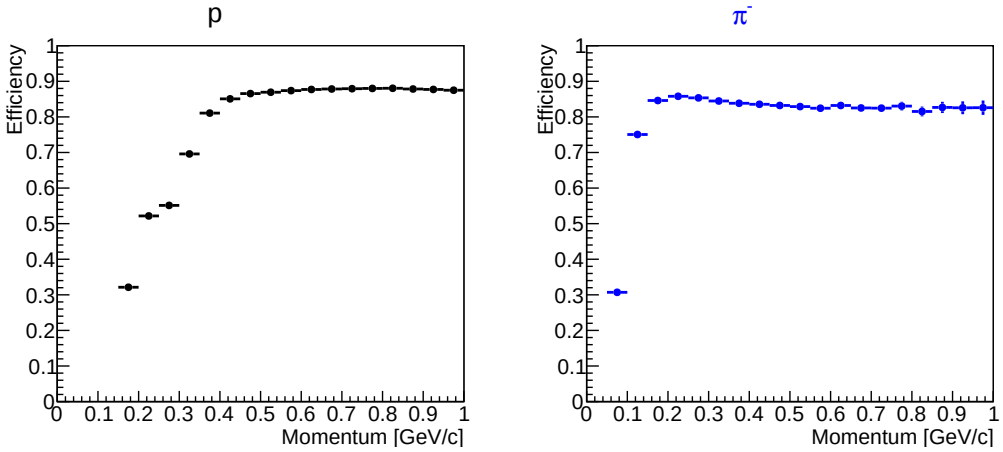

Figure 3.23: Track reconstruction efficiency of protons (left) and negative pions (right) as a function of momentum.

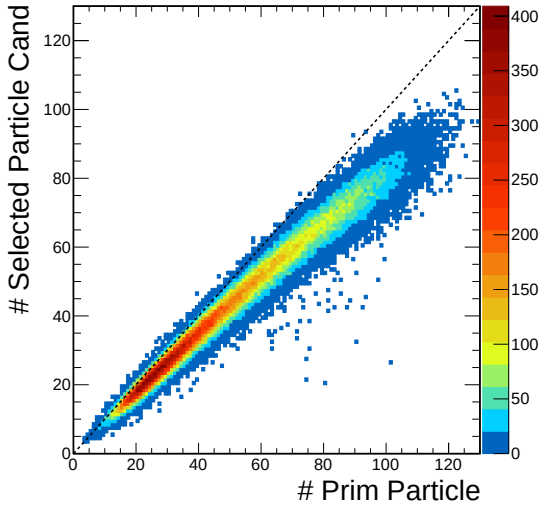

Figure 3.24: Correlation between the number of expected primary particles inside the HADES acceptance and selected tracks after the rejection of tracks which share segments or hits in the META-detectors from the Monte-Carlo simulation. The deviation from the linear correlation (dashed line) illustrates the expected track reconstruction efficiency which is slightly lower for more central collisions.

bigger at the geometrical edges of the drift chambers. Which can be seen in figure 3.25 where the ratio between data and simulation of the x-y-position of the intersection point of the reconstructed track segment with the two 40° layers of the corresponding drift chamber (MDCI upper left, MDC II upper right, MDC III lower left and MDC IV lower right) is shown. This ratio is at unity in most places of the chambers, but deviates close to the edge. Meaning that in this region less tracks are reconstructed in the real data compared to the simulation. In order to remove this systematic deviation, tracks which have been reconstructed in the area indicated by the black boxes in the figure are discarded in addition from the analysis.

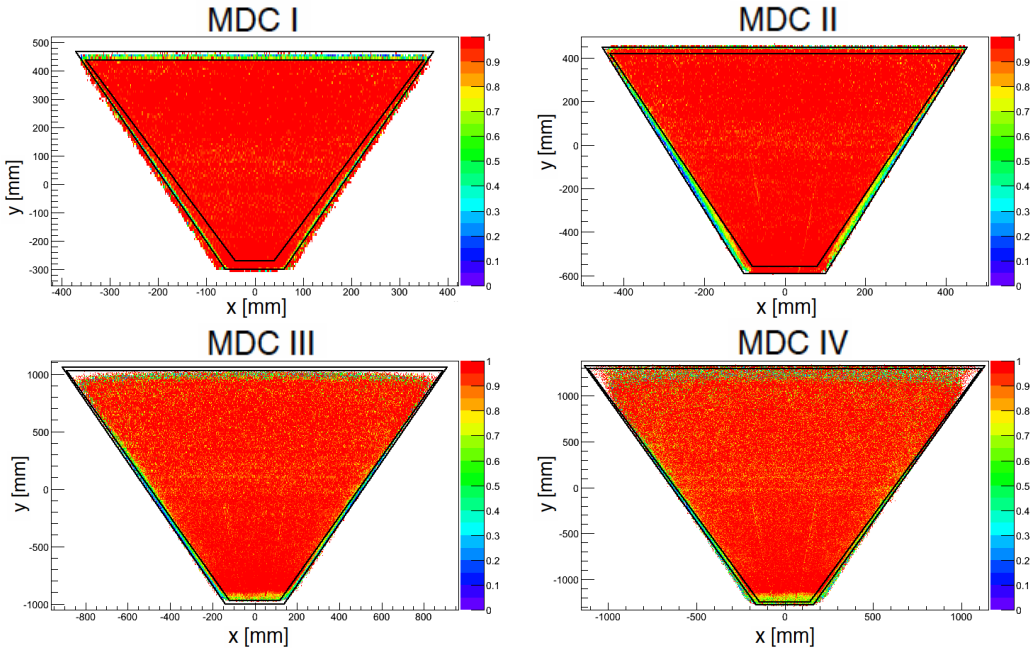

Figure 3.25: Ratio between data and simulation of the x-y-position in the MDC segment coordinate system of the intersection point of the reconstructed track segment with the two 40° layers of the corresponding drift chamber (MDCI upper left, MDC II upper right, MDC III lower left and MDC IV lower right). The tracks which have been reconstructed at the edges of the drift chambers indicated by the black boxes are discarded from the analysis. [122]

3.7 Particle identification using the momentum and time-of-flight information

The magnetic field of the HADES detector forces charged particles on curved trajectories. By measuring the track of the particle in front and behind the magnetic field, the deflection, and with it the momentum p and polarity q of the particle, can be estimated (compare section 3.6.1). The magnetic field is oriented such that positive particles are bend in and negative ones away from the direction of the beam axis. In combination with the measurement of the time-of-flight, which is given by the difference between the reaction start time measured between the START-detector (t_0) and the arrival time in the META-detector (t_1) at the end of the setup: $\Delta t = t_1 - t_0$, the different particle species can be identified. As the length s of the reconstructed track is known from the Runge-Kutta method, the velocity of the particle can be calculated:

$$\beta = \frac{v}{c} = \frac{s}{c\Delta t}. \tag{3.5}$$

The mass of the particle can then be calculated according to:

$$m/q = \frac{p/q}{\gamma \cdot \beta \cdot c}, \tag{3.6}$$

with the Lorentz-factor $\gamma = \frac{1}{\sqrt{1-\beta^2}}$. Uncertainties of the time or momentum measurement can lead to velocities higher than the speed of light. To avoid imaginary masses, the square of the mass is used in the analysis. Figure 3.26 shows the correlation between the momentum and β information after

event and track reconstruction and the rejection of tracks which share segments of hits in the META-detectors, measured by the two time-of-flight detectors RPC and TOF separately, since the resolution of the two detectors is slightly different (see section 2.4.2). The various particle species are distributed around the expected values according to:

$$\beta = \frac{p}{m} \frac{1}{\sqrt{(\frac{p}{m})^2 + 1}}. \tag{3.7}$$

The reconstructed mass spectra from the shown tracks in the region of the RPC- and TOF-detector are displayed in figure 3.27. The particles are distributed around their nominal mass.

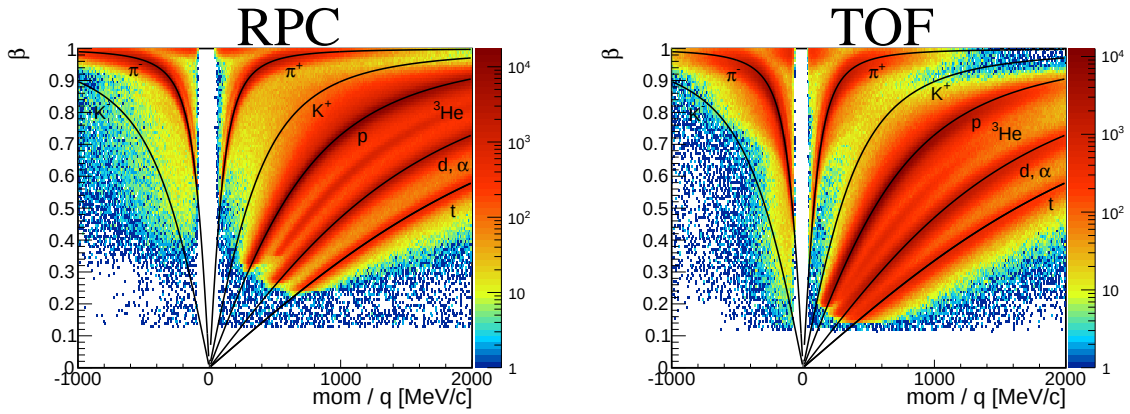

Figure 3.26: Correlation between the momentum and β information of all selected tracks measured in the RPC- (left) and TOF-detector (right). Black lines correspond to the expected values for the different particle species according to equation 3.7.

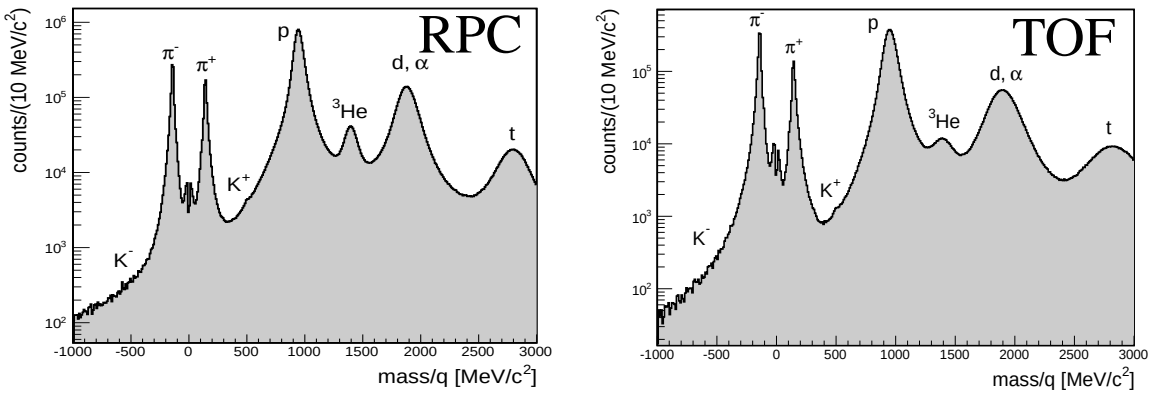

Figure 3.27: Mass distributions of all selected tracks after the event and track selection (see sections 3.3 and 3.6.3) in the RPC- (left) and TOF-detector (right).

3.8 Particle identification using the specific energy loss

The mean rate of energy loss of a particle -$\langle dE/dx \rangle$ depends on the velocity and charge of the particle. This allows to separate different particle species by their specific energy loss information, if their momenta are known. A description of the mean energy loss -$\langle dE/dx \rangle$ in the region of $0.1 \leq \beta\gamma \leq 1000$ for a particle with speed $v = \beta c$, charge z and energy E, traveling a distance x inside a material with atomic number and mass Z, A and mean excitation energy I, is given by the Bethe-Bloch formula [138, 139]:

$$-\left\langle \frac{dE}{dx} \right\rangle = K \frac{Z}{A} \frac{z^2}{\beta^2} \left[\frac{1}{2} \ln \left(\frac{2m_e c^2 \beta^2 \gamma^2 T_{max}}{I^2} \right) - \beta^2 - \frac{\delta(\beta\gamma)}{2} \right] \tag{3.8}$$

with

K	-	$4\pi N_A r_e^2 m_e c^2$ = 0.307 MeV mol cm^2
m_e, r_e	-	electron rest mass and radius
N_A	-	Avogadro constant = 6.022 x 10^{23} mol^{-1}
$\delta(\beta\gamma)$	-	density correction term

T_{max} corresponds to the maximum kinetic energy which can be deposited on a free electron in an elastic scattering process and is given by:

$$T_{max} = \frac{2m_e c^2 \beta^2 \gamma^2}{1 + 2\gamma m_e/M + (m_e/M)^2}, \tag{3.9}$$

with M being the mass of the particle. At the lower limit ($\beta\gamma < 0.1$) the projectile velocity becomes comparable to the velocity of electrons bound in atoms, whereas at the higher edge ($\beta\gamma > 1000$) radiative effects become important. Figure 3.28 shows the mean energy loss of muons inside copper as a function of $\beta\gamma = p/Mc$. In the momentum relevant region at which HADES is operating, the Bethe-Bloch formula is indeed a good approximation of the mean rate of energy loss. For more details see [139].

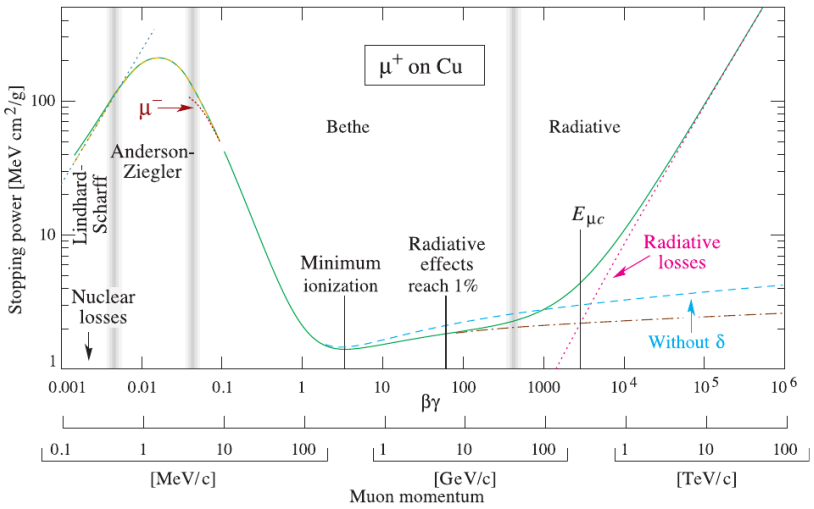

Figure 3.28: Mean energy loss of muons in copper as a function of $\beta\gamma = p/Mc$. Figure taken from [139].

The specific energy loss inside the TOF-detector is displayed as a function of the momentum of the particles in figure 3.29 and figure 3.30 shows the correlation between the specific energy loss in the

drift chambers and the momentum measured with the two different time-of-flight detectors RPC and TOF. After calibration, the particles are distributed around the expected curves according to the Bethe-Bloch formula (equation 3.8). The deviation from the Bethe-Bloch curve at low momenta is due to stopping of the slow particles in the detector material. Only with a certain momentum the particles can punch through the material.

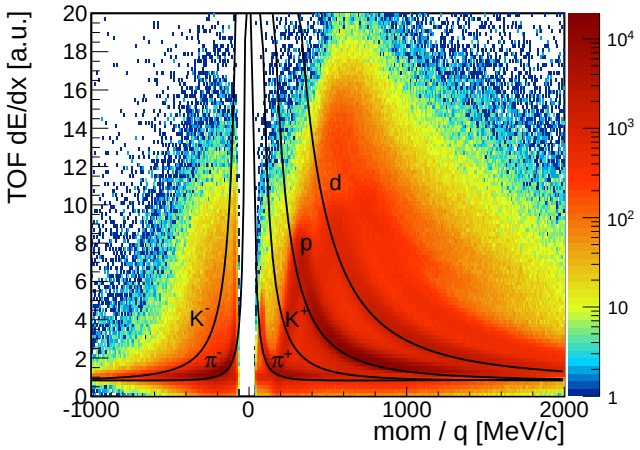

Figure 3.29: Specific energy loss in the TOF-detector as a function of momentum. Black lines correspond to the expected values for the different particle species according to the Bethe-Bloch formula (equation 3.8). The deviation from the Bethe-Bloch curve at low momenta is due to stopping of the slow particles in the detector material.

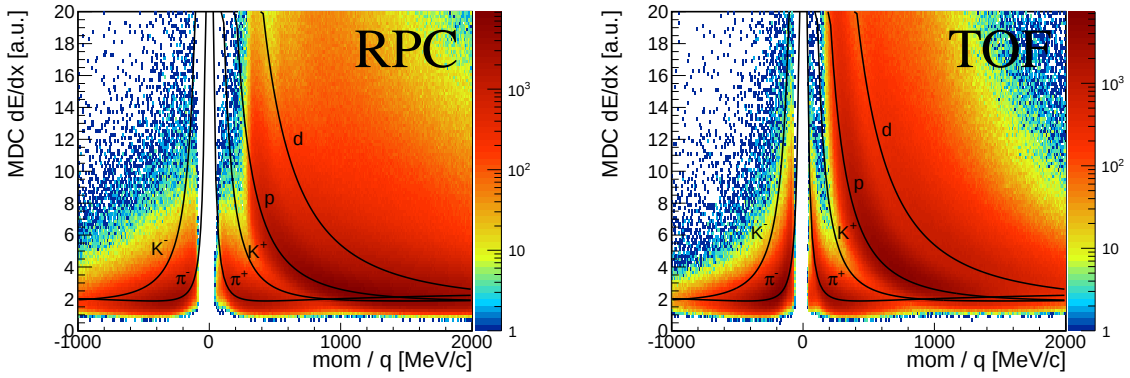

Figure 3.30: Correlation between the specific energy loss in the drift chambers and the momentum measured with the RPC- (left) and TOF-detector (right). Black lines correspond to the expected values for the different particle species according to the Bethe-Bloch formula (equation 3.8).

3.9 Reaction start time recalculation

In order to improve the resolution of the time-of-flight measurement of the particles, the reaction start time t_0 provided by the START-detector is recalculated in an iterative procedure [136]. As a first step, the particles are identified using the information on the correlation between the measured β and

momentum of the track and the correlation between β and the specific energy loss in the drift chambers for each track simultaneously. Each track candidate is tested for the theoretical hypothesis from both mentioned correlations and gets the PID with the smallest deviation to the expected value assigned. The correlation between β and momentum of the particle gets hereby a higher priority than the energy loss information. Using all identified particle tracks, the start time of the reaction can be precisely determined and is recalculated. In the second step, the particle identification methods, introduced in the previous sections, are repeated with the recalculated t_0. With this method the resolution of the t_0 measurement can be improved and variations in time and from the different START-detector stripes are corrected.

3.10 Energy loss calibration of the HADES drift chambers

The energy loss of a particle is proportional to the measured integrated signal in the detector. The readout electronics of the HADES drift chambers measures the time the signal is above a specific threshold (Time-over-Threshold ToT, see section 2.3.2), instead of the integral of the collected charge or the amplitude of the induced signal. The amplitude and the resulting specific energy loss of the particle in a given drift cell does not depend linearly on the measured ToT, as illustrated in figure 3.31.

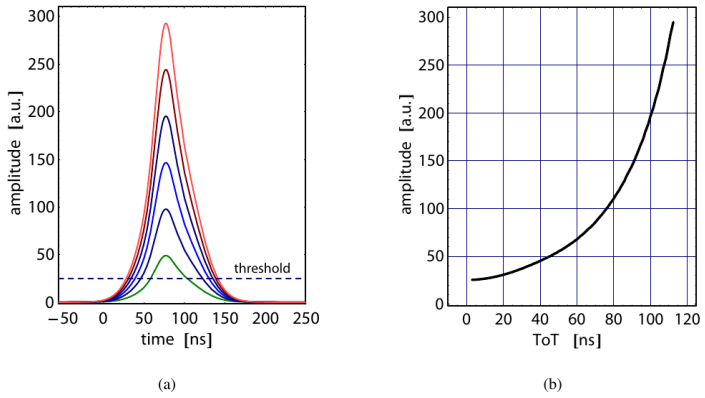

Figure 3.31: Illustration of the non-linear dependence of the amplitude on the measured ToT in the drift cell. Left: Generated signals with the same width but different amplitudes. The time the signals are above the threshold is defined as ToT. Right: The amplitude shows a non-linear behavior to the measured ToT. Figure taken from [137].

Furthermore, the measured ToT depends on the geometry of the track in the drift cell. Tracks with the same -$\langle dE/dx \rangle$ can have different ToT values, depending on their path length in the cell. Additionally, the ToT values are affected by inhomogeneities of the electric field. A further complication of the measurement is the optimization of the drift chambers for small area density (see section 2.3.2), which reduces the strength of the specific energy loss. As a consequence, it is crucial to calibrate the specific energy loss measurement for the particles which pass the HADES drift chambers. The method was developed in [137] and [126], where detailed studies about the achieved resolution of the energy loss measurement in the HADES drift chambers can be found, and has been applied for previous beam times. In advance of the Au+Au beam time, the drift gas in the first module was changed from Ar/isobutane to Ar/CO_2, additionally the high track multiplicities in Au+Au are the biggest challenge for the HADES tracking detectors so far. Therefore, the specific energy loss measurement had to be

re-calibrated and a few changes had to be implemented in the framework of this thesis in order to deal with the new challenges[7].

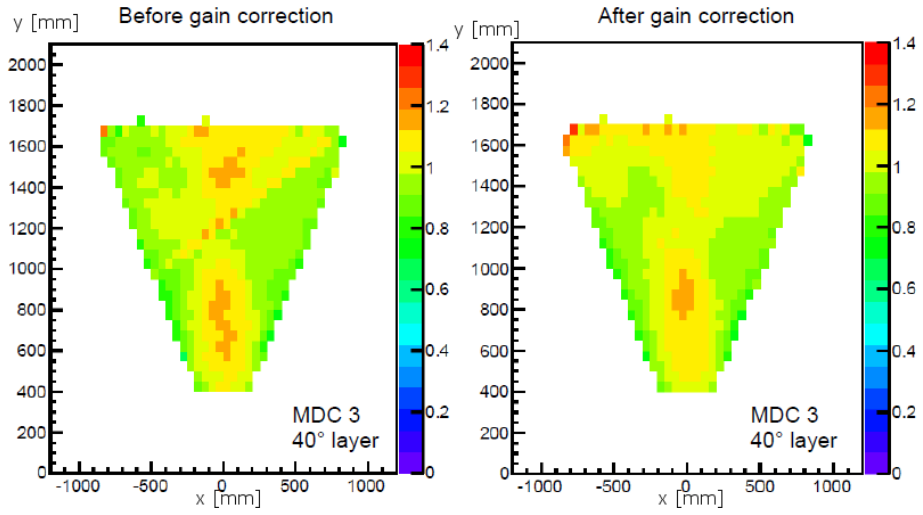

Figure 3.32: Ratio between the measured and calculated ToT, using the Bethe-Bloch formula in dx-dy chamber coordinates of one 40° layer of MDC III before (left) and after (right) gain correction. The ratio should show a smooth behavior with only statistical fluctuations around unity. After gain correction the visible structures from single wires are removed.

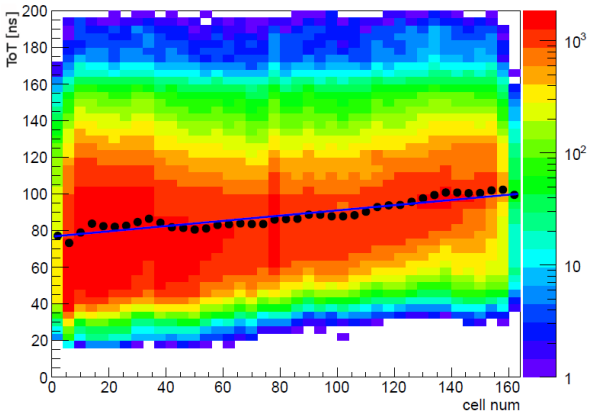

Figure 3.33: Example of the measured ToT for each wire in one layer. The mean values (black points) are fitted with a linear function in each layer. The deviation from the measured ToT in each specific wire to the function is used as a correction factor for the different gain of the read-out electronics.

In order to optimize the performance of the drift chambers, the high voltages of the different chambers were fine tuned individually during the beam time. Also, differences of the intrinsic gain of the ASD8 read-out chips, which shape, amplify and discriminate the induced signal, were observed. This results in mean ToT values for some wires which differ from the average, as can be seen for example in one 40° layer in MDC III on the left side of figure 3.32, where the measured ToT in this layer is compared to the calculated one based on the Bethe-Bloch formula (equation 3.8). The ratio is expected to show a smooth distribution with only statistical fluctuations around unity after the calibration, but still residual structures are visible, which follow the orientation of the single wires. In order to remove

[7] In August 2014 the HADES collaboration undertook a π beam measurement campaign. The drift gas of the second drift chamber MDC II has also been changed from Ar/isobutane to Ar/CO_2. As a consequence, the specific energy loss had to be re-calibrated in the framework of this thesis, which will be addressed in appendix B.

these structures, a correction factor for each wire is needed. In figure 3.33 the ToT distribution for each wire in a 40° layer of the drift chamber MDC III is displayed. The deviations from a linear parametrization to the mean values are used as correction factor[8]. Right side of figure 3.32 shows the same layer of MDC III after the gain correction. The visible structures from the wires are removed.

To reduce the dependency on chamber inhomogeneities, the measured ToT values are additionally divided by the length of the track in the cell. The single -$\langle dE/dx \rangle$ measurements in all passed cells of a particle track are combined and normalized to the Bethe-Bloch formula (equation 3.8). In order to calibrate the dependencies of the measurement on the geometry of the tracks, the relation between energy loss and ToT is parametrized in terms of impact angle α and minimum distance d to the sense wire of the track for each sector and MDC plane individually. The procedure will be explained in the next section. Figure 3.34 shows a schematic view of a 2-dimensional projection of a drift cell, in order to illustrate the impact angle and minimum distance of the track to the sense wire.

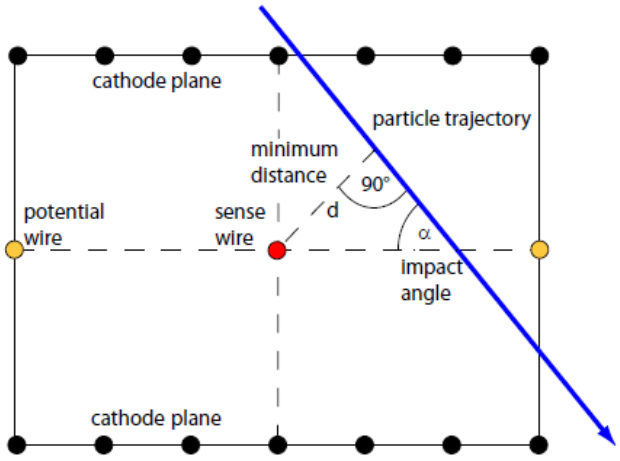

Figure 3.34: Schematic view of a particle passing a drift cell. The track has the minimum distance d to the sense wire and an impact angle α.

3.10.1 Calibration procedure

As a first step of the calibration procedure, the correlation between calculated energy loss and measured ToT is parametrized for each sector and module, as a function of impact angle and minimum distance of the track to the sense wire. This parametrization is determined for low multiplicity events and for tracks of protons, pions and deuterons. The impact angle is divided into 18 bins with a width of $\Delta\alpha$ = 5° from 0° to 90° (inclined to perpendicular impact). The minimum distance is divided into 40 bins from 0 μm to a maximum value depending on the size of the drift chamber resulting in different widths Δd = (100, 100, 200, 225) μm for the four drift chambers.

In high multiplicity Au+Au events the probability of double hits in one cell is increased compared to previous measuring campaigns. Therefore, it is crucial for calibration to select events where only a small amount of tracks (in this calibration less than seven per sector) is reconstructed in the HADES acceptance, in order to minimize distortions of the ToT signals due to double hits in the drift cells. For the calibration only PT3-triggered events, with a maximum number of 42 selected particle candidates and a hit multiplicity in the META-detectors less than 42, are selected. Additionally, one hit in the START-detector is requested in order to select clean events. Only tracks with good track quality parameters (compare section 3.6):

[8]This correction is just a simple way of calibrating the different gain of the electronics in order to get a more uniform measurement. To improve the resolution the correction should be at least 2-dimensional.

- $\chi^2_{Rk} \leq 8$
- $\chi^2_{In/Ou} \leq 5$
- $\chi^2_{MM} \leq 1$

and with a minimum number of fired drift cells (more than 10 layers per segment) are taken into account. Furthermore, the following cuts on the reaction vertex are applied:

- $-59 \leq VertexZ \leq 0$ mm
- $(VertexX)^2$ + $(VertexY)^2 < 3$ mm
- Difference of primary vertex and vertex from cluster fit < 6 mm
- χ^2 of vertex < 40.

After the track and momentum reconstruction, the mass, momentum, impact angle and minimum distance, path length in the cell and the measured ToT are known and the expected loss can be calculated using the Bethe-Bloch formula. In order to select pions, protons and deuterons, cuts on the correlation between the measured mass and momentum are used. First the measured ToT of the particle is corrected for the gain of the fired wires and then normalized to the path length of the track in the cell. Left side of figure 3.35 shows as an example the correlation between the measured ToT and calculated energy loss in MDC I for tracks with perpendicular impact α = 85 - 90° and a small distance from the sense wire between 0.1 and 0.2 mm. The distributions are projected for small slices of the energy loss on the ToT axis. The right side of figure 3.35 shows the projection over the complete energy loss range of the previous shown distribution on the ToT axis. The projections can be described by an asymmetric Gaussian distribution of the following form:

$$f(x) = C \cdot \left(\exp \frac{(x-\mu)^2}{\sigma} \right) \begin{cases} \sigma = \sigma_1, & \text{for } x < \mu \\ \sigma = \sigma_2, & \text{for } x \geq \mu \end{cases} \tag{3.10}$$

with a constant C, the mean value μ and two different widths σ_1 and σ_2. The calculated mean values of the fitted asymmetric Gaussian distribution as a function of the calculated -$\langle dE/dx \rangle$ can be described by the following equation:

$$\langle ToT \rangle = f(dE/dx) = par0 + par1 \cdot [\log_{10}(dE/dx + par3)]^{par2}. \tag{3.11}$$

The inverse function is given by:

$$-\langle dE/dx \rangle = f(ToT) = 10^{[(ToT - par0)/par1]^{1/par2}} - par3, \tag{3.12}$$

and is later on used to translate the measured ToT into a -$\langle dE/dx \rangle$ value. The points in figure 3.35 correspond to the mean values of the asymmetric Gaussian parameterization and the line to the fit according to equation 3.11. The parameters from equation 3.11 are stored for each sector, module, α and d and the inverse function 3.12 is used to transform the ToT measurement in the cells into a -$\langle dE/dx \rangle$ value. The measurements from the single cells passed by one track are fluctuating around the arithmetic mean. In order to improve the resolution of the energy loss measurement, the truncated mean method is used. This method excludes wrong measurements in a window of 3σ around the arithmetic mean.

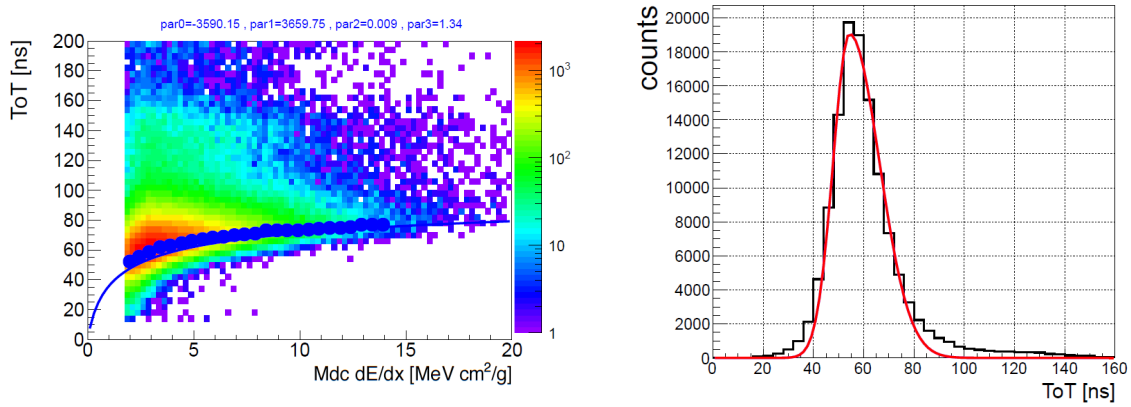

Figure 3.35: Left: Correlation between the measured ToT and calculated energy loss in MDC I for tracks of pions, protons and deuterons with perpendicular impact α = 85 - 90° and a small distance from the sense wire between 0.1 and 0.2 mm. The mean values of the projections in small slices of energy loss on the ToT axis (points) are fitted with equation 3.11. Right: Projection of the correlation for the complete energy loss range on the ToT axis with the corresponding asymmetric Gaussian parametrization according to equation 3.10 (red).

3.10.2 Results of the new calibration

After calibration, the mean energy loss is expected to show similar distributions for each sector of the HADES spectrometer. The top row of figure 3.36 shows the ratio of the calculated energy loss, using the Bethe-Bloch formula, and the measured energy loss, transforming the measured ToT, before and after calibration as a function of the azimuthal and polar angle ϕ and θ of the track. This ratio is expected to be around unity over the whole ϕ and θ range. The results can be further improved after excluding tracks with a high minimum distance to the sense wire. The lower row of figure 3.36 shows the measured energy loss in the drift chambers as a function of momentum before (left) and after calibration (center) and after applying a cut on the maximum allowed minimum distance of a track to the sense wire in the drift cell (right). One can directly see the improvements due to the new calibration, especially in the region of deuterons. The resolution of the calibrated energy loss as a function of momentum for protons and pions is presented in section 4.1.2.2.

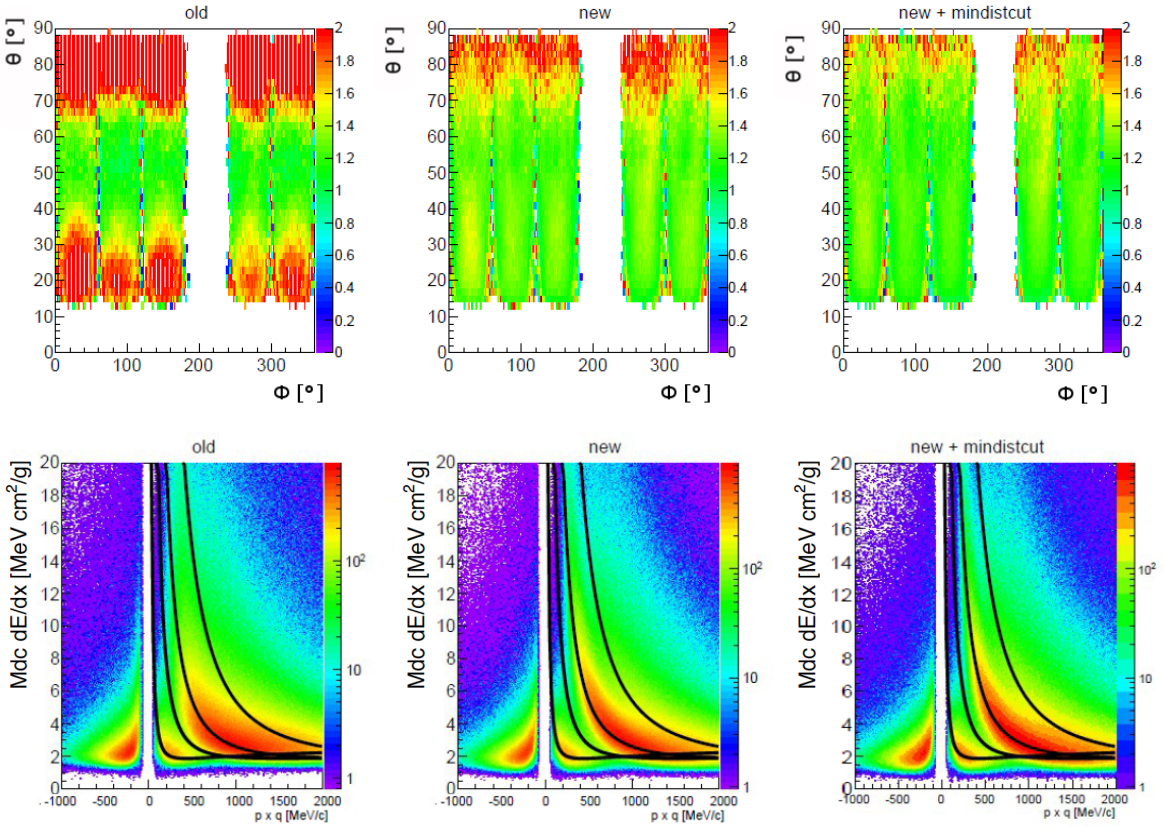

Figure 3.36: Top row: Ratio of the calculated and the measured energy loss before (left), after calibration (center) and after excluding tracks with a high minimum distance to the sense wire (right) as a function of azimuthal and polar angle ϕ and θ of the track. Lower row: Measured energy loss as a function of momentum before (left), after calibration (center) and after excluding tracks with a high minimum distance to the sense wire (right). Black lines correspond to the expected values according to the Bethe-Bloch formula.

3.10.3 Implementation into the simulation

To implement a realistic resolution of the specific energy loss measurement in the HADES drift chambers into the simulation, the widths of the single projections of the correlation between measured ToT and calculated energy loss on the ToT axis are obtained based on the parametrization with the asymmetric Gaussian function (see right side of figure 3.35). In the simulation the energy loss is smeared accordingly. This is crucial to estimate the efficiency of cuts applied on the specific energy loss for particle identification. As the tails of the distributions are not perfectly described by this parametrization, small residual differences between data and simulation can not be removed completely with the calibration procedure. However, the applied cuts used for particle identification can be adapted between data and simulation, as will be explained in section 4.1.2.2. Figure 3.37 shows a comparison between the real and the simulated energy loss in the HADES drift chambers. The simulation has been performed with UrQMD. In this simulation no light nuclei, like deuterons and tritons, are included, which explains the difference of the distributions in the high mass area. The projections of this distribution will be shown in section 4.1.2.2.

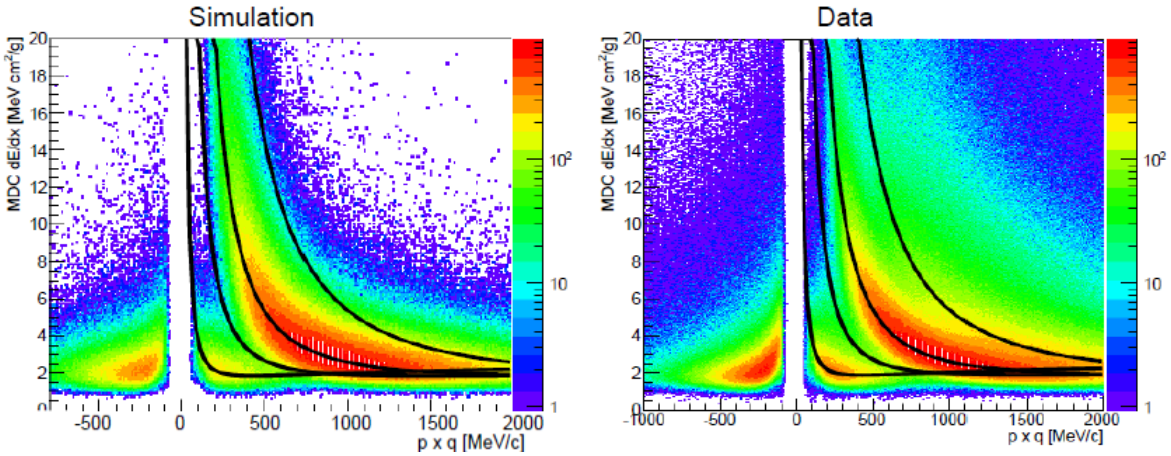

Figure 3.37: Comparison between simulated (left) and measured energy loss (right) in the HADES drift chambers after calibration.

Chapter 4

Hadron Analysis

The main focus of the investigation performed in the context of this thesis is the reconstruction of charged kaons and ϕ mesons. Those particles carrying strangeness are produced very rarely at the analyzed energy compared to non-strange particles like pions and protons (about 4 - 6 orders of magnitude differences in their abundances). The non-strange hadrons are better suited to estimate some of the systematic uncertainties of the reconstruction procedure, due to their smaller statistical uncertainties. Furthermore, their signals have a high purity without further track selections. Therefore, first the analysis of p and π^- are used to estimate systematic uncertainties introduced by the analysis procedure, before analyzing the rare kaons. In table 4.1 the properties mass m, mean lifetime τ or full decay width Γ and decay length $c\tau$ of the analyzed particles p, π^-, K^+, K^- and ϕ are summarized.

p ($\|uud\rangle$)	π^- ($\|d\bar{u}\rangle$)
m_p = 938.272 MeV/c^2	m_{π^-} = 139.57 MeV/c^2 τ_{π^-} = 2.6033x10^{-8} s $c\tau_{\pi^-}$ = 7.0845 m
K^+ ($\|u\bar{s}\rangle$), K^- ($\|s\bar{u}\rangle$)	ϕ ($\|s\bar{s}\rangle$)
$m_{K^\pm}$ = 493.677 MeV/c^2 $\tau_{K^\pm}$ = 1.238x10^{-8} s $c\tau_{K^\pm}$ = 3.713 m	m_ϕ = 1019.455 MeV/c^2 Γ = 4.26 MeV $c\tau_\phi$ = 46.3 fm BR($\phi \rightarrow K^+K^-$) = 48.9%

Table 4.1: Properties mass m, mean lifetime τ or full width Γ and decay length $c\tau$ of the analyzed particles p, π^-, K^+, K^- and ϕ.

Charged particles interact with the active detector material and can be directly identified via their measured velocity (β), momentum (see section 3.7) and specific energy loss (see section 3.8). Neutral particles which decay into charged particles before reaching the detector, like the ϕ meson, have to be reconstructed using the information of their decay products, making use of energy and momentum conservation (section 4.2). The reconstruction of rare signals in a high multiplicity environment created in Au+Au collisions requires a careful event (section 3.3) and track selection (section 3.6.3). The analysis strategy is the following: After identification of the particles, the differential count rate is determined (section 4.1.5). The measured count rates are then corrected for the geometrical acceptance, detector and track reconstruction efficiency, and inefficiencies introduced by cuts for the particle identification (section 4.3). The resulting corrected spectra are presented in chapter 5.

4.1 Analysis of charged particles

4.1.1 Identification of protons and π^-

To select high quality tracks from the list of selected hadron track candidates, which was explained in section 3.6.3, and reduce the contribution from fake track segment matches further, only tracks with a $\chi^2_{RK} \leq 400$ are selected. The reduction of the tails in the mass distribution of the particles can be seen in figure 4.1. In total 3% of the track candidates are discarded.

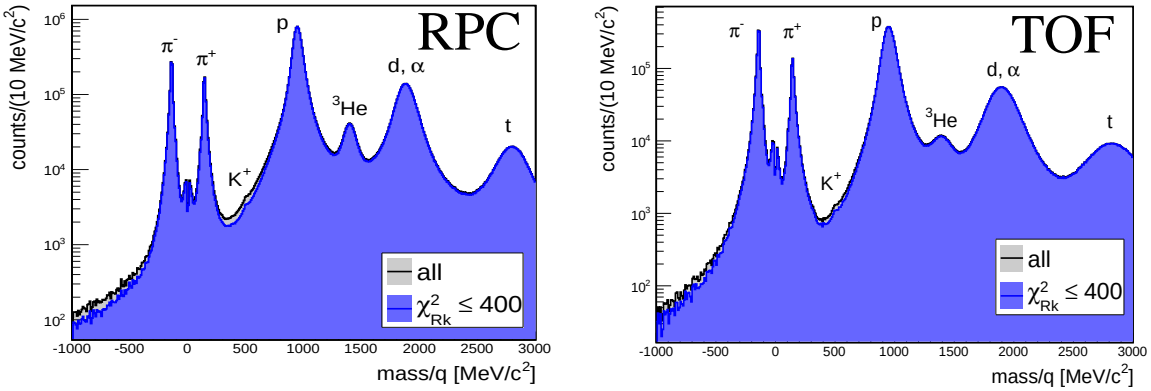

Figure 4.1: Mass distribution with (grey) and without (blue) application of a cut on $\chi^2_{RK} < 400$ used for proton and π^- analysis in the RPC- (left) and TOF-detector (right). In total 3% of the track candidates are discarded.

Protons and π^- are identified by applying cuts on the correlation between β and momentum of the particles. As shown and explained in section 3.7, the pions and protons are well described by the expected correlation of these observables according to equation 3.7. The graphical cuts are systematically calculated separately for the two time-of-flight detector systems RPC and TOF. The procedure has been performed in the framework of [116]. For each system the distribution is projected for steps of 40 MeV/c in momentum on the β-axis for both charges separately. The projections are adapted with a Gaussian distribution (see figure 4.2). The obtained mean follows to high accuracy the expected values according to equation 3.7. The cuts are defined as 2σ wide bands around the mean value. Figure 4.3 shows the correlation between β and momentum together with the resulting cuts used for π^- and proton analysis. The same procedure is performed for the simulated data, such that little differences between the resolution of the β and momentum measurement in simulation and real data are taken care of. Hence, the Monte-Carlo simulation can be used to correct for losses of real particles (see section 4.3). To reduce systematic uncertainties of the momentum reconstruction, the momentum of the protons and pions is restricted to the ranges of $300 \leq \text{mom}_p \leq 1800$ MeV/c and of $80 \leq \text{mom}_{\pi^-} \leq 1300$ MeV/c respectively.

In addition to the β and momentum information, the specific energy loss measurement -$\langle dE/dx \rangle$ in the drift chambers can be used to identify particles (see section 3.8). For protons and pions this information is not included via a hard cut on the correlation between energy loss and momentum, but as a weighted combination of both identification methods, as explained in section 3.9 for the recalculation of the reaction start time t_0. All track candidates are tested simultaneously for the best match of their correlation between β and momentum and between β and -$\langle dE/dx \rangle$ to the expected curves. The track gets the PID assigned with the smallest deviation to ideal values. The correlation between β and momentum is weighted higher than the correlation between -$\langle dE/dx \rangle$ and β due to its higher

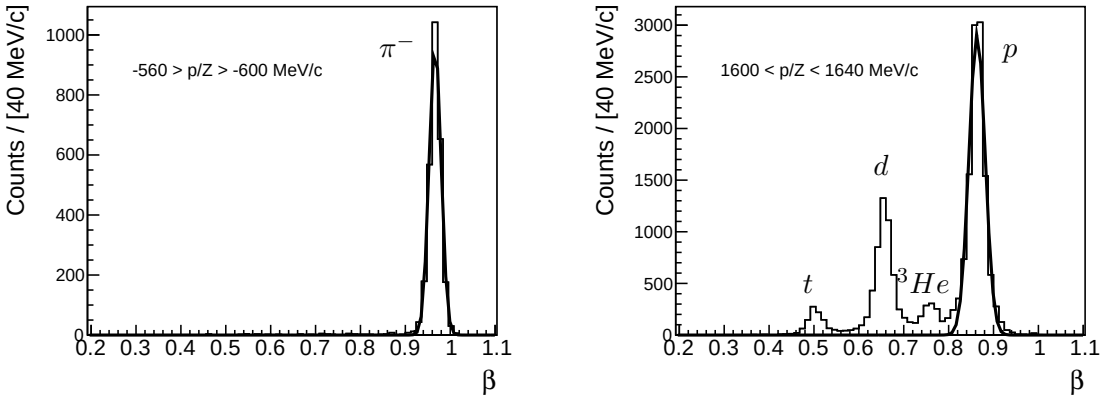

Figure 4.2: Projection of the correlation between β and momentum in the RPC region on the β-axis for two different slices in momentum and charge (p/Z) to systematically calculate cuts for particle identification. The distributions can be described by a Gaussian parameterization and the mean values follow to high accuracy the expected value according to equation 3.7.

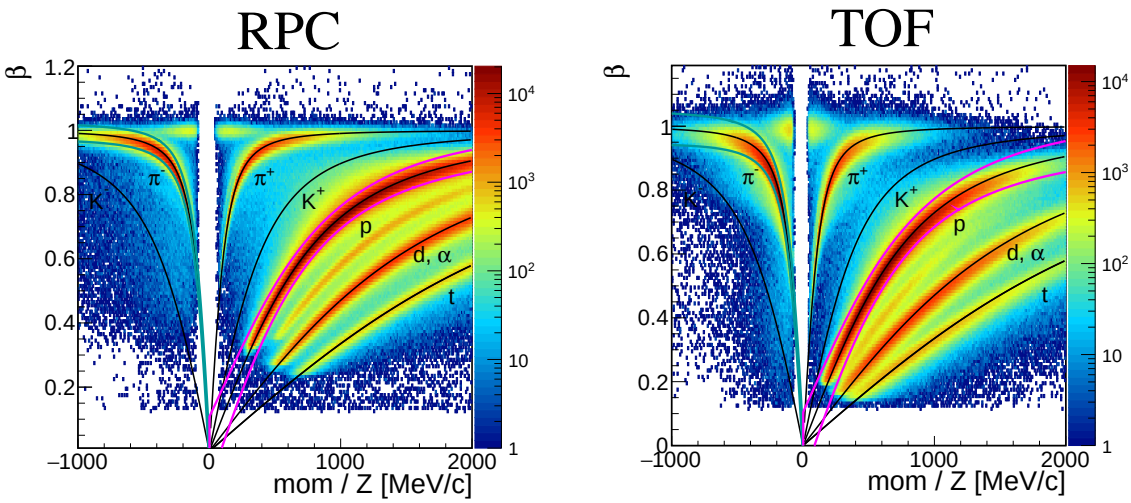

Figure 4.3: Cuts on the correlation between β and momentum used for proton (magenta) and pion identification (green) in the region covered by the RPC- (left) and the TOF-detector (right). Black lines correspond to the expected values according to function 3.7.

separation power. This procedure is applied after the t_0 recalculation. This weighted identification method is used to estimate systematic uncertainties from the particle identification method based on hard cuts (see sections 5.1.1 and 5.2.1).

4.1.2 Kaon identification

The kaon identification is performed in terms of the calculated mass (explained in section 3.7). As shown in figure 4.1 only the most abundant particles like pions, protons and deuterons are clearly visible in the mass distribution around their nominal mass. The signals of the rarely produced kaons are covered by the non-gaussian tails of the pions and protons, which originate mainly from the momentum and time-of-flight resolution of the detectors, but also due to mis-identification of particles. In order to reduce these tails and obtain a clear signal with sufficient signal-to-background ratio, stronger cuts on the track quality parameters χ^2_{RK} and χ^2_{MM} (section 4.1.2.1) and additionally cuts on the specific energy loss information in the MDCs and TOF are applied for kaon identification (section 4.1.2.2).

4.1.2.1 Cuts on track quality variables

Figure 4.4 shows the distribution of the track quality parameters χ^2_{RK} and χ^2_{MM} for 1 million proton, π^- and kaon track candidates. The protons and pions are identified using graphical cuts on the correlation between β and momentum (see section 4.1.1). The protons have a higher energy loss and typically a higher average number of fired wires in the drift chambers per track candidate. This leads to a better constrained trajectory and hence as a result, there are more proton tracks with small track quality parameters as π^-. The kaon candidates shown in the figure are selected via a cut on the mass in the region 200 $\leq$ mass $\leq$ 700 MeV/c^2. The track quality parameter distributions of those tracks tend to higher χ^2-values, as they are dominated by the tails those tracks with larger deviation from the ideal values of the protons and pions. To reduce the contribution from those tracks, only kaon candidate tracks with a χ^2_{RK} < 100 and a χ^2_{MM} < 2 are selected for further analysis.

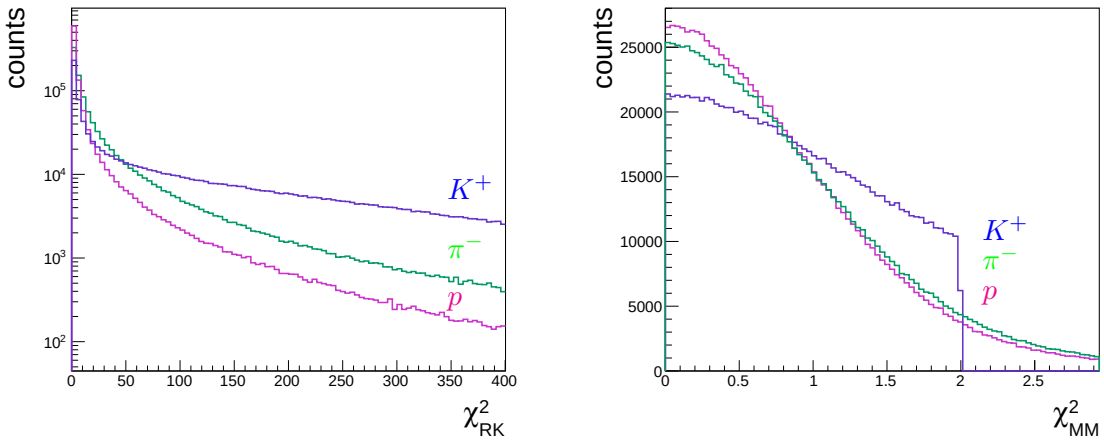

Figure 4.4: χ^2_{RK} (left) and χ^2_{MM} (right) distribution of proton (magenta), π^- (green) and K^+ (purple) candidates. The protons and pions are identified using a selection on the correlation between β and momentum (see section 4.1.1). The kaon candidates are selected via a cut on the mass in the region 200 $\leq$ mass $\leq$ 700 MeV/c^2.

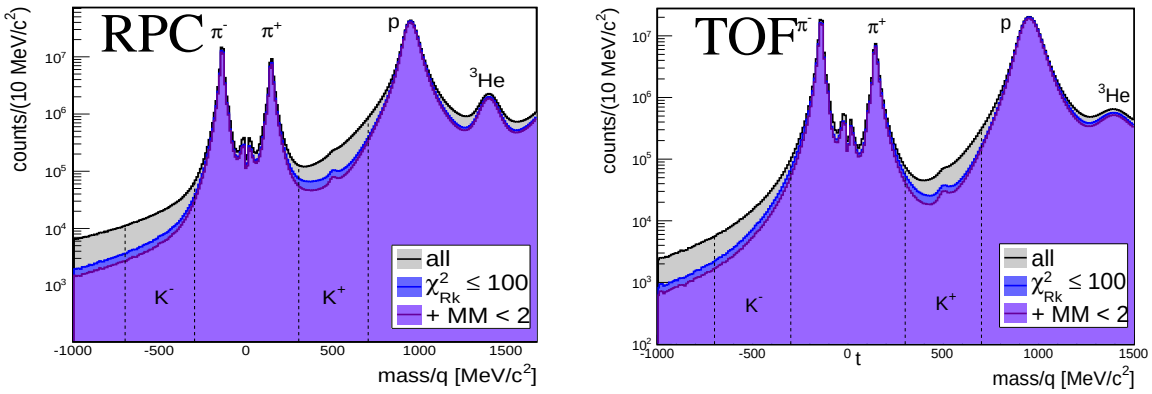

Figure 4.5: Mass distribution after application of a cut on $\chi^2_{RK} < 100$ and $\chi^2_{MM} < 2$ as used for charged kaon analysis in the RPC- (left) and TOF-detector (right).

Both cuts are improving the signal-to-background ratio in the kaon mass region (see figure 4.5), but unfortunately it may happens that also real particles are removed by these cuts, which can be seen in the maxima of the proton and pion signals. Therefore, the spectra have to be corrected for the so-called cut-efficiency, which will be explained in section 4.3. The correction is performed using the Monte-Carlo simulation which requires a good description of all experimental distributions by the simulation. However, it was shown in section 3.6.3, that the simulation is not perfectly reproducing the distributions of the track quality parameters obtained in real data. In order to avoid a wrongly estimated count rate, the used values for the applied selections are a compromise between a high signal-to-background ratio and high efficiency. Note that a small uncertainty on top of a huge correction factor results in large overall uncertainties. A detailed comparison of the effect of the applied cuts for kaon identification on the mass spectra between data and simulation will be presented in section 4.1.3.

4.1.2.2 Cuts on the specific energy loss

The K^- is produced about two orders of magnitude less frequently than K^+ and is therefore completely suppressed by the tail of the π^-. In order to observe a K^- signal and to improve the signal-to-background ratio for K^+, cuts on the specific energy loss in the drift chambers and the TOF are applied.

Cuts on the correlation between energy loss in the MDC and momentum

As already discussed in the previous chapter, the most abundant particles are, after the calibration procedure performed in the framework of this thesis (section 3.10), visible in the correlation between momentum and specific energy loss in the drift chambers around the expected values according to the Bethe-Bloch formula (equation 3.8). However, the resolution of the energy loss information is not sufficient to directly observe the signal from kaons, which is located in the intermediate region between pions and protons. Therefore, the cuts used for kaon identification are systematically calculated using the simulation and experimentally identified pion and proton candidates separately for the two time-of-flight detectors. First, a high purity sample of protons and pions is selected by applying a 2σ cut on the correlation between β and momentum as explained in section 4.1.1.

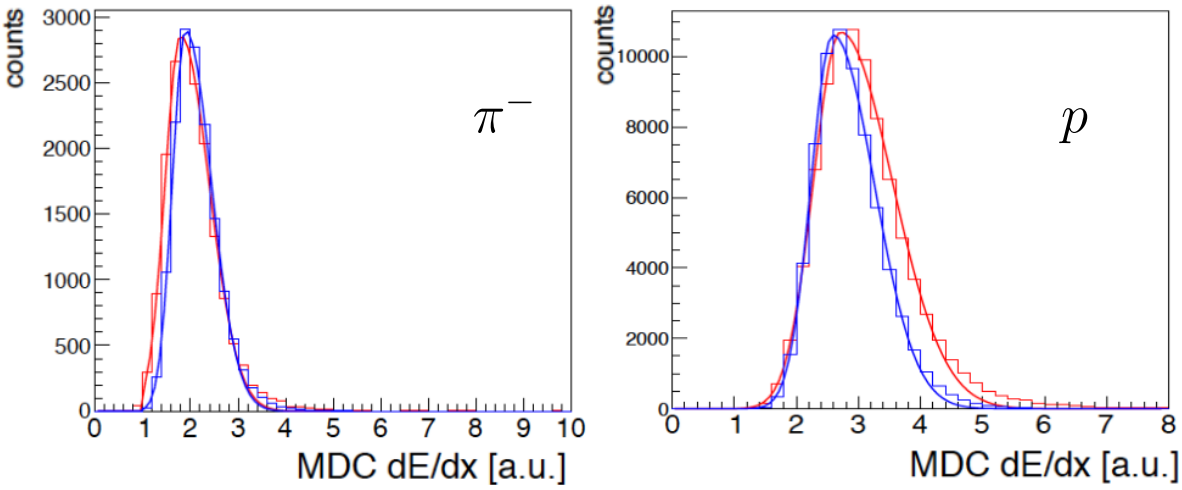

Figure 4.6: Projection of the specific energy loss measurement for π^- (left) and protons (right) in the drift chambers for a 20 MeV/c momentum slice for data (red) and simulation (blue). The spectra can be described by a Gaussian parameterization with the two different widths σ_1 and σ_2 (according to equation 3.10).

For these selected particles the correlation between momentum and the energy loss information in the drift chambers is projected in momentum steps of 20 MeV/c on the energy loss axis. The procedure is repeated for the simulated signals. Figure 4.6 shows an example for the projections of the data (red) in comparison to the simulation (blue) in a given momentum slice for pions and protons. As presented in section 3.10, the projections can be described by a Gaussian parameterization with two different widths σ_1 and σ_2 (according to equation 3.10), which both are momentum dependent. The momentum dependence of the widths of the projections is shown in figure 4.7 for both particle species. As one can see, the experimental data is not perfectly reproduced by the simulation, but rather shows a slight difference for both extracted widths in the TOF and σ_2 in the RPC. The ratio of the results from simulation and data, shown in the lower row of figure 4.7, is almost constant as a function of momentum and in case of the TOF-detector in the order of $\approx 25\%$ for pions and protons, whereas in the RPC-detector the deviation is with $\approx 30\%$ higher for protons than for pions which is in the order of $\approx 20\%$. The cut widths for kaon identification are first obtained for simulation, as here a pure kaon sample can be selected, by projecting again the distribution of the correlation between energy loss and momentum in 20 MeV/c momentum steps on the energy loss axis. To account for the differences between simulation and data, the cuts used for data analysis are scaled according to the factors obtained with pions and protons, assuming that the kaon energy loss is between the one of those particles. That means, that in case of the TOF detector both widths σ_1 and σ_2 are $\approx 25\%$ broader for data than for simulation and for the RPC only σ_2 is $\approx 25\%$ broader. With this appropriative scaling, the efficiency correction should account for any losses of real particles. The resulting cuts used in the analysis are shown in figure 4.8.

Cuts on the correlation between β and energy loss in the TOF

The correlation between the energy loss in the TOF-detector and the β measurement is used to remove wrong matches between the reconstructed tracks and the TOF-detector. Incorrectly matched pion tracks to proton hits in the META-detector are resulting in an assignment of a wrong time-of-flight (systematically too long) to the pion track.

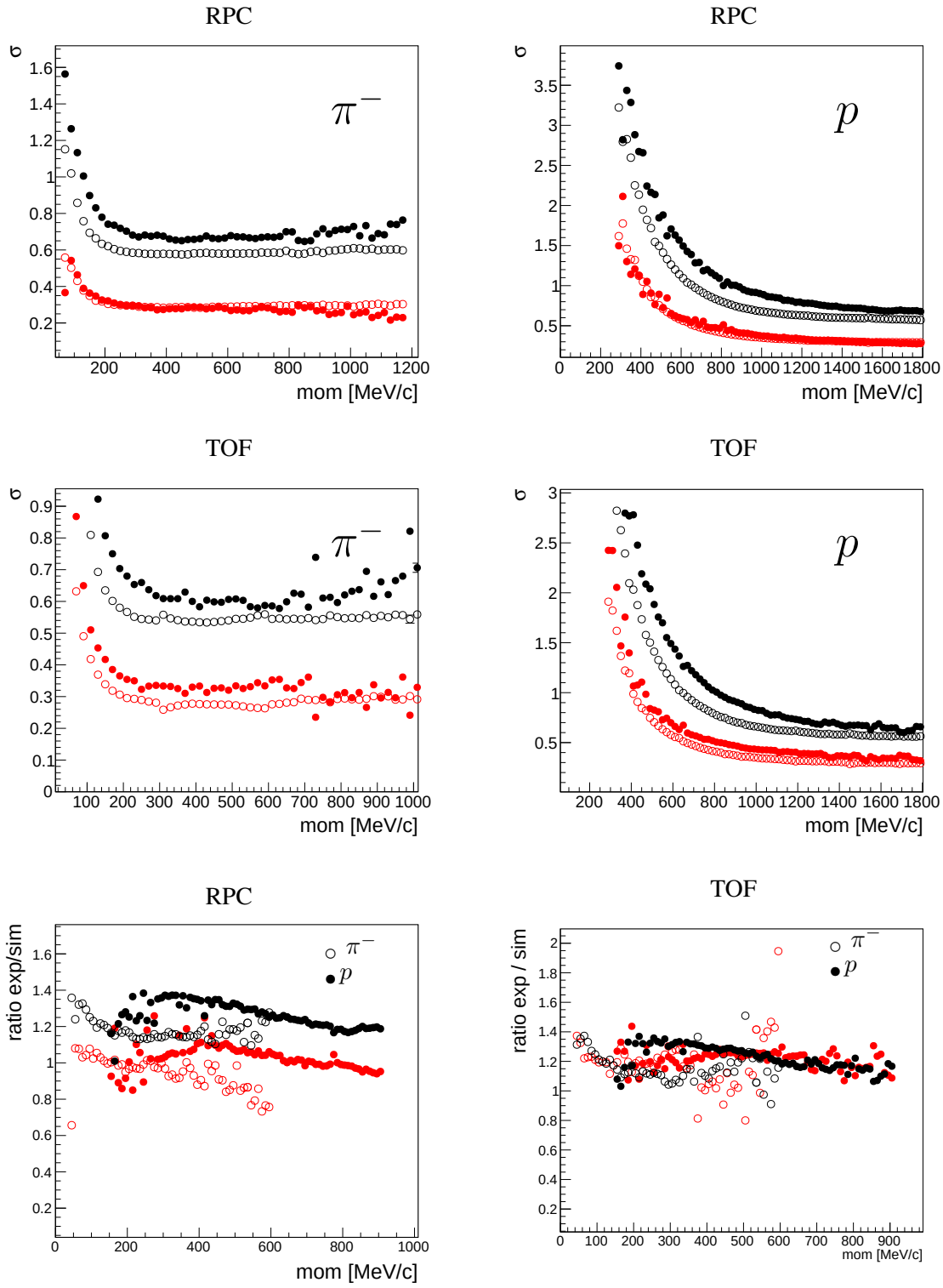

Figure 4.7: Momentum dependence of the widths of the projected energy loss in the drift chambers σ_1 (red) and σ_2 (black) for data (solid circles) and simulation (open circles) of π^- (left) and protons (right) measured in the RPC-detector (upper row) and in the TOF-detector (middle row). Lower row: Momentum dependence of the ratio between data (exp) and simulation (sim) of the widths of the projected energy loss in the drift chambers σ_1 (red) and σ_2 (black) of π^- (open circles) and protons (solid circles) measured in the RPC- (left) and the TOF-detector (right).

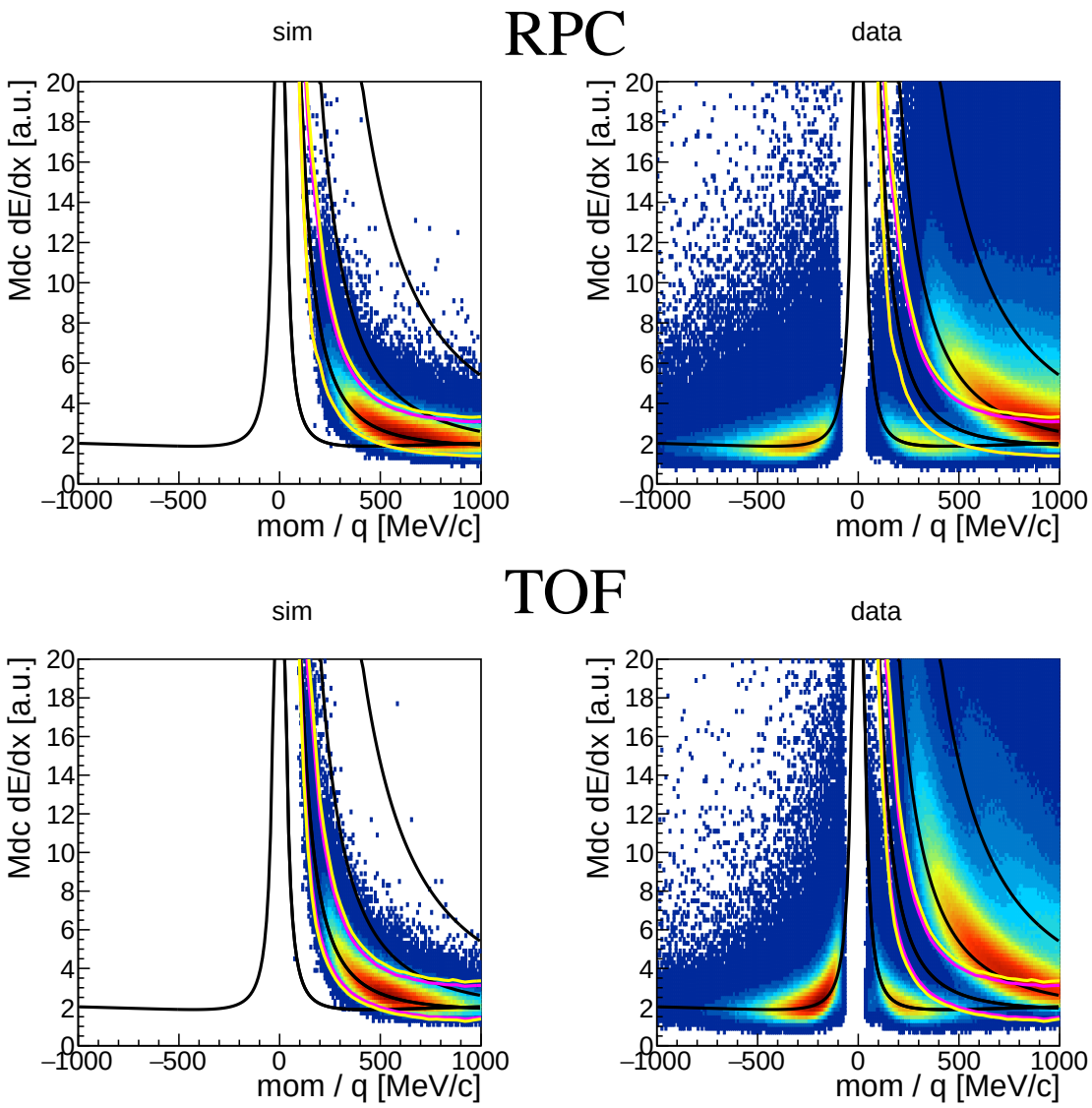

Figure 4.8: Correlation between the energy loss in the drift chambers and the momentum measured within the region of the RPC- (top) and TOF-detector (bottom) for simulated K^+ (left) and experimental data (right). Black lines correspond to the expected correlation for the different particle species according to equation 3.8. Colored lines correspond to the cuts on the specific energy loss of kaons used in this analysis, the magenta bands are used for simulation and yellow bands for real data.

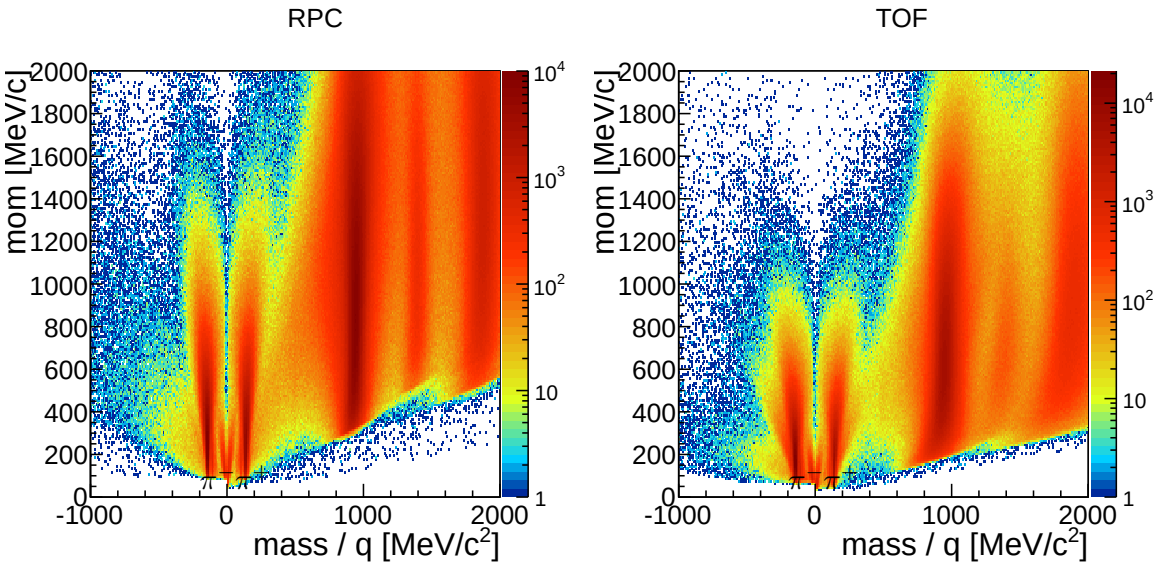

Figure 4.9: Mass vs. momentum distribution for all track candidates. The correlations left of the π^- and right of π^+ correspond to wrong matches between pion tracks and protons hits in the META-detector.

As a consequence the calculated mass (compare section 3.7) is systematically higher than the one of pions. The relative strength of the effect increases with increasing momentum due to the increasing velocity of the pions and is not reproduced by the simulation. The effect is visible in form of a diagonal correlation in the mass vs. momentum distribution displayed in figure 4.9, next to the true correlation of pions. At momenta of $\approx$ 500 MeV/c this fake contribution populates the kaon mass region and hence hampers the kaon identification. Especially the rarely produced K^- are strongly affected, as the effect is at the same order or even higher than the true signal and must therefore be removed in the analysis. Figure 4.10 shows the correlation between the energy loss in the TOF-detector and β for K^- candidates. Additionally to the physical correlation of particles with charge = -1, a correlation between tracks with high β-values and a high specific energy loss can be seen inside the dashed area. The correlation corresponds to these wrong matches of fast pion tracks to hits of high-ionizing protons and are removed from the future analysis by applying the displayed graphical cut.
The effect on the mass of the previously discussed cuts used for kaon analysis are visualized step by step in figure 4.11.

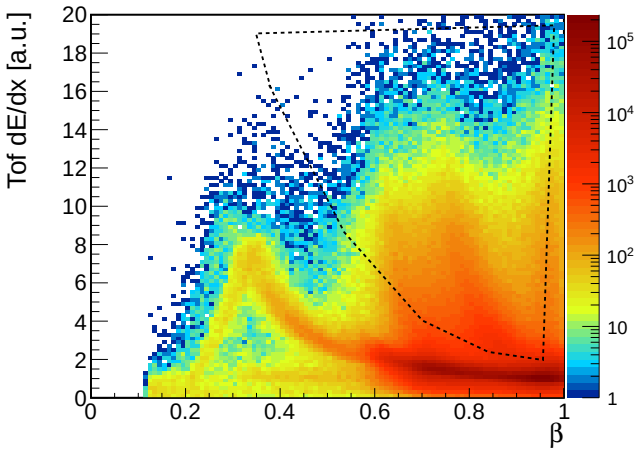

Figure 4.10: Correlation between the specific energy loss in the TOF-detector and β of K^- candidates. The maximum corresponds to the physical correlation for charge -1 particles. The high β region is populated from π^-. The correlation inside the dashed area corresponds to wrong matches of pion tracks to hits of protons in the TOF-detector (explanation see text) which are removed from the analysis.

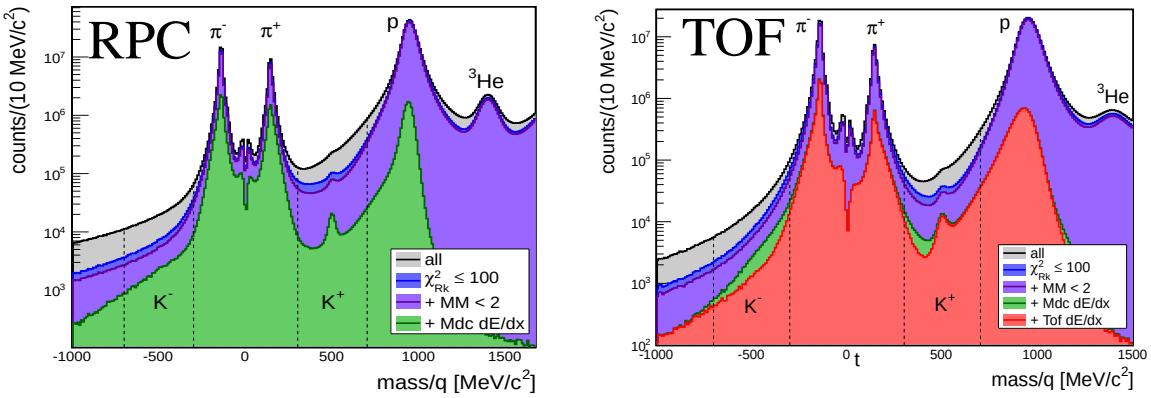

Figure 4.11: Mass distribution of particles measured in the RPC- (top) and TOF-detector (bottom). Before (black) and after applying cuts on the track quality parameters and on the specific energy loss in MDC and TOF for particle identification of charged kaons (colors see legend and explanation see text).

4.1.3 Comparison of the kaon selection to the full Monte-Carlo simulation

As already mentioned in the previous sections, the applied cuts for kaon identification have to be corrected for eventual efficiency losses using a Monte-Carlo simulation, which will be explained in section 4.3. To guarantee that the losses of real particles introduced by the selections are similar in data and simulation, in order to avoid a corruption of the estimated corrected count rate, the distributions must look similar. In figure 4.12 a comparison between data and simulation of the χ^2_{RK} and the χ^2_{MM} from 1 million identified proton, π^- and K^+ track candidates is shown. The Monte-Carlo simulation shows on average smaller χ^2-values than the real data. However, it reproduces the trend observed in the real data, that the distributions from protons and pions tend to have smaller χ^2-values than the kaon candidates, which are still dominated by the tails of the protons and pions and resulting in a lower purity and worse quality of the tracks.

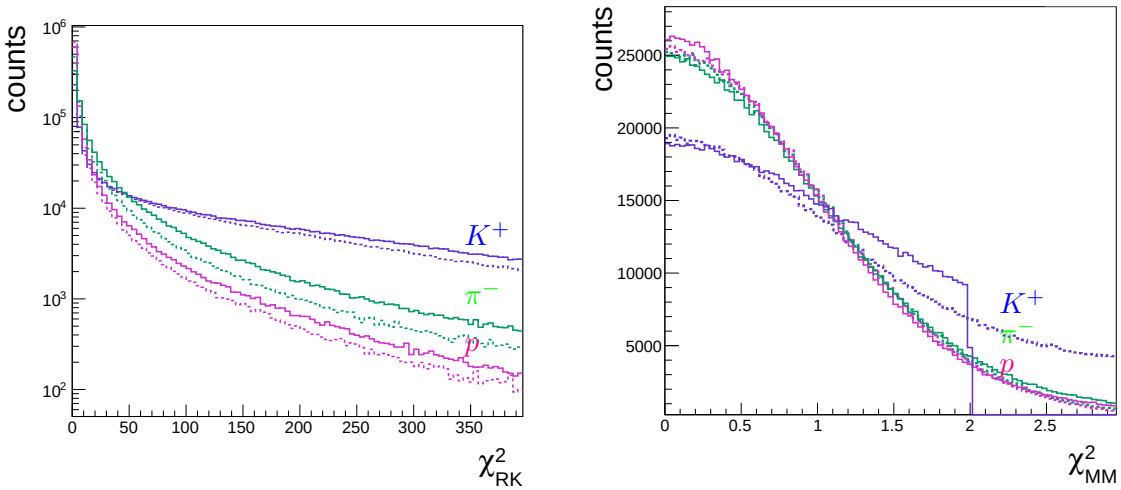

Figure 4.12: χ^2_{RK} (left) and χ^2_{MM} (right) distribution of proton (magenta), π^- (green) and kaon (purple) candidates after particle identification from experimental data (solid lines) in comparison to simulation (dashed lines).

The comparison of the mass distribution between experimental data and simulation after applying the different cuts for kaon identification (see section 4.1.2) are shown in figure 4.13 and 4.14 for the two time-of-flight walls separately. In order to compare the improvement of the signal-to-background ratio and the reduction of the background, the spectra are described using a Gaussian distribution in the signal region plus a polynomial third order. The signal S is determined by integrating the spectra within a 2σ region around the mean μ. Furthermore the background left B_L and right B_L from the kaon signal is estimated by integrating the spectrum in a region $[|\mu \pm 3\sigma|, |\mu \pm 5\sigma|]$. The reduction of these values by applying the cuts iteratively is summarized in tabular 4.2. In both detector systems, the reduction of the protons and pions besides the kaon mass region is slightly stronger in the simulation than in the experimental data. However, the enhancement of the kaon signal over the background is very similar. Whereas the relative loss of counts in the kaon mass region is in the TOF-detector very similar between data and simulation, the reduction is stronger for the simulation in the RPC-detector when applying cuts on the track quality parameters. The reason for this stronger loss could be due to additional background sources, not included in the simulation, leading to a high occupancy in the drift chambers especially in the lower theta angle region. It seems that even after including a higher contribution of δ-electrons into the simulation (see section 3.5.1), it is still not sufficient to explain the full effect. Differences between data and simulation lead to a systematic bias on the estimated count rates. However, this bias can be corrected for, using proton and pion candidates which have a purity close to 100%, as will be discussed in section 5.3.1.

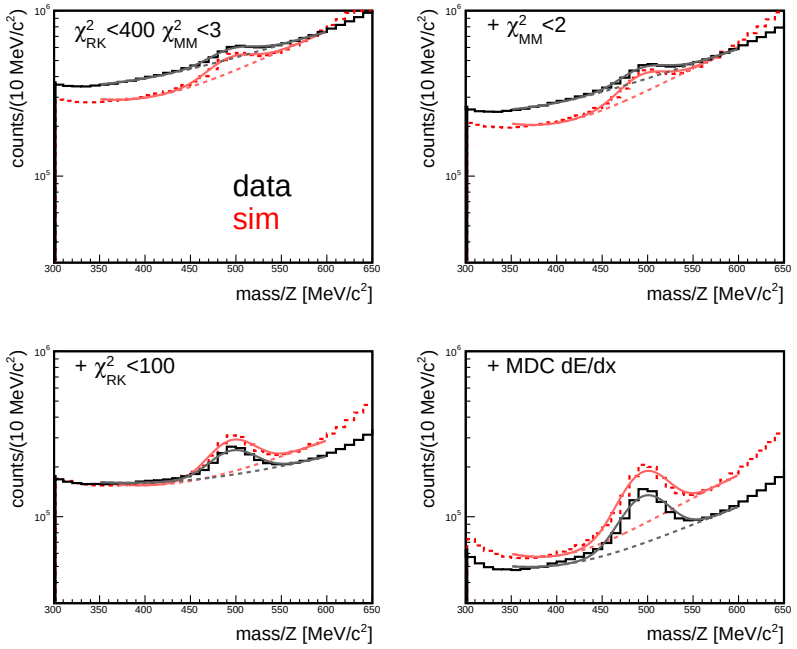

Figure 4.13: Zoom into the mass spectrum in die region of K^+ in the RPC-detector after applying the various cuts for kaon identification iteratively on experimental (black) and simulated data (red). In order to obtain the signal, background and signal-to-background ratio, the spectrum is described using a Gaussian distribution in the signal region plus a polynomial third order (lines).

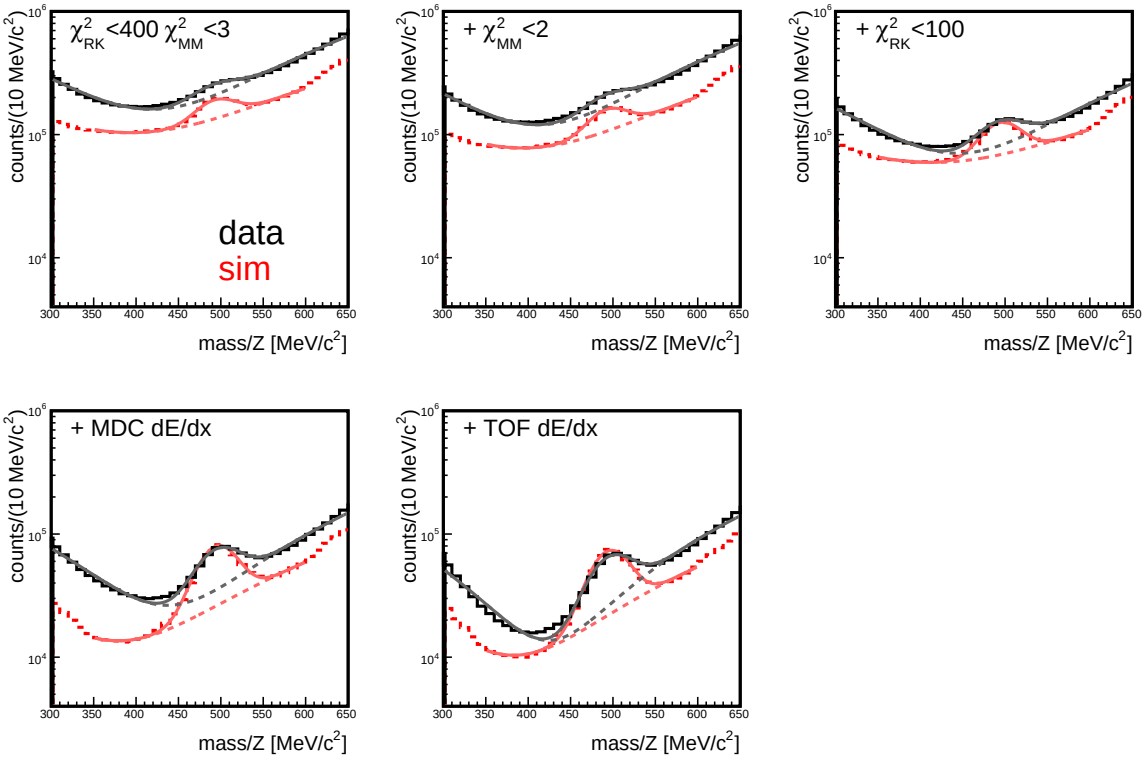

Figure 4.14: Zoom into the mass spectrum in die region of K^+ in the TOF-detector after applying the various cuts for kaon identification iteratively on experimental (black) and simulated data (red). In order to obtain the signal, background and signal-to-background ratio, the spectrum is described using a Gaussian distribution in the signal region plus a polynomial third order (lines).

	Cut	Data				Simulation			
		S	B_L	B_R	S/B	S	B_L	B_R	S/B
RPC	χ^2_{RK}<400 χ^2_{MM}<3	3.2x10^6	1.4x10^7	2.1x10^7	0.09	4.2x10^6	1.1x10^7	2.0x10^7	0.15
	+ $\chi^2_{MM} < 2$	5.2%	27.6%	22.6%	0.11	3.7%	27.8%	20.5%	0.19
	+ $\chi^2_{RK} < 100$	0.3%	45.2%	57.9%	0.24	7.8%	28.8%	47.6%	0.33
	+ MDC dE/dx	7.7%	64.9%	53.2%	0.55	3.7%	57.5%	41.3%	0.62
TOF	χ^2_{RK}<400 χ^2_{MM}<3	2.6x10^6	7.3x10^6	1.7x10^7	0.14	2.8x10^6	4.3x10^6	8.4x10^6	0.25
	+ $\chi^2_{MM} < 2$	12.8%	25.7%	13.4%	0.15	4.7%	24.2%	15.1%	0.29
	+ $\chi^2_{RK} < 100$	12.2%	35.5%	52.8%	0.32	9.3%	21.5%	40.4%	0.48
	+ MDC dE/dx	14.3%	62.3%	46.0%	0.63	11.8%	74.6%	45.0%	1.18
	+ TOF dE/dx	17.5%	48.1%	8.5%	0.81	4.9%	23.3%	9.1%	1.32

Table 4.2: Comparison of the effect of the cuts applied for kaon identification between data and simulation. S: Reduction of the signal S in a 2σ region around the mean μ, B_L/B_R: Reduction of the background in the region $[|\mu \pm 3\sigma|, |\mu \pm 5\sigma|]$ (left below, right above μ) and S/B: signal-to-background ratio.

4.1.4 Summary of the particle identification and track selections

The applied cuts for particle identification and track selections for the different particle species are summarized in table 4.3. For the rarely produced kaons also the information of the specific energy loss in the drift chambers and the TOF-detector is taken into account in order to enhance the separation power.

Particle	χ^2_{RK}	χ^2_{MM}	MDC dE/dx	TOF dE/dx
p	400	3	-	-
π^-	400	3	-	-
K^+	100	2	✓	✓
K^-	100	2	✓	✓

Table 4.3: Applied cuts for the identification of all analyzed charged hadrons.

4.1.5 Estimation of the differential count rate

To estimate the differential count rates of the different particles, the measured phase space distributions are divided into cells in transverse mass $m_t - m_0$ and rapidity y. The cells are chosen to be symmetric around mid-rapidity[1] (y_{cm} = 0.74) and their sizes are optimized individually for each particle species to guarantee sufficient statistics of the rarely produced particles in each cell. The chosen phase space regions for the different charged particles are summarized in table 4.4.

Particle	y	NBins(y)	Δy	$m_t - m_0$ [MeV/c^2]	NBins(m_t) [MeV/c^2]	Δm_t [MeV/c^2]
p	0.09 - 1.29	12	0.1	0 - 1000	40	25
π^-	0.09 - 2.09	20	0.1	0 - 1000	40	25
K^+	0.09 - 1.09	10	0.1	0 - 350	14	25
K^-	0.04 - 0.84	4	0.2	0 - 200	8	25

Table 4.4: Analyzed phase space regions and number of cells for the different charged particles.

4.1.5.1 Protons and negative pions

The most abundantly produced particles are protons and pions which can be reconstructed with high purity in a wide phase space region inside the HADES acceptance. The reconstructed protons and pions are therefore counted in each differential cell of the phase space without subtraction of additional background. The small residual impurities from the particle mis-identification can be corrected for by using simulated Monte-Carlo data, which will be explained in section 4.3. Figure 4.15 shows the raw count rates of protons and π^- inside the HADES acceptance for the analyzed day of the beam time. Both particles are reconstructed down to the lowest values of transverse mass and around mid-rapidity. Especially the light π^- shows an astonishing wide phase space coverage, which will allow to do a multi-differential analysis without strongly depending on model assumptions in the future.

[1] Mid-rapidity corresponds to the rapidity of the center-of-mass in the heavy-ion collision.

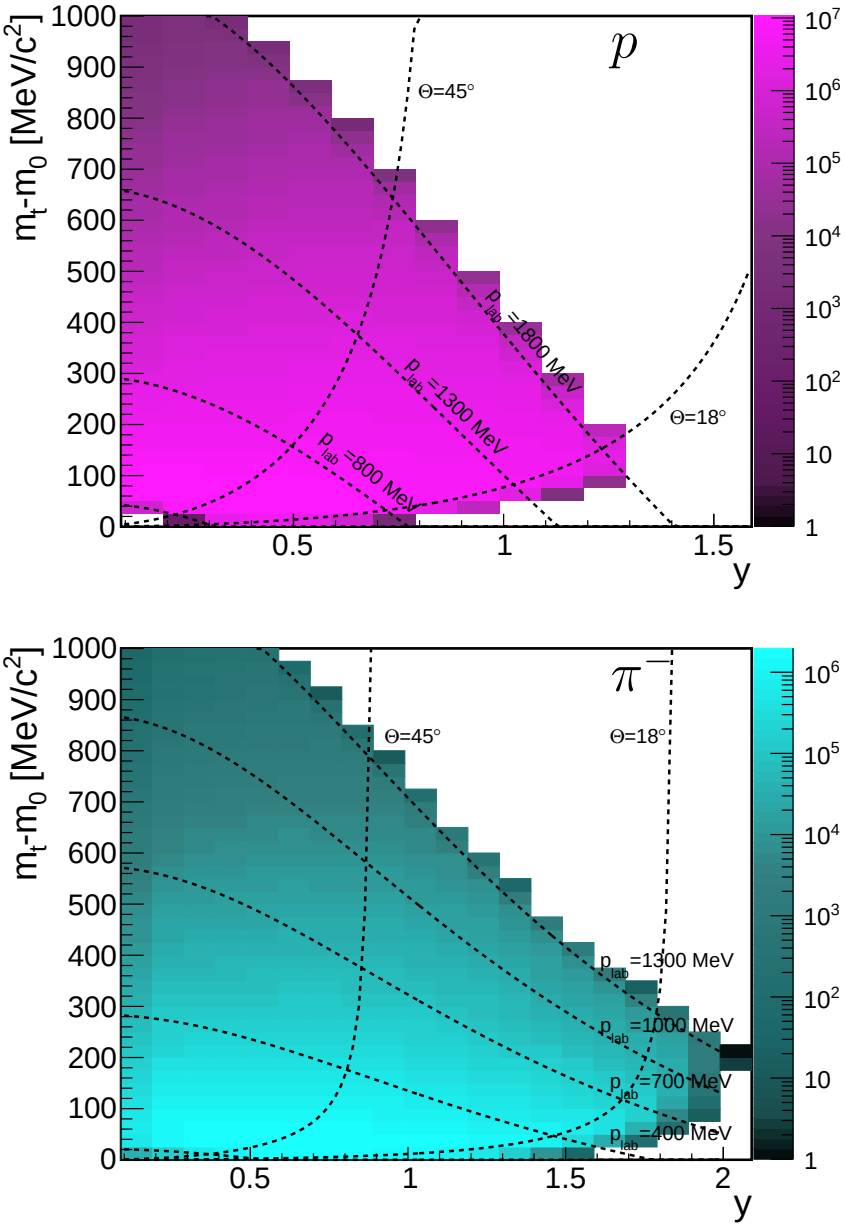

Figure 4.15: Reconstructed raw yield of protons (top) and π^- (bottom) inside the HADES acceptance as a function of $m_t - y$ for the analyzed day of the beam time. The vertical lines indicate the polar angle regions between θ = 18 - 45° covered by the RPC and higher angles covered by the TOF. Horizontal lines indicate different regions of constant momentum p_{lab} in the laboratory.

4.1.5.2 Kaons

The kaons are identified via their reconstructed mass in different cells in m_t-y. In each of the phase space cells, the mass distribution in the region $350 \leq |m_{K^{\pm}}| \leq 600$ MeV/c^2 around the nominal mass is contemplated. A zoom into the charged particle mass spectrum in a single phase space cell in the RPC- and the TOF-detector in the region of K^+ and K^- is shown in figure 4.16[2]. Even after full particle identification there is still some background left, which has to be subtracted before estimation of the real kaon count rate. The signal can be described with a Gaussian distribution on top of the background.

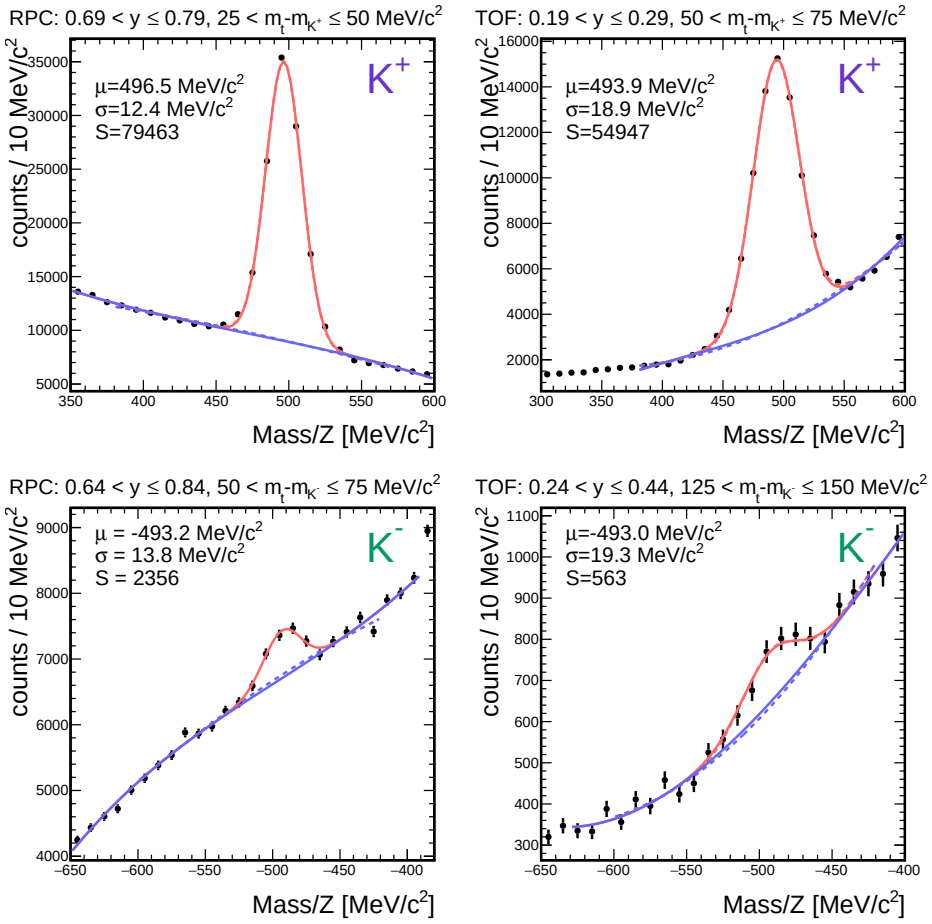

Figure 4.16: Zoom into the charged particle mass spectrum in the region of K^+ (top) and K^- (bottom) in a specific phase space cell (see legend) measured with the RPC- (left) and the TOF-detector (right). The kaon signal is described by a Gaussian parameterization with mean μ and width σ. The residual background is subtracted using a polynomial function third order (solid blue line). In order to investigate systematic uncertainties of the background description, the background is varied to a polynomial second order (dashed blue line).

The background subtraction is the most crucial part of the kaon analysis and happens individually in each phase space cell, as it is strongly momentum dependent. In low momentum regions, the pions

[2]The mass spectra in the analyzed transverse mass cells for mid-rapidity from 0 - 40% most central collisions and centrality dependent can be found in appendix A in figures A.4, A.5, A.6, A.7, A.8 for K^+. and in figures A.11, A.12, A.13 for K^-

are dominating the K^+ signal, whereas the protons are strongly pronounced in the high momentum regions. As there are no anti-protons produced in the analyzed energy regime, the K^- mass spectra are only contaminated by the tails of π^-. However, as the K^- mesons are produced two orders of magnitude less than the K^+, they are strongly affected by falsely matched pion tracks to proton hits in the META-detector, which lead to a wrong momentum dependent calculated mass in the region of the kaon signals (see section 4.1.2.2). Due to these strong variations, the residual background is estimated in an iterative fitting procedure. First, a second order polynomial function is adapted to the background outside the signal region. Then the signal region is included and a Gaussian plus the previously used polynomial function is used to describe the spectrum. As starting parameters for the combined fit, the previous fit parameters are used. Additionally, the pure kaon signal from the full Monte-Carlo simulation is used to constrain the mean and width of the Gaussian distribution[3]. In a next step, a combination of a polynomial third order, with starting parameters for the first parameters from the second order polynomial, plus the constrained Gaussian function is used to describe the spectrum. To guarantee a proper stability of the fits, the mean- and σ-values of the Gaussian parameterization in each cell are inspected for each slice in rapidity as a function of m_t (see figure 4.17 as an example). Due to the momentum resolution of the detector, the parameters are expected to increase monotonously with momentum. Each rapidity region is therefore carefully inspected for monotonous behavior.

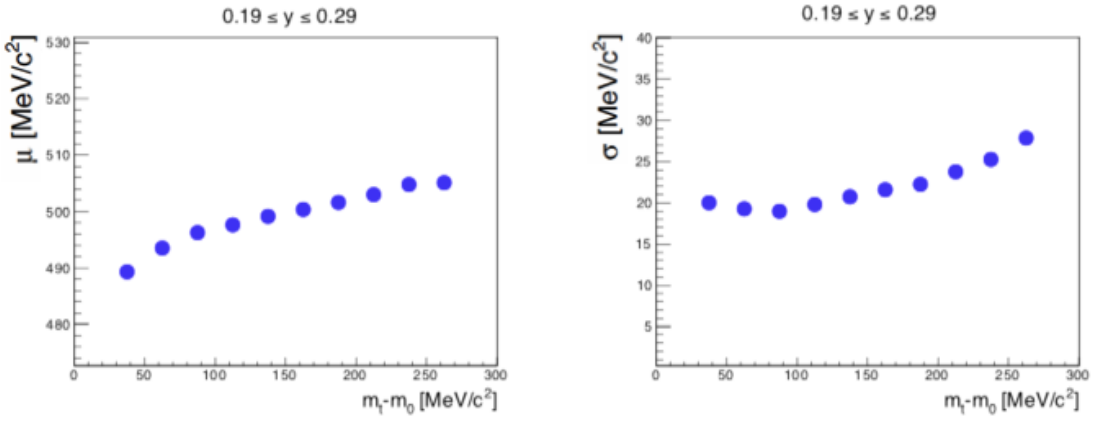

Figure 4.17: Mean (left) and σ (right) of the Gaussian parameterization used for signal extraction as a function of transverse mass for the rapidity region $0.19 \leq y \leq 0.29$ measured in the TOF-detector. Due to the momentum resolution of the detector, both parameters are expected to increase with momentum. To guarantee a proper stability of the fits, this increase should be monotonously.

After background subtraction, the signal is integrated within a 3σ-region around the mean value μ obtained from the Gaussian parameterization. The obtained integral and the parameters of the combined fit function is used as input for the finally used fit function, which is again a combination of a Gaussian and a polynomial third order, however, the third parameter of the Gaussian function is directly the integral instead of the height of the Gaussian function. This allows to obtain the statistical error of the signal and take into account the quality of the background description of the fit function

[3] As the resolution of the calculated mass is exactly reproduced by the simulation, the width of the Gaussian fit to the real data is fixed on exactly the value given by the simulation. The calculated mass of the measured data is not corrected for the energy loss within HADES, therefore the mean has a slight offset to the simulation and is only constrained.

directly. Furthermore, the description of the background is varied using a polynomial function second order in order to evaluate the systematic uncertainty on the extracted signal counts. The difference of the two background count rates was found to be smaller than the overall description within the statistical uncertainty of the experimental data. The signal-to-background ratio varies between values of 0.4 at the edge of the acceptance and 2.7 for identified K^+ (see upper part of figure 4.18). The K^- is reconstructed with a lower signal-to-background ratio (about one order of magnitude) between values of $0.03 \leq S/B \leq 0.15$ (see lower part of figure 4.18). The resulting phase space distributions of the extracted raw differential count rates inside the HADES acceptance for all analyzed events are displayed in figure 4.19. Both kaon species can be reconstructed down to the lowest values of transverse mass and around mid-rapidity. However, due to the higher statistics and signal-to-background ratio, the K^+ has a slight wider phase space coverage than the K^-.

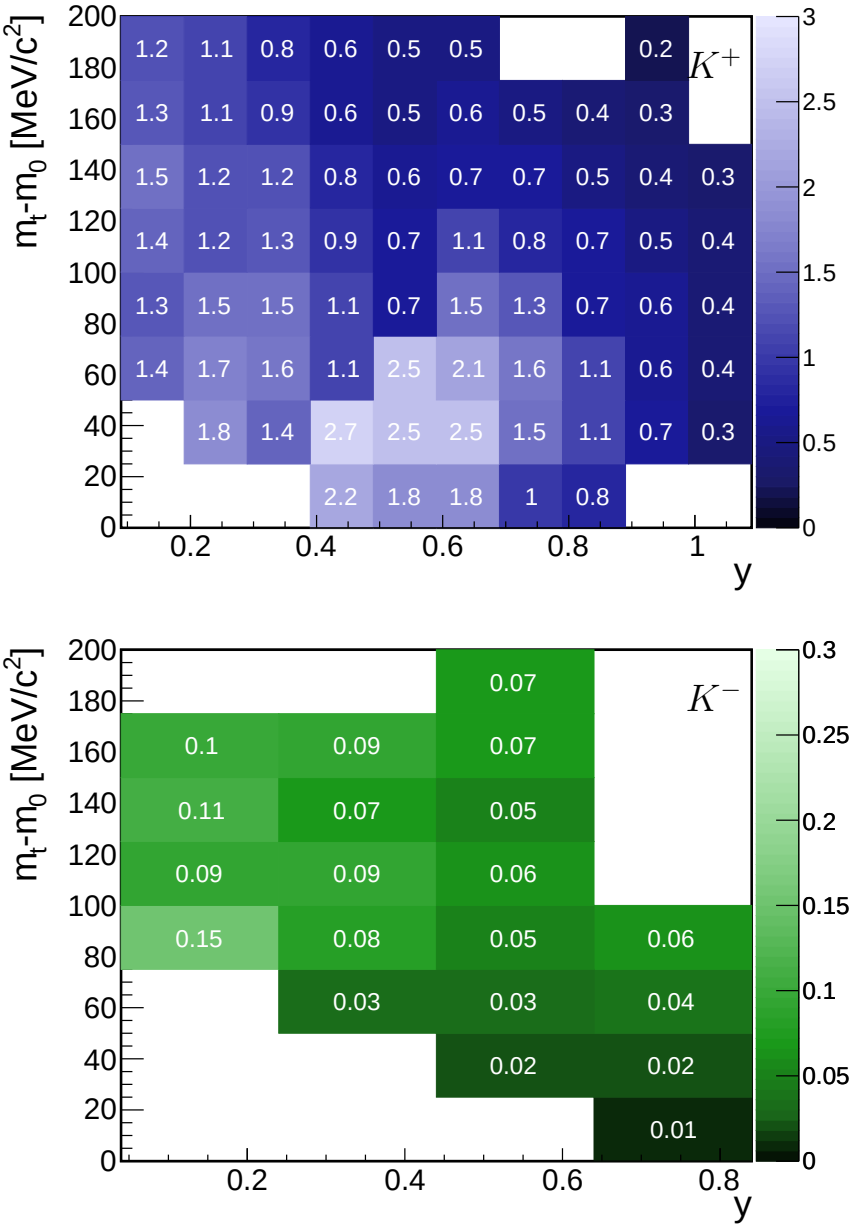

Figure 4.18: Signal-to-background ratio as a function of m_t-y for K^+ (top) and K^+ (bottom).

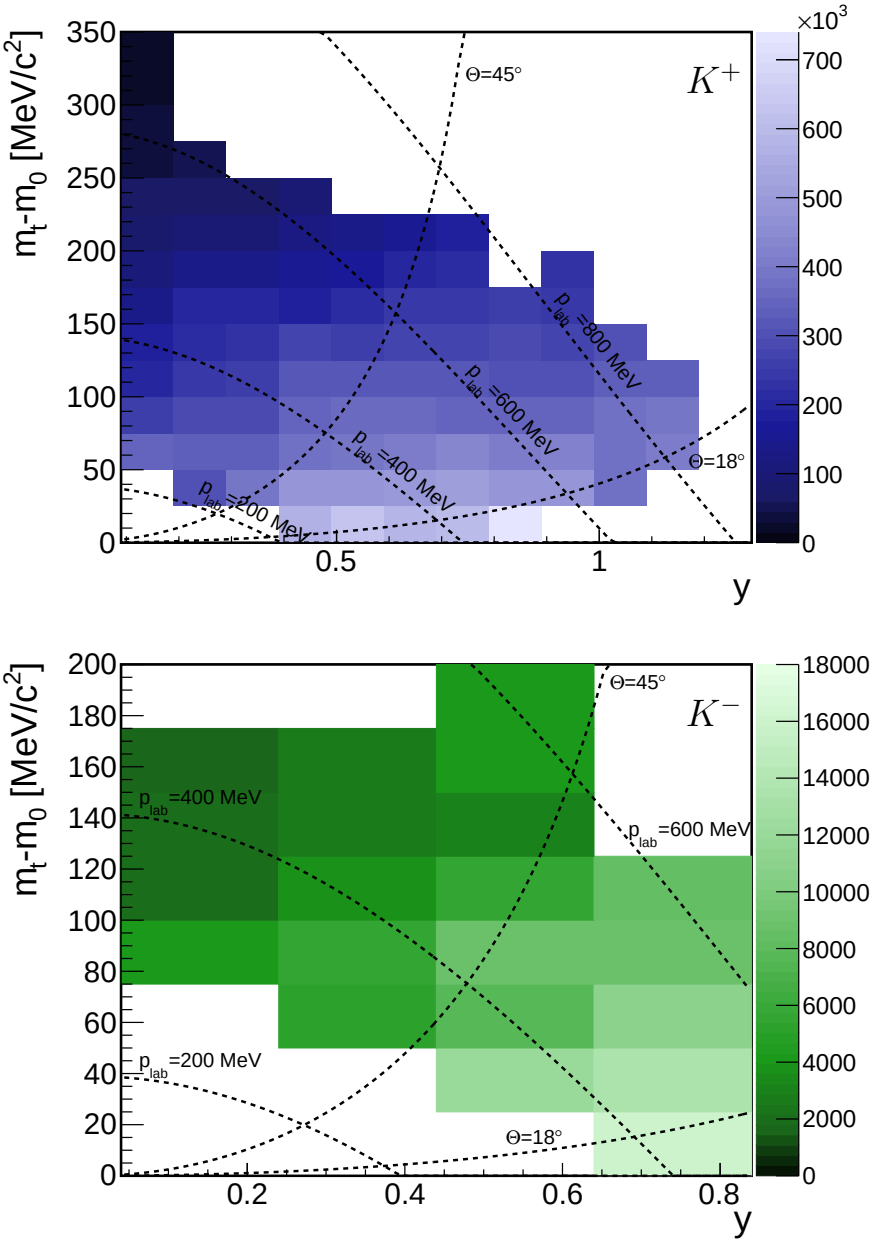

Figure 4.19: Reconstructed raw yield as a function of m_t-y for K^+ (top) and K^- (bottom) inside the HADES acceptance. The vertical lines indicate the polar angle regions between θ = 18 - 45° covered by the RPC and higher angles covered by the TOF. Horizontal lines indicate different regions of constant momentum in the laboratory p_{lab}.

4.2 Reconstruction of the neutral ϕ meson

The previously explained methods for particle identification are only applicable for charged particles which have a lifetime long enough to ionize the material in the active detector volume. To reconstruct unstable neutral particles which are decaying into charged particles before they reach the detector,

like the ϕ meson, the invariant mass from the four-momentum vectors of the daughter particles is calculated. In this analysis the ϕ is reconstructed via its decay into charged kaons, with a branching ratio of 48.9%.

4.2.1 Invariant mass

The invariant mass of a decaying particle M_{inv} is defined as the sum of the two four-momentum vectors of its daughter particles, in case of the ϕ: P_{K^+} and P_{K^-}

$$\begin{aligned} M_{inv}^2 &= (P_{K^+} + P_{K^-})^2 \\ &= (E_{K^+} + E_{K^-})^2 - |\vec{p}_{K^+} + \vec{p}_{K^-}|^2 \\ &= E_{K^+}^2 - |\vec{p}_{K^+}|^2 + E_{K^-}^2 - |\vec{p}_{K^-}|^2 + 2E_{K^+}E_{K^-} - 2\vec{p}_{K^+}\vec{p}_{K^-}. \end{aligned}$$

With the relativistic relation between energy and momentum:

$$E^2 = p^2c^2 + m^2c^4, \tag{4.1}$$

this can be written as:

$$M_{inv} = \sqrt{(m_{K^+}^2 + m_{K^-}^2) + 2\left(\sqrt{m_{K^+}^2 + \vec{p}_{K^+}^2}\sqrt{m_{K^-}^2 + \vec{p}_{K^-}^2} - |\vec{p}_{K^+}||\vec{p}_{K^-}|\cos\Theta\right)}. \tag{4.2}$$

To reconstruct the ϕ, the momenta $\vec{p}_{K^+}$ and $\vec{p}_{K^-}$, the angle Θ between the two tracks and the masses m_{K^+} and m_{K^-} of the kaons have to be known. To reduce the systematic errors introduced from uncertainties in the time-of-flight measurement, the nominal mass, rather than the measured mass, of the daughter particles is used in formula 4.2.1. The width of the reconstructed ϕ in the invariant mass spectrum is therefore only given by its intrinsic decay width, the momentum resolution of the detector and the opening angle between the two kaon tracks.

4.2.2 Kaon identification

The reconstruction of the produced ϕ meson in this analysis is performed via its decay into K^+ and K^-. As the kaons are produced orders of magnitude less than pions and protons it is crucial to apply strong cuts on the candidates to reduce mis-identification, as also done for the single track analysis of kaons. The following selections are applied:

- **Mass cut**: A mass cut around the nominal mass of the kaons is applied: 440 MeV/c^2 $\leq m_{K^\pm} \leq$ 550 MeV/c^2.
- **Momentum selection**: The allowed momentum of kaon candidates is restricted to values below 1000 MeV/c, as for higher momenta the pion and proton tails are entering the kaon mass region due to the momentum resolution of the spectrometer.
- **Cuts on track quality parameters**: The effect of the track quality cuts χ^2_{MM} and χ^2_{RK} has been systematically studied with respect to the best signal-to-background ratio, significance and description of the spectrum by the obtained mixed-event background, which will be explained in the next section. Since we know from single track analysis, that some systematic effects are introduces when applying a cut on the track quality parameters which are not perfectly reproduced by the simulation (see section 4.1.3), the chosen upper values used in the analysis are χ^2_{RK} = 100 and χ^2_{MM} = 2 as used in single kaon analysis (see section 4.1.2.1).

- **Cuts on the specific energy loss**: To improve the purity of the identification, the specific energy loss information of the kaons is used. For all candidates, the same cut on the correlation between the specific energy loss in the drift chambers and the momentum as used in the single kaon analysis (see section 4.1.2.2) is applied. Additionally, the cut used in single kaon analysis on the correlation between the specific energy loss in the TOF-detector and β of the tracks is applied, to remove wrong matches of pion tracks to hits of protons in the META-detector in the region of the TOF-detector, which are leading to a momentum dependent calculated mass in the region of the physical kaon mass.

The identification of kaon candidates for ϕ reconstruction are basically identical to the identification of kaons for the single track analysis, only the selection of the mass region is smaller in case of the pair analysis, as no residual background subtraction is performed.

4.2.3 Invariant mass spectrum and combinatorial background

After the kaon candidate selection, the invariant mass of the ϕ can be calculated (see section 4.2.1). To calculate the invariant mass spectrum of the ϕ decaying as $\phi \rightarrow K^+ + K^-$, all daughter particles of species K^+ and K^- measured in one event are combined into pairs. The information whether the kaons originate from the decay of the same mother or from another production mechanism is lost. As a consequence, also *uncorrelated pairs*, which are not coming from the decay of a ϕ can populate the invariant mass spectrum. Those pairs are not correlated in energy and momentum and therefore are continuously overlaying the real ϕ signal in the invariant mass spectrum. The mass of the two decay products is almost as high as the mass of the ϕ, which has the consequence that there is not much kinetic energy available to populate the phase space. Therefore the true signal of the ϕ is located in the lowest part of the invariant mass distribution close to the edge of the available phase space. The most dominant contribution to the background in the invariant mass spectrum are particles, which are wrongly identified as being one of the decay products K^+ or K^-. This leads to an enhancement in the spectrum in a certain mass region away from the real signal, as there may be a correlation between those particles with a preferred phase space configuration. In contrast to dilepton analysis[4], there is no type of background source known which could generate correlated K^+K^- pairs.

4.2.3.1 Cuts on the decay topology

A possibility to decrease the amount of pairs which are not coming from the decay of the neutral particle of interest, is provided by cuts on its specific **decay topology**. Figure 4.20 sketches the decay of the ϕ meson into charged kaons. The tracks of the kaons and their distance to the reconstructed primary vertex of the reaction can be precisely measured with the tracking algorithm in HADES (see section 3.6). Usually in the analysis of neutral particles, like K^0_S or Λ [116], the following variables are used:

[4]In dilepton analysis a further contribution to the background, so-called *correlated background*, in the invariant mass spectrum has to be taken into account: the combinations of two particles which originate from the decays of two different mother particles, which may are decay products of the same particle. Imagine the decay $A \rightarrow B + B'$. The decay products of B ($B \rightarrow C + D$) and B' ($B' \rightarrow C' + D'$) can be arbitrarily combined, but show a correlation between each other. One example is the π^0-Dalitz decay. The π^0 is decaying into a dilepton pair and a photon. The photon can convert inside the detector material into a dilepton pair. In the calculation of the invariant mass, it can not be distinguished whether the electrons and positrons come from the same photon or from the other, but as the photons have the same mother (the π^0) they show a correlation between each other.

- **Dist A** & **Dist B**: Minimum distance of the prolonged tracks of the two daughter particles to the primary vertex
- **Dist X**: Minimum distance of the decay vertex of the neutral particle to the primary vertex
- **Track Dist**: Maximum distance between the two tracks of the decay products to the decay vertex
- $\Delta\alpha$: Opening angle between the two reconstructed tracks of the decay products.

As the ϕ is decaying via the strong interaction into kaons after a short mean life time of about 1.55 x 10^{-22} s, which is in the order of the life time of the created fireball in the collision, it can not be distinguished if the kaons have been produced in the collision at the primary vertex or if they are decay products from a secondary vertex. In contrast to the analysis of weak decays no off-vertex cuts can be applied to improve the signal-to-background ratio in the invariant mass distribution. Only a cut on the opening angle $\Delta\alpha$ is applied in the analysis and will be introduced in the next section.

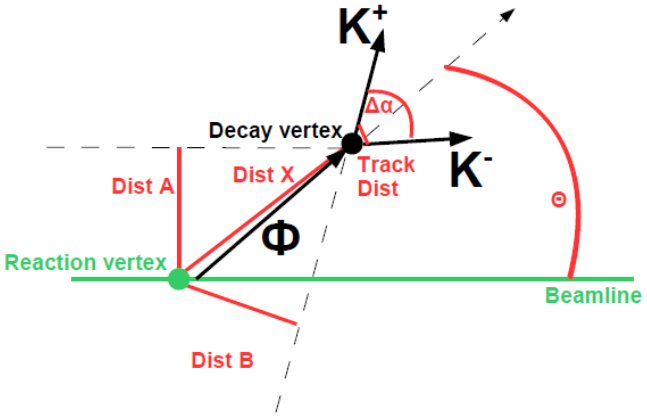

Figure 4.20: Topology of the ϕ meson decay into K^+K^-.

4.2.3.2 Mixed-event technique

To describe the underlying uncorrelated combinatorial background the mixed-event technique is used. In this method, the invariant mass is calculated for all kaon candidates which come from different events where at least one K^+ and one K^- candidate has been identified. Those particles can not have any physical correlation between each other. For a realistic description of the same-event spectrum only candidates from events with a similar multiplicity environment (Δ(mult) < 10) and target slice (Δ(prim vertex) < 5 mm) are used for the mixing. The kaon candidates are selected with exactly the same criteria as for the same-event analysis.

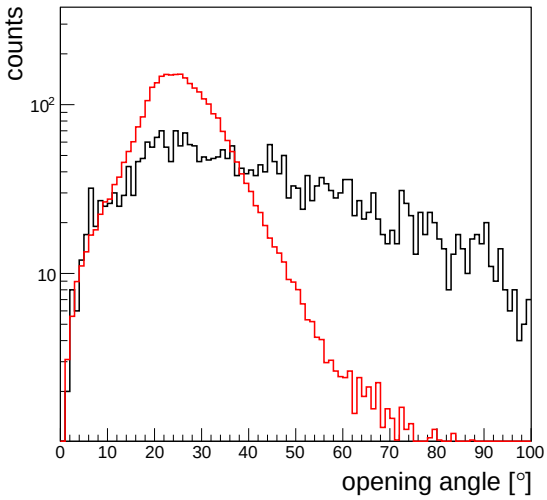

Figure 4.21: Distribution of the opening angle between kaon candidate tracks of real ϕ meson decays from the simulation (red) compared to the one of the data (black). The shown experimental data have a signal-to-background ratio of about S/B = 0.5, hence the discrepancy at high opening angles is due to background tracks still contained in the selected sample.

To improve the description of the mixed-event background in the region of high invariant masses far away from the real signal, which is very important for the normalization of the mixed-event to the same-event spectrum, an upper cut on the opening angle between the two kaon tracks, which excludes opening angles larger than 70° is applied. The value has been estimated by comparing the opening angle distribution of kaons from real ϕ decays obtained from a simulation and the one of the data for all selected kaon candidates from the same-event shown in figure 4.21. It can be clearly seen that most kaon candidates from ϕ decays have due to the small Q-value of the decay a small opening angle, as there is not much kinetic energy left. The shown experimental data have a signal-to-background ratio of about S/B = 0.5, hence the discrepancy at high opening angles is due to background tracks still contained in the selected sample. By taking only track candidates with smaller opening angles, no real ϕ signal is lost as only the high invariant mass region is affected, which has been carefully cross checked against real data.

4.2.4 Result of the particle identification

In figure 4.22 the invariant mass distribution with the corresponding mixed-event background after applying all mentioned cuts is shown. The mixed-event background has been normalized to the same-event spectrum simultaneously in the region below and above the ϕ signal in the regions: 980 $\leq$ $M_{K^+K^-}$ $\leq$ 1005 MeV/c^2 and 1030 $\leq$ $M_{K^+K^-}$ $\leq$ 1150 MeV/c^2. The background describes the spectrum and is subtracted from the same-event spectrum. The resulting ϕ signal can be described with a Gaussian parameterization from which the mass of the signal is estimated to μ = 1019.1 MeV/c^2 and a width of σ = 5.2 MeV/c^2 is extracted. In the region of $\mu \pm 2\sigma$ about 1000 ϕ mesons are reconstructed in the HADES acceptance with a signal-to-background ratio of S/B = 0.5.

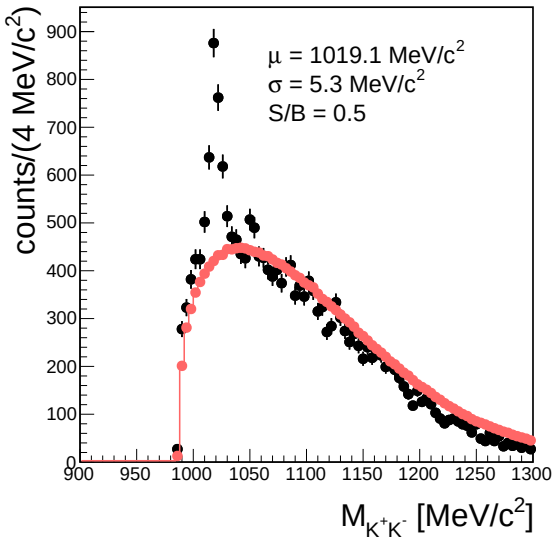

Figure 4.22: Invariant mass distribution of all K^+K^- candidates from the same event (black) with corresponding mixed-event background (red). The ϕ signal can be described with a Gaussian parameterization from which the mass μ and width σ are extracted. In the region of $\mu \pm 2\sigma$ about 1000 ϕ mesons are reconstructed in the HADES acceptance with the signal-to background-ratio S/B.

To obtain the real produced yield in full phase space, the differential count rate in cells in the rapidity and transverse mass plane has to be extracted, corrected for geometrical acceptance plus detector and cut efficiencies and extrapolated to unmeasured phase space regions, which will be explained in the following sections.

4.2.5 Comparison of the experimental data to the full Monte-Carlo simulation

In order to use the simulation to correct the obtained count rates of the ϕ meson for eventual efficiency losses introduced due to the cuts applied for kaon identification, all experimental distributions should be reproduced by the simulation. In section 4.1.3 the distributions from the single kaon analysis have already been compared to the simulation. For the reconstruction of the ϕ only kaons are taken into account which have been produced in an event where at least one K^+ and one K^- candidate has been found. The resulting invariant mass spectrum of the selected kaon candidates is shown in figure 4.23. Whereas the shape of the combinatorial background is well reproduced, the ϕ production cross section is clearly underestimated from the used version of the UrQMD transport model (UrQMD v3.3 patch 2). Figure 4.24 shows the comparison between simulation and data for the kinematic observables of the reconstructed ϕ candidates: momentum distributions of and opening angle between the two kaon tracks; momentum, reduced transverse mass $m_t - m_0$ and rapidity of the reconstructed ϕ. The simulation is reproducing the measured data. The small differences are due to the mentioned underestimation of the ϕ production cross section within the used version of the UrQMD transport model. However, the efficiencies are obtained for a generated ϕ, embedded into this simulation and therefore the production cross-section is negligible.

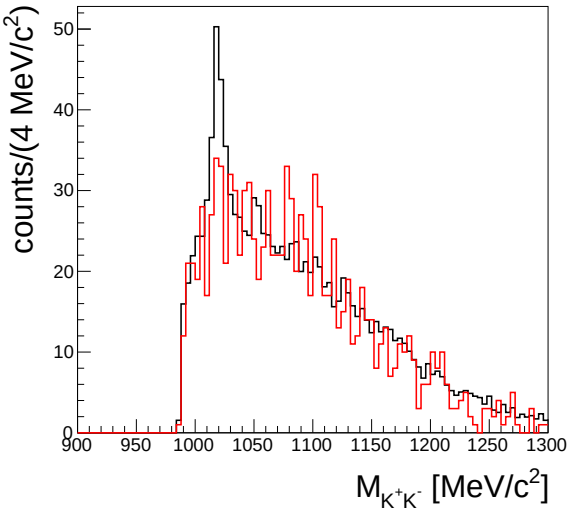

Figure 4.23: Comparison of the invariant mass distribution from K^+K^- candidates between experimental data (black) and simulation (red). In order to compare the shape, the data is normalized to the simulation.

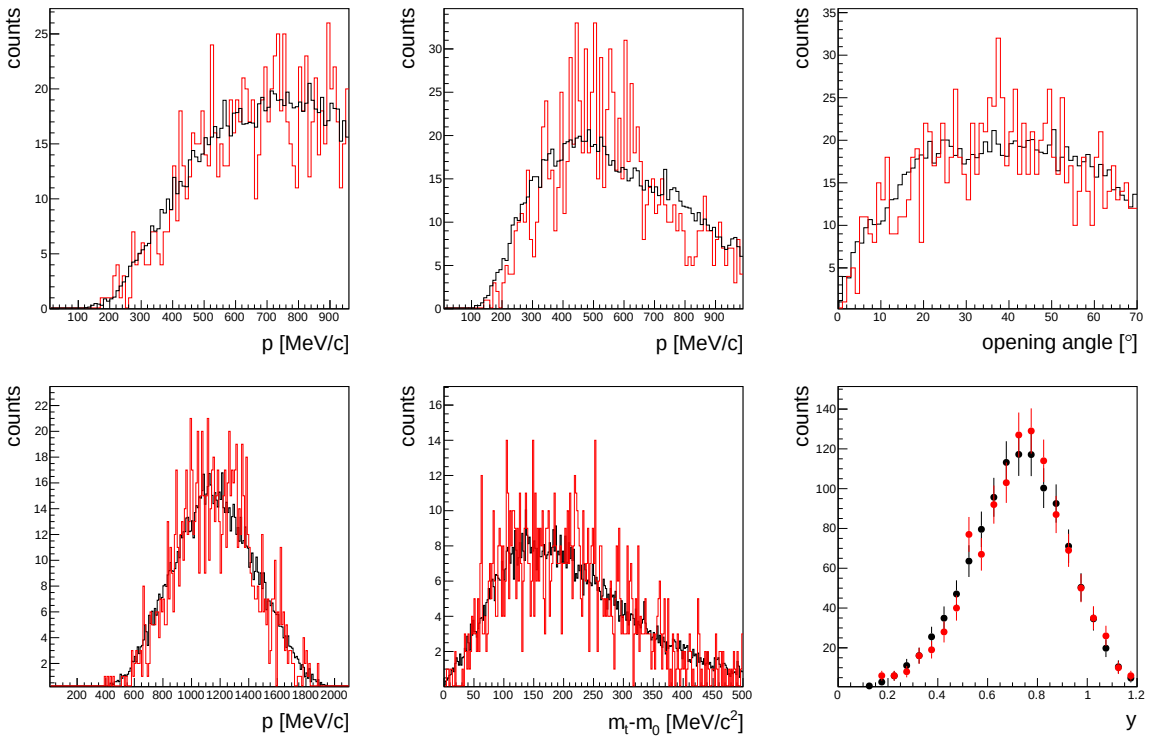

Figure 4.24: Comparison of the momentum distributions of selected K^+ (top left) and K^- (top center) candidates for ϕ reconstruction and the opening angle between the tracks (top right) and of the resulting kinematic distributions of the reconstructed ϕ: momentum (lower left), transverse mass (lower center) and rapidity (lower right) between experimental data (black) and simulation (red). All experimental distributions are normalized to the simulated data and are reproduced.

4.2.6 Estimation of the differential count rate

Due to small statistics of reconstructed ϕ mesons, the phase space is divided in 3x3 cells in transverse mass and rapidity. In each of the phase space cells, the invariant mass distribution of all K^+K^- candidates is shown with the corresponding mixed-event background in the upper part of the figures 4.25, 4.26 and 4.27[5],. The normalization region of the mixed-event to the same-event spectrum is chosen between 980 $\leq M_{K^+K^-} \leq$ 1005 MeV/c^2 and between 1030 $\leq M_{K^+K^-} \leq$ 1150 MeV/c^2 simultaneously. The shape of the same-event spectrum by the mixed-event distribution is reproduced in each phase space cell and is therefore subtracted in order to estimated the true ϕ signal. The resulting signal is parameterized with a Gaussian fit, which is shown in the lower row of the figures 4.25, 4.26 and 4.27. The differential count rate is defined as the integral of the spectrum in a 2σ-interval around the mean μ. The signal-to-background ratios for the different phase space cells are displayed on the right side of figure 4.28. It is varying between 0.3 at the edge of the acceptance and 1.4. The right side of figure 4.28 shows the raw counts reconstructed in the HADES acceptance.

Systematic and statistical uncertainty on the differential count rate

The combinatorial background in the invariant mass spectrum of K^+K^- is subtracted using the mixed-event technique (see section 4.2.3.2). To get a handle on the systematic errors introduced by this method the mixed-event is normalized to the same-event spectrum in different invariant mass regions away from the ϕ signal. The best description is obtained by normalizing in a region below and above the ϕ mass between 980 $\leq M_{K^+K^-} \leq$ 1005 MeV/c^2 and between 1030 $\leq M_{K^+K^-} \leq$ 1150 MeV/c^2 simultaneously. However, as the statistical uncertainties in the same event spectrum are high, also the normalization only in the high invariant mass region between 1050 - 1150 MeV/c^2 can properly describe the spectrum. To take into account those uncertainty on the background description, the count rate is estimated using both variations to subtract the background and treat the difference $\Delta N_B = |N_{S,ME1} - N_{S,ME2}|$ as systematic uncertainty for each individual phase space cell. The absolute error of the extracted signal is therefore given by:

$$\Delta N_S = \sqrt{(\Delta N_S)^2 + (\Delta N_B)^2}, \tag{4.3}$$

with the statistical error of the extracted signal count rate $\Delta N_S = \sqrt{N_S}$ and the mentioned systematic uncertainty of the background subtraction ΔN_B.

[5]The invariant mass spectra in the analyzed transverse mass cells for mid-rapidity for the centrality dependent analysis can be found in appendix A in figures A.16 and A.17

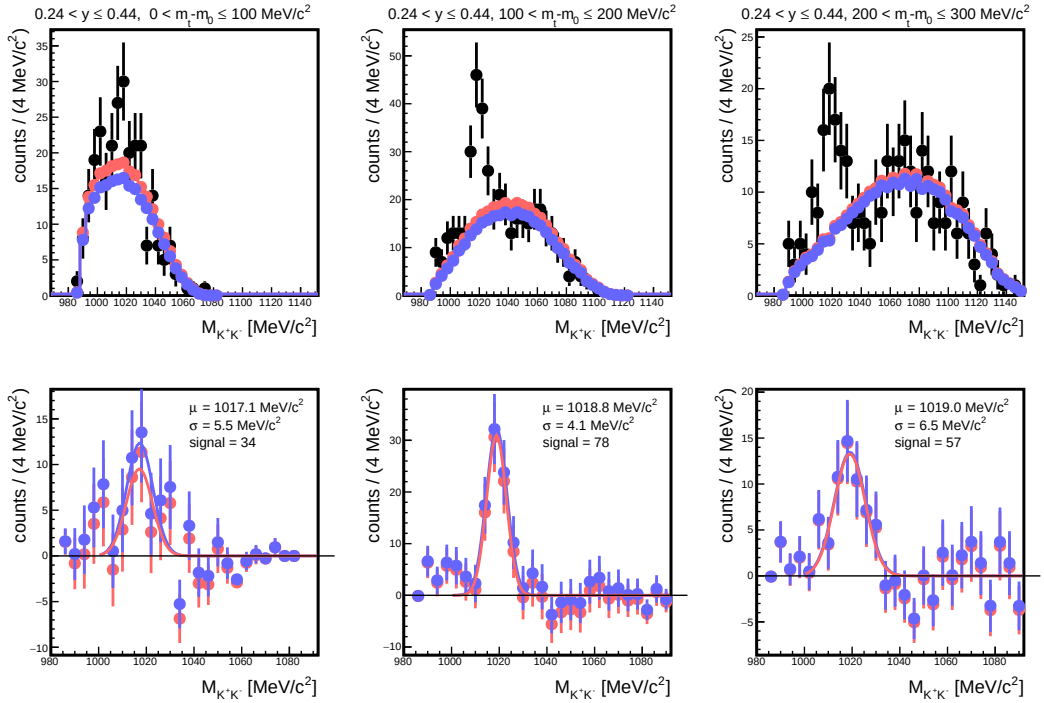

Figure 4.25: Top: Invariant mass distributions as a function of m_t for the rapidity region $0.24 < y \leq 0.44$, of all K^+K^- candidates with corresponding mixed-event background, normalized in the region $980 \leq M_{K^+K^-} \leq 1005$ MeV/c^2 and $1030 \leq M_{K^+K^-} \leq 1150$ MeV/c^2 simultaneously (red), respectively $1050 \leq M_{K^+K^-} \leq 1150$ MeV/c^2 (blue). Bottom: After subtraction of the mixed-event background, the ϕ meson signal can be described by a Gaussian parameterization to extract the mean μ, width σ and the differential count rate (signal).

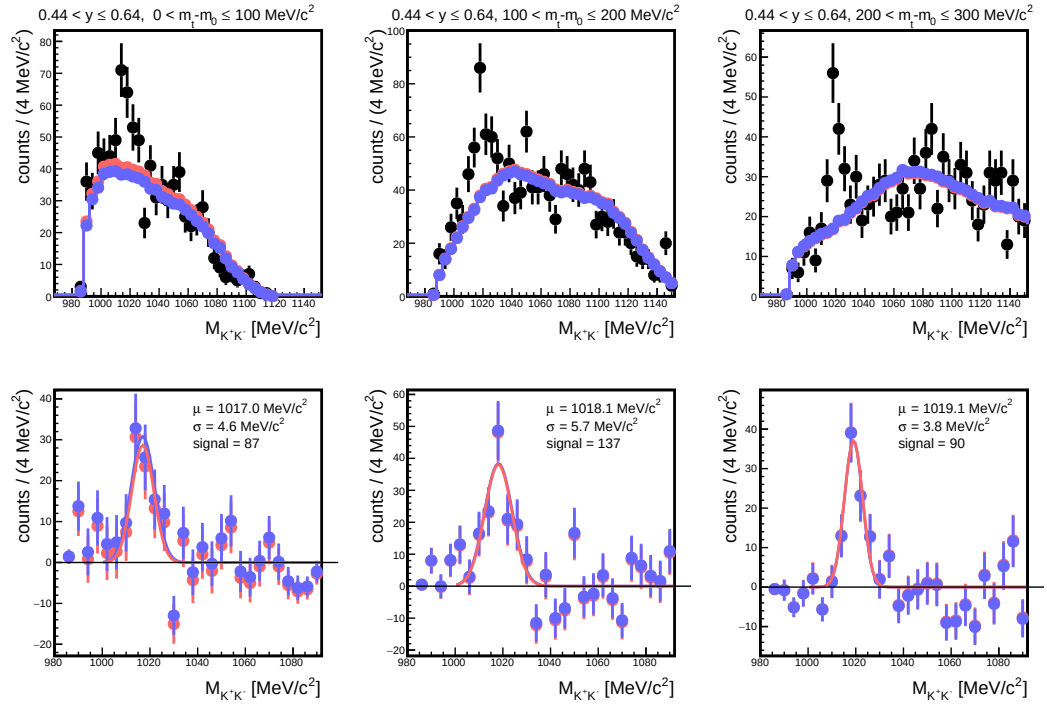

Figure 4.26: Top: Invariant mass distributions as a function of m_t for the rapidity region $0.44 < y \leq 0.64$, of all K^+K^- candidates with corresponding mixed-event background, normalized in the region $980 \leq M_{K^+K^-} \leq 1005$ MeV/c^2 and $1030 \leq M_{K^+K^-} \leq 1150$ MeV/c^2 simultaneously (red), respectively $1050 \leq M_{K^+K^-} \leq 1150$ MeV/c^2 (blue). Bottom: After subtraction of the mixed-event background, the ϕ meson signal can be described by a Gaussian parameterization to extract the mean μ, width σ and the differential count rate (signal).

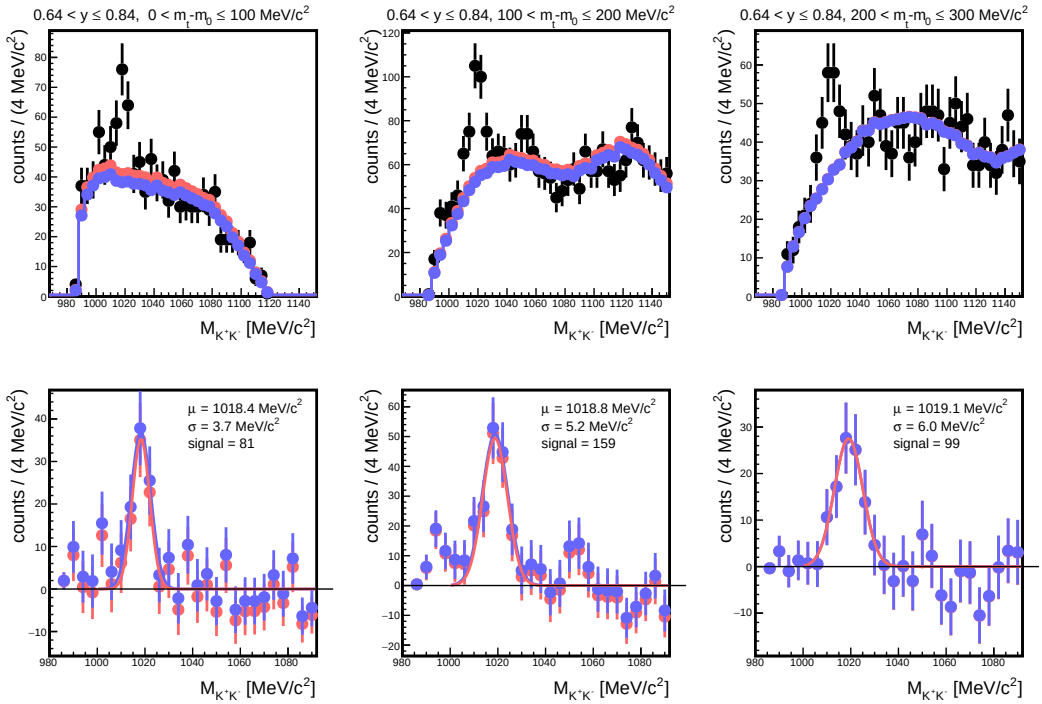

Figure 4.27: Top: Invariant mass distributions as a function of m_t for the rapidity region $0.64 < y \leq 0.84$, of all K^+K^- candidates with corresponding mixed-event background, normalized in the region $980 \leq M_{K^+K^-} \leq 1005$ MeV/c^2 and $1030 \leq M_{K^+K^-} \leq 1150$ MeV/c^2 simultaneously (red), respectively $1050 \leq M_{K^+K^-} \leq 1150$ MeV/c^2 (blue). Bottom: After subtraction of the mixed-event background, the ϕ meson signal can be described by a Gaussian parameterization to extract the mean μ, width σ and the differential count rate (signal).

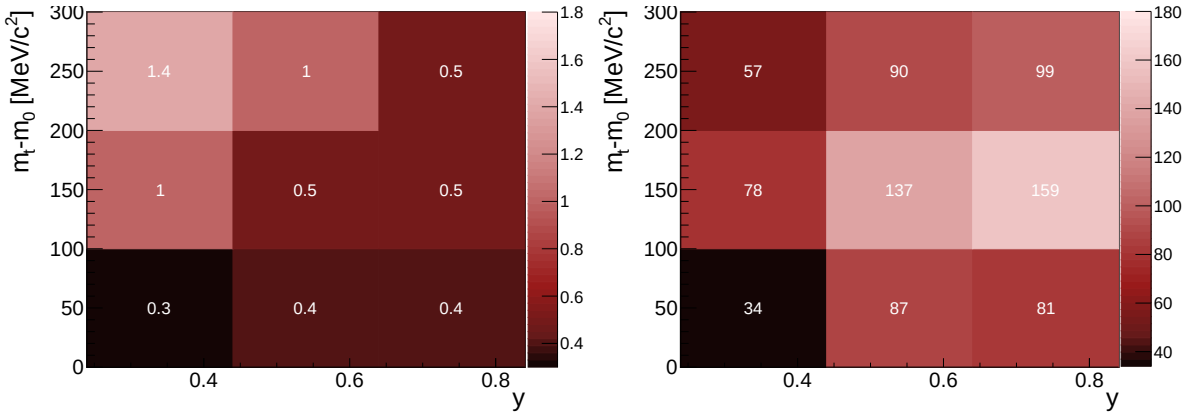

Figure 4.28: Signal-to-background ratio and reconstructed raw yield of ϕ mesons as a function of m_t-y inside the HADES acceptance.

4.3 Efficiency and acceptance corrections

As particles produced in a heavy-ion collision are emitted in full phase space but are only reconstructed in the active volume of the HADES detector, the measured particle spectra have to be corrected for the **geometrical acceptance** of the detector. The phase space coverage differs for different particle species and depends on the reaction vertex and the strength of the magnetic field. A particle is counted as accepted if its trajectory gets in contact with a minimum number of layers in the drift chambers (four per module) and the detectors of the time-of-flight wall. In case of infinitesimal small phase space cells, the acceptance matrix can therefore have either the value 1 for accepted or 0 for not accepted. In the analysis, the particles are identified and need to be corrected in finite phase space cells. This leads to values of the acceptance between 0 and 1, as parts of the phase space cells may lie outside the geometrical acceptance. The acceptance is defined as:

$$acc(m_t, y) = \frac{N_{\text{accepted}}(m_t, y)}{N_{\text{emitted}}(m_t, y)}, \tag{4.4}$$

with $N_{\text{accepted}}(m_t, y)$ being the count rate of particles reaching the active detector volume and $N_{\text{emitted}}(m_t, y)$ being all primary emitted particles.

Even in the active parts of the detector, it can happen that not all tracks are properly registered and reconstructed. This leads to the need of an additional correction factor for the particle spectra, the **detector and track reconstruction efficiency**. The intrinsic detector efficiencies are estimated using cosmic radiation and reactions reconstructed without a magnetic field. To estimate the track reconstruction efficiency and take into account hardware failures, different thresholds in the read-out electronics, cuts used in the digitization of drift times and noise of the detectors, a realistic detector and background description is necessary. The reconstruction efficiency is defined as:

$$\epsilon_{\text{rec}} = \frac{N_{\text{reconstructed}}(m_t, y)}{N_{\text{accepted}}(m_t, y)}. \tag{4.5}$$

Each selection applied in the analysis for particle identification reduces not only background, but also real signal of the particle of interest. The measured count rate has therefore to be additionally corrected for the different **cut efficiencies**:

$$\epsilon_{\text{cut}} = \frac{N_{\text{cut}}}{N_{\text{w/o cut}}}, \tag{4.6}$$

N_{cut} equates the measured count rate after the corresponding applied cut and $N_{\text{w/o cut}}$ before applying the cut.

4.3.1 Estimation of the acceptance and efficiency matrices

The estimation of the acceptance and efficiency matrices is performed using simulations. As a first step, the distributions of the analyzed particle species are generated using the PLUTO- [140] or the UrQMD-eventgenerator (see section 3.5). PLUTO is a C++ based simulation framework, which allows to generate any particle and its decay with a certain momentum and angular distribution. In this analysis, the strange particles are produced according to a thermal distribution with a certain temperature (see tabular 4.5) to generate a realistic phase space distribution, whereas for the pions and protons the pure distribution from UrQMD is used. In order to investigate the systematics of the production mechanism, π^- and protons are additionally produced with PLUTO. The input temperatures are again chosen to be T = 80 MeV. The resonant production of π^- is simulated by introducing a

contribution with a second temperature T = 40 MeV (see section 5.2). To take into account possible effects of radial flow of the reaction zone, protons are furthermore produced with a radial flow velocity β_r = 0.3. The production parameters for the analyzed particles are summed up in tabular 4.5. To get an adequate background description, the simulated tracks from PLUTO are embedded into the events of the UrQMD simulation or in real events with the *track embedding method*. The particles from this analysis are embedded into the events of UrQMD, which has been tuned with an additional contribution from δ-electrons (see section 3.5.1). As a next step, the produced particles are passing a HGeant-simulation, which generates a realistic detector response, as explained in section 3.5. To estimate the acceptance, reconstruction and cut efficiencies, the simulated data are analyzed exactly in the same way as the real data, which is sketched in figure 3.7). The different matrices can be extracted independently after different steps of the analysis chain if the correction factors have no dependencies among each other. Since this is not fully true, a combined correction factor is used, which will be discussed in the next section for each particle individually.

Simulated particle	Pluto
p	T = 80 MeV β_r = 0.3
π^-	T_1 = 40 MeV T_2 = 80 MeV
K^+	T = 80 MeV
K^-	T = 70 MeV
ϕ	T = 100 MeV

Table 4.5: Input parameters for PLUTO of the simulated particles for efficiency and acceptance corrections.

4.3.1.1 Efficiency and acceptance matrices of protons and π^-

Protons and pions are identified using graphical selections on the correlation between β and momentum of the track candidates. The cuts have been systematically calculated for the two time-of-flight walls in data and simulation separately, to account for the different resolution. To estimate the combined acceptance and efficiency factor, which is displayed in figure 4.29 for protons (top) and π^- (bottom), the phase space distribution of the reconstructed simulated particles which are identified with the adapted selection in the correlation between β and momentum are divided by the input distribution from primary protons or π^- from the UrQMD model. The factors are rather constant around 50 - 60%. However, a big drop at the edge of the acceptance is visible. The matrices of the acceptance and the reconstruction efficiency separately can be found in appendix A in figure A.2, respectively A.3.

The π^- is decaying to 99.99% in a muon - neutrino pair with a mean decay length of 7.8 m, such that most of the pions decay outside the HADES detector and can be reconstructed. Even in case the pion is decaying inside HADES, most of the decay products are due to the finite mass resolution identified as being a pion, because the muon and the pion have very similar masses. As a result, the procedure to calculate the correction matrix is taking into account losses of pions which are decaying before leaving the acceptance of the spectrometer, because the resulting muons are showing up in the selected graphical cut in the correlation between β and momentum. Additionally, this way of doing the correction is directly accounting for possible impurities of the particle identification in the experiment. It can happen that due to e.g. mis-matches of the tracking algorithm also tracks are counted as being a proton or a pion, as they by chance show the right correlation between β and momentum.

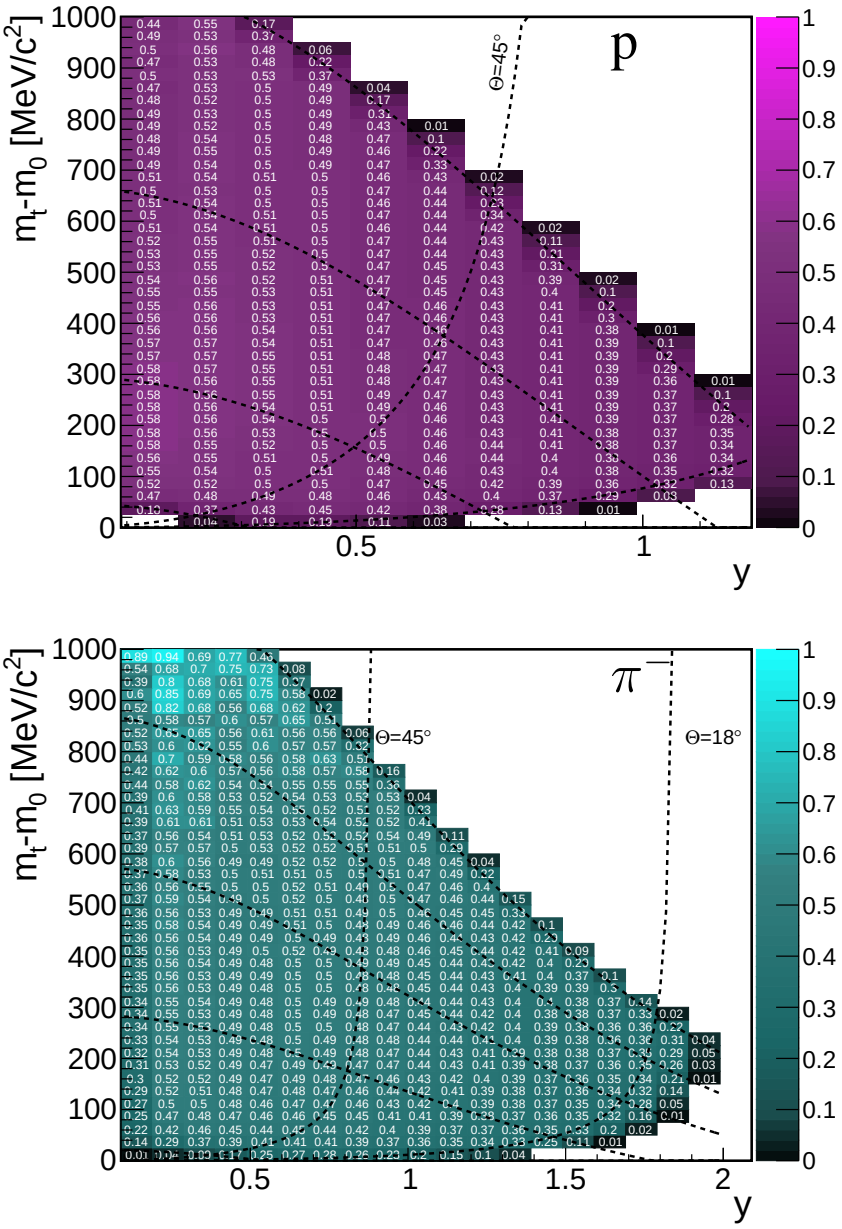

Figure 4.29: Combined efficiency and acceptance correction factor for protons (top) and π^- (bottom) in the analyzed phase space cells as a function of m_t-y.

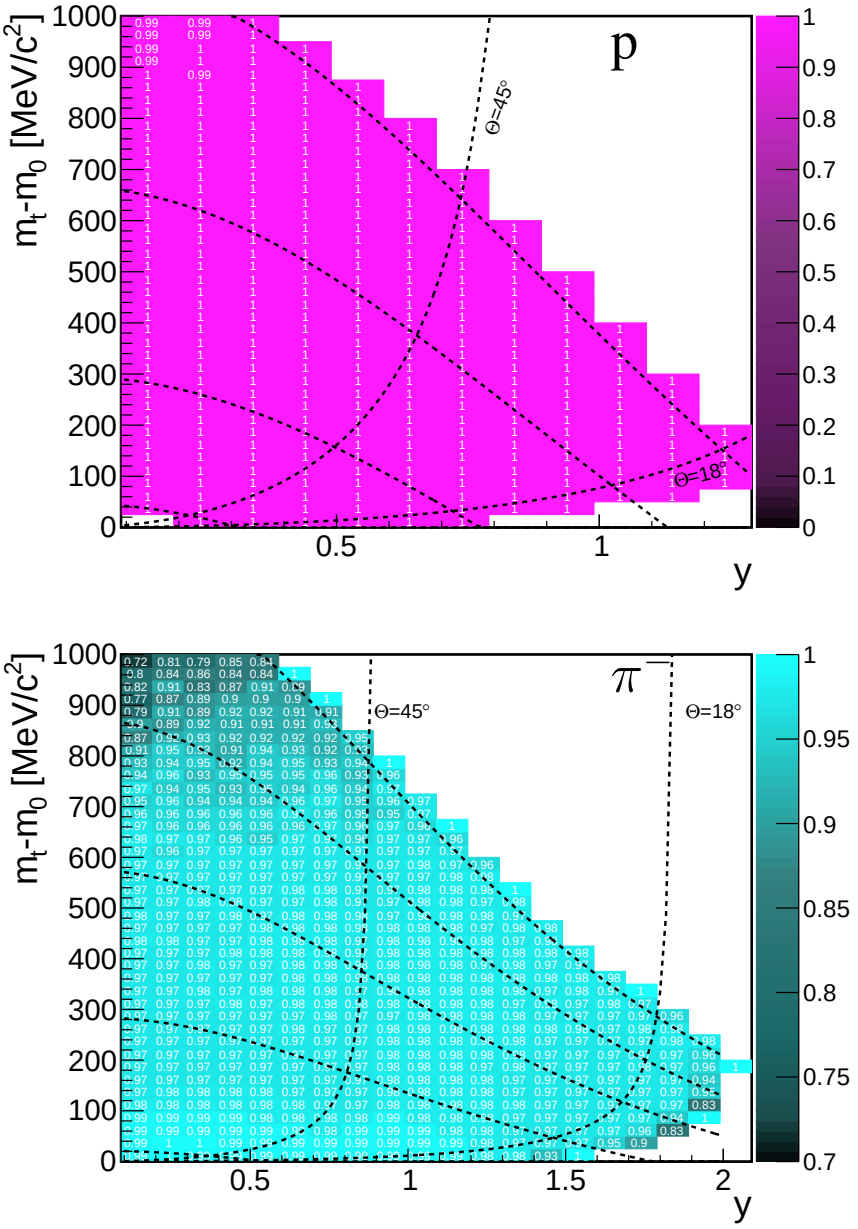

Figure 4.30: Purity matrices of protons (top) and π^- (bottom) in the analyzed phase space cells as a function of m_t-y.

The purity matrices are obtained by identifying the particles not only via the selection on the correlation between β and momentum of the tracks, like in the experiment, but asking additionally for the GEANT information of the particles, which contains the information if the reconstructed particle is a true primary simulated proton or pion. The matrices are shown in figure 4.30. The protons can be reconstructed with a perfect purity of 100% inside the complete HADES acceptance, while the π^- show some impurities around 2 - 3%, which is increasing towards the highest transverse masses. The main source for wrongly identified π^- tracks are protons, which get a negative charge assigned. This is more likely to happen at high momenta, as the curvature of the tracks due to the deflection inside the magnetic field is less, which explains the lower purity in the high transverse mass region.

In order to investigate if there is any dependence of the correction factors on the input distribution, the correction factors are additionally obtained using only tracks which have been generated with PLUTO (see table 4.5). The pions are generated with two input temperatures T_1 and T_2 to reproduce the experimentally measured distribution. Protons are because of their high mass very sensitive to radial flow and therefore are generated with a temperature and a radial flow velocity β_r. Again the selections on the correlation between β and momentum for proton identification are applied and the reconstructed distribution is divided by the generated input. With this method the spectra are not corrected for impurities, as only true generated particles are reconstructed. The residual difference of the correction matrices, after taken the purity into account is less than 1% and used as systematic error later on. Furthermore, the tracks are not only embedded into UrQMD events but into real data. With this method it can be cross-checked if all detector and background effects are reproduced by the Monte-Carlo simulation. The difference in correction factors was found to be around 1% and is kept as systematic error.

4.3.1.2 Efficiency and acceptance matrices of kaons

The production cross-section of kaons is very small in the analyzed energy regime. In order to enhance the kaon statistic, the correction matrices are obtained using one embedded kaon track per event, generated with the PLUTO event generator according to a realistic phase space distribution, into the UrQMD simulation (see table 4.5). The particle identification is done exactly in the same way as for the experimental data with applying cuts on the track quality parameters and the specific energy loss inside the drift chambers and the TOF-detector (see section 4.1.2). As explained in section 4.1.2.2, the cuts on the energy loss in the drift chambers are scaled in order to account for the different resolution of this quantity in simulation and experiment. To estimate the differential count rate in the experiment, the residual background populating the kaon mass region is subtracted in each phase space cell individually (see section 4.1.5.2), therefore the purity of the selected sample is $\approx$ 100%. To account for the momentum dependent mass resolution of the spectrometer, the extraction of the count rate of reconstructed simulated kaons is done adapting a Gaussian parameterization to the mass distribution in the same phase space cells similar as for the experimental data. Like for real data, the full region around the mean is selected. This count rate is divided by the input distribution from the generated primary kaons in full phase space. The obtained combined efficiency and acceptance matrices for K^+ and K^- are shown in figure 4.31. The correction factors are in the order of about 20%, which is clearly lower than for proton and pion analysis, as stronger cuts for particle identification have to be applied. The matrices of the acceptance and the reconstruction efficiency separately can be found in appendix A in figure A.10, A.14 respectively. In order to investigate if the UrQMD simulation generates a realistic background, the thermal kaon track is additionally embedded into real events. The difference on the correction factors was found to be negligible.

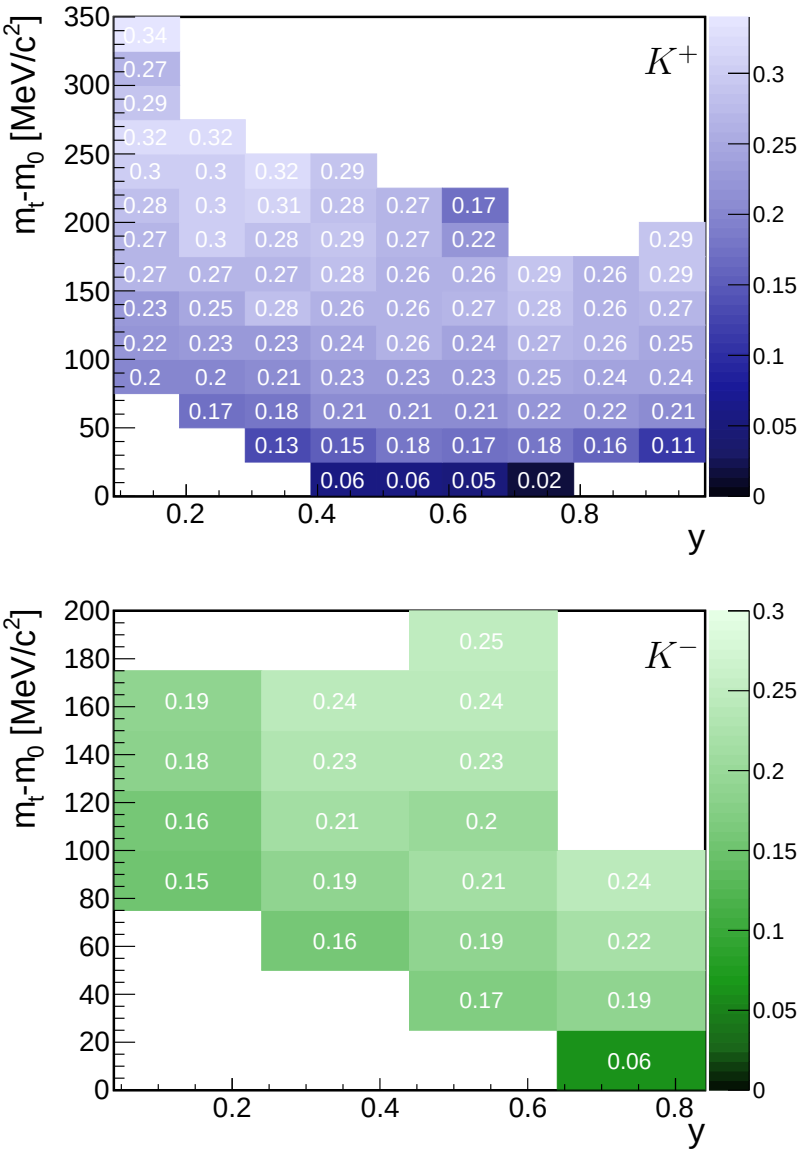

Figure 4.31: Combined efficiency and acceptance correction factor for K^+ (top) and K^- (bottom) in the analyzed phase space cells as a function of m_t-y.

4.3.1.3 Efficiency and acceptance matrix of ϕ

The ϕ meson is also generated with PLUTO and embedded into UrQMD events to obtain the combined efficiency and acceptance correction factor matrix, as its cross-section is even lower than the one of kaons and the used version of UrQMD is underestimating the ϕ production yield. The kaons originating from a ϕ decay are reconstructed in the same way as in real data. As the phase space distribution of ϕ mesons in the low energy regime below its elementary production threshold is not well known experimentally, the chosen input temperature is varied and estimated in an iterative procedure. First, the same temperature of T = 80 MeV as used for K^+ and π^- analysis is used to correct the differential count rates. The transverse mass spectra are parameterized with Boltzmann functions to obtain the so-called effective temperature of about $T_{eff} \approx 103$ MeV. The procedure will be explained in detail in chapter 5. The efficiency and acceptance matrix estimation is repeated with a PLUTO input temperature of T = 100 MeV. The resulting correction matrix is displayed in figure 4.32. As the same cuts for kaon identification like for the single kaon analysis are used, the corresponding correction factors are one order of magnitude below the factors for kaon analysis.

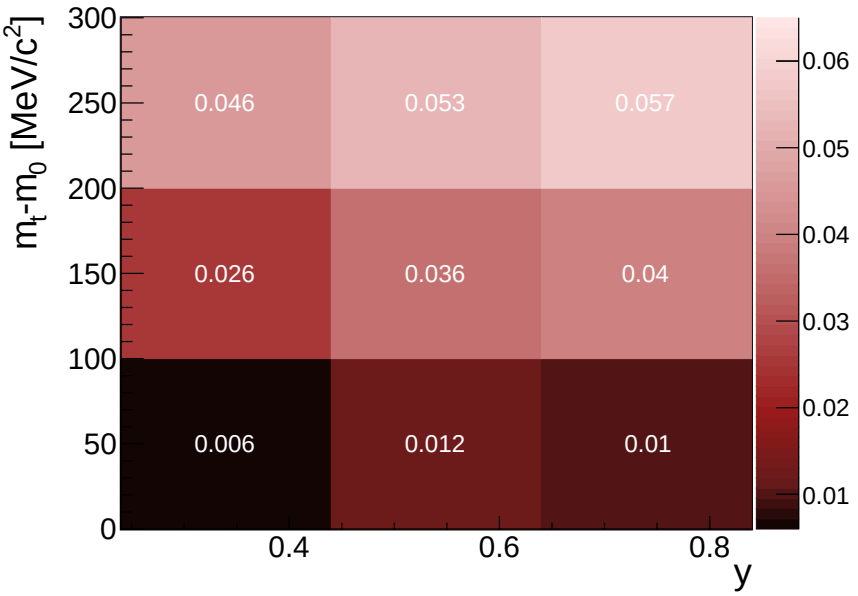

Figure 4.32: Combined efficiency and acceptance correction factor for ϕ mesons, decaying into K^+K^- in the analyzed phase space cells as a function of m_t-y.

Chapter 5

Results

The goal of the analysis of the different hadrons, namely p, π^-, $K^\pm$ and ϕ, performed in this thesis, is the estimation of the particle multiplicities and a complete characterization of the thermodynamic properties of the created system in Au+Au-collisions at 1.23 AGeV.

The particles are only reconstructed and the resulting spectra corrected for acceptance and efficiency inside the phase space region covered by the HADES detector. To estimate the multiplicities, the spectra have to be extrapolated to full phase space. To do so, first the transverse mass spectra are extrapolated to the unmeasured transverse mass regions for slices in rapidity. Assuming that the system created in a heavy-ion collision is in thermal equilibrium, the particles are small compared to the system size, the particles are in constant, random and rapid motion and interact constantly among themselves in elastic collisions, the kinematic distributions of the particles can be described analogue to an ideal gas in kinetic gas theory based on Maxwell-Boltzmann velocity distributions [141, 142]. According to that the transverse mass spectra of particles created in relativistic heavy-ion collisions can be described with Boltzmann functions of the following form [143]:

$$\frac{1}{m_t^2}\frac{d^2N}{dm_t dy} = C(y)\exp\frac{-(m_t - m_0)c^2}{T_B(y)}. \tag{5.1}$$

For easy comparison between the different hadrons the nominal particle mass m_0 is subtracted from the transverse mass m_t and the differential count rate is scaled by $1/m_t^2$, called *Boltzmann representation* in the following. The inverse slope parameter T_B depends on the rapidity. The inverse slope at mid-rapidity, called *effective temperature* T_{eff} in the following, can be related to the kinetic freeze-out temperature T_{kin} of the system in this purely thermal scenario:

$$T_{kin} = \frac{T_{eff}}{\cosh y_{cm}}. \tag{5.2}$$

By integrating equation 5.1 over m_t, the differential rapidity particle density can be estimated. The result of the analytic integration starting from m_t = m_0 to m_t = ∞ with the parameters of the fits, constant $C(y_i)$ and inverse slope $T_B(y_i)$ is given by:

$$\left.\frac{dN}{dy}\right|_{y_i} = C(y_i)\left[(m_0c^2)^2 T_B(y_i) + 2m_0c^2T_B^2(y_i) + 2T_B^3(y_i)\right]. \tag{5.3}$$

In a next step, the resulting rapidity density distribution has to be extrapolated to rapidity regions not covered by the HADES detector. The differential rapidity distribution can be described with

a Gaussian function around mid-rapidity, whereas the width σ_y for a pure thermal source can be approximated given by:

$$\sigma_y \approx \sqrt{\frac{T_{eff}}{m_0 c^2}}. \tag{5.4}$$

The particle yield in full phase space is derived by integration of the data points and the Gaussian function in those regions of rapidity not covered by HADES.

In the following sections, the previously explained method is used to estimate the multiplicity and effective temperatures of the different particle species. In addition the following systematic error sources, which influence the estimation of multiplicities and inverse slope parameters are evaluated:

- **Particle identification: cuts on track quality variables and the correlation between β, momentum and specific energy loss**
  To estimate the systematic error, the particle identification cuts are varied individually for each particle in the corresponding section of this chapter.

- **Difference between the sectors of the spectrometer**
  The particles are reconstructed inside five different sectors of the spectrometer, whereas one sector (sector 2) had to be removed from the analysis due to instabilities in the high voltage (see section 3.2). The analysis of protons and π^- is performed separately for each sector and compared to the average of the five analyzed sectors. Differences between the results after correcting for the corresponding efficiency of the different sectors are systematic uncertainties. An average systematic error based on proton and π^- analysis is assumed for the more rarely produced particles.

5.1 Protons

On the left side of figure 5.1 the efficiency and acceptance corrected transverse mass spectra for the different rapidity slices, scaled by $1/m_t^2$, for protons are shown together with the parameterization from equation 5.1 fitted to the spectra. The ratio between the fits and the spectra is displayed on the right side of the figure. If the fit would be able to describe the measured spectrum, the ratio would be around one, respectively around the value of the scaling factor for each rapidity slice used to get a better visibility in the figure. A more detailed comparison of the spectra and the corresponding fit is shown in figure 5.5 for the spectrum around mid-rapidity. The spectrum deviates from the parameterization at low and high m_t. The trend is similar for all rapidity regions. The deviation can be explained by the assumption, that the protons are emitted from an expanding thermal source with a constant radial velocity β_r, as we will see later on. The corresponding inverse slope parameters from the Boltzmann fit to the transverse mass spectra are displayed in figure 5.2. The inverse slope parameters can not be described by a $\cosh y_{cm}$ distribution, which is expected for an expanding thermal source. Therefore, the effective temperature is extracted directly from the data, taking the inverse slope at mid-rapidity of T_{eff}^{data} = (130.7 $\pm$ 2.0$|_{PID}$ $\pm$ 1.9$|_{sec}$) MeV. The stated systematic uncertainties will be explained in section 5.1.1.

An Ansatz to describe transverse mass spectra emitted from a thermal source which is expanding radially are, as explained in section 1.1.2, Siemens-Rasmussen functions of the following form [41]:

$$\frac{dN}{2\pi m_t dm_t dy} = C \cdot E \cdot \exp\left(-\frac{\gamma \cdot E}{T}\right) \cdot \frac{\sinh\alpha}{\alpha} - \frac{T}{E} \cdot \cosh\alpha, \tag{5.5}$$

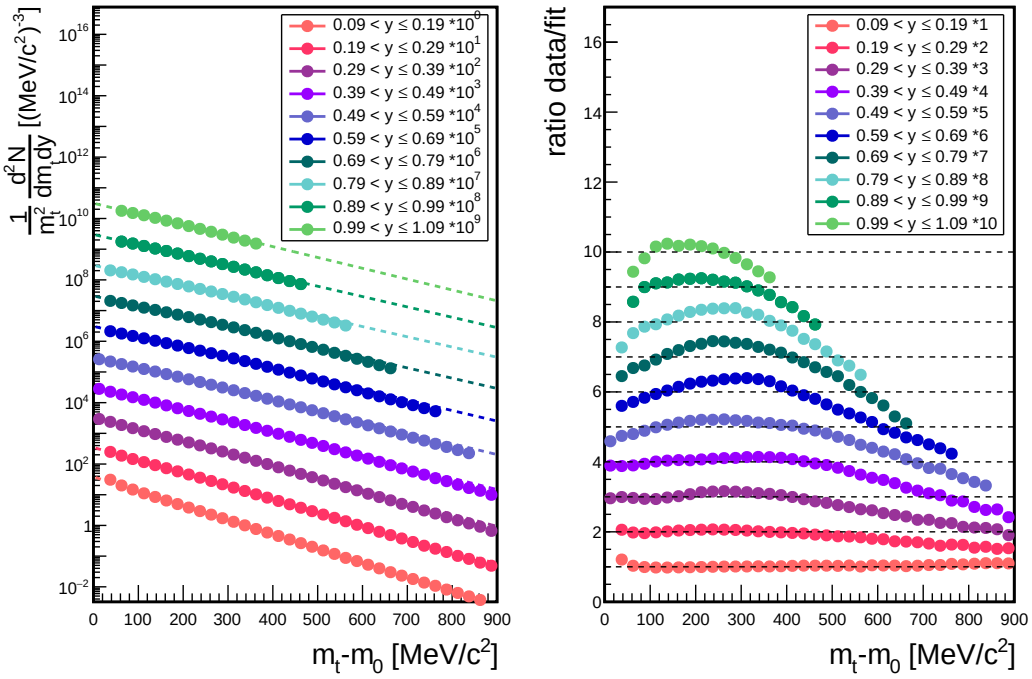

Figure 5.1: Left: Efficiency and acceptance corrected transverse mass spectra of protons scaled by transverse mass squared ($1/m_t^2$) for all measured rapidity regions. The different spectra are scaled by different powers of ten for a better visibility (see legend). Lines correspond to a Boltzmann fit according to equation 5.1, from which the inverse slope parameters are extracted. Right: Ratio of the measured transverse mass spectra and the Boltzmann fit, scaled for a better visibility.

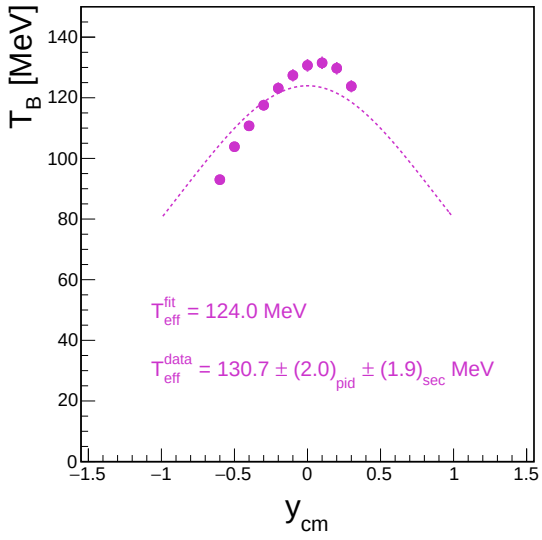

Figure 5.2: Distribution of the inverse slope parameters of the transverse mass spectra obtained with parameterization 5.1. The $\cosh y_{cm}$ parameterization (dashed line) is not reproducing the measured data, therefore the effective temperature T_{eff}^{data} is extracted directly from the data and equates the inverse slope at mid-rapidity.

with the center-of-mass energy E, center-of-mass momentum p, $\alpha = (\gamma\beta_r p)$ and $\gamma = \frac{1}{\sqrt{1-\beta_r^2}}$. T corresponds to the kinetic freeze-out temperature and β_r to the radial flow velocity of the system. T and β_r are next to constant C the free parameters of the function, but as they are strongly correlated, the determination of the parameters which give the best description of the transverse mass spectra is done systematically. In order to avoid that the fit of the transverse mass spectra based on equation 5.5 finds a local minimum instead of the global one, a χ^2-mapping in the T-β_r-plane is performed. The method was developed for the analysis of the light fragments deuterons and tritons in Ar+KCl reactions in [118]. The parameters T and β_r are systematically varied in small steps within their physical range[1] and the χ^2-value of the corresponding fit is calculated. The fit is performed in the different rapidity intervals, whereas the parameters should not depend on the rapidity. The resulting χ^2-distributions are added and divided by the total number of degrees of freedom. This method equates to a simultaneous two-dimensional fit of the particle spectra, but is much more stable in practice. Figure 5.3 displays the resulting χ^2-distribution in the T-β_r-plane. The global minimum corresponds to the combination of parameters T = (70 $\pm$ 4) MeV and β_r = 0.41 $\pm$ 0.01. The error on the temperature is derived by projecting the inverse of the two-dimensional reduced χ^2-distribution on the temperature axis for the value β_r = 0.41. The distribution can be roughly described by a Gaussian distribution and the obtained width is used as the error, neglecting the systematic correlation of the two parameters. The error on β_r is obtained using the same method but projecting on the β_r-axis for the temperature T = 70 MeV. The corresponding projections are shown in figure 5.4. When comparing the parameterization according to equation 5.5 with the simple Boltzmann parameterization 5.1 shown in figure 5.5, one can clearly see, that the assumption of a radially expanding source instead of a static source seems to be a more realistic scenario. Again this holds for all rapidities, as can be seen in figure 5.6. The shape of the transverse mass spectra is better reproduced by this parameterization than by the simple Boltzmann fit, note that in case of the Siemens-Rasmussen approach T and β_r are global parameters and therefore the same for all rapidity regions. To estimate the differential rapidity distribution, the different transverse mass spectra are parametrized by equation 5.5 with fixed parameters T and β_r according to the values obtained by the simultaneous fit and used to extrapolate to unmeasured phase space regions. The resulting rapidity density distribution is displayed in figure 5.7. The error band correspond to 5% systematic uncertainty and will be discussed in the following section 5.1.1. The distribution is symmetric around mid-rapidity within errors and can therefore be reflected. The number of protons which are emitted into the rapidity window covered by HADES is deduced to 39 per event. The shape of the rapidity distribution is changing strongly with the centrality of the collision, due to the reason that a huge contribution of protons is not in thermal equilibrium with the system, as will be discussed in section 5.1.2. It has been investigated that it takes typically three interactions for particles to assume thermalization [1]. A lot of the measured protons are coming simply from fragmentation of the target and projectile nucleons and hence, in the corona of the collision there are always protons which have only interacted one or two times with the medium. The polar angle coverage of the HADES detector is not large enough to fully accept the contribution from fragmentation, as these particles are emitted in the low transverse mass region at beam and target rapidity and hence constrain this contribution by extrapolation of its shape to mid-rapidity. Therefore, it is not trivial to extrapolate the measured spectrum to rapidity regions outside the HADES acceptance to obtain the total proton yield in case of the large geometrical centrality class covering the 0 - 40% most central collisions. The measured yield at mid-rapidity per unit in rapidity is deduced to 41.5 $\pm$ 2.1.

[1] $20 \leq T \leq 100$ MeV in ΔT = 2 MeV and $0 \leq \beta_r \leq 0.55$ in $\Delta\beta_r$ = 0.01.

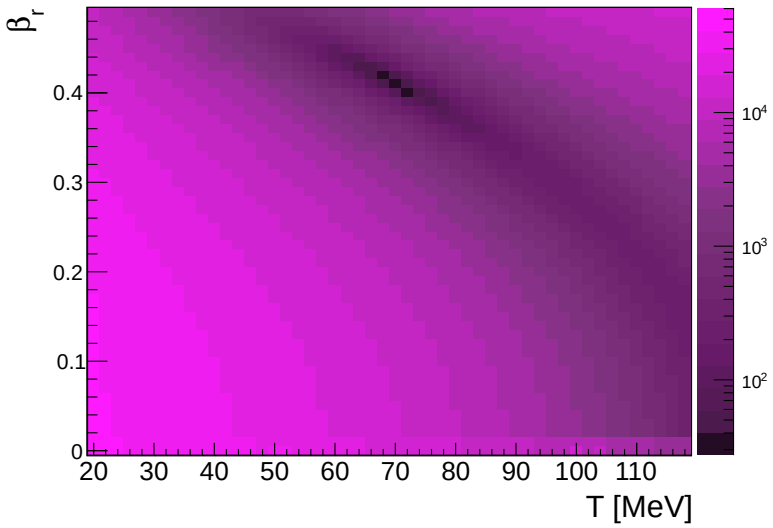

Figure 5.3: Result from the χ^2-mapping in the T-β_r-plane for description of the transverse mass spectra of protons with the Siemens-Rasmussen function in the rapidity regions between 0.19 - 0.89.

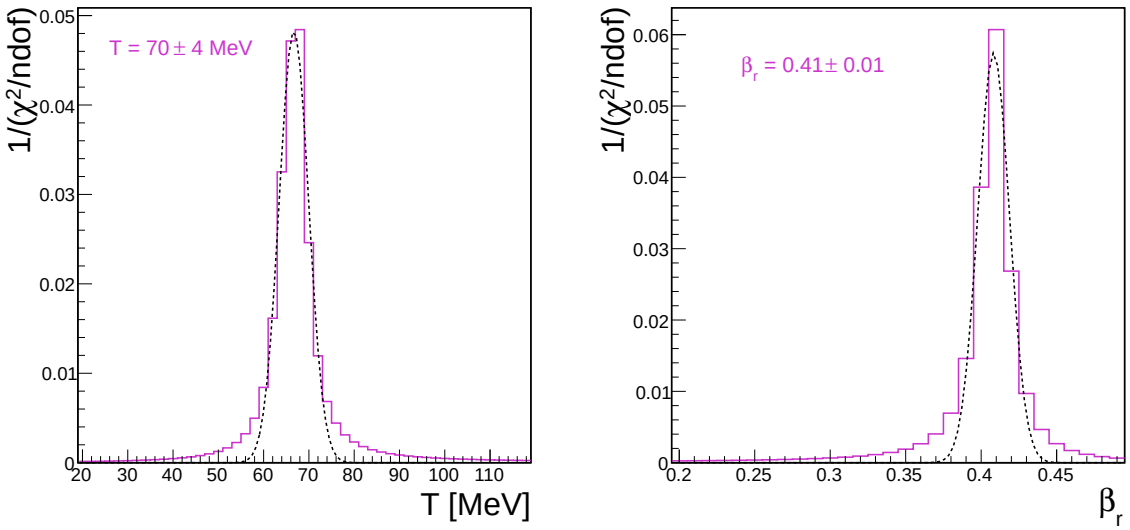

Figure 5.4: Inverse of the projection of the reduced χ^2-distribution on the temperature axis for β_r = 0.41 (left) and on the β_r-axis for T = 70 MeV (right) used for estimation of the errors of the obtained parameters.

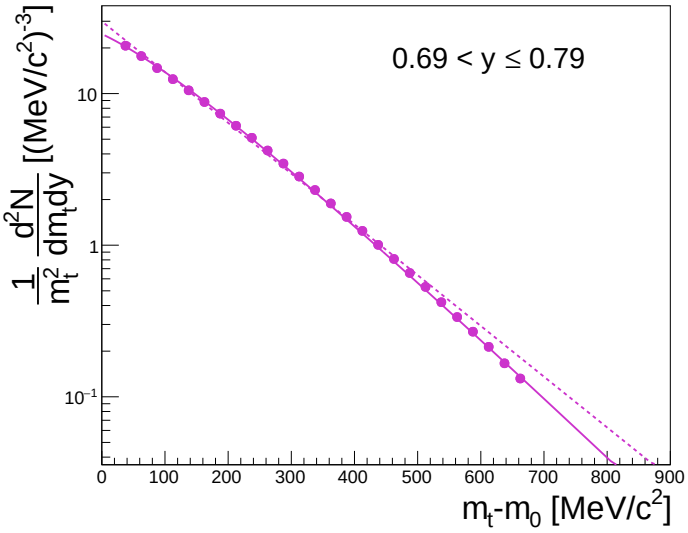

Figure 5.5: Efficiency and acceptance corrected transverse mass spectra of protons in the Boltzmann-representation at mid-rapidity. The solid line corresponds to the parameterization 5.5 with fixed parameters T = 70 MeV and β_r = 0.41, to extrapolate to unmeasured transverse mass regions. The dashed line corresponds to a Boltzmann fit according to equation 5.1, from which the effective temperature can be extracted.

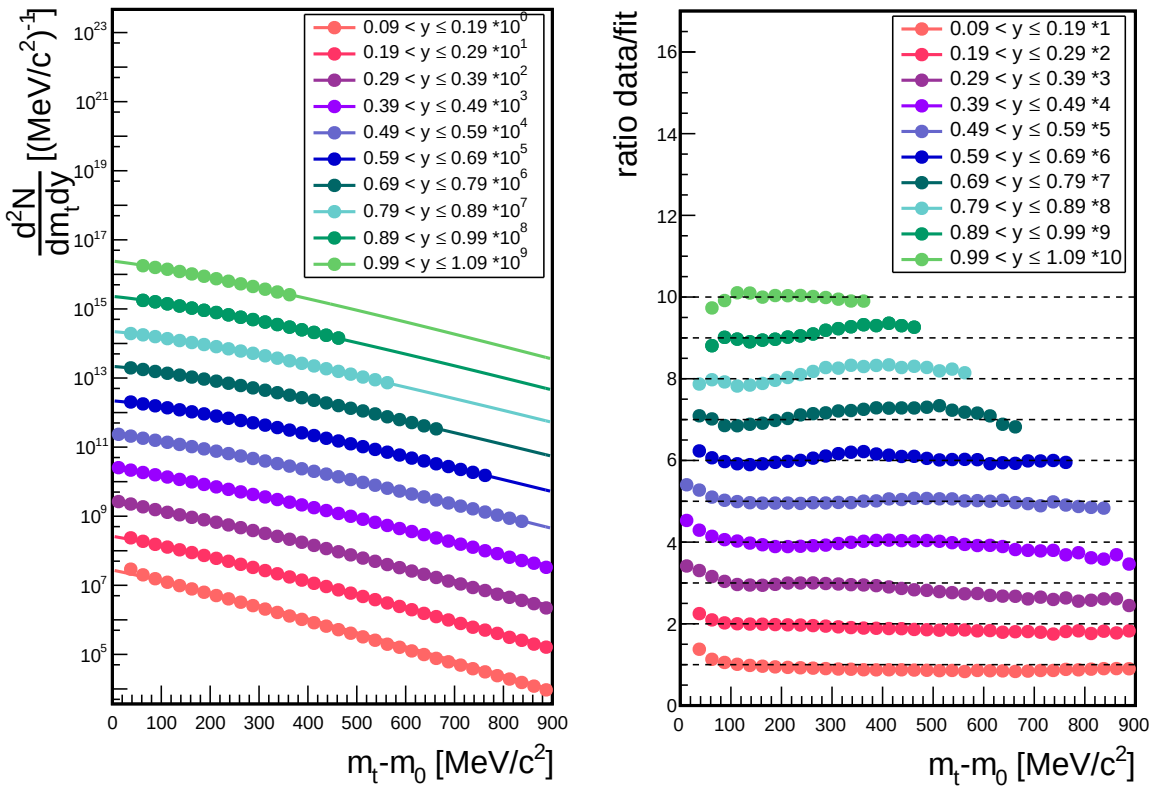

Figure 5.6: Left: Efficiency and acceptance corrected transverse mass spectra of protons. The different spectra are scaled by different powers of ten for better visibility (see legend). Lines correspond to parameterization 5.5 with fixed parameters T = 70 MeV and β_r = 0.41, used to extrapolate to unmeasured transverse mass regions to obtain the rapidity density distribution. Right: Ratio of the spectra and the Siemens-Rasmussen parameterizations. The ratios are scaled to get a better visibility.

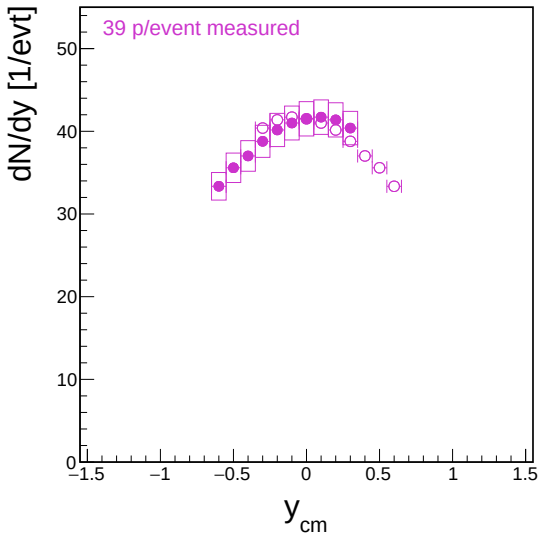

Figure 5.7: Measured (solid) and reflected (open symbols) rapidity density distribution of protons normalized to the number of analyzed events. The error band corresponds to 5% systematic uncertainty (see section 5.1.1).

5.1.1 Systematic error evaluation

Whereas the statistical error of the proton distributions is due to their high abundance and the collected statistics negligible, all possible systematic biases on the extracted count rate and effective temperature have to be evaluated.

- **Particle identification**
  In the presented analysis a 2σ-selection, around the expected value of protons in the correlation between β and momentum is applied to select a high purity proton sample. Any removal of true protons or impurities due to this cut should be accounted for by the efficiency correction. In order to investigate if there are some residual differences between data and simulation, the analysis is repeated with a broader selection of 2.5σ and with an additional selection making use of the energy loss information in the drift chambers. All cuts have been introduced in section 4.1.1. The resulting efficiency and acceptance corrected m_t-y-distributions, projected on the rapidity axis are displayed on left side of figure 5.8. The difference after correction between the cut values of 2σ and 2.5σ is well below 1% and can therefore be neglected. The residual difference of the proton yield obtained with the alternative PID method including the energy loss information of the drift chambers in addition is around 2%.

- **Sector dependence**
  In the analysis the results from all sectors (except sector 2) are combined. To see, if there are significant differences between the different sectors, the analysis is repeated for each sector separately. On the right side of figure 5.8, the resulting efficiency and acceptance corrected projections of the m_t-y-distribution for the different sectors and the average over all sectors can be seen. The deviation between the different sectors is observed to be at the order of 3 - 4%.

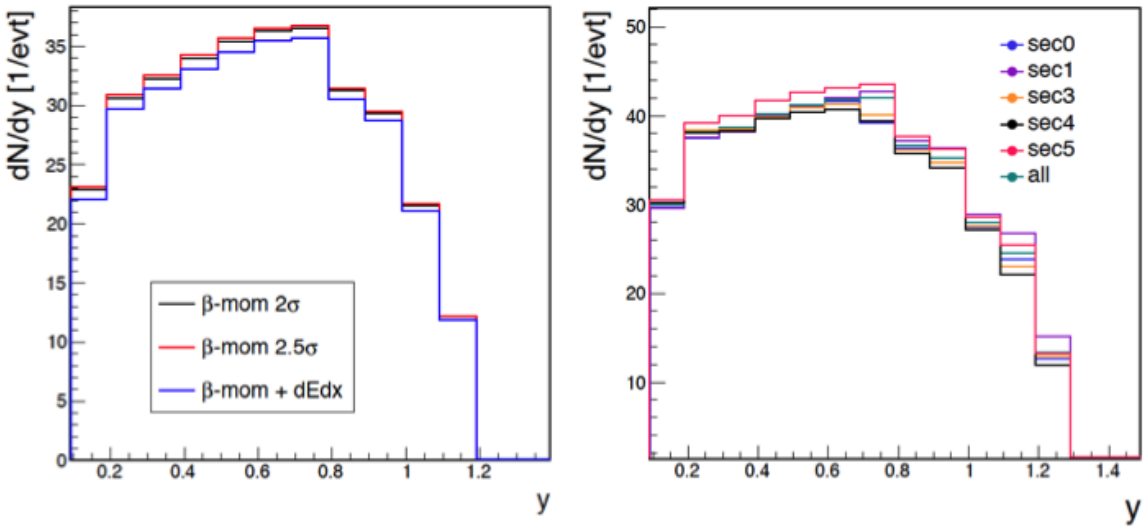

Figure 5.8: Left: Projection of the efficiency and acceptance corrected m_t-y-distribution of protons for various particle identification methods to estimate the systematic error of the identification method with a 2σ-selection on the correlation between β and momentum used in the analysis (black). The red line corresponds to a selection with a 2.5σ-selection and blue line to a more selective identification method, including the measured specific energy loss in the drift chambers. Right: Projection of the efficiency and acceptance corrected m_t-y-distribution of protons for the different sectors independently and the average over all sectors except sector 2 as used in the analysis (see legend) to estimate any systematic uncertainty introduced.

- **Extrapolation to unmeasured transverse mass regions**
  The estimation of the differential count rate is done using equation 5.5 with fixed global parameters T = (70 $\pm$ 4) MeV and β_r = 0.41 $\pm$ 0.01 to extrapolate to unmeasured transverse mass regions. To estimate the possible systematic effects introduced by this extrapolation, these global parameters are varied inside the estimated corresponding errors. This means, that the transverse mass spectra are parametrized with the variations summarized in table 5.1. Figure 5.9 shows the efficiency and acceptance corrected transverse mass spectrum at mid-rapidity with the resulting parameterizations for the variation of the temperature (left) and the variation of the radial flow velocity (right). It is obvious to see that the variation of the temperature is mainly changing the tails of the contribution at high transverse mass, which is affecting the obtained overall yield only weakly. On the contrary, the variation of β_r is changing the shape of the spectrum quite strongly, which influences the rapidity distribution. However, as the maximum of the proton yield, which is located at normalized transverse masses around 100 MeV/c^2 is measured and the extrapolation is contributing only to a small extend to the final yield, the systematic bias introduced by the extrapolation method is estimated to be 1%.

T = 70 MeV	β_r = 0.40 β_r = 0.42	β_r = 0.41	T = 66 MeV T = 74 MeV

Table 5.1: Combinations of the parameters from the Siemens-Rasmussen parameterization, inside the obtained errors, for systematic error evaluation on the extrapolation to unmeasured transverse mass regions for protons.

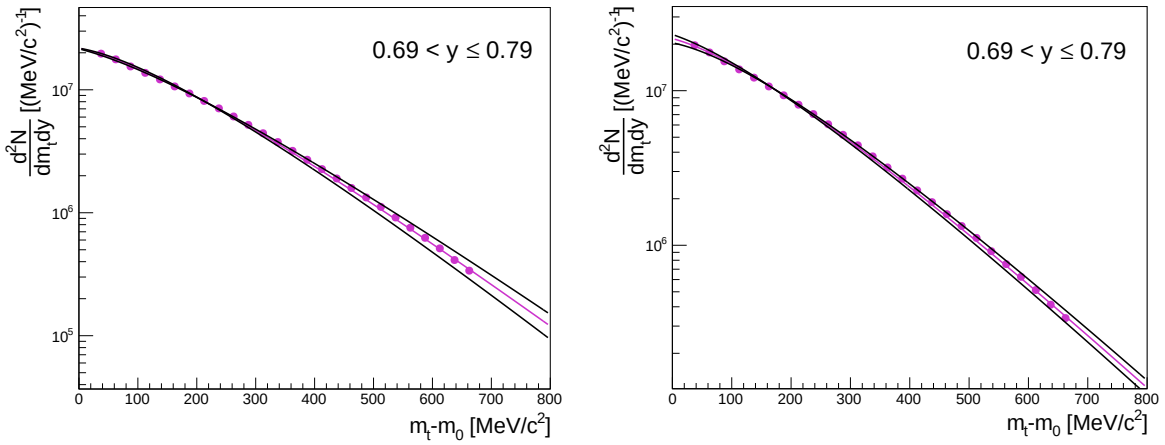

Figure 5.9: Efficiency and acceptance corrected transverse mass spectrum at mid-rapidity parameterized with Siemens-Rasmussen functions with varied global parameters T and β_r to evaluate the systematic error on the differential count rate due to extrapolation to unmeasured transverse mass regions. The magenta line corresponds to the parameter combination T = 70 MeV and β_r = 0.41. Left: Black lines correspond to the variation of the temperature T = 66 MeV and T = 74 MeV with fixed β_r. Right: Black lines correspond to the variation of the radial flow velocity β_r = 0.40 and β_r = 0.42.

- **Efficiency and acceptance correction**
  In section 4.3.1.1 the systematic uncertainty from the efficiency and acceptance correction has been estimated to be 1%.

The systematic error on the obtained yield of protons is in the order of 5% when summing up quadratically the systematic bias of the particle identification (PID), the difference of the sectors (sec), the extrapolation to unmeasured transverse mass regions (extr) and the efficiency correction (eff) according to:

$$err_{sys} = \sqrt{(2\%|_{PID})^2 + (4\%|_{sec})^2 + (1\%|_{extr})^2 + (1\%|_{eff})^2} \approx 5\%. \tag{5.6}$$

5.1.2 Centrality dependent analysis

To get more information about the contribution of protons from fragmentation of the target and projectile nucleons and the contribution from protons thermalized in the reaction zone, the analysis is repeated for the four different centrality classes introduced in section 3.4. The χ^2-mapping in the T-β_r-plane is performed for the different centrality classes independently and the obtained parameters temperature and the radial flow velocity are summarized in tabular 5.2. Whereas the temperature is relatively constant and only slightly increasing for more central collisions, the increase is stronger for the radial flow velocity. The increase of the radial flow velocity towards more central collisions can be seen on the left side of figure 5.10 in the stronger deformation of the transverse mass spectra at mid-rapidity. The Siemens-Rasmussen parameterization with the obtained parameters is again used to extrapolate the transverse mass spectra to unmeasured phase space regions and the rapidity density distribution is obtained. The latter is displayed on the right side of figure 5.10 for the different centrality classes. It can be seen how the contribution from the target and projectile nucleon fragmentation is increasing for more peripheral collisions, which enhances the yield at beam and target rapidity regions. For most central collisions the distribution narrows. The extraction of a centrality dependent

mult	T [MeV]	β_r
0% - 40%	70 ± 4	0.41 ± 0.01
0% - 10%	70 ± 4	0.45 ± 0.01
10% - 20%	70 ± 4	0.41 ± 0.01
20% - 30%	68 ± 5	0.37 ± 0.02
30% - 40%	68 ± 5	0.34 ± 0.03
0% -20%	70 ± 4	0.43 ± 0.01
20% - 40%	68 ± 5	0.36 ± 0.02

Table 5.2: Centrality dependence of the global parameters T and β_r for the description of the transverse mass spectra of protons with formula 5.5 obtained with a χ^2-mapping.

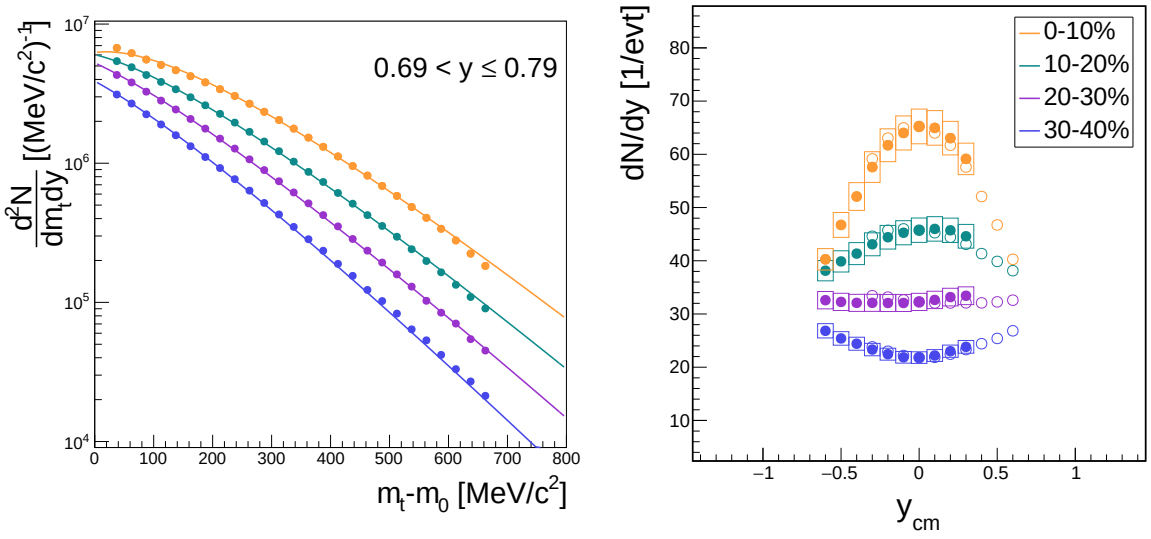

Figure 5.10: Left: Efficiency and acceptance corrected transverse mass spectra of protons around mid-rapidity for the different centrality classes together with the parameterization according to equation 5.5 (lines) with different parameters obtained from individual χ^2-mapping in the T-β_r plane (see table 5.2). Right: Measured (solid) and reflected around mid-rapidity (open symbols) rapidity density distribution of protons for different centrality classes (see legend) normalized to the number of analyzed events.

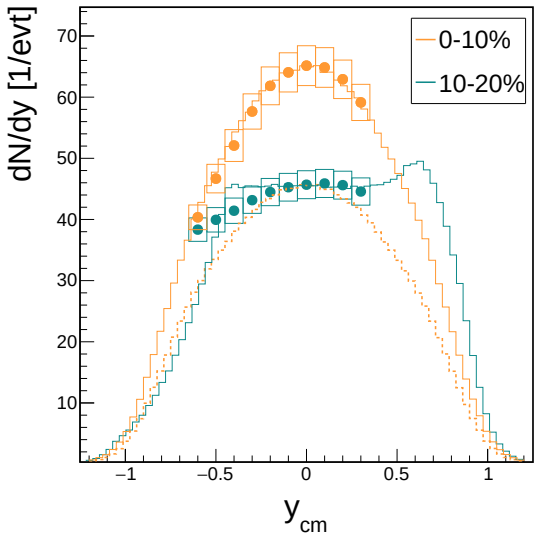

Figure 5.11: Rapidity density distribution of protons in the center-of-mass representation for 0 - 10% and 10 - 20% most central collisions (points) normalized to the number of analyzed events in comparison to UrQMD distributions (lines), normalized to match the experimental data at mid-rapidity. For the distribution of the 10 - 20% most central collisions, a lower momentum cut of 300 MeV/c is applied to investigate possible acceptance effects on the measurement of the spectator contribution. Whereas the distribution of the most central collisions looks very close to a thermal one, already for the next centrality class a huge contribution from spectator protons is entering the rapidity region according to the model. To estimate the yield of protons in thermal equilibrium to compare to SHM model fits (see section 6.4), the distribution from the most central collisions is scaled to match the data from 10 - 20% most central collisions and is integrated (orange dashed line).

production yield is not carried out here, as the extrapolation to unmeasured rapidity regions is not trivial.

In section 6.4 the measured particle yields from the 0 - 20% most central collisions will be compared to a statistical hadronization model (SHM) fit. In order to extract the corresponding proton yield, the UrQMD model is used to extrapolate to unmeasured rapidity regions. The SHM is used to describe particle production from a homogenous source, therefore only the contribution from thermalized protons and not those from the spectator matter should be taken into account by the fit. This is realized by the following procedure. The rapidity distribution for the most central events looks very much like a thermal proton spectrum without a big spectator contribution and its shape is well described by UrQMD, shown in figure 5.11. The extracted yield is obtained to 87 protons per event. For the 10 - 20 % most central collisions already a visible spectator contribution is entering the distribution, leading to a broadening. In order to investigate the effect of the acceptance on the spectator distribution, a lower momentum cut of 300 MeV/c is applied to the UrQMD distribution for 10 - 20% most central collisions. Note that this cut is reducing the contribution from the spectators located around target rapidity but is not affecting the one with beam rapidity. In order to extract only the yield from protons in thermal equilibrium, the UrQMD distribution from the 0 - 10% most central collisions is scaled down to match the semi-central spectrum at mid-rapidity and used to obtain the proton yield of 61 protons per event for the 10 - 20% most central collisions.

5.2 π^-

On the left side of figure 5.12 the efficiency and acceptance corrected transverse mass spectra of π^- scaled by $1/m_t^2$ for all measured rapidity regions are displayed. The spectra can not be described by a single Boltzmann-like function over the complete transverse mass range, as they are developing a second slope for higher transverse masses. This is usually interpreted in literature that most of the pions are produced at these low energies via the decay of Δ resonances, mostly Δ_{1232} (see for example [85]). The available phase space of these decay pions is constrained by the Q-value and kinematics of the resonance decay and they are therefore mostly populating the low transverse mass region. This leads to a steep spectrum, resulting in a relatively low inverse slope parameter. The higher transverse mass regions show a moderately steep shape, comparable to the one of kaons. This contribution has been interpreted as coming directly from thermally produced pions from the fireball and can be used to extract the effective temperature of the pions. In order to describe the transverse mass spectra and extrapolate to unmeasured phase space regions, Boltzmann functions with two slopes of the following form are used:

$$\frac{1}{m_t^2}\frac{d^2N}{dm_t dy} = C_1(y)\exp\frac{-(m_t-m_0)c^2}{T_{B,1}(y)} + C_2(y)\exp\frac{-(m_t-m_0)c^2}{T_{B,2}(y)}. \tag{5.7}$$

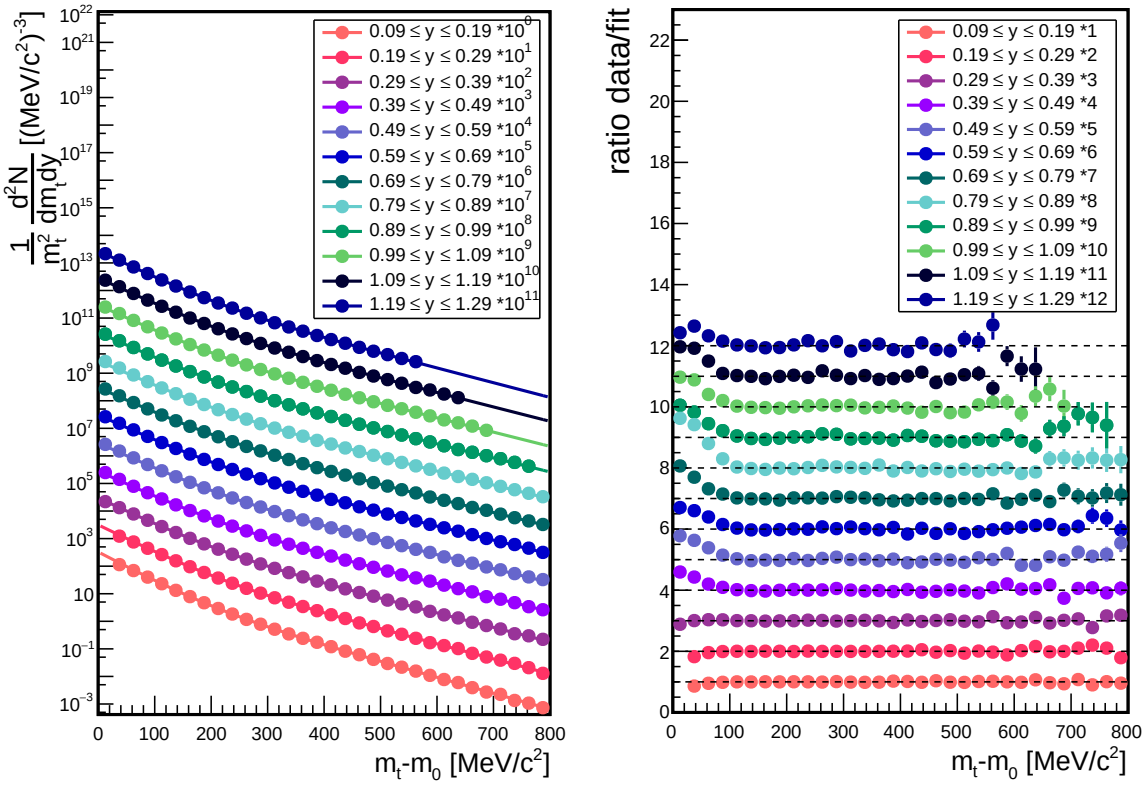

Figure 5.12: Left: Efficiency and acceptance corrected transverse mass spectra of π^- scaled by $1/m_t^2$ for all measured rapidity regions. The spectra are scaled by different powers of ten for a better visibility (see legend). Lines correspond to a two slope Boltzmann fit according to equation 5.7, to extrapolate to unmeasured transverse mass regions and from which the inverse slope parameters are extracted. Right: Ratio of the spectra and the fit. The ratios are scaled for a better visibility.

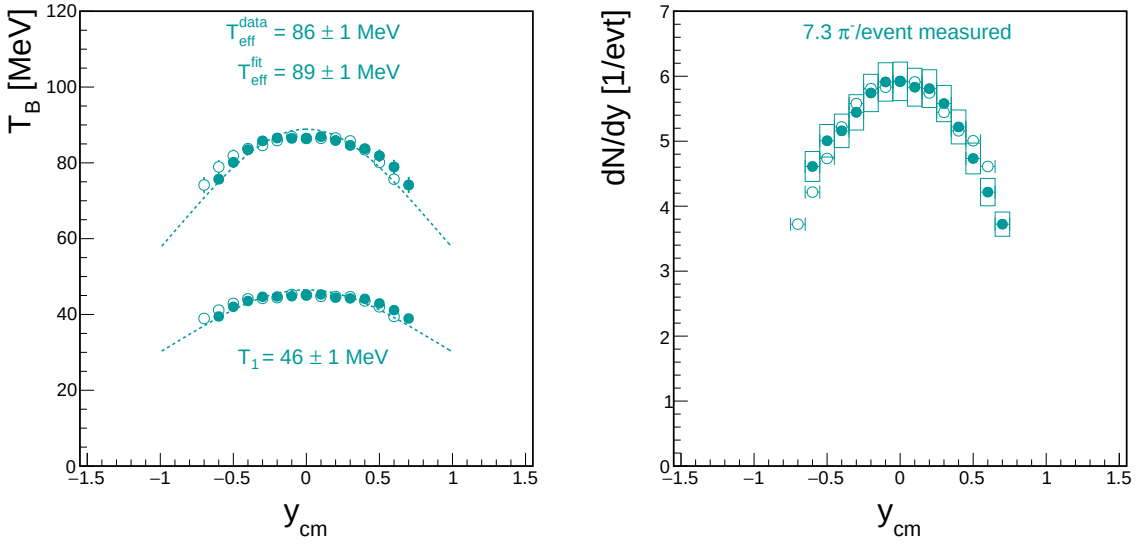

Figure 5.13: Left: Measured (solid) and reflected (open symbols) distributions of the inverse slope parameters $T_{B,1}$ and $T_{B,2}$ of π^- obtained with parameterization 5.7. Both distributions can be described with a $\cosh y_{cm}$ parameterization (dashed lines), which is used to extract the effective temperature T_{eff}. Right: Measured (solid) and reflected (open symbols) rapidity density distribution of π^- normalized to the number of events. The error bars correspond to 5% systematic uncertainty (see section 5.2.1).

Of course, this is a very simplified scenario, which is not taking the contribution from higher mass resonances and any rescattering and absorption processes of the pions inside the medium into account. However, as can be seen on the right side of figure 5.12 the simple parameterization 5.7 is reproducing the shape of the spectra[2], as the ratio between the data and the fit is ≈ 1, respectively the value according to the used scaling factor used to get a better visibility, and can be used to extrapolate to unmeasured transverse mass regions and extract the inverse slope parameters. The distributions of the two inverse slope parameters $T_{B,1}$ and $T_{B,2}$ are shown on the left side of figure 5.13 together with the corresponding $\cosh y$ parameterization. The shape of both spectra can be reproduced by the parameterization, which is therefore used to extract the effective temperature T_{eff}^{fit} = (89 $\pm$ 1) MeV. The analytic integration of equation 5.7 is given by:

$$\begin{aligned}\left.\frac{dN}{dy}\right|_{y_i} &= C_1(y_i)\left[(m_0c^2)^2 T_{B,1}(y_i) + 2m_0c^2 T_{B,1}^2(y_i) + 2T_{B,1}^3(y_i)\right] \\ &+ C_2(y_i)\left[(m_0c^2)^2 T_{B,2}(y_i) + 2m_0c^2 T_{B,2}^2(y_i) + 2T_{B,2}^3(y_i)\right].\end{aligned} \tag{5.8}$$

After integration of the measured transverse mass spectra and using the fit to extrapolate to unmeasured phase space regions, the rapidity density distributions are obtained and displayed on the right side of figure 5.13. The error band corresponds to 5% systematic uncertainty and will be discussed in the following section 5.2.1. In total 7.3 π^- per event have been reconstructed inside the rapidity region covered by the spectrometer.

[2]The slight deviation in the lowest transverse mass region is not playing a role, as this region is covered by the acceptance of the spectrometer.

5.2.1 Systematic error evaluation

Due to the high statistics of the collected data sample and the high abundance of pions, the statistical error on the pion multiplicity is negligible. To estimate the systematic error on the effective temperature and the yield, the particle identification cuts and the extrapolation to unmeasured phase space regions are varied and the analysis is repeated for the different sectors of the spectrometer independently in a similar way as for the protons before.

- **Particle identification**
  As explained in section 4.1.1, the particle identification is performed by applying a 2σ wide cut around the expected π^- distribution in the correlation between β and momentum. In order to investigate a possible systematic bias introduced by this cut, the identification is varied using a cut of 2.5σ and require in addition the energy loss information in the drift chambers. On the left side of figure 5.14 the projections of the efficiency and acceptance corrected m_t-y distributions on the rapidity axis for the different particle identification criteria are shown. After correction all lines should lie on top of each other and the possible differences can be interpreted as systematic error of the particle identification. The deviation after correction between the cut values of 2.5σ and 2σ is less than 1%, therefore the estimated systematic error on the count rate is taken from the deviation to the alternative PID method, including the energy loss information, which is observed to be 1.5%.

- **Sector dependence**
  The projection of the corrected m_t-y-distribution on the rapidity axis from the analysis within the different sectors of the spectrometer separately is shown on the right side of figure 5.14. Sectors 0, 1, 4 and 5 are within 2% identical, but sector 3 shows a systematic deviation up to 4%.

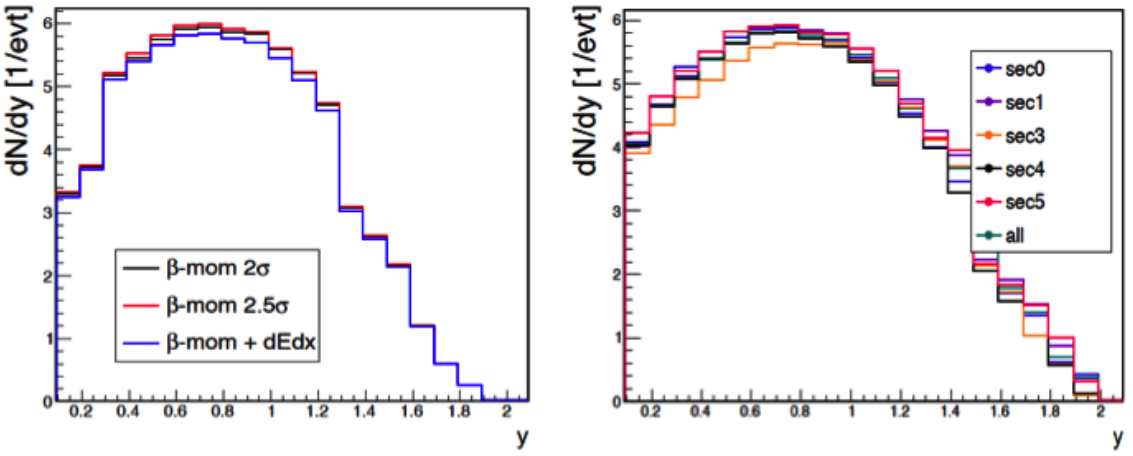

Figure 5.14: Left: Projection of the efficiency and acceptance corrected m_t-y-distribution of π^- for various particle identification methods to estimate the systematic error of the identification with a 2σ-selection around the expected distribution in the correlation between β and momentum used in the presented analysis (black). The red line correspond to a wider selection of 2.5σ and the blue line to a selection including the measured specific energy loss in the drift chambers. Right: Projection of the efficiency and acceptance corrected m_t-y-distribution of π^- for the different sectors separately and the average over all sectors (except sector 2) as used in the analysis (see legend) to estimate any systematic uncertainty introduced.

- **Extrapolation to unmeasured transverse mass regions**
  For easy comparison between the different hadrons, the particles are analyzed in the Boltzmann-representation of reduced transverse mass $m_t - m_0$, scaled with $1/m_t^2$. In order to evaluate the systematic bias introduced by the extrapolation to unmeasured transverse mass regions with parameterization 5.7, the analysis of pions is repeated in the transverse momentum representation. The transverse momentum p_t is directly related to the transverse mass via:

$$p_t^2 = m_t^2 + m_0^2. \tag{5.9}$$

  On the left side of figure 5.15 the efficiency and acceptance corrected transverse momentum spectrum at mid-rapidity is displayed. In this representation, it can be seen that the maximum of the produced pions is reconstructed in HADES, and only a small amount of yield has to be extrapolated. Again, a two slope Boltzmann function is used and the result on the differential count rate in comparison to the one obtained in the transverse mass representation is shown on the right side of figure 5.15. The difference of the two methods is 3%.

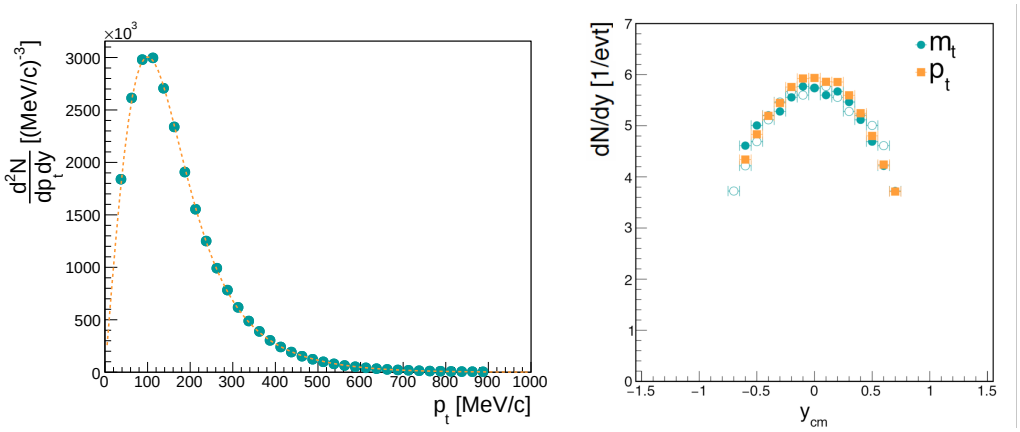

Figure 5.15: Left: Transverse momentum spectrum at mid-rapidity of π^-. The orange line correspond to a two-slope Boltzmann parameterization to extrapolate to unmeasured transverse momentum regions. Right: Measured (solid) and reflected (open symbols) rapidity density distribution of π^- obtained from extrapolating in transverse mass (green) in comparison to extrapolating in transverse momentum (orange), to evaluate the systematic error introduced by extrapolation.

- **Efficiency and acceptance correction**
  The systematic uncertainty from the efficiency correction has been obtained in section 4.3.1.1 to be 1%.

The systematic error on the differential count rate sums up quadratically to 5% when taking all error sources into account:

$$err_{sys} = \sqrt{(1.5\%|_{PID})^2 + (4\%|_{sec})^2 + (3\%|_{extrapol})^2 + (1\%|_{eff})^2} \approx 5\%. \tag{5.10}$$

The inverse slope of the corrected transverse mass spectra is independent of the particle identification method and less than 1% different for the analysis of the individual sectors. Therefore the systematic error on the extracted effective temperature is only given by the difference of the result from the used $\cosh y_{cm}$ fit T_{eff}^{fit} = 89 MeV to the measured inverse slope at mid-rapidity T_{eff}^{data} = 86 MeV of 3 MeV, which corresponds roughly to 3%.

5.2.2 Determination of the π^- production yield

Inside the rapidity regions covered by the HADES acceptance, a yield of 7.2 π^- per event is reconstructed. To determine the production yield in the full phase space, the measured rapidity distribution has to be extrapolated. The distribution peaks at mid-rapidity and is decreasing towards beam and target rapidity. The simplest approximation is therefore based on a Gaussian parameterization shown as black line in figure 5.16. The resulting distribution is relatively broad (σ_y = 0.8), which results that the extrapolation contributes about 35% to the measured yield to a total production yield of 11.5 π^- per event. The UrQMD transport model takes the different production, rescattering and absorption mechanisms of pions into account, leading to a more realistic phase space distribution than the simple thermal assumption. To be not fully model dependent in the analysis, the simulated rapidity spectrum is scaled to match the experimental data at mid-rapidity and is afterwards used only to extrapolate to unmeasured rapidity regions ending up to a π^- yield of 11.1 per event. The difference of the two extrapolation methods is 4%. A final production yield of 11.1 $\pm$ 0.6$|_{sys}$ $\pm$ 0.4$|_{extrapolation}$ π^- per event is obtained.

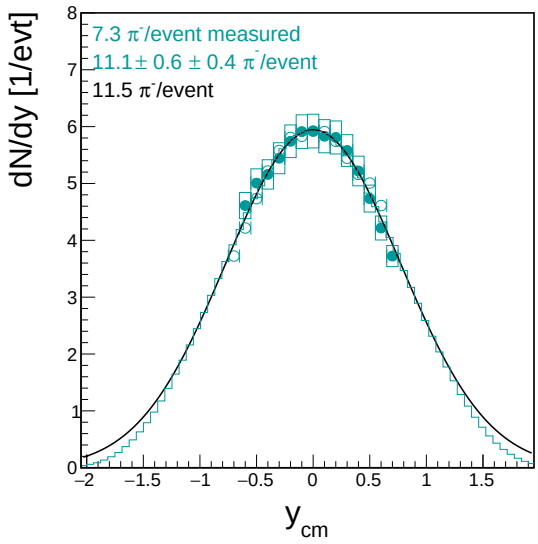

Figure 5.16: Measured (solid) and reflected around mid-rapidity (open symbols) rapidity density distribution of π^- normalized to the number of analyzed events. The green line corresponds to the distribution from UrQMD, scaled to match the data at mid-rapidity, used to extrapolate to unmeasured phase space regions to obtain the final π^- yield displayed in the plot (green). The uncertainty of the extrapolation to rapidity regions not covered by HADES is obtained using a single Gaussian parameterization (black line).

5.2.3 Centrality dependent analysis

In order to get more insight about the pion production mechanisms, the analysis is repeated for different collision centralities. As already introduced in section 3.4, the data sample is divided in four different centrality classes based on the number of hits in the META-detector. The efficiency and acceptance corrected transverse mass spectra can be described with parameterization 5.7 for all centrality bins. The corresponding distributions of the two inverse slope parameters for the different centralities are displayed in figure 5.17. Both slopes are increasing with centrality. All distributions are well described by a $\cosh y_{cm}$ parameterization, which is again used to extract the effective tem-

perature T_{eff}. On the left side of figure 5.19 the extracted effective temperature is displayed as a function of the corresponding mean number of participating nucleons $\langle A_{part} \rangle$ for the given centrality class. The effective temperature is rising with $\langle A_{part} \rangle$. To quantify the increase of the effective temperature with centrality, the data is parameterized with a linear function and a slope of m = 0.07 MeV is obtained. The Boltzmann function is used to extrapolate the efficiency and acceptance corrected transverse mass spectra to unmeasured regions, to obtain the rapidity density distributions displayed in figure 5.18. The distributions are normalized to the number of events from the corresponding centrality class. The number of produced pions is higher in case of central than of peripheral collisions. The numbers of produced pions per event, are obtained using the centrality dependent distributions from UrQMD, scaled to the measured yield at mid-rapidity, to extrapolate to rapidity regions not covered by HADES. The multiplicities are scaled with the corresponding $\langle A_{part} \rangle$ and displayed as function of $\langle A_{part} \rangle$ on the right side of figure 5.19. The multiplicity per $\langle A_{part} \rangle$ is constant within errors as a function of centrality.

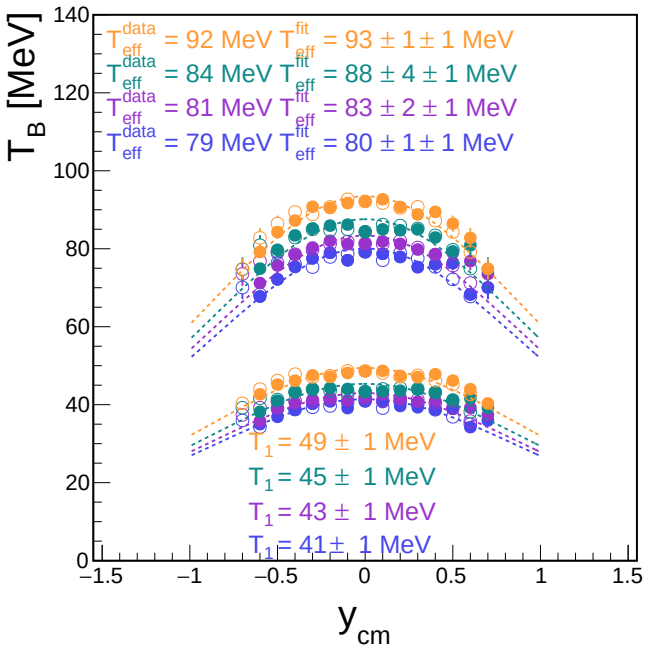

Figure 5.17: Measured (solid) and reflected (open symbols) distributions of the inverse slope parameters $T_{B,1}$ and $T_{B,2}$ of π^- for different centrality classes obtained with parameterization 5.7. All distributions can be described with a $\cosh y_{cm}$ parameterization, which is used to extract the effective temperatures T_{eff}^{fit}.

5.3 K^+

The efficiency and acceptance corrected transverse mass spectra of positively charged kaons are shown in the Boltzmann representation together with the parameterization according to formula 5.1 on the left side of figure 5.20. The shape of the spectra is reproduced by the parameterization, which can be seen on the right side of the figure, in which the ratio between the data and the fit is presented. The

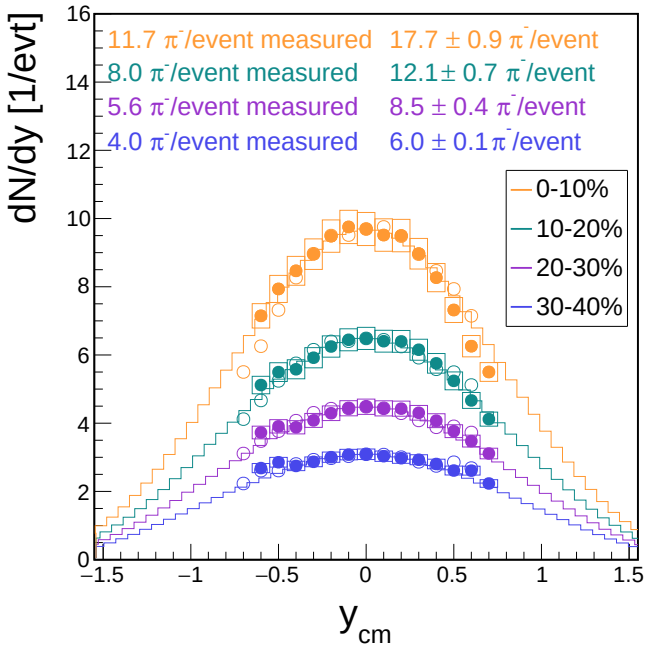

Figure 5.18: Measured (solid) and reflected around mid-rapidity (open symbols) rapidity density distribution of π^- for different centrality classes (see legend) normalized to the number of analyzed events. The lines correspond to the distributions from UrQMD, scaled to match the data at mid-rapidity, which are used to extrapolate to rapidity regions not covered by HADES to obtain the final π^- yield.

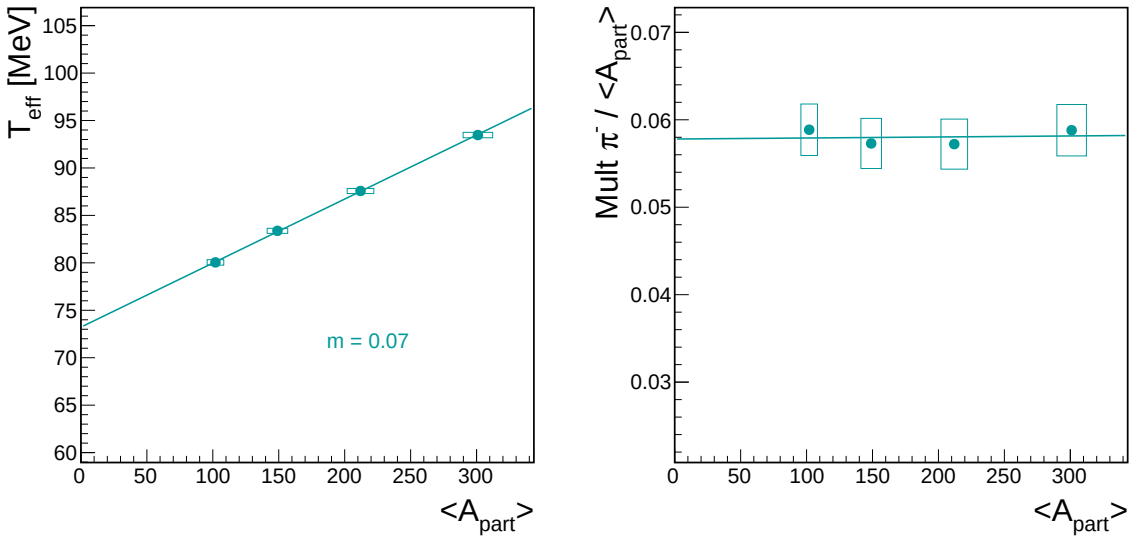

Figure 5.19: Centrality dependence of the effective temperature (left) and the multiplicity per $\langle A_{part} \rangle$ (right) of π^-. To quantify the increase of the effective temperature with centrality, the data is parameterized with a linear function (green line) and the slope m is obtained. The multiplicity is constant as function of centrality.

ratios are scaled for better visibility. The ratio is fluctuating around unity, respectively the values used for scaling.

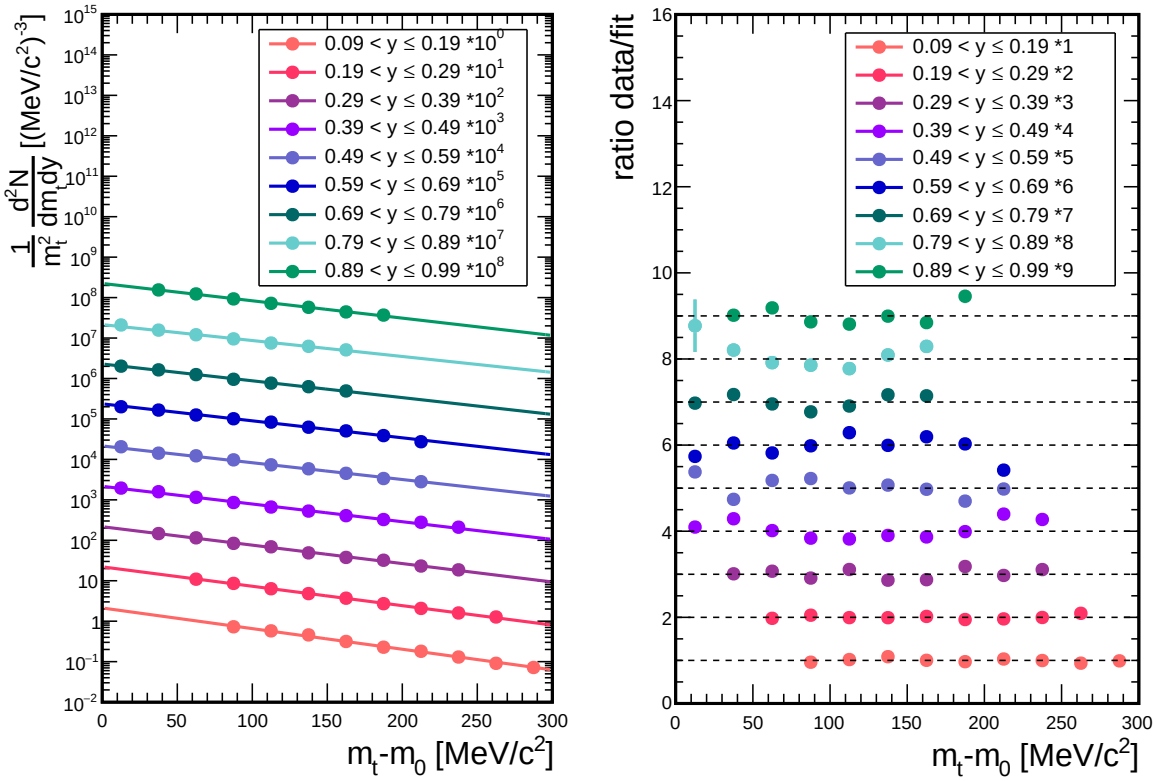

Figure 5.20: Left: Efficiency and acceptance corrected transverse mass spectra of K^+ for the different rapidity slices in the Boltzmann representation. The spectra are multiplied by different powers of ten for better visibility (see legend). Lines correspond to Boltzmann parameterizations according to equation 5.1 to determine the effective temperature and extrapolate to unmeasured transverse mass regions. Right: Ratio of the spectra and the fits, scaled for better visibility.

The corresponding inverse slope parameters follow a $\cosh y_{cm}$ distribution, which can be seen on the left side of figure 5.21. The effective temperature determined with the fit T_{eff}^{fit} is in agreement with the measured inverse slope at mid-rapidity and is determined to T_{eff} = (104 $\pm$ 1$|_{stat}$ $\pm$ 1$|_{sys}$) MeV. The estimation of the systematic error will be explained in section 5.3.1. After integrating the data and using the Boltzmann parameterization to extrapolate to unmeasured transverse mass regions, the rapidity density distribution is obtained, see right side of figure 5.21. The shown distribution is normalized to the number of analyzed events and scaled with the factor 1.03. The systematic error bands correspond to 5%. The estimation of the scaling factor and the systematic error will be explained in the following section 5.3.1. In total 1.94 x 10^{-2} K^+ per event are measured within the rapidity region covered by HADES, when mirroring the measured data points around mid-rapidity. A Gaussian parameterization is used to extrapolate to rapidity regions not covered by the spectrometer to extract the final K^+ production yield of (3.01 $\pm$ 0.03$|_{stat}$ $\pm$ 0.15$|_{sys}$ $\pm$ 0.30$|_{extrapolation}$)x10^{-2}. The error of the extrapolation is obtained by varying the parametrization, which will be explained in the next section 5.3.1.

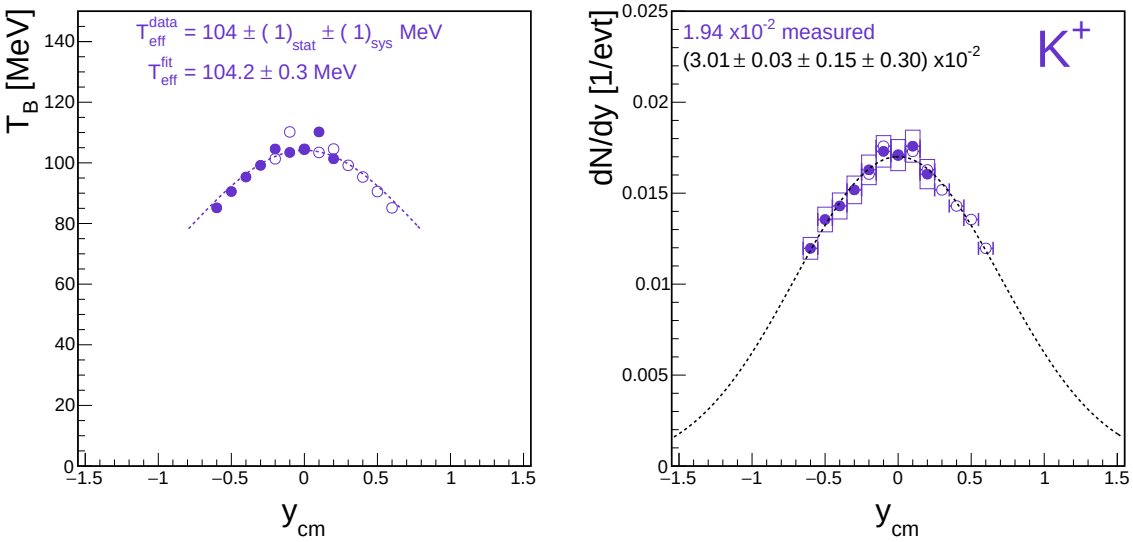

Figure 5.21: Left: Measured (full circles) and mirrored (open circles) inverse slope parameter distribution of K^+ as a function of rapidity. Dashed lines correspond to a $\cosh y_{cm}$ parameterization to extract the effective temperature T_{eff}^{fit}. Right: Measured (full circles) and mirrored (open circles) rapidity density distribution of K^+ normalized to the number of analyzed events. The shown distribution is scaled with the factor 1.03 and the systematic error bands correspond to 5% (see section 5.3.1). A Gaussian parameterization (dashed line) is used to extrapolate to rapidity regions not covered by HADES.

5.3.1 Systematic error evaluation

Systematic uncertainty on the obtained rapidity density distribution

For the kaon analysis it is crucial to apply stronger cuts than for the analysis of pions and protons on the track quality variables χ^2_{RK} and χ^2_{MM} and to make use of the specific energy loss of the kaons inside the drift chambers and the TOF-detector. A huge effort was made to tune the digitizers from the simulation such, that all distributions look as realistic as possible, to be able to correct for losses of real particles by applying those cuts to Monte-Carlo generated data. But as the distributions, especially of the χ^2_{RK}, are not perfectly reproduced by the simulation (compare sections 3.6.3 and 4.1.3), it is important to estimate any possible introduced systematic bias.

- **Cuts on the track quality parameters**
  The systematic effect of the cuts on the track quality parameters are obtained using pions and protons. Figure 5.22 shows the projection of the m_t-y-distributions of π^- (left) and protons (right), after reducing the allowed track quality parameters χ^2_{RK} from 400 to 100 and χ^2_{MM} from 3 to 2, which are used in the kaon analysis. The simulation is not perfectly correcting for the introduced losses of real particles. For protons the loss is in the order of 2.5% and for pions of almost 4% after applying both cuts. The effect is therefore energy loss dependent, as it is higher for the mostly minimum ionizing pions in comparison to protons. The energy loss

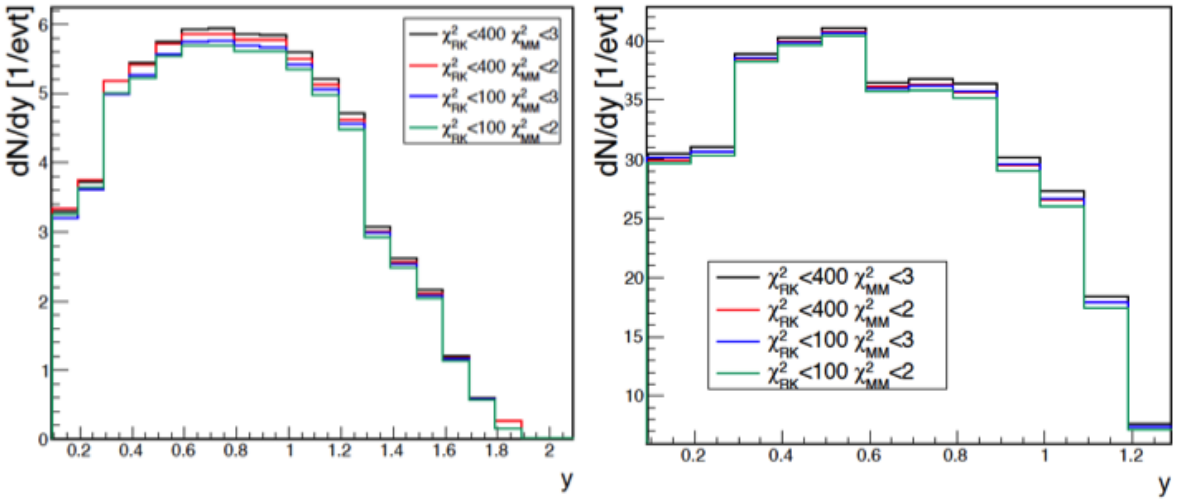

Figure 5.22: Projection of the efficiency and acceptance corrected m_t-y-distribution of π^- (left) and protons (right) after applying cuts on the track quality parameters χ^2_{RK} and χ^2_{META}, which are used for charged kaon analysis, to estimate the systematic bias introduced by this cut.

of kaons is in-between the one of pions and protons, which leads to an expected loss of kaons of approximately 3% after cutting on the track quality parameters, using simply the average between the values obtained for protons and π^-. As a result the obtained rapidity density distributions of kaons have to be scaled with a factor 1.03, to avoid a wrongly estimated production rate, with an uncertainty of $< 1\%$.

- **Cuts on the specific energy loss**
  The systematic calculation and appropriative scaling of the cuts on the specific energy loss has been explained in section 4.1.2.2. In order to investigate if there is still any systematic bias introduced by this cut, which is not corrected for by the scaling, the analysis of K^+ is repeated first without applying the cut on the correlation between β and the energy loss in the TOF detector and second without applying the cut on the correlation between momentum and energy loss in the drift chambers. The resulting difference on the rapidity density distribution for the three different scenarios is less than 1.5% which can be seen on the left side of figure 5.23.

- **Cuts on the mass**
  As explained in section 4.1.5.2 the estimation of the differential count rate of kaons is done by integrating a Gaussian function around the mean of the mass distribution after subtraction of the background. The width of the integration region is varied to 1.5σ, 2σ and 2.5σ but the effect on the resulting rapidity density distribution is less than the uncertainty from the background description and can therefore be neglected (see right side of figure 5.23).

- **Sector dependence**
  The kaons and ϕ mesons are produced rarely, therefore the analysis can not be performed for the different sectors of the spectrometer separately, as could be done for the pion and proton analysis, neither for only a few selected days where all sectors were working under stable conditions. Therefore, sector 2 is completely removed from the analysis and the efficiency and acceptance correction is done using the average value from the other sectors. The uncertainty of averaging is obtained from the proton and pion analysis to be 4% (see sections 5.1.1 and 5.2.1).

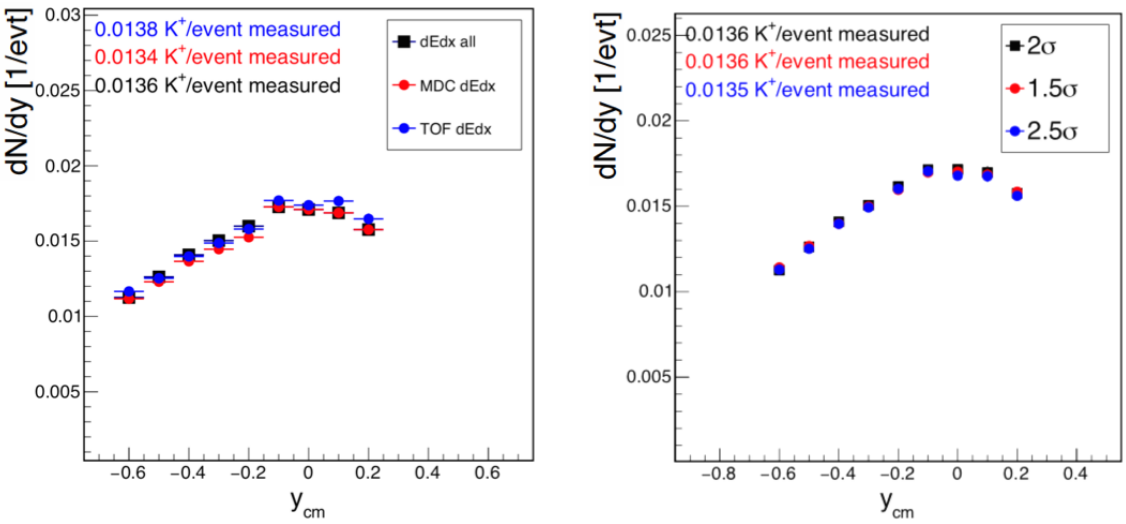

Figure 5.23: Left: Rapidity density distribution of K^+ after applying all cuts for particle identification (black squares) and to evaluate the systematic error introduced from applied cuts on the specific energy loss, the distribution after applying only a cut on the specific energy loss in drift chambers as a function of momentum (red), and after only applying a cut on the specific energy loss in the TOF-detector as a function of β (blue). The resulting systematic uncertainty is 1.5%. Right: Rapidity density distribution of K^+ to evaluate the systematic error introduced from selecting a region of 2σ around the mass after subtraction of the background

- **Extrapolation to unmeasured transverse mass regions**
  The extrapolation of the transverse mass spectra of K^+ is performed assuming purely thermal production using Boltzmann functions. The parameterization is reproducing the shape of the spectra, but is varied to estimate a possible systematic effect on the production rate introduced by this assumption. To take into account, that the analysis of protons shows that the system is additionally expanding radially, the extrapolation is varied using the same Siemens-Rasmussen parameterization as used in proton analysis. In the simple picture of an expanding thermal source with the constant radial flow velocity β_r, the kaon spectra are not as sensitive on the deformation from a thermal exponential shape as the heavy protons, due to their relatively low mass. As a consequence, the obtained parameters T = 70 MeV and β_r = 0.41 from the analysis of protons (compare section 5.1) are used as fixed quantities for the description of the kaon transverse mass spectra. The only free parameter of parameterization 5.5 is the constant C. Left side of figure 5.24 shows the comparison of the description of the transverse mass spectra with Boltzmann and Siemens-Rasmussen functions. It can be seen that both parameterizations are reproducing the shape of the spectra, whereas the quality of the Boltzmann fit is a bit higher. The difference of the extrapolated differential count rate is less than 1.5% (see right side of figure 5.24).

- **Efficiency and acceptance correction**
  The systematic uncertainty of the generated input for the efficiency correction has been estimated using protons and π^- (see section 4.3.1.1). The efficiency matrices have been obtained using pure UrQMD events and have been varied to thermally produced particles generated with PLUTO. The difference was found to be in the order of 1%. Furthermore, the possible bias of

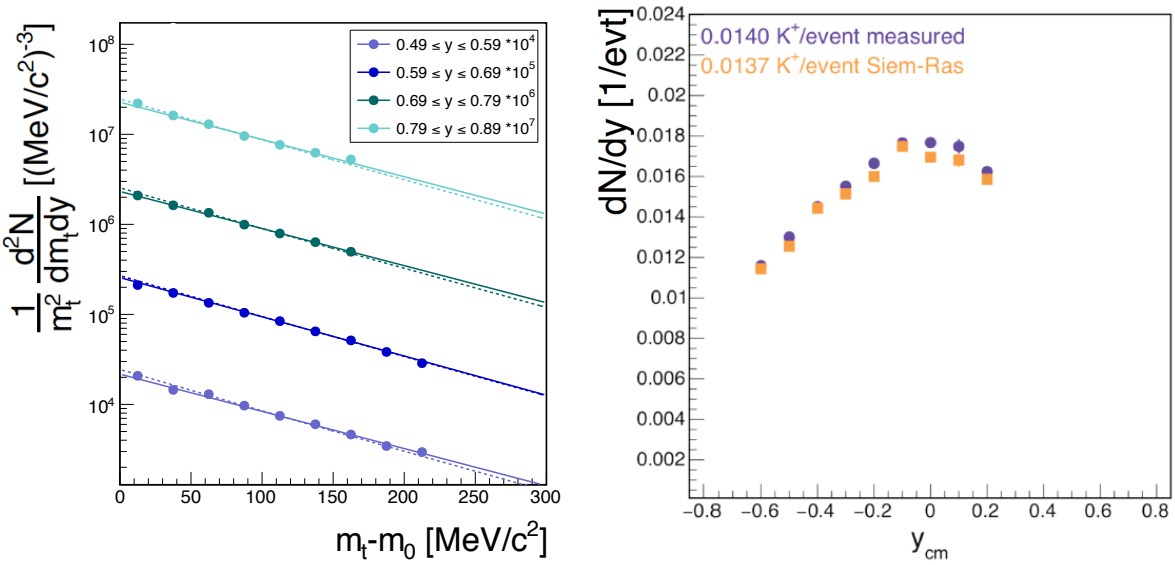

Figure 5.24: Left: Zoom into the efficiency and acceptance corrected transverse mass spectra of K^+ for different rapidity regions (see legend), scaled with $1/m_t^2$, together with a simple Boltzmann parameterization (solid line) which is used to extrapolate to unmeasured transverse mass regions and the Siemens-Rasmussen parameterization (dashed line) with fixed T and β_r from proton analysis, which is used to evaluate the systematic uncertainty on the count rate introduced by the extrapolation. Right: Resulting rapidity density distribution after using the Boltzmann (purple circles) and the Siemens-Rasmussen parameterization (yellow squares) to extrapolate to unmeasured transverse mass regions. The difference results a systematic uncertainty of less than 1.5%.

the background description within the UrQMD model has been investigated by embedding the generated particle tracks of protons, π^- and K^+ also in real events. Especially in case of the kaons, no systematic effect has been observed.

The investigation of any possible systematic bias from the analysis method on the kaon production rate leads to an overall scaling factor for the rapidity density distribution of 1.03 and the systematic uncertainty is determined to:

$$err_{sys} = \sqrt{(0.5\%|_{SCcuts})^2 + (1.5\%|_{dE/dx})^2 + (4\%|_{sec})^2 + (1.5\%|_{extrapol})^2 + (1\%|_{eff})^2} \approx 5\%. \tag{5.11}$$

Systematic uncertainty on the effective temperature

The extraction of the effective temperature is not sensitive on any variations of the cuts on the specific energy loss and mass for particle identification as deduced for variation of those quantities shown in figure 5.25. The investigation of the effective temperature for π^- for the different sectors of the spectrometer separately resulted in a systematic change of the extracted slope of less than 1%, corresponding to roughly ΔT_{sys} = 1 MeV. The uncertainty on the obtained effective temperature is therefore dominated by the statistical uncertainty and the uncertainty from the background subtraction, which is directly obtained from the data point at mid-rapidity to ΔT_{stat} = 1 MeV.

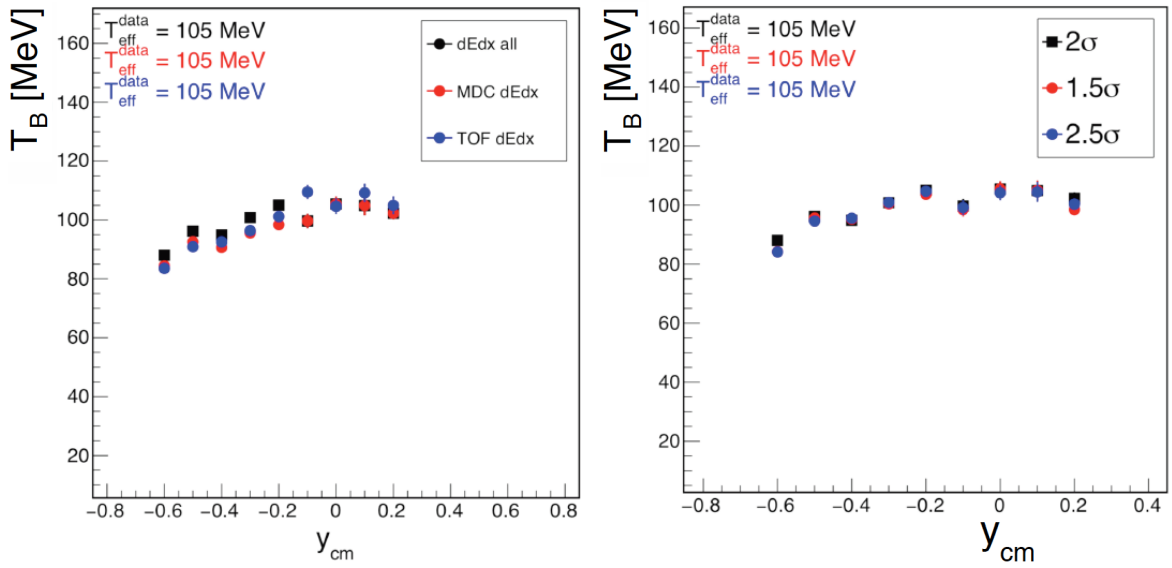

Figure 5.25: Inverse slope parameter distribution of K^+ for the different variations of the cuts on the specific energy loss (left) and mass (right) for particle identification.

Systematic uncertainty of the extrapolation to obtain the final production yield

The final production yield of 3.01 x 10^{-2} K^+ per event is estimated using a Gaussian parameterization to extrapolate to unmeasured rapidity regions, which is a very simple assumption about the phase space distribution. The contribution of the extrapolation in the unmeasured region corresponds with 1.06 x 10^{-2} to 35% of the total yield.

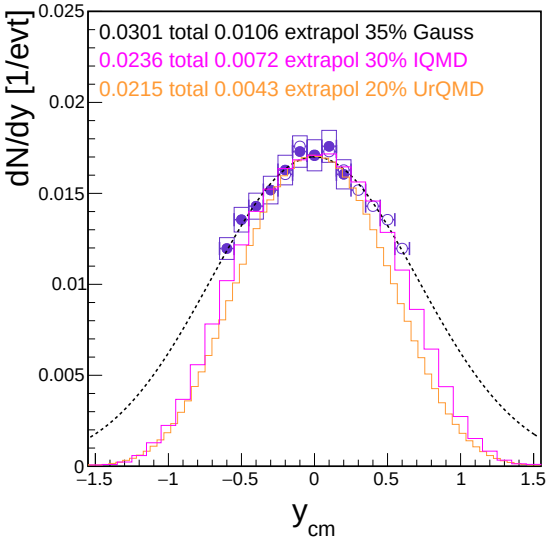

Figure 5.26: Measured (full circles) and mirrored (open circles) rapidity density distribution of K^+ compared to UrQMD (orange line) and IQMD (purple line) to evaluate the systematic error of the extrapolation using a Gaussian distribution (dashed line) to rapidity regions not covered by HADES.

In order to estimate the systematic uncertainty introduced by the extrapolation, the parameterization is varied using the rapidity distribution of the IQMD and UrQMD transport models. In principle transport models should give a more realistic phase space description than the simple Gaussian. However, in contrast to the reproduced yield and rapidity distribution of negative pions, the production yield of kaons is overestimated and the rapidity density distribution has a smaller width (see figure 5.26). Nevertheless, the models can be used to extract the uncertainty of the extrapolation when only relative and not absolute values are used. The total integral of the distribution from UrQMD correspond to 2.15 x 10^{-2}, whereas the unmeasured rapidity region is contributing with an integral 0.43 x 10^{-2}, which corresponds to 20% to the total yield. In case of the IQMD model the extrapolation is with 0.72 x 10^{-2} contributing to 30% to the total yield of 2.36 x 10^{-2}. In case of the model assumptions, the unmeasured region is contributing 10% different between each other and 5% respectively 15% different than the assumed contribution using a simple Gaussian distribution. The systematic uncertainty of the extrapolation method is therefore assumed to be in the order of 10%.

5.3.2 Centrality dependent analysis

To learn more about the sub-threshold production of positive kaons, the analysis is repeated for four different centrality classes. The corresponding efficiency and acceptance corrected transverse mass spectra can be found in appendix A in figure A.9. The distributions of the inverse slope parameters are shown in figure 5.27. Again, $\cosh y_{cm}$ parameterizations are used to extract the effective temperatures. The effective temperatures are rising with centrality, which can be seen on left side of figure 5.29, where the extracted temperatures are displayed as a function of $\langle A_{part} \rangle$. To quantify the increase of the effective temperatures with centrality, the data is parameterized by a linear function and a slope of m = (0.10 $\pm$ 0.01) MeV is obtained. Figure 5.28 shows the rapidity density distributions for the different centrality classes, which have been already scaled accordingly to correct for losses after applying cuts on the track quality parameters for kaon identification. The scaling factor is centrality dependent and is obtained using pions and protons (see tabular 5.3 and compare section 5.3.1). The error bands correspond to 5% systematic uncertainty. To extrapolate to rapidity regions not covered by the spectrometer, a Gaussian parameterization is used. The obtained production yields with statistical error, systematic uncertainty and error of the extrapolation to unmeasured rapidity regions are summarized in the figure. The multiplicity normalized to $\langle A_{part} \rangle$ as a function of centrality is shown on the right side of figure 5.29. The statistical and systematic errors are added quadratically. The production yield is increasing more than linear with $M \sim \langle A_{part} \rangle^{\alpha}$, with α = 1.51 $\pm$ 0.15.

mult class	scaling factor
0% - 40%	1.03
0% - 10%	1.045
10% - 20%	1.035
20 %- 30%	1.015
30 %- 40%	1.015
0% - 20%	1.04
20% - 40%	1.015

Table 5.3: Scaling factors for charged kaons obtained using proton and π^- analysis to correct for losses after applying cuts on the track quality parameters for different centrality classes.

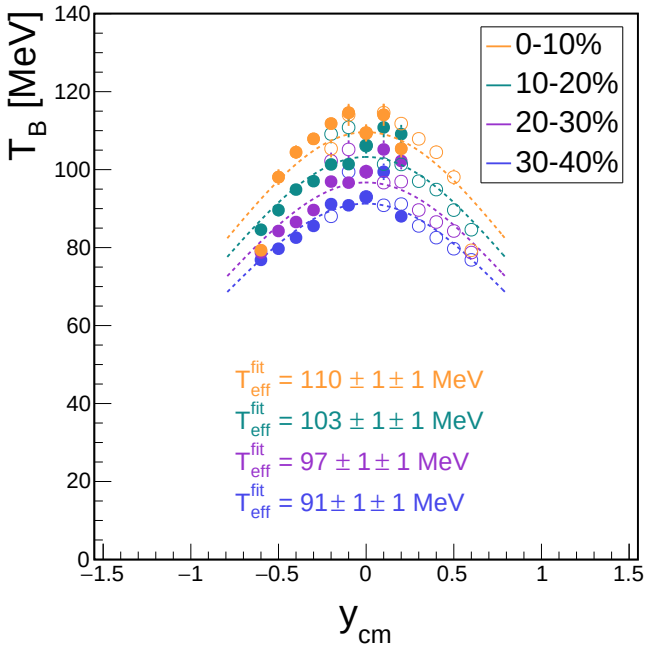

Figure 5.27: Measured (solid circles) and reflected (open circles) distribution of the inverse slope parameters of K^+ for four different centrality bins (see legend). $\cosh y_{cm}$ parameterizations (dashed lines) are used to extract the effective temperatures.

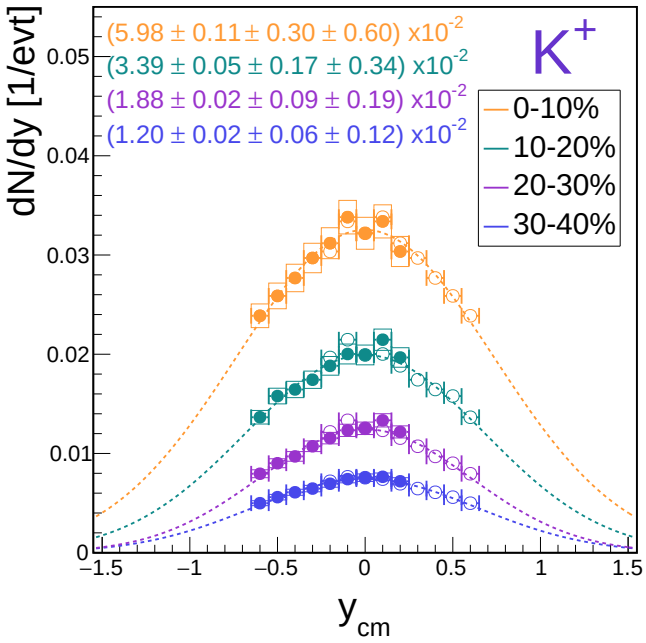

Figure 5.28: Measured (solid) and reflected (open symbols) rapidity density distribution of K^+ for different centrality classes (see legend) normalized to the number of analyzed events. Lines correspond to Gaussian parameterizations to extrapolate to rapidity regions not covered by the spectrometer and extract the production yield, which is summarized in the plot together with the statistical error, the systematic uncertainty and the error of the extrapolation to unmeasured rapidity regions.

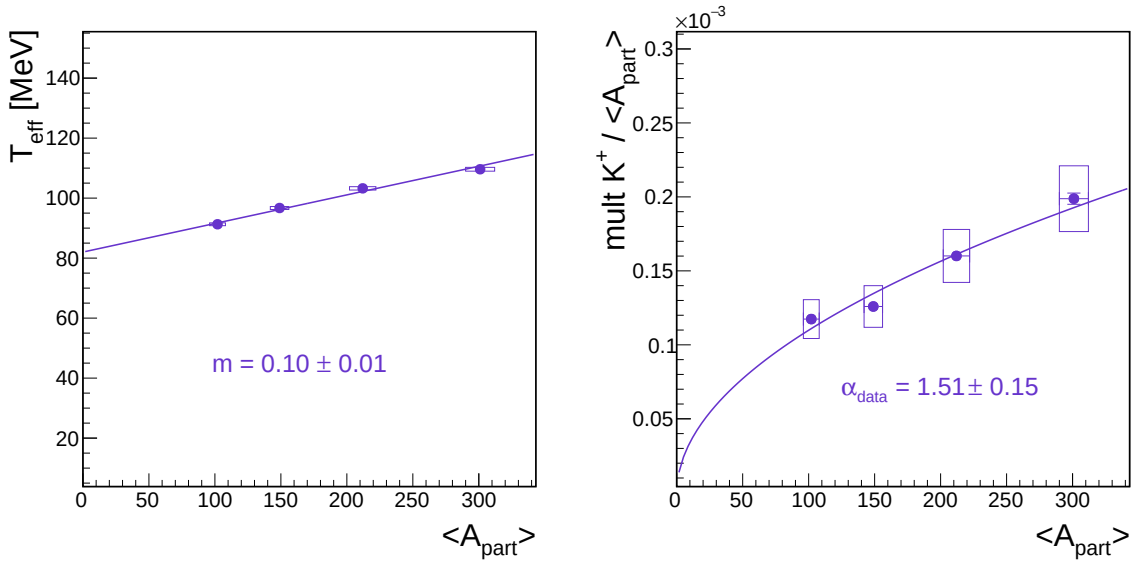

Figure 5.29: Left: Effective temperature of K^+ as a function of $\langle A_{part} \rangle$. To quantify the increase with centrality, the temperatures are parameterized with a linear function (purple line) and the slope m is obtained. Right: Multiplicity of K^+ normalized to $\langle A_{part} \rangle$ as a function of centrality. The statistical and systematic errors are added quadratically. The production yield is increasing more than linear with $M \sim \langle A_{part} \rangle^{\alpha}$ (solid line).

5.4 K^-

The efficiency and acceptance corrected transverse mass spectra for the different analyzed rapidity regions of K^- are displayed on the left side of figure 5.30 in the Boltzmann representation. The accessible transverse mass region is due to lower statistics and signal to background ratio limited in comparison to positive kaons, resulting in a higher uncertainty on the obtained inverse slope from the Boltzmann fits. As the transverse mass spectra of positive kaons can also be described using the Siemens-Rasmussen parameterization (equation 5.5) with the parameters T = 70 MeV and β_r = 0.41 fixed on the values obtained for proton analysis (compare section 5.3.1 and 5.1), the same parameterization is used to describe also the K^- spectra. Both functions are reproducing the shape of the transverse mass spectra within the given errors, which can be seen more clearly on the right side of figure 5.30, where ratios of the measured spectra and the two parameterizations are shown.

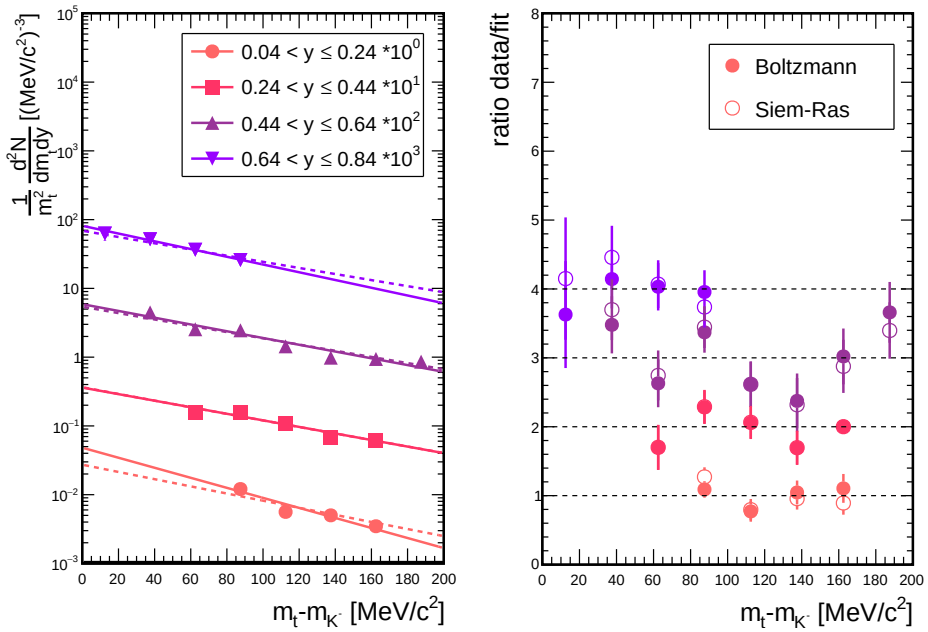

Figure 5.30: Left: Efficiency and acceptance corrected transverse mass spectra of K^- for the different rapidity slices in the Boltzmann representation. The spectra are scaled with different powers of ten for better visibility (see legend). Solid lines correspond to Boltzmann parameterizations according to equation 5.1 to determine the effective temperature and the rapidity density distribution. Dashed lines correspond to Siemens-Rasmussen parameterizations according to equation 5.5 with fixed parameters T = 70 MeV and β_r = 0.41, obtained from proton analysis. Right: Ratio between the spectra and the two fit functions. The spectra are scaled for better visibility.

The extracted inverse slope parameters are shown as a function of rapidity on the left side of figure 5.31. The shape of the distribution is within the errors reproduced by a $\cosh y_{cm}$ parameterization, which is used to extract the effective temperature of T_{eff}^{fit} = (84 $\pm$ 6) MeV. The Boltzmann parameterization is used to extrapolate the transverse mass spectra to unmeasured regions in order to obtain the rapidity density distribution, shown on the right side of figure 5.31. Since it can not be perfectly distinguished which parameterization gives the best description of the transverse mass spectra, the difference of the Boltzmann and the Siemens-Rasmussen function is taken as systematic uncertainty for each rapidity slice. The shown error bands correspond to the sum of the 5% systematic uncertainty from particle identification, obtained for the K^+ due to the higher statistics (compare section 5.3.1)

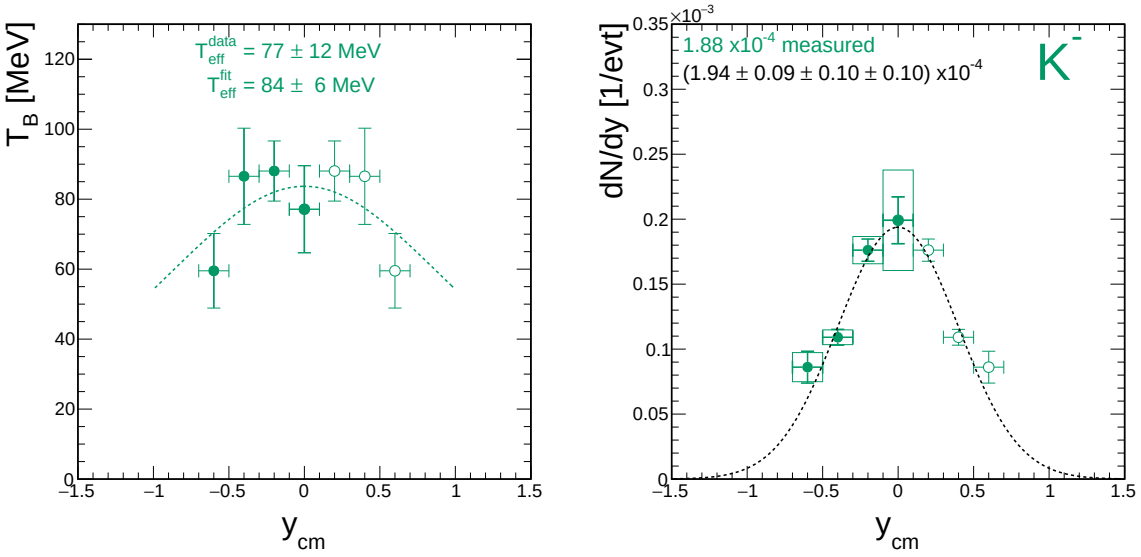

Figure 5.31: Left: Measured (solid circles) and reflected (open circles) inverse slope parameter distribution of K^- as a function of rapidity. Dashed lines correspond to a $\cosh y_{cm}$ parameterization to extract the effective temperature T_{eff}. Right: Measured (solid circles) and reflected (open circles) rapidity density distribution of K^-. Within the acceptance 1.88 x 10^{-4} K^- are measured per event. To obtain the final production yield of $(1.94 \pm 0.09|_{stat} \pm 0.10|_{sys} \pm 0.10|_{extrapolation})x10^{-4}$ a Gaussian parameterization (dashed line) is used to extrapolate to rapidity regions not covered by the detector.

and the difference between the integral of the Boltzmann and the Siemens-Rasmussen parameterization. Additionally, the distribution is scaled by the factor 1.03, obtained using pions and protons, to correct for losses of real particles due to cuts on the track quality variables χ^2_{RK} and χ^2_{MM} (compare section 5.3.1). As the rapidity distribution is symmetric around mid-rapidity in a symmetric collision system, like Au+Au, the data points can be mirrored, resulting in 1.88 x 10^{-4} measured K^- per event within the rapidity region covered by HADES. To extrapolate to rapidity regions not covered by the detector a Gaussian parameterization is used and a final K^- production yield of $(1.94 \pm 0.09|_{stat} \pm 0.10|_{sys} \pm 0.10|_{extrapolation})x10^{-4}$ is deduced. Due to the steeply falling rapidity density distribution towards beam and target rapidity, the extrapolation is not contributing strongly to the overall production yield of K^-. To evaluate the stated systematic error introduced by using the Gaussian parameterization for extrapolation, the rapidity distribution of a two component model simulation, including 70% thermally produced K^- and 30% K^- stemming from ϕ feed-down decays is used. This simulation and a comparison to the measured rapidity distribution will be explained in detail in section 6.3. The relative difference of the extrapolated yields using the two parameterizations to extrapolate, compared to the measured yield is 9% in case of the Gauss, respectively 14% for the two component model, resulting in a systematic uncertainty of 5% of the extrapolation method.

5.4.1 Centrality dependent analysis

To learn more about the production of K^- in heavy-ion collisions, it is crucial to study also the dependence of the multiplicity and effective temperature on the centrality of the collision. With the given statistics it is possible to repeat the analysis of rarely produced K^- in two centrality classes 0 - 20% and 20 - 40%. The corresponding efficiency and acceptance corrected transverse mass spectra can be found in appendix A in figure A.15. The resulting distributions of the inverse slope parameters

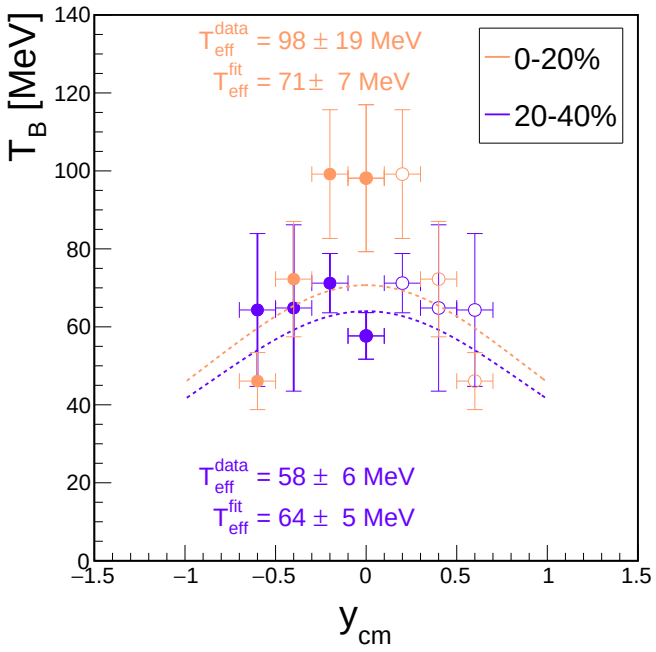

Figure 5.32: Measured (solid circles) and reflected (open circles) inverse slope parameter distributions of K^- for central (orange) and semi-central collisions (purple). The $\cosh y_{cm}$ parameterization is used to estimate the effective temperatures T_{eff}^{fit}.

from the Boltzmann fits to the transverse mass spectra are shown in figure 5.32. The distributions can be fairly described by the $\cosh y_{cm}$ parameterization, which is used to obtain the effective temperature T_{eff}^{fit} = 64 ± 5 MeV for semi-central and T_{eff}^{fit} = 71 ± 7 MeV for central collisions. The inverse slopes at mid-rapidity are slightly deviating from the effective temperature. Hence, the two centrality classes show a different trend: Whereas the inverse slope at mid-rapidity of the most central collisions is with T_{eff}^{data} = 98 ± 19 MeV higher, the one of the semi-central collisions is with T_{eff}^{data} = 58 ± 6 MeV lower than the result from the $\cosh y_{cm}$ fit. The effective temperatures T_{eff}^{fit} are displayed as a function of $\langle A_{part} \rangle$ on the left side of figure 5.34. Like in case of K^+ the temperatures rise towards more central collisions. To quantify the increase with centrality, the temperatures are parameterized with a linear function and the slope m = (0.05 ± 0.06) MeV is obtained. To obtain the rapidity density distribution, shown in figure 5.33, the transverse mass spectra are again extrapolated using the Boltzmann fit. The difference between the Boltzmann and the Siemens-Rasmussen function, the latter one with fixed parameters according to the centrality dependent analysis of protons, is added to the systematic uncertainty of 5% of the particle identification. Again, the distributions are scaled up to correct for losses of real particles introduced by the cuts on the track quality parameters with the factor 1.015 for semi-central and 1.04 for central collisions. Gaussian parameterizations are used to extract the final production yields $(1.28 \pm 0.11|_{stat} \pm 0.06|_{sys} \pm 0.06|_{extrapol})\text{x}10^{-4}$ for semi-central and $(3.36 \pm 0.31|_{stat} \pm 0.17|_{stat} \pm 0.17|_{extrapol})\text{x}10^{-4}$ for central collisions. The uncertainty of the extrapolation of 5% is obtained by varying the parameterization to the one of the two component simulation as explained in section 6.3. The multiplicity scaled by $\langle A_{part} \rangle$ as a function of centrality is shown on the right side of figure 5.34. The statistical and systematic errors are added quadratically. The multiplicity rises more than linear with centrality with $M \sim \langle A_{part} \rangle^{\alpha}$, with α = 1.35 ± 0.23.

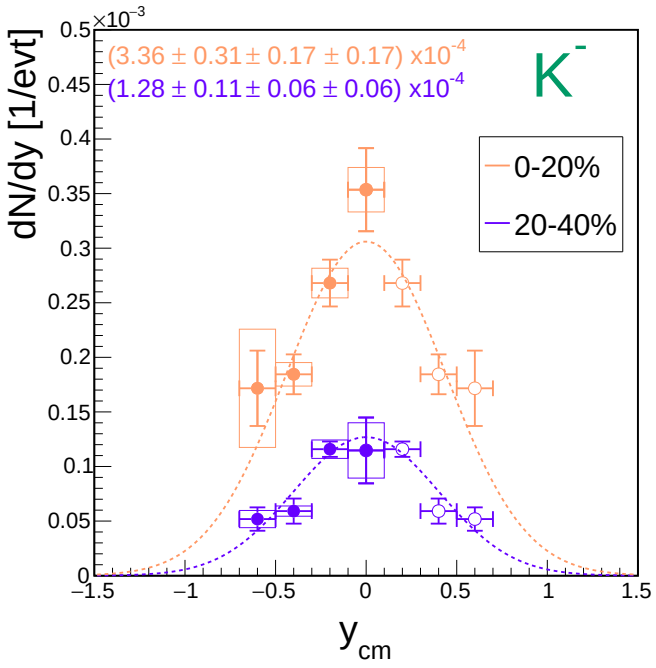

Figure 5.33: Measured (filled circles) and reflected (open circles) rapidity density distribution of K^- for central (orange) and semi-central (purple) collisions. Gaussian parameterizations (dashed lines) are used to extrapolate to rapidity regions not covered by the detector to obtain the final production yield.

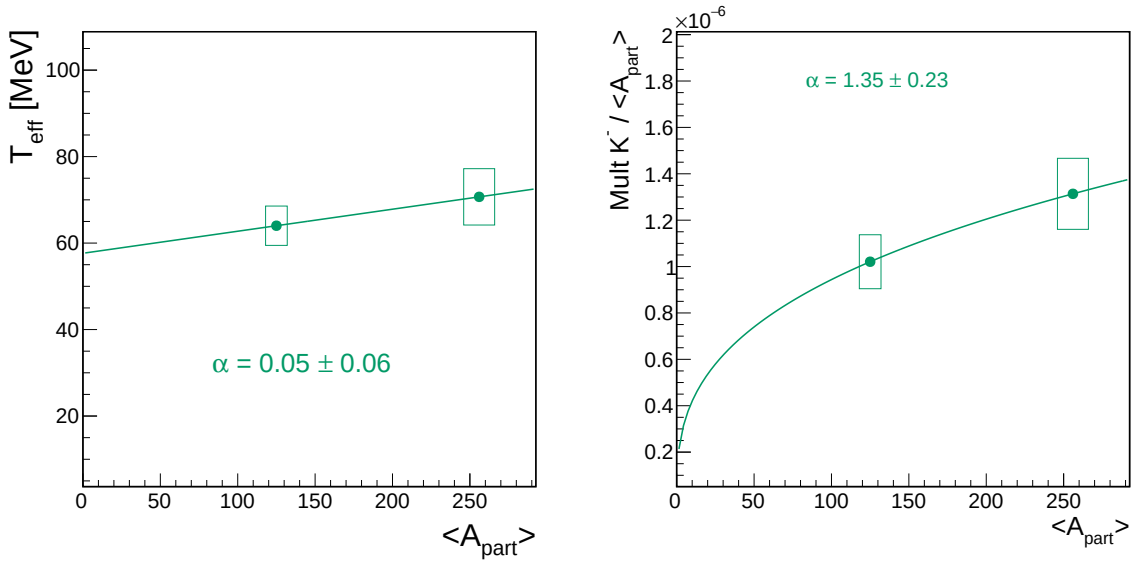

Figure 5.34: Left: Effective temperature of K^- as a function of $\langle A_{part} \rangle$. To quantify the increase with centrality, the temperatures are parameterized with a linear function (green line) and the slope m is obtained. Right: Multiplicity per $\langle A_{part} \rangle$ as a function of $\langle A_{part} \rangle$. The production yield rises more than linear with centrality according to $M \sim \langle A_{part} \rangle^{\alpha}$ (solid line). The statistical and systematic errors are added quadratically.

5.5 ϕ

The efficiency and acceptance corrected transverse mass spectra of ϕ mesons are shown in the Boltzmann representation on the left side of figure 5.35. The shape of the spectra can be reproduced by Boltzmann parameterizations according to equation 5.1, which can be seen more clearly on the right side of the figure, where the ratio between the measured spectra and the fits are displayed.

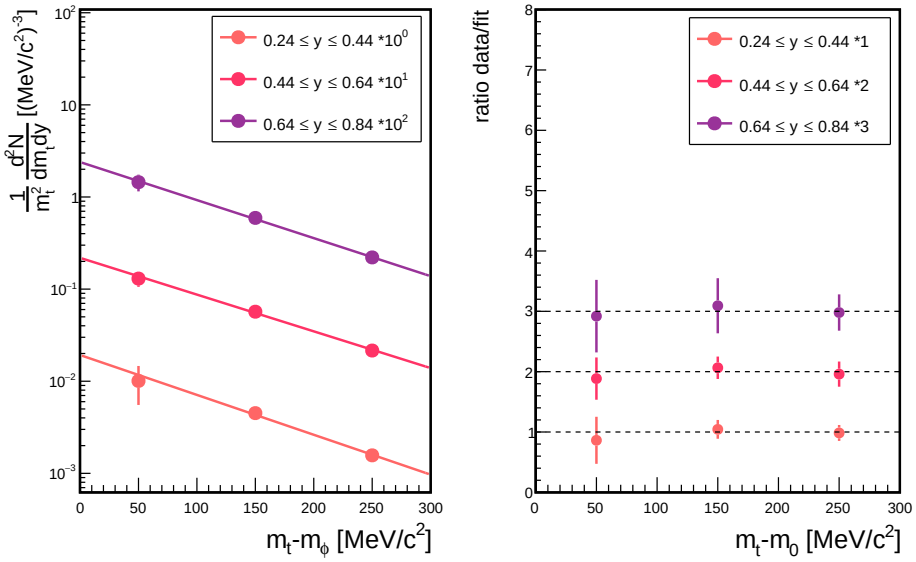

Figure 5.35: Left: Efficiency and acceptance corrected transverse mass spectra of ϕ for the different rapidity slices in the Boltzmann representation. The spectra are multiplied by different powers of ten for better visibility (see legend). Lines correspond to Boltzmann parameterizations according to equation 5.1 to determine the effective temperature and extrapolate to unmeasured transverse mass regions. Right: Ratio between the spectra and the fit function. The ratios are scaled in order to get a better visibility.

The resulting inverse slope parameters are displayed on the left side of figure 5.36. The distribution can be described by a $\cosh y_{cm}$ function from which the effective temperature of T_{eff}^{fit} = (108 $\pm$ 7) MeV is extracted. After integration of the data and using the Boltzmann fits to extrapolate to unmeasured transverse mass regions, the particle density as a function of rapidity is obtained and displayed on the left side of figure 5.36. The distribution is scaled with the factor 1.03 x 1.03, to correct for losses of real K^+K^- candidates due to cuts on the track quality parameters (compare section 5.3.1). The systematic errors of 5% for single kaon identification (compare section 5.3.1) add up to 10% systematic uncertainty for ϕ reconstruction and is shown in the figure as error band. The rapidity distribution should be symmetric around mid-rapidity and can therefore be reflected. In total 0.7 x 10^{-4} ϕ mesons are measured per event inside the rapidity region covered by the spectrometer. To extrapolate to unmeasured rapidity regions, a Gaussian parameterization is used, which is reproducing the shape of the distribution. A final production yield of $(0.99 \pm 0.24|_{stat} \pm 0.10|_{sys} \pm 0.05|_{extrapolation})x10^{-4}$ ϕ per event is obtained. The uncertainty of the extrapolation is evaluated by varying the single Gaussian parameterization to a combination of two Gaussians. This combination changes the tail of the extrapolation and the relative difference of two distributions to the measured yield is 35% for the single, respectively 30% for the two Gaussian parameterization, resulting in a systematic bias of 5% from the extrapolation method.

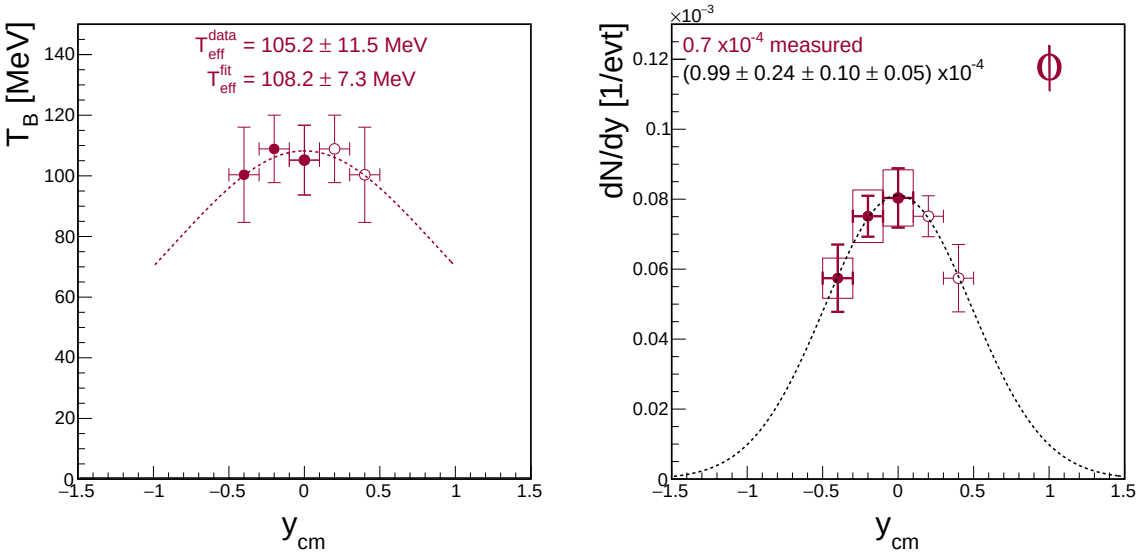

Figure 5.36: Measured (solid circles) and reflected (open circles) inverse slope parameter distribution of ϕ as a function of rapidity. Dashed lines correspond to a $\cosh y_{cm}$ parameterization to extract the effective temperature T_{eff}^{fit}. Measured (solid circles) and reflected (open circles) rapidity density distribution of ϕ mesons normalized to the number of analyzed events and scaled with the factor 1.03 x 1.03, to correct for losses of real kaon candidates due to cuts on the track quality variables. The error band corresponds to 10% systematic uncertainty from K^+K^- identification. To obtain the final production yield stated in the figure, a Gaussian parameterization (dashed line) is used.

5.5.1 Centrality dependent analysis

To study the centrality dependence of the ϕ production, which is important to learn more about the particle production mechanisms in heavy-ion collisions below the elementary production threshold, the data sample is divided in two different centrality classes: 0 - 20% and 20 - 40%. The corresponding efficiency and acceptance corrected transverse mass spectra can be found in appendix A in figure A.9. The transverse mass spectra are in both cases described with Boltzmann parameterizations and the resulting distributions of the inverse slope parameters for the two centrality classes are shown in figure 5.37. Both can be described within the errors with a $\cosh y_{cm}$ parameterization from which the effective temperature T_{eff} = (91 $\pm$ 7) MeV for semi-central and T_{eff} = (99 $\pm$ 8) MeV for central collisions is obtained. The temperature is slightly increasing for more central collisions, which is displayed on the left side of figure 5.39. To quantify the increase with centrality, the temperatures are parameterized with a linear function and the slope m = (0.06 $\pm$ 0.08) MeV is obtained. The Boltzmann functions are used to extrapolate to unmeasured transverse mass regions and the resulting rapidity density distribution is obtained, see figure 5.38. Again the distributions are normalized to the number of analyzed events and scaled with the factor 1.015 x 1.015 for semi-central, respectively 1.04 x 1.04 for central collisions, to correct for losses of real K^+K^- candidates due to cuts on the track quality parameters used for kaon identification. The shown error bands correspond to 10% systematic uncertainty from kaon identification (compare section 5.3.1). To obtain the final production yields, Gaussian parameterizations are used to extrapolate to unmeasured rapidity regions. In case of the most central collisions, the measured distribution shows a rather flat top, leading to a broad width of the free Gaussian fit. This results that also regions far above target and beam rapidity are contributing substantially to the obtained yield, which is not very reasonable. To keep the width of the

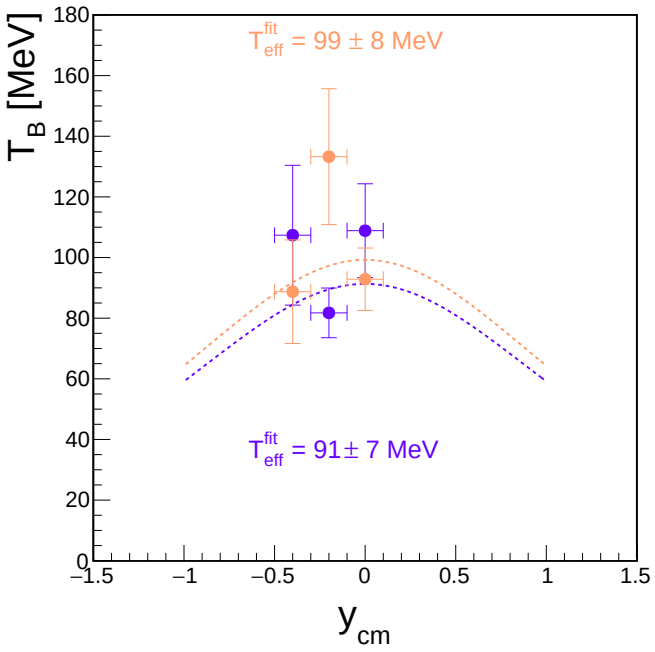

Figure 5.37: Measured (solid circles) and reflected (open circles) distribution of the inverse slope parameters of ϕ for the two analyzed centrality bins. The data is described by a $\cosh y_{cm}$ parameterization, which is used to extract the effective temperatures T_{eff}^{fit}.

Gaussian in a physical range, the parameter is fixed on the value obtained for the inclusive analysis of the complete data set of 0 - 40% most central collisions of σ_y = 0.54. The final multiplicities of (0.53 $\pm$ 0.08|$_{stat}$ $\pm$ 0.05|$_{sys}$ $\pm$ 0.04|$_{extrapolation}$)x10^{-4} for semi-central and (1.55 $\pm$ 0.28|$_{stat}$ $\pm$ 0.15|$_{sys}$ $\pm$ 0.11|$_{extrapolation}$)x10^{-4} for central collisions are obtained. The systematic uncertainty of the extrapolation is again estimated by varying the single Gaussian parameterization to a combination of two Gaussian functions. For central collisions the relative contribution of the extrapolation to the total yield is with 35% for single, respectively 28% for the two Gaussian parameterization, as expected from the width of the distribution, much higher than for the semi-central collisions with 15%, respectively 8%. However, in both cases the uncertainty of the extrapolation method is therefore 7%. The right side of figure 5.39 shows the multiplicities normalized to $\langle A_{part} \rangle$ as a function of $\langle A_{part} \rangle$. The statistical and systematic errors are added quadratically. The production yield rises more than linear with $M \sim \langle A_{part} \rangle^{\alpha}$ with α = 1.51 $\pm$ 0.43.

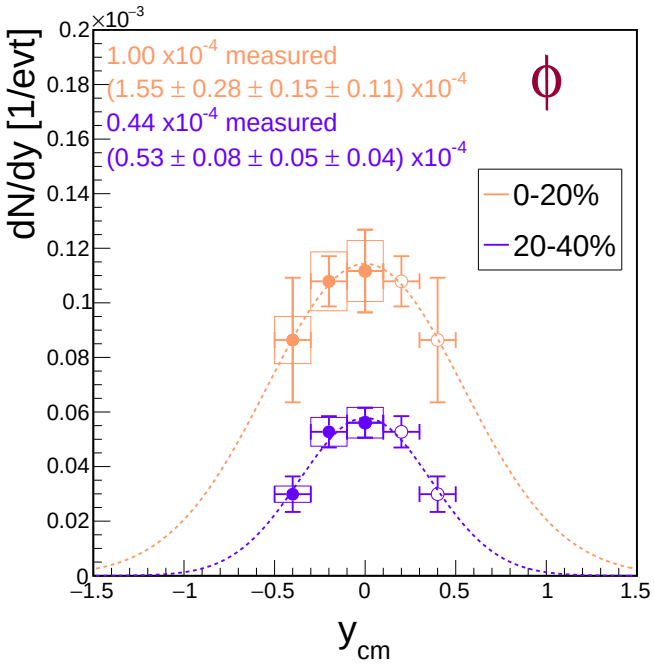

Figure 5.38: Measured (solid circles) and reflected (open circles) rapidity density distribution of ϕ for semi-central (purple) and central (orange) collisions, normalized to the number of analyzed events and scaled with the factor 1.015 x 1.015 for semi-central, respectively 1.04 x 1.04 for central collisions, to account for losses of real K^+K^- candidates due to cuts on the track quality parameters. The final production yields are obtained using Gaussian parameterizations (dashed lines) to extrapolate to unmeasured rapidity regions. The width of the Gaussian fit to the central distribution is fixed to the value obtained from the analysis of the full data sample of 0 - 40% most central collisions.

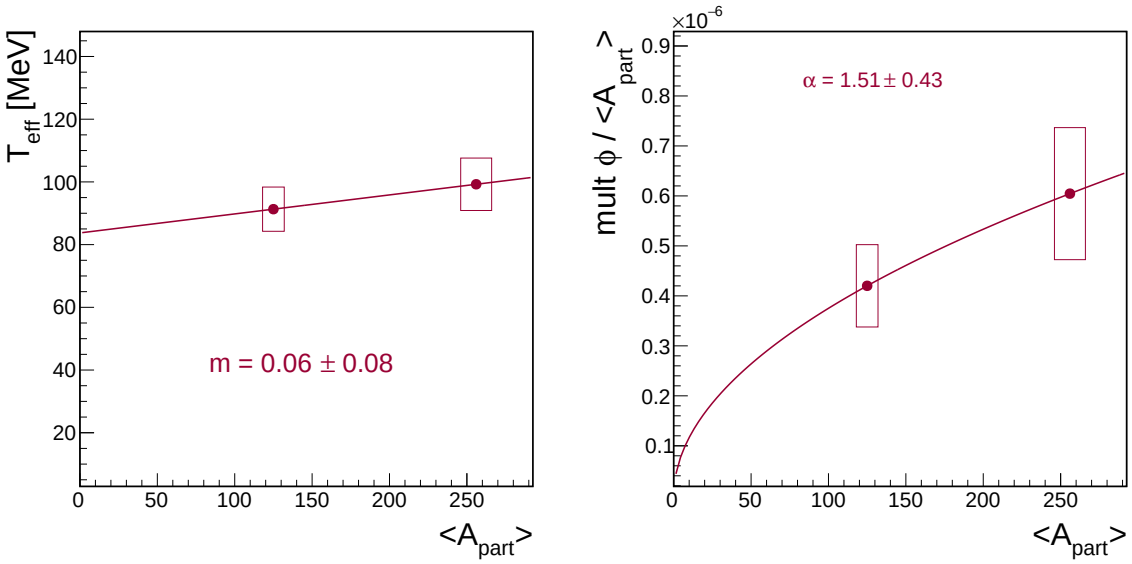

Figure 5.39: Left: Effective temperature of ϕ as a function of $\langle A_{part} \rangle$. To quantify the increase with centrality, the temperatures are parameterized with a linear function (red line) and the slope m is obtained. Right: Multiplicity normalized to $\langle A_{part} \rangle$ as a function of $\langle A_{part} \rangle$. The yield rises more than linear with centrality with $M \sim \langle A_{part} \rangle^{\alpha}$.

5.6 Summary of the obtained yields and freeze-out parameters of the analyzed particles

The goal of this thesis is to obtain the yields and freeze-out parameters for protons, π^-, $K^\pm$ and ϕ. For this purpose the efficiency and acceptance corrected transverse mass spectra are adapted using Boltzmann and/or Siemens-Rasmussen parameterizations. The inverse slope parameter of the Boltzmann function at mid-rapidity corresponds to the effective temperature T_{eff} of the respective particle. Whereas these parameters are particle specific, the parameters of the Siemens-Rasmussen function, kinetic freeze-out temperature T_{kin} and radial flow velocity β_r, are global characteristics of the produced system. The parameterizations are used to extrapolate the data to unmeasured regions to obtain the rapidity density distribution of the particles. These distributions are furthermore extrapolated to rapidity regions not covered by HADES using Gaussian parameterizations to obtain the final production yield of the particles. The analysis of the particles is performed in different centrality classes to get more insight about particle production mechanisms. The obtained yields and freeze-out parameters for the various analyzed particle species and centrality classes are summarized in table 5.4.

p	yield [1/evt]	T_{kin} [MeV]	β_r
0 - 40%	$41.5 \pm 2.1^*$	70 ± 4	0.41 ± 0.01
0 - 10%	87^{**}	70 ± 4	0.45 ± 0.01
10 - 20%	61^{**}	70 ± 4	0.41 ± 0.01
20 - 30%	-	68 ± 5	0.37 ± 0.02
30 - 40%	-	68 ± 5	0.34 ± 0.03
π^-	yield [1/evt]	T_{eff} [MeV]	$T_{B,1}$ [MeV]
0 - 40%	$11.1 \pm 0.6 \pm 0.4$	$89 \pm 3 \pm 1$	46 ± 1
0 - 10%	17.7 ± 0.9	$93 \pm 1 \pm 1$	49 ± 1
10 - 20%	12.1 ± 0.7	$88 \pm 4 \pm 1$	45 ± 1
20 - 30%	8.5 ± 0.4	$83 \pm 2 \pm 1$	43 ± 1
30 - 40%	6.0 ± 0.1	$80 \pm 1 \pm 1$	41 ± 1
K^+	yield [1/ evt]	T_{eff} [MeV]	
0 - 40%	$(3.01 \pm 0.03 \pm 0.15 \pm 0.30)$ x 10^{-2}	$104 \pm 1 \pm 1$	
0 - 10%	$(5.98 \pm 0.11 \pm 0.30 \pm 0.60)$ x 10^{-2}	$110 \pm 1 \pm 1$	
10 - 20%	$(3.39 \pm 0.05 \pm 0.17 \pm 0.34)$ x 10^{-2}	$103 \pm 1 \pm 1$	
20 - 30%	$(1.88 \pm 0.02 \pm 0.09 \pm 0.19)$ x 10^{-2}	$97 \pm 1 \pm 1$	
30 - 40%	$(1.20 \pm 0.02 \pm 0.06 \pm 0.12)$ x 10^{-2}	$91 \pm 1 \pm 1$	
K^-	yield [1/evt]	T_{eff} [MeV]	
0 - 40%	$(1.94 \pm 0.09 \pm 0.10 \pm 0.10)$ x 10^{-4}	84 ± 6	
0 - 20%	$(3.36 \pm 0.31 \pm 0.17 \pm 0.17)$ x 10^{-4}	71 ± 7	
20 - 40%	$(1.28 \pm 0.11 \pm 0.06 \pm 0.06)$ x 10^{-4}	64 ± 5	
ϕ	yield [1/evt]	T_{eff} [MeV]	
0 - 40%	$(0.99 \pm 0.24 \pm 0.10 \pm 0.05)$ x 10^{-4}	108 ± 7	
0 - 20%	$(1.55 \pm 0.28 \pm 0.15 \pm 0.11)$ x 10^{-4}	99 ± 8	
20 - 40%	$(0.53 \pm 0.08 \pm 0.05 \pm 0.04)$ x 10^{-4}	91 ± 7	

* Yield at mid-rapidity per unit in rapidity
** Yield obtained assuming thermal distribution from UrQMD explained in section 5.1.2

Table 5.4: Summary of the obtained yields, effective temperatures T_{eff}, the kinetic freeze-out temperature T_{kin} and radial flow velocity β_r of the different particle species $p, \pi^-, K^\pm, \phi$ for the 0 - 40% most central collisions and for the different analyzed centrality classes.

Chapter 6

Discussion

In the following chapter the experimental results on the multiplicities and effective slope parameters of charged kaons and ϕ mesons will be discussed and compared with respect to each other, as well as to previous experiments and to theoretical models. The simultaneous measurement of charged kaons and ϕ mesons reconstructed in the same data sample of Au+Au collisions at 1.23 AGeV will be the ultimate test to differentiate between the different sources for sub-threshold K^- production in heavy-ion collisions, as it is a very large system and the particles are produced deeply below their respective elementary production threshold energies. Especially the study of particle ratios has the huge advantage, that experimental biases and systematic errors, introduced by detection and cut efficiencies and acceptance losses cancel out to some extend. Furthermore, the obtained hadron yields from this analysis, complemented by the measurement of Λ and K^0_S performed in [116], will be confronted to a statistical hadronization model fit in order to characterize the thermodynamic properties of the created system in the Au+Au collision.

As mentioned in section 1.1.1 all strange particles are produced in Au+Au collisions at a center-of-mass energy of $\sqrt{s}$ = 2.4 GeV below their respective elementary nucleon-nucleon threshold energy $\sqrt{s_{thr}}$ which can be calculated for the energetically cheapest channel to produce a K^+

$$NN \rightarrow N\Lambda K^+, \tag{6.1}$$

respectively a K^-

$$NN \rightarrow NNK^+K^- \tag{6.2}$$

as follows:

$$\sqrt{s^{K^+}_{thr}} = m_{Nucleon} \cdot c^2 + m_{\Lambda} \cdot c^2 + m_{K^+} \cdot c^2 = 2.55 \text{ GeV} \tag{6.3}$$

$$\sqrt{s^{K^-}_{thr}} = 2 \cdot m_{Nucleon} \cdot c^2 + m_{K^-} \cdot c^2 + m_{K^+} \cdot c^2 = 2.86 \text{ GeV}. \tag{6.4}$$

The so-called excess energy $\sqrt{s_{exc}}$ defines the difference between the available energy and the elementary threshold energy and can be calculated for K^+ and K^- production at the given center-of-mass energy:

$$\sqrt{s^{K^+}_{exc}} = \sqrt{s} - \sqrt{s^{K^+}_{thr}} = 2.4 \text{ GeV} - 2.55 \text{ GeV} = -0.15 \text{ GeV} \tag{6.5}$$

$$\sqrt{s^{K^-}_{exc}} = \sqrt{s} - \sqrt{s^{K^-}_{thr}} = 2.4 \text{ GeV} - 2.86 \text{ GeV} = -0.46 \text{ GeV}. \tag{6.6}$$

The excess energy for ϕ production can be calculated according to:

$$\sqrt{s^{\phi}_{exc}} = \sqrt{s} - (2 \cdot m_{Nucleon} \cdot c^2 + m_{\phi} \cdot c^2) = 2.4 \text{ GeV} - 2.91 \text{ GeV} = -0.49 \text{ GeV}. \tag{6.7}$$

As explained in section 1.1.1, the necessary excess energy to produce the particles in a heavy-ion collision below their respective nucleon-nucleon threshold can be gained in many ways, by making use of the Fermi momentum or in multi-particle interactions. An example for the latter ones is the excitation of a baryon resonance, which can interact further with nucleons from the medium and accumulate the necessary energy to overcome the threshold energy, or the strange particle is produced off-shell and gains the necessary energy in a second collision with another particle. The probability for such processes increases with the created particle density and the life time of the produced system. The clear hierarchy of the excess energies is reflected in the production yields of the various particle species. Whereas the protons and π^- yields are in the order of $\sim 10^2$ and ~ 10, the K^+ production is already strongly reduced and in the order of $\sim 10^{-2}$ due to the negative excess energy. The K^- and ϕ mesons are produced three times further below the threshold, leading to a production yield in the order of $\sim 10^{-4}$.

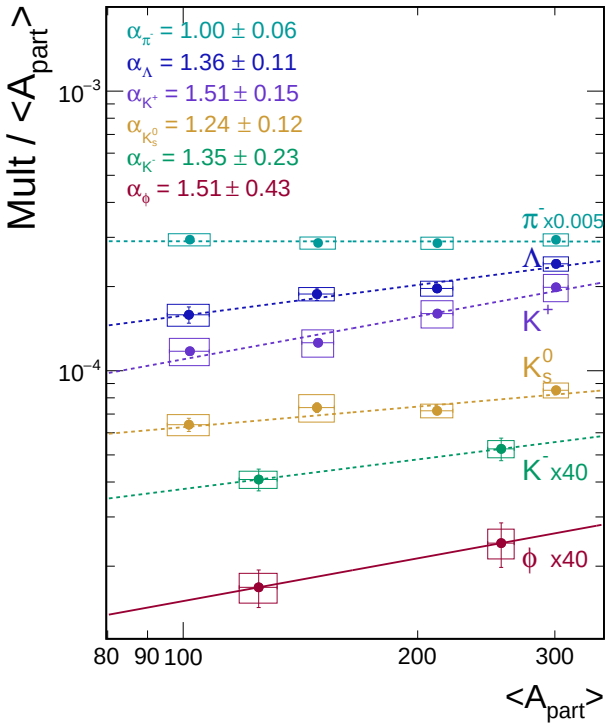

Figure 6.1: Centrality dependence of the measured multiplicity per $\langle A_{part} \rangle$ of π^-, K^+, K^- and ϕ from this analysis, complemented by K^0_S and Λ from [116]. For better visibility the K^- and ϕ yields are scaled with the factor 40, and the one of π^- is down scaled by the factor 0.005. The lines correspond to a function $M \sim \langle A_{part} \rangle^{\alpha}$. The obtained values for α are displayed in the plot.

In figure 6.1 the centrality dependencies of the π^-, kaon ($K^{\pm}$, K^{01}_S), Λ^1 and ϕ multiplicities per $\langle A_{part} \rangle$ are summarized. Whereas the normalized pion multiplicity is constant as a function of the mean number of participating nucleons $\langle A_{part} \rangle$, the multiplicities of all strange particles are increasing more than linear with this quantity. The threshold beam energy for pion production is as calculated in section 1.1.1 with E_{thr} = 0.29 GeV clearly below the kinetic beam energy of the measured system.

[1] Taken from [116]

Therefore, it is expected from transport models that the pion multiplicities show a linear rise with $\langle A_{part} \rangle$ [1]. On the other hand the strange particles are produced below their respective threshold energy, which leads to an expected stronger dependence on the number of participating nucleons, as more medium is available for scattering in the reaction zone in central collisions. The data points for the strange particles are described with a function according to:

$$M \sim \langle A_{part} \rangle^{\alpha}, \tag{6.8}$$

as used in previous publications (compare section 1.7.1). The linear rise with $\langle A_{part} \rangle$ of the π^- multiplicity corresponds to an $\alpha \approx 1$. For charged kaons and ϕ the following parameters are obtained by fitting the data points with function 6.8: α_{K^+} = 1.51 $\pm$ 0.15, α_{K^-} = 1.35 $\pm$ 0.23 and α_{ϕ} = 1.51 $\pm$ 0.43. The systematic and statistical uncertainties of the data points have been added quadratically. Given the fact that the K^- and ϕ have much higher excess energies, it is surprising that all particles show within the errors a similar increase with $\langle A_{part} \rangle$. The K^- and ϕ production yields should scale much stronger with centrality than the K^+[2].

The resulting α parameter for charged kaons and ϕ can be compared to previous measurements of the KaoS and FOPI collaboration. In Au+Au collisions at 1.5 AGeV, KaoS observed within the errors a similar rise of the multiplicities of the two kaon species with values of α_{K^+} = 1.34 $\pm$ 0.16 and α_{K^-} = 1.22 $\pm$ 0.27 [4]. Respectively, an α parameter for the ϕ meson of 1.7 $\pm$ 0.5 was obtained for the first time at 1.9 AGeV by FOPI [144]. Taken the fact into account that these values have been obtained at higher energies and hence smaller excess energies of the corresponding particles, it is rather surprising that the values are similar to the ones obtained in this analysis. On the other hand it suits the observed trend that all particles carrying strangeness show a similar α value though the clear hierarchy on excess energies. Therefore, the centrality dependence of sub-threshold strangeness production is not well understood in the picture of transport models.

The centrality dependence of the effective temperatures of K^+, K^- and ϕ is summarized in figure 6.2. The effective temperatures show a slight increase with $\langle A_{part} \rangle$, but the errors from the K^- and ϕ analysis are too high to make a strong statement. However, to quantify the increase of the temperatures with centrality, the data points are parameterized with a linear fit function:

$$T_{eff} = m \cdot \langle A_{part} \rangle + b. \tag{6.9}$$

The slope of the function is similar for all particle species with m_{K^+} = (0.10 $\pm$ 0.01) MeV, m_{K^-} = (0.05 $\pm$ 0.06) MeV and m_{ϕ} = (0.06 $\pm$ 0.08) MeV. The rise of the temperature towards more central collisions can be explained on a microscopic level by the fact that due to a higher compression, more scattering processes take place in the medium, which is enhanced when more nucleons are participating in the reaction zone. Due to re-scattering, the transverse momenta of the particles can be shifted towards higher values, leading to an increase of the inverse slope parameter of the spectra. The occurrence of scattering processes brings the K^+ into a kinetic equilibrium after $\approx$ 2 interactions according to transport models [1], which results that the slope of the transverse mass spectrum can be related to a temperature on the macroscopic level.

Although the effective temperatures of charged kaons show, like the multiplicities, a similar behavior as a function of centrality, the kinematic distributions show a significant difference: the effective temperatures are always higher of about 20 - 30 MeV for K^+ than for K^-. This difference is significant for the inclusive analysis of 0 - 40% most central collisions ($T_{eff}^{K^+}$ = (104 $\pm$ 1) MeV and $T_{eff}^{K^-}$

[2] Or the other strange hadrons K_S^0 or Λ, whose multiplicities show also within the errors a similar increase with centrality for the given collision system [116]

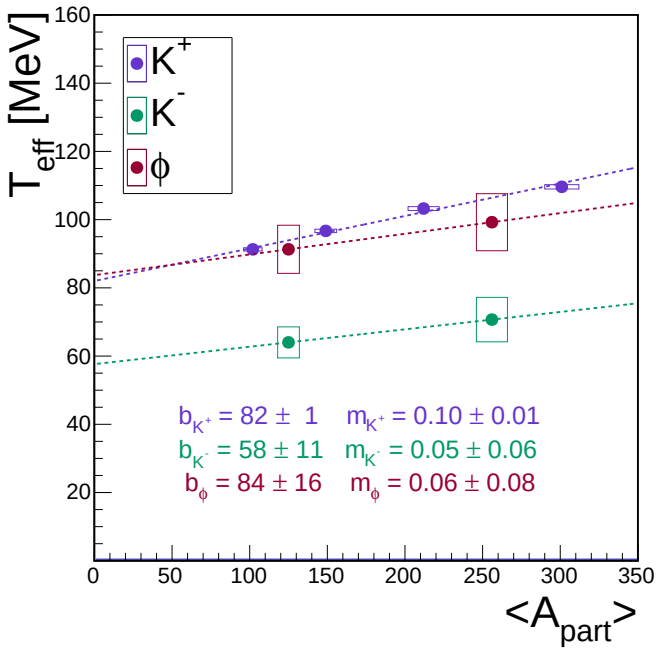

Figure 6.2: Centrality dependence of the measured effective temperatures of K^+, K^- and ϕ. The data points are parameterized with linear functions according to equation 6.9 (dashed lines).

= (84 $\pm$ 6) MeV), as well as for the centrality dependent analysis, however the centrality dependent analysis suffers from large errors. This systematic behavior has been observed by KaoS as well, independently of the energy or system size of the collision system, as already mentioned in section 1.7.1. The measured effective temperatures from the 0 - 40% most central collisions fit into the obtained systematics from KaoS, as can be seen in figure 6.3. The slightly higher value of K^+ from the analysis presented in this thesis can be a result of the different centrality selections from the two experiments, as the effective temperatures increase slightly as a function of $\langle A_{part} \rangle$. KaoS selected minimum bias events resulting in a smaller $\langle A_{part} \rangle$ as from our analysis of 0 - 40% most central collisions with a mean $\langle A_{part} \rangle$ of 191 $\pm$ 7. It is interesting to note that the effective temperatures of K^+ are following a clear mass ordering, depending on the size of the colliding system, and a linear increase, depending on the beam energy. In case of the effective slope of K^- the energy dependence is not as strong as for K^+, but shows a rather flat behavior. Again, a mass ordering, depending of the system size is observed.

The observation of the systematic lower effective temperature of K^- compared to K^+ and the similar behavior of the production yields as a function of centrality, independent of the system size and the collision energy will be addressed in greater detail in the following section 6.1.

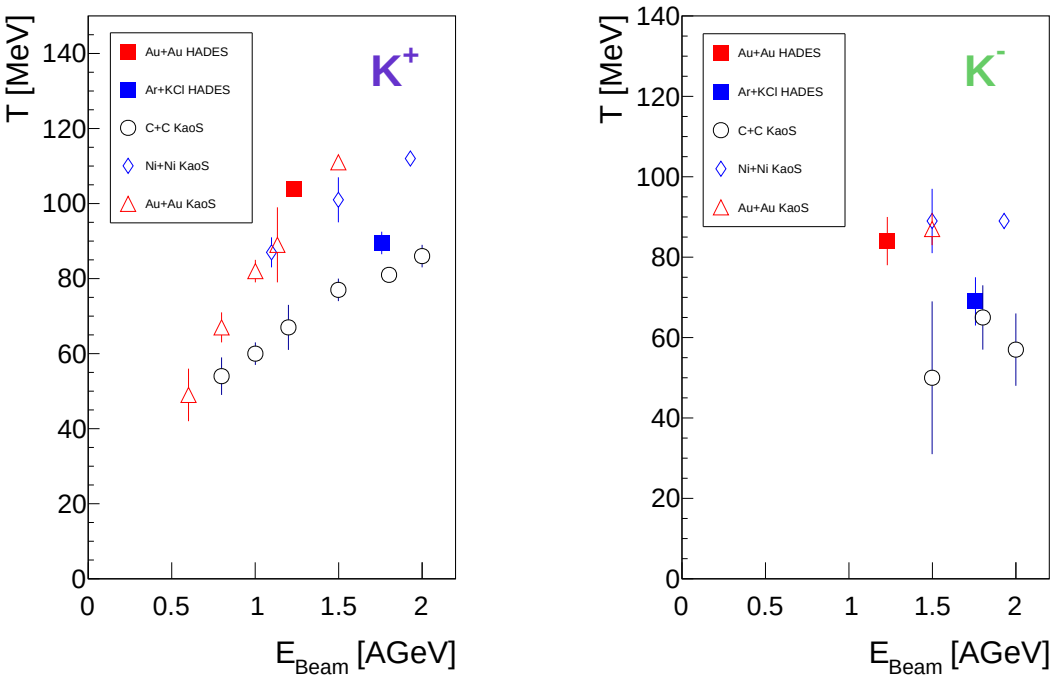

Figure 6.3: Energy and system size dependence of the effective temperatures of K^+ (left) and K^- (right) in comparison to KaoS data [4]. The red squares correspond to the data points obtained in this analysis for Au+Au collisions.

6.1 K^+ / K^- ratio and different freeze-out criteria?

The relative production yield of K^- to K^+ in 0 - 40% most central Au+Au collisions at 1.23 AGeV is deduced to:

$$\frac{K^-}{K^+} = (6.45 \pm 0.77)\text{x}10^{-3}. \tag{6.10}$$

The stated error corresponds to the quadratic sum of the statistical error, as well as the systematic uncertainties on the extrapolation to phase space regions not covered by the spectrometer. The systematic errors from the particle identification method cancel out, as exactly the same cuts have been used.

To get more insight about the particle production of the two kaon species, the ratio is estimated for different collision centralities as shown in figure 6.4. As expected from the similar rise of the K^+ and K^- multiplicities with $\langle A_{part} \rangle$ discussed in the previous section, the K^-/K^+ ratio is constant within errors as a function of centrality. This behavior has been observed by the KaoS collaboration as well and was interpreted as a sign for the coupling of the production of the two kaon species. Since the ratio is nearly independent from the collision centrality, the obtained result can be compared to published inclusive data for various colliding systems from KaoS as a function of $\sqrt{s_{NN}}$ shown in figure 6.5, without correcting for the different centrality selections of the two experiments. The HADES data point fits into the obtained systematic behavior of increasing with $\sqrt{s_{NN}}$. To quantify the increase, the data points at higher energies are parameterized with a linear fit. A slope of m = (0.089 $\pm$ 0.024) GeV is obtained. For the highest beam energies at RHIC and LHC the ratio is approaching unity, because the production happens far above the NN threshold energy [146].

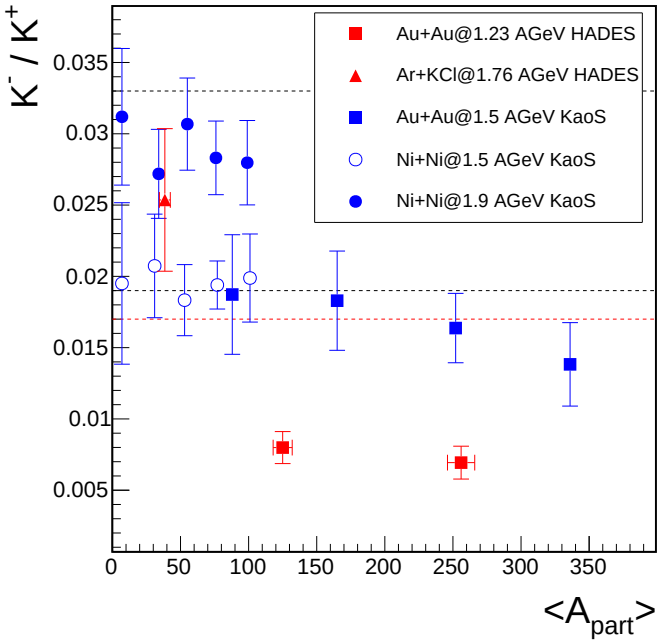

Figure 6.4: K^-/K^+ ratio as a function of centrality compared to results from the KaoS collaboration for different collision systems and energies and the result from HADES for Ar+KCl reactions (see legend). The dashed lines correspond to calculations from the statistical model [145].

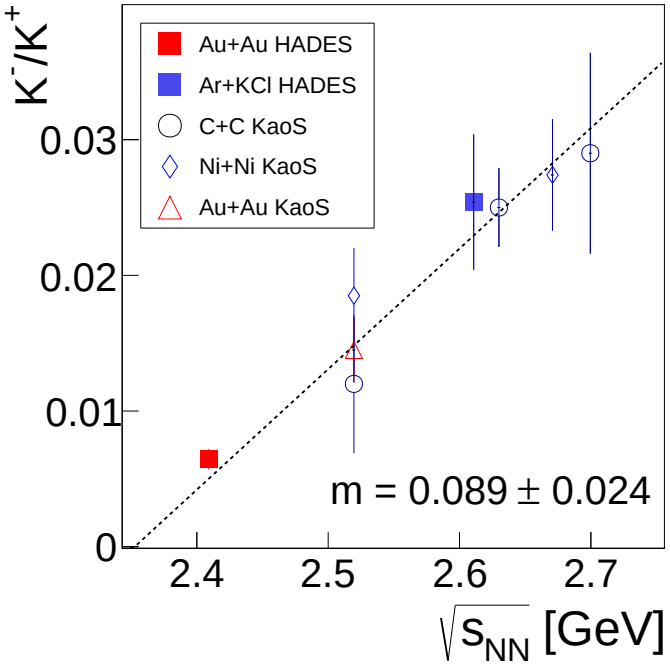

Figure 6.5: K^-/K^+ ratio as a function of center-of-mass energy. The presented data (red square) fits well into the extrapolation from higher energies, realized by fitting the previous results with a linear parameterization (dashed line). A slope of m = (0.089 $\pm$ 0.024) GeV is obtained.

As already mentioned in section 1.7.1, from the observation of the similar centrality dependence of the two kaon species and the systematic lower effective temperature of K^- compared to K^+, the following, at that time conclusive picture from experiment and transport theory about kaon production emerged [1]:

(i) The main production mechanism for K^+ deeply below the free nucleon-nucleon threshold is the accumulation of the necessary energy by multiple collisions of particles inside the collision zone, according to various transport models [106, 147, 148]:

$$\begin{aligned} NN &\rightarrow N\Delta \\ N\Delta &\rightarrow NK^+Y, \end{aligned} \tag{6.11}$$

$$\begin{aligned} NN &\rightarrow NN\pi \\ \pi N &\rightarrow K^+Y \end{aligned} \tag{6.12}$$

with Y, being a hyperon. These processes would most likely occur in the high density phase of the heavy-ion collision. As the K^+, carrying the $\bar{s}$-quark, can be hardly absorbed inside baryon dominated matter, it may leaves the reaction zone relatively undisturbed and carries the information about the hot and dense phase, which would explain the high effective slope parameter.

(ii) The production of K^- was concluded to be coupled to the K^+ production via strangeness exchange reactions:

$$\pi Y \rightleftharpoons K^-N, \tag{6.13}$$

with Y being the hyperons Λ or Σ, which have been produced together with K^+ in the reactions 6.11 or 6.12, and therefore explains the similar centrality dependence observed for the two particles. This secondary reaction happens later in time, because first the hyperon has to be produced and then interact with the pion. Furthermore, the K^- has a high chance to be reabsorbed in the medium quickly by the inverse process. As a result, the reaction might undergoes various cycles till the final K^- freeze-out. Therefore, the lower effective slope of the K^- spectrum is also naturally explained as the K^- leaves the reaction zone on average later in time when the system has cooled further down.

(iii) Furthermore, in the framework of transport models the kaon kinematics can be explained when including in-medium modifications of kaonic properties by a KN potential inside the dense medium. In general, the kaon yields are nicely described when in-medium modifications are incorporated, which is typically modeled by mass shifts of kaons as a function of the density. The potential was obtained in the analysis of out-of plane and sideward flow to be mildly repulsive for the K^+ and attractive for the K^- [149, 150, 151, 152, 153], leading to a lower in-medium mass for K^- and a slightly higher one for K^+. The lowered effective mass of the K^- is enhancing the probability for strangeness exchange reactions. Additionally, the inclusion of the KN potential is accelerating K^+ and decelerating K^-, which explains the different slopes of both kaon species.

Although this is a very consistent picture, transport models are not taking into account or are not able to reproduce the significant ϕ yield measured by HADES and FOPI (compare sections 1.7.2 and 1.7.3). While the influence on the K^+ kinematics is negligible, as it is produced two orders of magnitude above the K^- and ϕ, it has a strong impact on the interpretation of the results for antikaon production and will be discussed in section 6.3. The measured spectra of K^+ will be compared to transport model calculations in the next section.

6.2 Comparison to transport model calculations

In order to draw any conclusion about in-medium nucleon potentials of the kaons, the data has to be compared to transport models. For this analysis three different transport models are utilized: the Ultrarelativistic Quantum Molecular Dynamics (UrQMD 3.4) [85], the Hadron String Dynamics (HSD 711n) [147] and the Isospin Quantum Molecular Dynamics (IQMD c8) [86] model. Whereas UrQMD does not employ any nucleon potentials[3], it is possible to include in-medium modifications of kaons in HSD and IQMD. HSD has implemented modifications of the kaonic properties according to chiral perturbation theory, whereas K^- is treated as off-shell particle in a coupled channel G-matrix approach [154]. In the IQMD model the relativistic mean-field model based on chiral SU(3) is used for both kaons and antikaons. As the influences of the ϕ meson decays on the K^- kinematics, which have been found to be non-negligible (see section 6.3) are underestimated (HSD) or missing (IQMD), only the results for K^+ analysis will be compared to the models.

In the presented analysis the impact parameter distributions are adapted according to the one estimated with the fit of the Glauber model to the experimental data (see section 3.4). The used K^+-nucleon potential is 40 MeV[4] at nuclear ground state density, depends linearly on the density and will be called *full pot* in the following. As already mentioned the potentials are predicted to be slightly repulsive for K^+ and attractive for K^-. The density dependence of the employed potentials lead to an enhancement of the effective energy of K^+ with increasing baryon density, meaning that more energy is needed to produce K^+ in compressed baryonic matter than in a free nucleon-nucleon collision. As a consequence, the modeled K^+ yields are lower if in-medium potentials are incorporated than in calculations without potentials. Furthermore, the potential should accelerate the K^+ mesons, leading to a change of the kinematic distributions. Apart from the nuclear potentials, the charged kaons feel additionally the Coulomb potential that is generated by the surrounding charged hadrons and is in the order of ≈ 20 MeV for the nuclear environment of a Au+Au collision. The Coulomb potential leads to an additional acceleration of the positively and deceleration of negatively charged kaons [156].

Figure 6.6 presents the comparison of the measured multiplicity of K^+ normalized to the mean number of participating nucleons $\langle A_{part} \rangle$ as a function of $\langle A_{part} \rangle$ to the various transport model approaches. The first observation is that all models clearly overestimate the total kaon yield in the measured collision system[5]. The inclusion of in-medium potentials reduces the yields. The IQMD model with full potential seems to be favored by the experimental data. To quantify the increase with the centrality of the collision system, the simulated spectra are fitted with a function according to equation 6.8, which has been already used to compare the different particle species in the experimental data. The resulting exponents α are summarized in figure 6.6. Within the errors, both versions of the HSD and IQMD models reproduce the centrality dependence of the experimental data, whereas the UrQMD model shows a stronger increase of the multiplicities with $\langle A_{part} \rangle$.

In addition to the multiplicities, also the measured kinematic distributions can be compared to the model calculations. The upper row of figure 6.7 shows the comparison between the measured efficiency and acceptance corrected transverse mass spectrum in a region $y_{cm} \pm 0.05$ to the models for 0 - 10% most central collisions. In order to compare only the shape of the distributions, the model calculations are normalized to the real data over the full measured range. The inverse slope of the UrQMD spectrum is less steep than the one of the experimental data. The comparison to HSD and IQMD shows the opposite effect when in-medium potentials are employed: HSD without potential

[3] Except a mean-field potential for pions, which is not employed in the used version.

[4] The strength of the potential of 40 MeV has been obtained by comparing transverse momentum spectra of K^0_S measured in Ar+KCl reactions at 1.76 AGeV with the HADES detector to IQMD calculations [155].

[5] And from the other strange particles K^0_S and Λ [116]

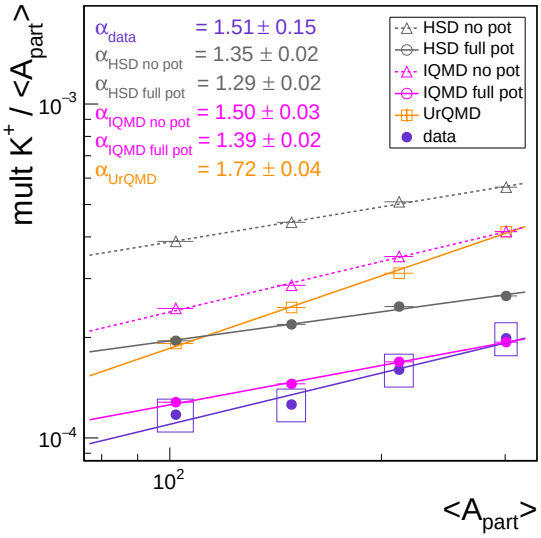

Figure 6.6: Multiplicity of K^+ normalized to the mean number of participating nucleons $\langle A_{part} \rangle$ as a function of $\langle A_{part} \rangle$ for the transport models UrQMD, HSD and IQMD in comparison to the experimental data. The normalized multiplicities are parameterized with function 6.8 (lines) in order to extract the corresponding proportionality factor α stated in the plot.

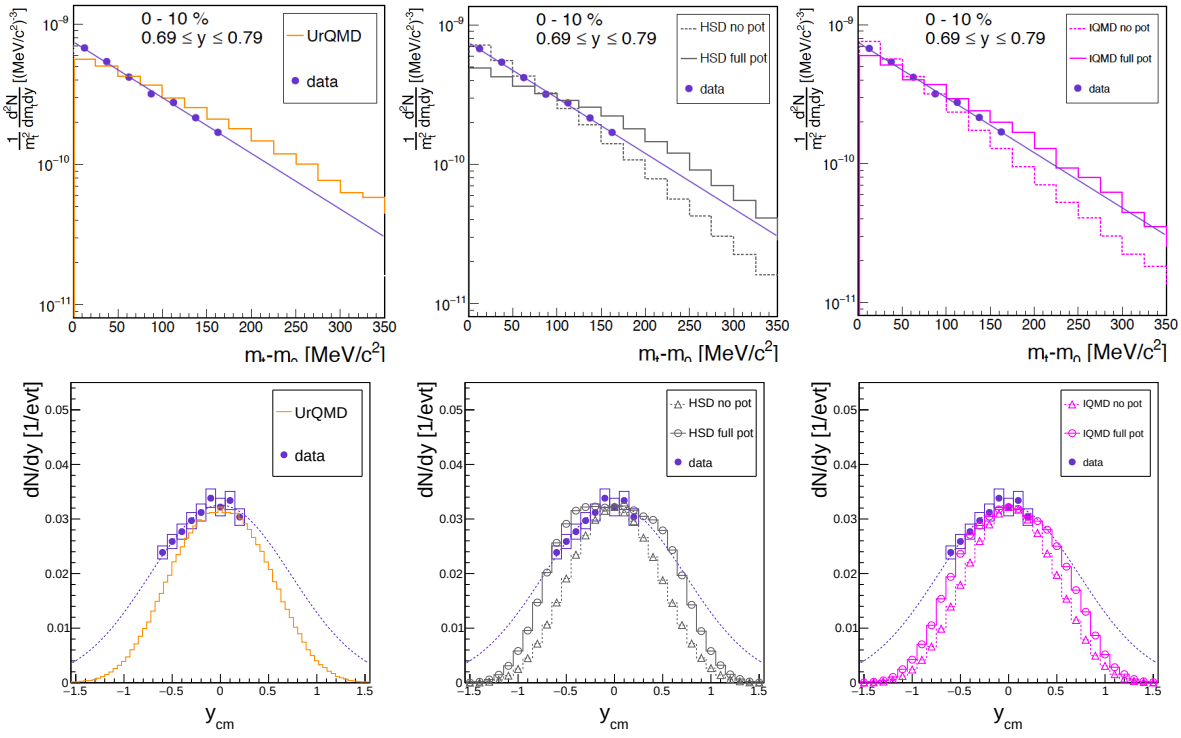

Figure 6.7: Transverse mass spectrum in a rapidity region $y_{cm} \pm 0.05$ (top row) and rapidity density distribution (bottom row) of K^+ for 0 - 10% most central collisions from UrQMD (left), HSD (middle) and IQMD (right) in comparison to the experimental data. The spectra of the transport models are normalized to the experimental data over the full measured range, in order to compare the shape of the distributions.

reproduces the shape of the transverse mass spectrum, whereas the spectrum gets deformed when the potential is switched on. On the other hand, the IQMD model with potential reproduces the shape of the spectrum, however without potential the spectrum is much steeper, leading to a lower inverse slope parameter. The strongest effect of the KN potential is expected to be in the lowest transverse momentum region ($\approx$ 0 - 200 MeV/c). The normalized transverse mass representation hides this effect slightly, as the most sensitive region is compressed to $\approx$ 0 - 50 MeV/c^2. Furthermore, the spectra of K^+ are slightly deformed in the corresponding region by the mentioned Coulomb effects. Therefore, it will be very interesting to compare also transverse momentum spectra of neutral kaons to the models, which will be done in the framework of [116], in order to extract the value of the kaon-nucleon potential.

The lower row of figure 6.7 shows the comparison between the measured rapidity density distribution of K^+ for 0 - 10% most central collision to the models. Again, the simulated distributions are normalized to the experimental data in order to compare only the shapes. The shapes of the distributions without any in-medium potentials look very similar for all models and have a smaller width than the data. The inclusion of the KN potential leads to a broadening of the distribution. Whereas the version of the HSD model with potential overestimates the width of the distribution, the IQMD model is reproducing the shape of the measured data.

In conclusion, we find the best agreement of the experimental data with the IQMD model with a momentum dependent kaon-nucleon potential of 40 MeV at nuclear ground state density.

6.3 ϕ / K^- ratio - What do we learn about K^- production?

The simultaneous measurement of ϕ and K^- in Au+Au collisions at 1.23 AGeV is the ultimate test to pin down the amount of K^- originating from ϕ decays, in order to evaluate the consequence on the K^- production mechanism far below the nucleon-nucleon threshold energy ($\sqrt{s_{exc}^{K^-}}$ = -450 MeV and $\sqrt{s_{exc}^{\phi}}$ = -490 MeV). It is the first measurement of both particle species at such low energies in central Au+Au collisions. The system created in such collisions is large and long-living and is therefore the ideal environment to be sensitive on any in-medium effects and strangeness exchange reactions to occur. The ϕ/K^- multiplicity ratio for 0 - 40% most central collisions is deduced to:

$$\frac{\phi}{K^-} = 0.52 \pm 0.16. \tag{6.14}$$

The quoted error is the quadratic sum of the statistical and the remaining part of the systematic uncertainty, as the contribution from the systematic uncertainty of the K^- identification cancels. Taking into account the $\phi \rightarrow K^+K^-$ branching ratio of 48.9% one finds that $\approx$ 25% of all emitted K^- mesons originate from ϕ decays. In addition, from the observation of ϕ mesons far below its elementary nucleon-nucleon threshold energy, also the direct production of a K^+K^- pair can become a possible production channel for K^- at these energies. The amount of non-resonant K^+K^- pairs in heavy-ion collisions can not be determined precisely, as the invariant mass spectrum contains also fake candidates (see section 4.2.3.2). However, it has been found to be in the same order as the resonant production in p+p reactions slightly above the NN threshold by the ANKE collaboration [157] and can therefore assumed to be in the order of 25% as well. As a consequence, our measurement indicates that strangeness exchange reactions are not as dominant as expected contributing to the production of K^- mesons below its elementary NN threshold (maximum 50%).

For the first time it is possible to deduce the centrality dependence of the ϕ/K^- ratio in the same data sample (see figure 6.8). As expected from the similar rise of the multiplicities with $\langle A_{part} \rangle$ of

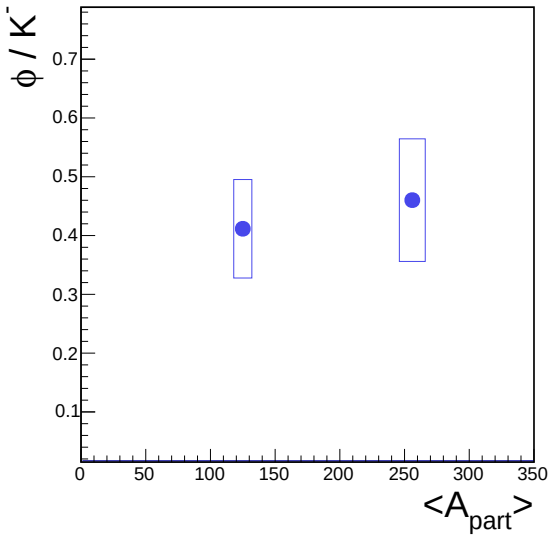

Figure 6.8: Ratio of the ϕ/K^- multiplicities in full phase space as a function of $\langle A_{part} \rangle$

the two particles, the ratio seems to be nearly independent from centrality and allows the comparison of our result from the inclusive analysis of 0 - 40% most central collisions to other experiments, without correcting for different multiplicity selections. Figure 6.9 shows the excitation function of the estimated ratio for the inclusive data sample of 0 - 40% most central reactions in comparison to other experiments. While the ratio is flat at values of around 0.1 - 0.2 for energies above a few AGeV, it is increasing towards lower $\sqrt{s}$ in the region below the elementary production threshold. The new data point from Au+Au collisions at $\sqrt{s}$ = 2.4 GeV obtained in this analysis is higher than the results at $\sqrt{s}$ = 2.6 GeV from smaller colliding systems measured with HADES and FOPI. This behavior is predicted by statistical hadronization model calculations, when open strangeness production is canonically suppressed by introducing the canonical suppression radius R_C. In contrast to the K^- the ϕ meson is not affected by this suppression, because it conserves strangeness by definition ($|s\bar{s}\rangle$). The lines in the figure correspond to calculations from the SHM with different values for R_C. Our new data point is in agreement with a radius $R_C \in$ [2.0, 3.2] fm. The measured excitation function of the ϕ/K^- ratio can be compared to the one obtained with a tuned version of the UrQMD transport model [5], including mass dependent branching ratios of high lying baryon resonances namely the N^*(1990), N^*(2080), N^*(2190), N^*(2250) and N^*(2250) into ϕ, in order to match elementary data on ϕ production (compare section 1.5), which is shown in figure 6.10. The model predicts a maximum of the ratio at the measured center-of-mass energy of $\sqrt{s}$ = 2.4 GeV and agrees with the obtained value from this analysis. Also previous experimental results from HADES and FOPI are well reproduced, while the model undershoots the data at higher energies. It would be interesting to compare also the shapes of the kinematic distributions from the model, like transverse mass spectra, besides only the yield in full phase space, as the spectral shape should depend on the resonance contribution as observed for π^- production (see section 5.2) and investigated in [161] for kaons with respect to the effect of kaon-nucleon potential.

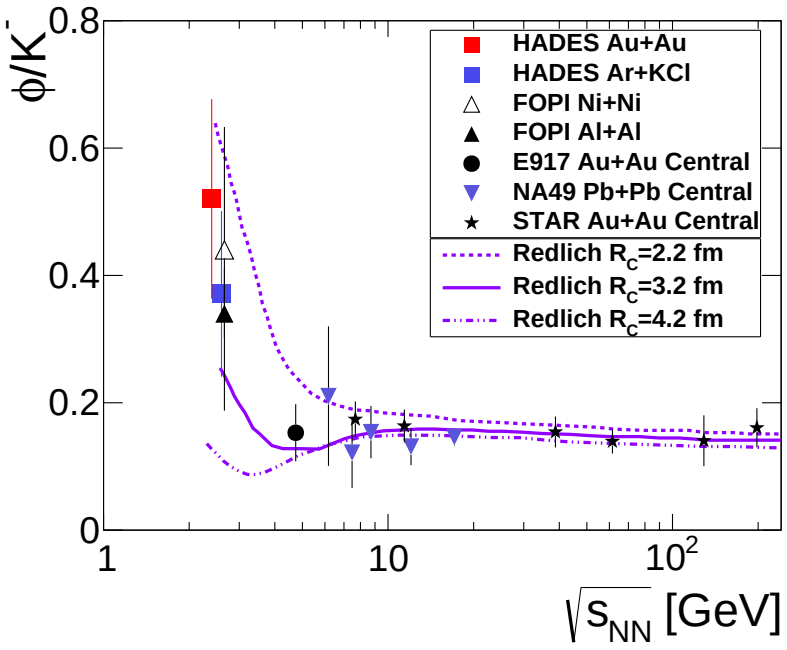

Figure 6.9: Excitation function of the measured ϕ/K^- ratio for various systems and energies (see legend) [2, 121, 3, 158, 159, 160]. While the ratio stays flat for energies above a few AGeV, it substantially increases towards lower energies around the elementary ϕ production threshold. Lines correspond to calculations from a statistical hadronization model for different values of the canonical suppression radius R_C (see legend).

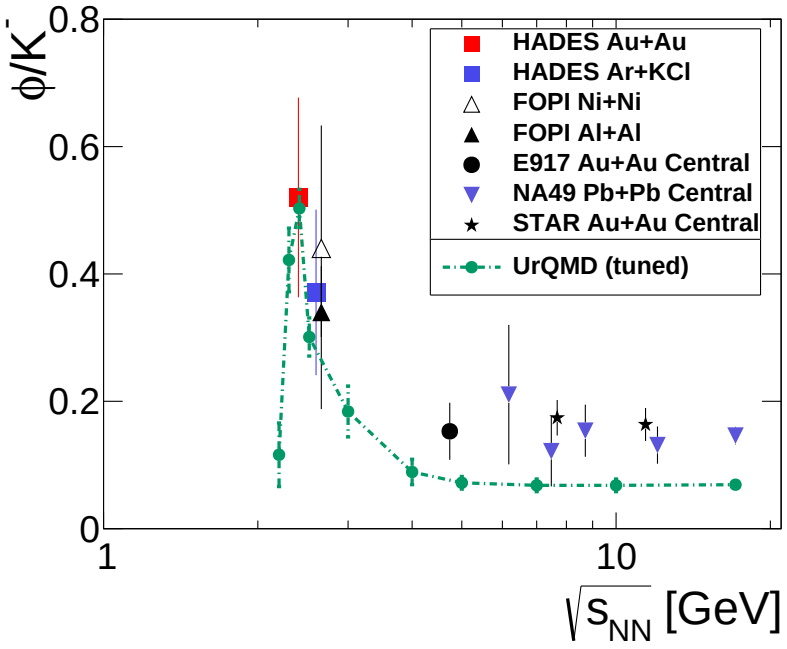

Figure 6.10: Excitation function of the measured ϕ/K^- ratio in comparison to the tuned version of the UrQMD transport model (green points) [5]. The model predicts a maximum of the ratio at the measured center-of-mass energy of $\sqrt{s}$ = 2.4 GeV and agrees with the obtained value from this analysis (red square).

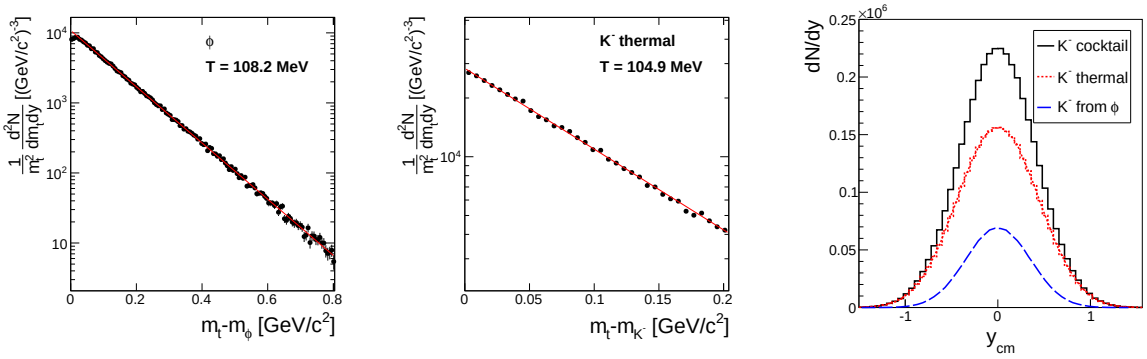

Figure 6.11: Input for the two component cocktail simulation for K^- production. Transverse mass spectrum in a region Δy = 0.1 around mid-rapidity of the ϕ (left) and and thermal K^- (middle) input source from the PLUTO two component cocktail simulation. Red lines correspond to a Boltzmann parametrization, which is used to extract the effective temperature T displayed in the plots. Right: The two components are scaled according to the measured ϕ/K^- ratio, such that 75% are produced thermally (red) and 25% via ϕ feed-down (blue), resulting in the black rapidity distribution.

In order to evaluate the influence of the high amount of ϕ mesons feeding the K^- yield on the kinematic properties of the measured K^-, a two component cocktail is generated with PLUTO [140]. The emission of negative kaons is assumed to arise from two components:

1. Direct thermal production from the reaction zone
2. Production via thermally produced ϕ mesons decaying into K^+K^-

The input for the simulation are the measured effective temperatures of K^+: $T_{K^-_{therm}} = T_{K^+}$ = 104 MeV and of ϕ: T_ϕ = 108 MeV. On the left side of figure 6.11 the transverse mass spectra of the two input sources are shown in a rapidity region Δy = 0.1 around mid-rapidity together with a Boltzmann fit (eq. 5.1) applied in the same acceptance range as accessible in the analysis $m_t - m_0$ < 200 MeV/c^2, to extract the effective temperatures T, which are displayed in the plot. The rapidity density distributions of the K^- produced by the two components are weighted according to the measured ϕ/K^- ratio, such that 75% of all K^- are produced thermally and 25% via ϕ decays. Right side of figure 6.11 shows the normalized rapidity density distributions of the two weighted contributions and the resulting K^- cocktail. In a next step, the two generated transverse mass spectra of K^- are summed up. The resulting distribution is shown on the left side of figure 6.12. Similar as for the data a Boltzmann parametrization is used to determine the inverse slope of the spectrum. First, the fit is performed over the complete simulated transverse mass range, which results an effective temperature of T = 89.5 MeV. When fitting in the experimentally accessible transverse mass region of $m_t - m_0$ < 200 MeV/c^2, a temperature of $T = 83.8^{+5}_{-4}$ MeV is extracted. The errors are estimated by varying the measured ϕ/K^- ratio within the errors. This obtained value agrees within the errors with the measured effective temperature of T_{eff} = (84 $\pm$ 6) MeV of the K^- mesons. On the right side of figure 6.12 the inverse slope parameters of the two generated K^- and of the scaled cocktail transverse mass spectra are displayed as a function of rapidity. Whereas the two generated spectra follow a $\cosh y_{cm}$ distribution, as expected in the simulated purely thermal picture, the inverse slope distribution of the cocktail is slightly deviating from this scenario. Nevertheless, as the deviation is small, the effect on the extracted effective temperature in the experiment assuming the simple scenario of a thermal distribution can be neglected. Furthermore, the resulting rapidity density distribution of

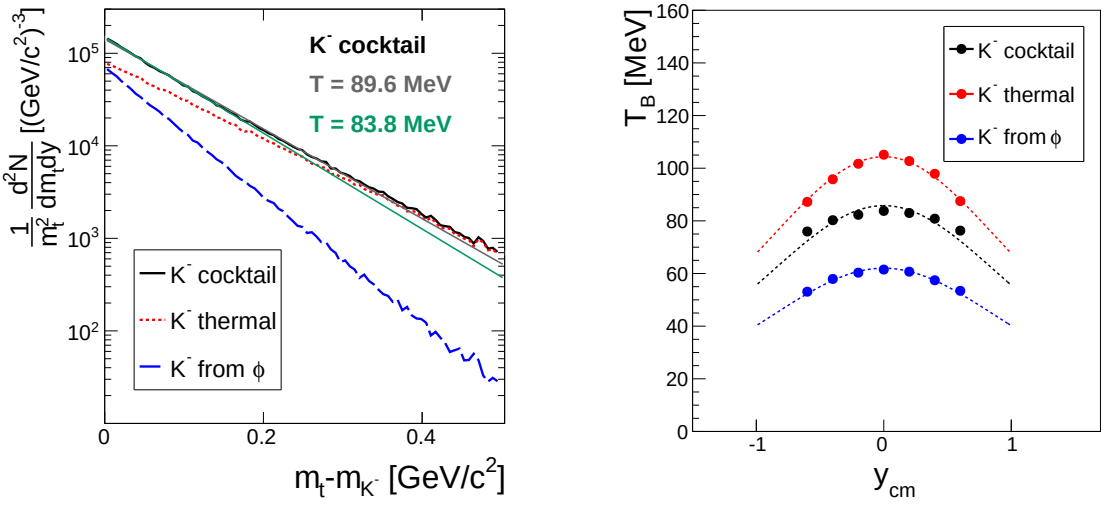

Figure 6.12: Left: Transverse mass spectrum at mid-rapidity of generated K^- from the two input sources ϕ (blue dashed line) and thermal K^- (red dotted line), which have been scaled according to the measured ϕ/K^- ratio and summed up to the final K^- distribution (black solid line). The solid red line corresponds to a Boltzmann fit in the experimentally accessible range up to $m_t - m_0 < 200$ MeV/c^2, whereas the grey line is a fit over the whole simulated transverse mass range, to determine the resulting effective temperature T of the K^- cocktail displayed in the plot. Right: Inverse slope parameter distribution of the two generated K^- spectra (thermal K^-: red, K^- from ϕ: blue) and of the resulting cocktail (black) together with $\cosh y_{cm}$ parameterizations (dashed lines).

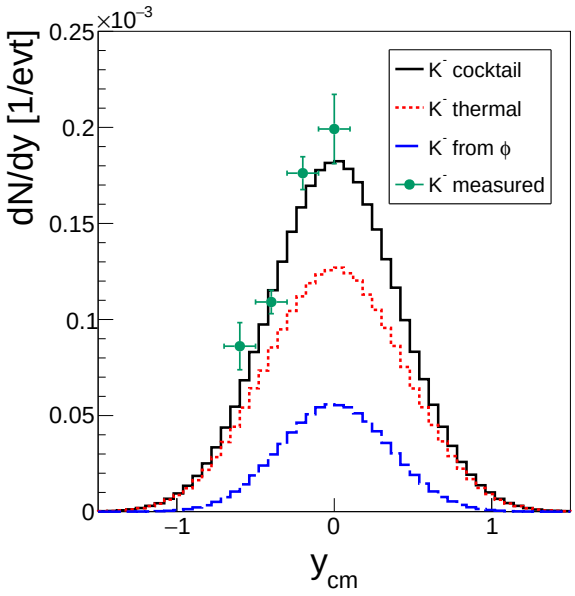

Figure 6.13: Measured rapidity density distribution of K^- (green points) in comparison to the distribution generated with the two component model simulation (black line).

the K^- cocktail is compared to the measured one. The shape of the measured distribution is perfectly reproduced by the cocktail (see figure 6.13). The same procedure is also applied for the results of the centrality dependent analysis. The input for the cocktail are again the measured temperatures of K^+ and ϕ. The two contributions are scaled according to the corresponding measured ϕ/K^- ratio. The input and the resulting effective temperatures from the cocktail are summarized in table 6.1 and compared to the measured effective temperatures of K^- mesons. Also for the two different centrality bins the measured rapidity distribution is well described by the two component model (see figure 6.14) and the inclusion of the ϕ feed-down contribution can explain the lower measured effective temperature of K^- in comparison to the one of K^+.

Centrality	ϕ/K^-	$T_{K^+}^{input}$ [MeV]	T_{ϕ}^{input} [MeV]	$T_{eff}^{cocktail}$ [MeV]	T_{eff}^{data} [MeV]
0 - 40%	0.52 ± 0.16	104	108	84^{+5}_{-4}	84 ± 6
0 - 20%	0.46 ± 0.10	106.5	99	83 ± 4	71 ± 7
20 - 40%	0.41 ± 0.08	94	91	78^{+3}_{-2}	64 ± 5

Table 6.1: Input parameters and result of the two component PLUTO simulation for K^- production, compared to experimental results on the effective temperature T_{eff}^{data} for the different analyzed centrality selections.

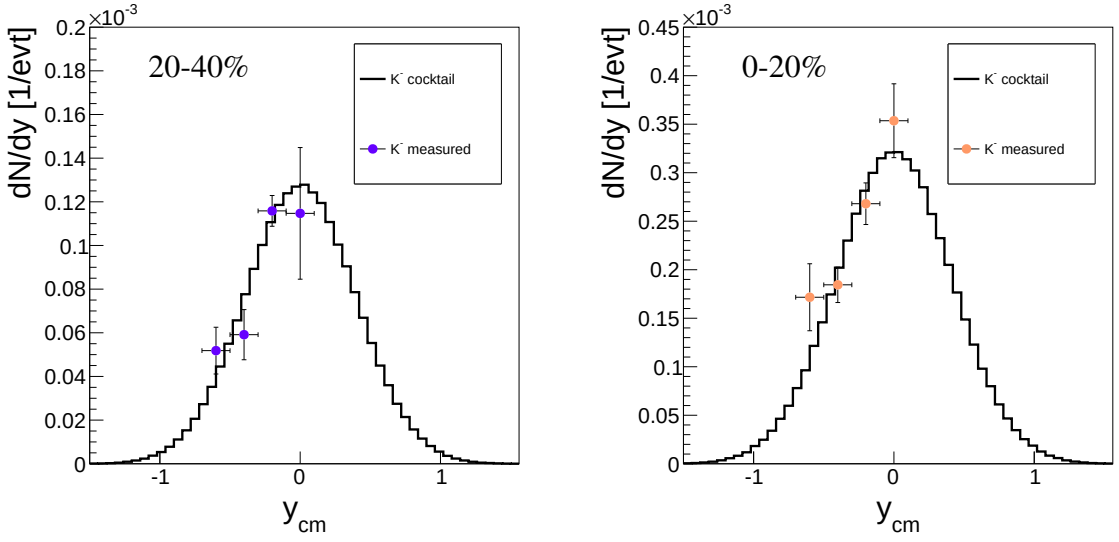

Figure 6.14: Rapidity density distributions of the two component cocktail simulation in comparison to measured data for semi-central (left) and central collisions (right).

In conclusion, we find no indication for different freeze-out criteria of the two charged kaon species, which was concluded from the systematically lower observed effective temperature of K^- in comparison to the one of K^+, when simply taking the contribution from the ϕ feed-down decay into account. This is in slight contradiction to the interpretation of KaoS data with transport models [1], in which the most dominant channel for K^- production are strangeness exchange reactions and kaon-nucleon potentials lead to the deceleration of the K^- spectra. Within the errors of the measurement there is still room for a higher effective temperature of K^+ in comparison to K^-, but its for sure not as prominent, when including the 25% contribution from ϕ feed-down decays, which show different kinematics. The explanation of the observed different K^- kinematics compared to K^+ using only

the ϕ feed-down instead of complicated production mechanisms and in-medium potentials, as used in transport models, is a very simple hypothesis and should with its fewer assumptions be the preferred alternative according to the well-known concept of *Occam's razor*.

6.4 Comparison of the measured particle yields to a statistical hadronization model

Statistical models have been established as a successful and relatively simple tool using only a few parameters to describe particle yields from heavy-ion collisions over almost the complete range of experimentally accessible energies [76]. The extracted freeze-out parameters seem to line up on one common curve in the temperature-baryochemical potential (T-μ_B) plane, which is usually interpreted as a sign for the achievement of (local) chemical equilibrium of the created system in the HIC. Surprisingly also data from lower energies, smaller systems and elementary data can be described by the model, which questions the conclusions of the reached equilibrium in the system and asks for more fundamental interpretation of the good agreement from the model to the data.

The high statistic data set collected by HADES allows for the first time in the low energy regime in Au+Au collisions to compare a very broad set of produced particles, namely protons, $\pi^{\pm}$, $K^{\pm}$ and ϕ from this analysis, as well as the Λ and K^0_S from the analysis performed in [116] and the η from [162] to the statistical hadronization model. We simultaneously apply a fit using the freely available THERMUS (v2.3) code [117] to the measured particle yields, as well as the mean number of participating nucleons $\langle A_{part} \rangle$, whereas the statistical and systematic uncertainties on the obtained yields are added quadratically. A mixed canonical ensemble is used, in which the parameters from the model are calculated grand canonically, except strangeness which has to be exactly conserved and is therefore calculated canonically. This is realized by introducing a sub-volume characterized by the canonical suppression radius R_C. As already mentioned in the previous section 6.3, the ϕ meson is not affected by this suppression radius, as it is conserving strangeness by definition containing the quark content $s\bar{s}$. The charge chemical potential μ_Q is constrained by the initial baryon and charge number of the collision system. Figure 6.15 shows the detailed comparison of the measured yields to the simultaneous fit of the data with the model. We find a good description of all measured particle yields with $\chi^2/ndof$ = 2.3 and extract the freeze-out parameters T = (68 $\pm$ 2) MeV and μ_B = (883 $\pm$ 25) MeV. The radius of the fireball is determined to R_V = (5.8 $\pm$ 0.9) fm and the canonical suppression radius to R_C = (2.1 $\pm$ 0.3) fm.

The obtained freeze-out parameters can be compared to the results from fits to other experimental data, shown in figure 6.16. Whereas the temperature is in the same order of previous results in this energy regime, the baryochemical potential shows a higher value compared to all previous analysis and can not be described by the simple parameterization with fixed energy per nucleon of $E/N \approx 1$ GeV which seems to describe the data over the complete energy range (see section 1.4.1). However, one has to take into account, that previous data sets of Au+Au collisions in the low energy regime contain only a limited amount of different particle species, which are not perfectly constraining all free parameters of the model. The effect of the inclusion of more or less particle species to the fit has been recently studied in [164] for Ar+KCl collisions and was leading to a change of the obtained parameters in the order of 5%.

Recently, the THERMUS code was updated to version v3.0 [165]. The main difference to the version used in this work, is the hadron spectrum included in the model, which was based for v2.3 on the report of the particle data group (PDG) from 2002 [166] but now on the updated report from 2014 [139], which includes additional new states containing strangeness and charm, as well as light

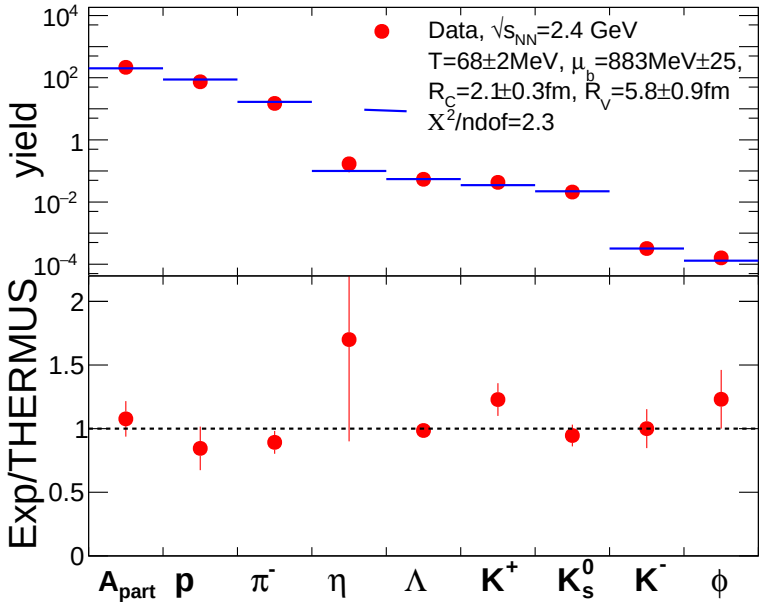

Figure 6.15: Upper row: Comparison of the measured particle yields produced in the 0 - 20% most central collisions (red circles) to the simultaneous fit of the data with THERMUS (v2.3) (blue lines). The obtained fit parameters are summarized inside the box in the upper right corner. Lower row: Ratio of the measured yields and the result from the SHM fit.

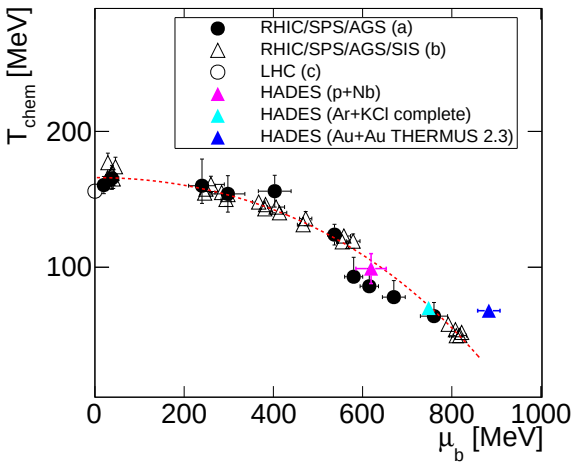

Figure 6.16: Compilation of chemical freeze-out points in the T-μ_B plane. Data taken from [76] (a), [78] (b), [163] (c) and [164] (HADES p+Nb and Ar+KCl). The dashed line correspond to a parameterization with fixed energy per nucleon of 1 GeV [78]. The result from the fit with THERMUS (v2.3) to the data presented in this thesis is shown as dark blue triangle.

nucleons like deuterons. In [164] the two versions have been compared for the HADES data from Ar+KCl reactions. The inclusion of new hadron states lead to a slightly lower baryochemical potential, which is compensated by a larger volume. This results in a lower temperature to compensate a higher pion rate when the volume increases. The deviation of the obtained parameters was found to be in the order of 5% for T and μ_B, but of 25% for the radii. It will be interesting to compare the measured data also to this version of the statistical model.

6.4.1 Comparison of the chemical to the kinetic freeze-out temperature of the produced system

The obtained chemical freeze-out temperature from the SHM fit to the measured particle yields can be compared to the kinetic freeze-out temperature of the system, which has been extracted from the transverse mass spectra of the particles. Figure 6.17 shows the measured effective temperatures as a function of the mass of the particles obtained in this analysis, as well as of K^0_S and Λ from the analysis performed in [116], for 0 - 20% most central collisions. The K^- is not included, as the effective temperature has to be corrected for the ϕ feed-down decay (see section 6.3) and is afterwards similar to the one of the other kaon species. In a purely thermal picture, the effective temperature directly corresponds to the kinetic freeze-out temperature of the system, but as already discussed in chapter 5, the created system in a heavy-ion collision can rather be characterized by a thermal source which is expanding radially, leading to the deformation of the transverse mass spectra of the particles from a pure thermal distribution. In this picture, the effective temperature is rather a composite of a pure kinetic component T_{kin} and a component depending on the square of the radial flow velocity β_r and the particle mass m:

$$T_{eff} = T_{kin} + \beta_r^2 \cdot m. \tag{6.15}$$

Therefore, the transverse mass spectra of protons are (because of the high mass of protons), more sensitive to this deformation as the kaons and pions and have been used to extract the kinetic freeze-out temperature of T_{kin} = (70 $\pm$ 4) MeV and radial flow velocity β_r = 0.41 $\pm$ 0.1 using a Siemens-Rasmussen parameterization (see section 5.1). All effective temperatures are above the chemical freeze-out temperature obtained from the SHM fit to the particle yields, which is a contradiction to the purely thermal assumption, as the kinetic freeze-out can only happen after the chemical freeze-out and hence, at lower temperatures.

Additionally, the effective temperatures of pions, kaons and protons seem to increase almost linearly with mass, whereas the heavier hadrons carrying strangeness ϕ and Λ show a temperature within the same order of the lighter kaons. The linear increase of the temperature with mass strongly supports the assumption of additional radial flow of the created system according to equation 6.15. The effective slope for m = 0 would correspond in this very naive picture to the kinetic freeze-out temperature of the system. In order to extrapolate to zero mass, the effective slopes of π^-, K^+ and p are fitted with the linear function 6.15. The resulting kinetic freeze-out temperature is T^{fit}_{eff} = (71.5 $\pm$ 4.2) MeV and is consistent with the measured freeze-out temperature from proton analysis and is furthermore in the same order as the chemical freeze-out temperature from the SHM fit. The square root of the slope of the linear function can be related to the radial flow velocity of the system in this naive picture and is extracted to β_r^{fit} = 0.28 $\pm$ 0.09, which is lower than the one extracted with the Siemens-Rasmussen parameterization. It would be important to include the light nuclei deuterons, tritons and ^3He into the analysis, as there are most sensitive on radial flow due to their high masses.

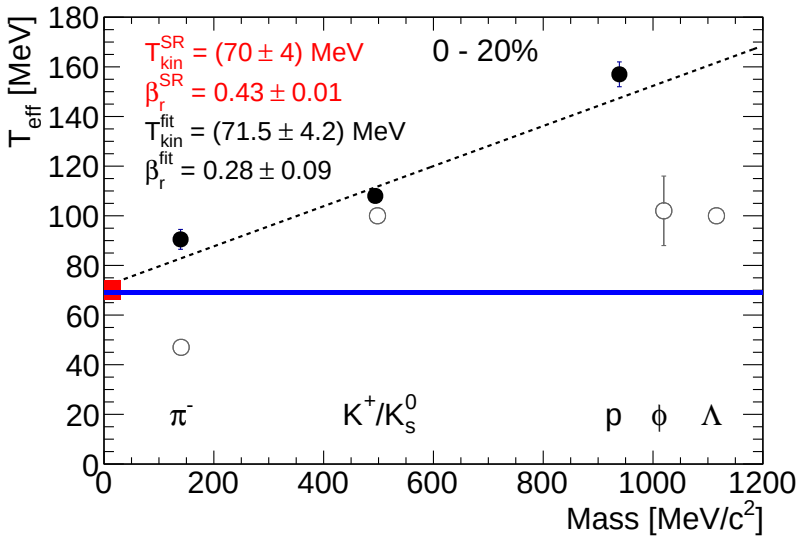

Figure 6.17: Effective temperatures as a function of the mass of the particles obtained in this analysis, as well as K^0_S and Λ from the analysis performed in [116] for 0 - 20% most central events in comparison to the extracted chemical freeze-out temperature from the SHM fit to the measured particle yields T_{chem} = (69 $\pm$ 1) MeV (blue line) and the kinetic freeze-out temperature obtained with a simultaneous Siemens-Rasmussen fit to the transverse mass spectra of protons T^{SR}_{kin} = (70 $\pm$ 4) MeV. The effective temperatures of π^-, K^+ and p are fitted with a linear function in order to extrapolate to zero masses and extract the kinetic freeze-out temperature T^{fit}_{kin} and radial flow velocity β^{fit}_r.

Chapter 7

Summary and Outlook

In this thesis the sub-threshold production of charged kaons and ϕ mesons in Au+Au collisions at $\sqrt{s_{NN}}$ = 2.41 GeV is studied. The main focus of this investigation is to differentiate between the different production mechanisms of K^- in heavy-ion collisions deeply below the free nucleon-nucleon threshold and a thermodynamic description of the created system.

The data taking took place in April/May 2012 with in total 557 hours Au beam with 1.23 AGeV kinetic energy on a 15-fold segmented Au target. Due to the high trigger rate of up to 8 kHz in spill, up to 7.3x10^9 reactions could be recorded. The trigger selected collisions in which at least 20 charged particles were registered inside the TOF-detector, corresponding to 40% most central collisions. After a careful event and track selection, the latter one based on χ^2 track quality parameters obtained from a Runge-Kutta tracking algorithm in order to suppress contributions from corrupted pion and proton tracks, the charged kaons are identified using their momentum, time-of-flight and energy loss information inside the detector material. The residual background coming from the mentioned corrupted pion and proton tracks hampering the kaon signals, is subtracted individually in the analyzed phase space cells using an iterative fitting procedure. The neutral ϕ meson is reconstructed via its decay into charged kaons, by calculating the invariant mass of all kaon candidates in each reaction. The combinatorial background is subtracted using the mixed-event method. In order to obtain the multiplicities of the particles, the differential count rates are corrected for the efficiency and acceptance of the spectrometer using a carefully tuned Monte-Carlo simulation. Furthermore, the spectra are extrapolated to phase space regions not covered by the detector, assuming thermal production from a homogenous source. In order to investigate any possible detector effects and study the thermodynamic properties of the created system, also protons and negative pions are analyzed in the framework of this thesis. The analysis is repeated for four (K^+, π^-, p), respectively two (K^-, ϕ), different centrality classes to get more inside about the strangeness production mechanisms in heavy-ion collisions.

The estimated particle multiplicities follow the clear hierarchy of the excess energy: $41.5 \pm 2.1|_{sys}$ protons at mid-rapidity per unit in rapidity, $11.1 \pm 0.6|_{sys} \pm 0.4|_{extrapol}$ π^-, ($3.01 \pm 0.03|_{stat} \pm 0.15|_{sys} \pm 0.30|_{extrapol}$)x$10^{-2}$ K^+, ($1.94 \pm 0.09|_{stat} \pm 0.10|_{sys} \pm 0.10|_{extrapol}$)x$10^{-4}$ K^- and ($0.99 \pm 0.24|_{stat} \pm 0.10|_{sys} \pm 0.05|_{extrapol}$)x$10^{-4}$ ϕ per event for 40% most central collisions. The multiplicities of charged kaons and ϕ are found to increase more than linear with the mean number of participating nucleons $M \propto \langle A_{part} \rangle^{\alpha}$. This behavior can be explained as the measured collision energy is below the elementary production threshold energy of the strange particles. Therefore, they can only be produced in multi-particle interactions, which are more likely to occur the more particles are present in the created system and the denser the medium gets. In this picture it is very surprising

that the proportionality of this increase is the same within errors of all particles, as the K^- and ϕ are produced much farther below the threshold than the K^+.

The centrality dependence and kinematic spectra of K^+ are compared to three different transport models: IQMD [86], UrQMD [85] and HSD [147]. All models overestimate the kaon multiplicity. The inclusion of in-medium potentials reduces the yields, which seems to be favored by the data. The centrality dependence of IQMD and HSD is in agreement with the data, whereas UrQMD shows a stronger increase with $\langle A_{part} \rangle$. Also the shape of the kinematic distributions can not be reproduced perfectly by the models. The width of the rapidity density distribution from the models without potentials is too small compared to data, however it is well reproduced by the IQMD model when in-medium potentials are incorporated. In order to pin down the value of the kaon-nucleon potential the transverse momentum spectra of neutral kaons are compared to the various models in the framework of [116]. This has the huge advantage in comparison to charged kaons, that no Coulomb interaction is deforming the spectra additionally and that the weakly decaying K^0_S can be reconstructed via its decay into charged pions in a wider acceptance. Furthermore, it will be interesting to study the elliptic flow of kaons, as it is predicted to be sensitive on the equation of state and in-medium potentials of the transport models [149, 152].

As expected from the similar rise of the multiplicities, the K^-/K^+ ratio is relatively constant as a function of centrality and obtained to be (6.45 $\pm$ 0.77) x 10^{-3} for the 40% most central collisions, which follows the energy dependence obtained from other experiments [4]. Furthermore, the effective temperature of K^- is for all centrality selections systematically below the one of K^+ which was also observed by previous experiments. This systematic behavior can be traced back to the high amount of produced ϕ mesons feeding the K^- yield even at this low energy.

The ϕ/K^- ratio is obtained to be 0.52 $\pm$ 0.16, meaning that $\approx$ 25% of all measured K^- originate from ϕ decays. Again this ratio is constant as a function of centrality. The value is higher than the ratio obtained from previous experiments at higher center-of-mass energies, which can be explained by a tuned version of the UrQMD transport model [5], when the ϕ production is enhanced due to additionally included higher mass baryonic resonances and by statistical hadronization models when open strangeness is suppressed by introducing a canonical suppression radius R_C. It will be very interesting to compare also the measured kinematic spectra, in addition to the production yields, to the tuned model in the future. The influence of the ϕ contribution on the observed K^- kinematics is studied using a two component PLUTO simulation. Hereby the K^- spectra are generated from two sources, thermally produced ϕ mesons decaying into K^- with the measured temperature for ϕ mesons of T^{ϕ}_{eff} = 103 MeV and directly thermal produced K^- with the input temperature of $T^{K^+}_{eff}$ = 104 MeV as measured for K^+. The contributions are scaled according to the measured ϕ/K^- ratio. The 25% contribution from ϕ decays lead to a softening of the transverse mass spectrum and therefore a lower effective temperature of T^{cock}_{eff} = (84 $^{+5}_{-4}$) MeV, which is in perfect agreement with the measured effective temperature of K^-. As a result we find no indication for strangeness exchange reactions being the dominant mechanism for K^- production at SIS18 energies.

Finally, the obtained particle yields for the 20% most central collisions are confronted with a statistical hadronization model fit [117] in order to extract the chemical freeze-out parameters of the system. The temperature is obtained to T_{chem} = (68 $\pm$ 2) MeV and the baryochemical potential μ_B = (883 $\pm$ 25) MeV. Whereas the temperature is comparable to the results from other experiments in the analyzed energy regime, the baryochemical potential shows a higher value than expected when assuming a simple parameterization of a fixed energy per nucleon of 1 GeV. Furthermore, the chemical freeze-out temperature is comparable to the kinetic freeze-out temperature of the system. This temperature is obtained assuming a homogenous source which is expanding radially, by fitting either

the transverse mass spectra of protons with a Siemens-Rasmussen function T_{kin}^{SR} = (70 $\pm$ 4) MeV or assuming a linear dependence of the effective temperature on the mass of the particles T_{kin} = (71.5 $\pm$ 4.2) MeV. The radial flow velocity of method one is with β_r^{SR} = 0.43 $\pm$ 0.01 higher compared to the second method β_r = 0.28 $\pm$ 0.09. It will be necessary in the future to include also light fragments, like deuterons and tritons into the analysis, as they are more sensitive on radial flow effects due to their higher masses. Recently, the used THERMUS code has been updated to version v3.0 [165], it will be very interesting to compare the measured particle yields also to this version.

7.1 HADES at FAIR

In the future HADES will continue to do detailed studies of the properties of dense baryonic matter at the Facility for Antiproton and Ion Research (FAIR). Starting in 2018 with the so-called FAIR phase 0, HADES will do measurements of elementary, like pion- and proton-induced reactions, as well as heavy-ion collisions with beams provided by the upgraded SIS18 accelerator. Of special interest is the planned measurement campaign of Ag+Ag collisions with the highest achievable energy at SIS18 of 1.65 AGeV. The main focus is hereby put on the production of Ξ^- mesons.

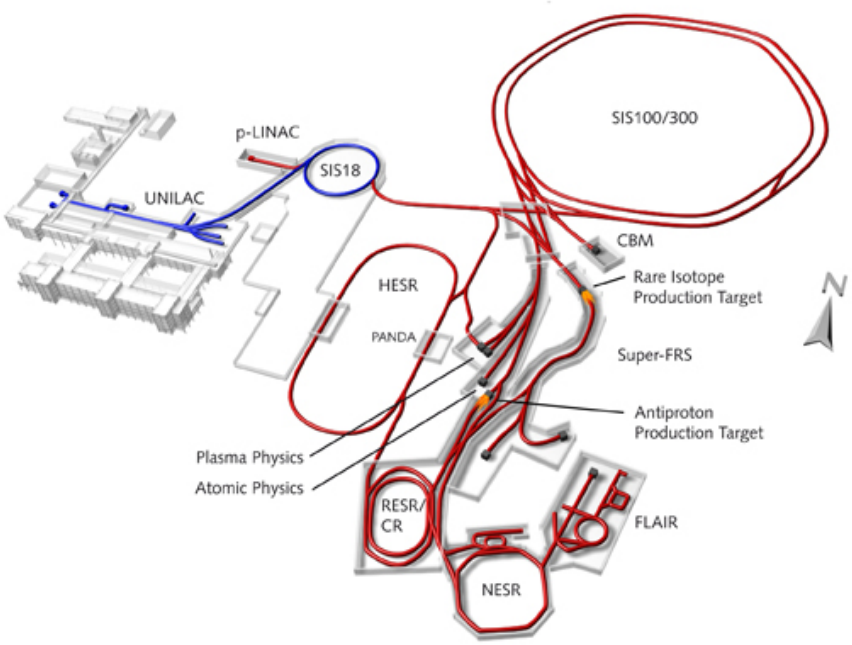

Figure 7.1: Sketch of the planned Facility for Antiproton and Ion Research (red), which will be newly build and complement the already existing accelerator complex at GSI (blue). The HADES detector will be installed in the CBM cave. [167]

Later on HADES will be installed in the same cave as the Compressed Baryonic Matter (CBM) experiment at the newly build SIS100 accelerator (see figure 7.1 and [167] for more details) and will perform important reference measurements for the latter one at beam energies of up to 8 AGeV. The systems created in such collisions will have the highest baryon densities comparable to those achieved inside neutron stars and is currently not achievable at any facility. One topic of interest is hereby the study of multistrange baryons (Σ^-, Ω^-), to probe hyperon interaction at highest baryonic densities.

7.2 Detector upgrades

Until the upcoming measuring campaigns starting in 2018, various upgrade projects are ongoing.

7.2.1 Electromagnetic calorimeter

For the future measurements at FAIR, an electromagnetic calorimeter (ECAL) will complement the HADES setup. The ECAL will allow to reconstruct neutral mesons via their decay into photons, like π^0 and η[1], and improve the electron-hadron separation at high momenta (over 400 MeV/c) in dilepton analysis. Furthermore, also photons from strange resonances (e.g. $\Lambda(1405)$ and $\Sigma(1385)$) can be detected. The detector will follow the HADES structure by being divided into six different sectors, covering almost the full azimuthal angle. It will be placed behind the RPC-detector, covering polar angles of $16^\circ \leq \theta \leq 45^\circ$ and will replace the Pre-SHOWER detector. The calorimeter will consists of 978 modules, consisting of a lead glass Cherenkov counter, photomultipliers, HV divider and an optical fiber. For more details see [168].

7.2.2 RICH-detector upgrade

The RICH-detector will be upgraded by installing a new UV photo detector into the current setup. The detector will be based on photo multipliers (MAPMT) which will be used for the RICH detector of the CBM experiment in the future. The replacement of the existing CsI photocathodes with MAPMTs will significantly enhance the e^+/e^- identification capability. [169].

7.2.3 Forward detector

In order to increase the HADES acceptance for exclusive channels, which is essential for acceptance corrections and partial wave analysis, hyperon reconstruction and reactions with small Q values, a forward detector will be installed at low polar angles. This forward detector is planned to cover the region between $0.5^\circ \leq \theta \leq 6.5^\circ$ and will replace the old forward wall. The detector will consist of two tracking stations with eight planes each, based on straw tubes for tracking. Furthermore, there will be a RPC for time-of-flight measurement and a segmented scintillator for energy loss information. [170].

7.2.4 MDC upgrade

In order to prepare the HADES tracking system for future runs with higher intensities and occupancies at the SIS18 and SIS100 accelerator, the drift chambers are being upgraded. To prevent the drift chambers from further aging effects, the drift gas in the outer chambers will be changed from Ar/isobutane to Ar/CO_2, as already happened for MDC I (previous to the Au+Au beam time) and MDC II (previous to the π beam time). To improve the stability of the front-end electronics of the chambers, improve the signal-to-noise ratio, reduce crosstalk between the wires and increase the bandwidth of data taking, an upgrade of the front-end electronics is in progress. Furthermore, to improve the redundancy and precision of the tracking, it is planned to restructure the geometry of the drift chambers by changing the pitch of the sense and/or cathode wires. [171].

[1] Up to now these meson could only be reconstructed via the conversion method, which suffers from very small conversion probabilities [162].

Chapter 8

Zusammenfassung

8.1 Motivation

Relativistische und ultra-relativistische Schwerionenkollisionen bieten die einzigartige Möglichkeit heiße und dichte hadronische Materie im Labor zu erzeugen und durch Variation der Reaktionssysteme und Kollisionsenergien das Phasendiagramm stark wechselwirkender Materie zu untersuchen. Bei Strahlenergien von 1 - 2 AGeV, welche am SIS18 Beschleuniger des Helmholtzzentrums für Schwerionenforschung GSI erreicht werden, wird die Kernmaterie auf eine Dichte auf das 2 - 3-fache nuklearer Grundzustandsdichte ρ_0 komprimiert. Diese Hochdichtephase ist jedoch mit 10^{-22} s sehr kurzlebig, weshalb man ausschließlich anhand der Reaktionsprodukte und dem Vergleich zu theoretischen Modellen Rückschlüsse auf die Eigenschaften des erzeugten Systems ziehen kann. Insbesondere die Produktion von Hadronen mit Seltsamkeitsinhalt unterhalb der elementaren Nukleon-Nukleon Schwelle sind sensitive Sonden für die kreierte Hochdichtephase. Zum Beispiel kann aufgrund des Verhältnisses von positiven Kaonen, welche in leichten Kollisionssystemen produziert wurden zu solchen aus der Kollision schwerer Kerne, auf die nukleare Zustandsgleichung geschlossen werden. Des Weiteren kann von Phasenraumverteilungen und sogenannten Flusseffekten die Modifizierung von Kaon-Nukleonen Potentialen studiert werden. Anhand von effektiven Modellen ist vorhergesagt, dass K^+ Mesonen ein repulsives und Antikaonen K^- ein attraktives Potential fühlen.

In den letzten zwei Dekaden wurden bereits detaillierte experimentelle Untersuchungen über die Produktion und in-medium Modifikation von Kaonen mithilfe des KaoS-, FOPI- und HADES-Detektors durchgeführt. Die Interpretation erfolgte meist mithilfe von mikroskopischen Transport-Modellen, in denen die Produktion in Schwerionenkollisionen unterhalb der NN-Schwelle über das Akkumulieren von Energie in Mehrstufenprozessen oder Austausch des Quark-Inhalts stattfindet. Hierbei ist es Voraussetzung, dass die Modelle möglichst viele Observablen gleichzeitig beschreiben können. Aus den experimentellen Beobachtungen der KaoS-Kollaboration, dass die geladenen Kaonen eine sehr ähnliche Abhängigkeit von der Zentralität des Schwerionenstoßes, jedoch die K^- systematisch niedrigere effektive Temperaturen aufweisen, wurde geschlossen, dass der dominante Produktionskanal für Antikaonen sogenannte *strangeness exchange* Reaktionen sind, bei dem ein Λ-Baryon, welches zuvor gekoppelt mit einem K^+ aufgrund von Seltsamkeitserhaltung produziert wurde, mit einem Pion aus der Umgebung das seltsame Quark austauscht.

Erst die Messungen mit dem FOPI- und HADES-Detektor ermöglichten die Rekonstruktion von ϕ-Mesonen, die zu 48,9% in geladene Kaonen zerfallen. Das Verhältnis von produzierten ϕ zu K^- wurde für mittelschwere Systeme (Ar+KCl, Ni+Ni und Al+Al) im Energiebereich von 1,76 - 1,91 AGeV zu 0.4 bestimmt, was bedeutet, dass ca. 20% aller gemessen K^- aus ϕ-Zerfällen resultieren.

Da die Kinematik sich stark unterscheidet, je nachdem ob ein Kaon direkt oder über den Zerfall von ϕ produziert wurde, ist es unverzichtbar den relativen Beitrag dieser Quelle zu berücksichtigen bevor Rückschlüsse auf in-Medium Modifikationen oder Potentiale anhand der kinematischen Verteilungen geschlossen werden. Das Verhältnis von ϕ/K^- ist für höhere Energien konstant und steigt um den Schwellenbereich stark an. Dieser Trend ist von Statistischen Hadronisations Modellen (SHM) vorhergesagt, wenn ein kanonischer Seltsamkeitsunterdrückungsradius R_C eingeführt wird, welcher nur auf K^-, jedoch nicht auf das ϕ wirkt. Die simultane Rekonstruktion von geladenen Kaonen und ϕ-Mesonen in Au+Au Kollisionen bei 1,23 AGeV ist die bisher niedrigste Messung unterhalb der elementaren NN-Schwellle und wird es ermöglichen mithilfe von Vergleichen zu Transport- und Statistischen Hadronisations-Modellen Rückschlüsse auf die fundamentalen Produktionsmechanismen von seltsamen Hadronen zu ziehen.

8.2 Hadronenrekonstruktion in Au+Au Kollisionen mit dem HADES Detektor

Das High Acceptance Di-Electron Spectrometer HADES ist speziell für die Messung von seltenen Sonden, Dielektronen Paaren und Hadronen mit Seltsamkeitsinhalt, ausgelegt. Hierfür ist ein sehr schneller Detektor mit einer hohen Akzeptanz von Nöten. HADES erfüllt diese Kriterien, da es den kompletten Polarwinkel und einen Azimuthalwinkel Bereich von 18 - 85° abdeckt und Triggerraten von bis zu 20 kHz erreichen kann. Das Spektrometer besteht aus sechs identischen Sektoren, die symmetrisch die Strahlachse umschliessen. Die Spuren geladener Teilchen werden in den Dirftkammern rekonstruiert. Es befinden sich jeweils zwei Kammern vor und zwei Kammern hinter einem Magnetfeld, wodurch die Teilchen auf gekrümmte Bahnen gezwungen werden und ihr Impuls und ihre Ladung bestimmt werden kann. In Kombination mit der Messung der Flugzeit der Teilchen durch die Koinzidenzmessung zwischen einem Diamantzähler kurz vor dem Target zur Messung des Reaktionsnullpunktes und dem Signal des jeweiligen Teilchens in dem sogenannten META-Detektor, bestehend aus einer Resistive Plate Chamber (RPC) bei kleinen Polarwinkeln (18 - 45°) und einer TOF-Szintillatorwand bei großen Winkeln (44 - 85°), kann das Teilchen eindeutig identifiziert werden. Um die Teilchenidentifikation zu verbessern kann zusätzlich die Information über den spezifischen Energieverlust des Teilchens in den Driftkammern und im TOF-Detektor verwendet werden. Für die Leptonenidentifikation steht ein Ring Imagining CHerenkov-Detektor zur Verfügung.

Die Datenaufnahme fand im April/Mai 2012 mit insgesamt 557 Stunden gemessenen Au-Strahl mit 1,23 AGeV kinetischer Energie auf einem Au-Target, bestehend aus 15 Segmenten statt. Durch die hohe Triggerrate von bis zu 8 kHz konnten insgesamt 7,3x10^9 Reaktionen aufgezeichnet werden. Der Trigger selektierte Reaktionen bei denen mindestens 20 geladene Teilchen im TOF-Detektor landeten, was mithilfe einer Glauber-Monte-Carlo Simulation einer Zentralitätsselektion von 0 - 40% der zentralsten Stöße zugeordnet werden konnte. Nach einer sorgfältigen Auswahl von den aufgezeichneten Kollisionen und rekonstruierten Spuren können die Teilchen identifiziert werden. Das neutrale ϕ-Meson wird über seine geladenen Zerfallsprodukte im Kanal $\phi \rightarrow K^+K^-$ rekonstruiert. Hierbei wird die invariante Masse aller Kombinationen von Kaonen Kandidaten in einer Reaktion berechnet. Der Untergrund wird mit der sogenannten Mixed-Event Methode bestimmt und abgezogen. Die erhaltenen Teilchenspektren müssen individuell auf die Akzeptanz des Spektrometers und Effizienzen der Spurrekonstruktion und angewandten Schnitte zur Teilchenidentifikation korrigiert werden. Dies erfolgt über Simulationen. Hierfür ist es insbesondere wichtig, dass die Simulation sehr gut alle gemessenen Observablen wiederspiegelt.

8.3 Ergebnisse

Um die Multiplizitäten der Teilchen bestimmen zu können müssen die auf Effizienz und Akzeptanz korrigierten Spektren zu Phasenraumbereichen extrapoliert werden, die nicht von dem HADES Detektor abgedeckt sind. Zunächst werden die Spektren zu ungemessenen transversalen Massenbereichen extrapoliert. Dies erfolgt mit Boltzmann-Funktionen. Die Boltzmann-Funktionen beschreiben die Teilchenproduktion von einer statischen thermischen Quelle, wobei die Temperatur durch den inversen Steigungsparameter bei Schwerpunktsrapidität gegeben ist. In einer Au+Au-Kollision herrschen jedoch grosse Drücke, weshalb das System zusätzlich radial expandiert. Diese Expansion führt zu einem züsätzlichen massenabhängigen Beitrag zu den inversen Steigungsparametern, der quadratisch mit der radialen Flußgeschwindigkeit β_r skaliert und zu einer Verformung der Spektren führt. Dieser Effekt ist für die schweren Protonen deutlicher zu sehen, weshalb die Extrapolation mithilfe von Siemens-Rasmussen-Funktionen erfolgt, die die radialen Flußeffekte direkt berücksichtigt. Der Hauptproduktionskanal von negativen Pionen ist der Zerfall von Δ-Resonanzen, was zu einer Verformung von den transversalen Massenspektren führt. Der Verlauf der π^- Spektren kann jedoch mit einer Kombination aus zwei Boltzmann-Funktionen hinreichend gut beschrieben werden. Nach Integration der gemessenen Daten und Extrapolation zu ungemessenen transversalen Massenbereichen kann die Rapiditäts-Dichteverteilung der Teilchen bestimmt werden. Diese werden mithilfe von Gauss-Funktionen zu Rapiditätsbereichen extrapoliert, die nicht vom Spektrometer abgedeckt sind, um die Multiplizität zu bestimmen. Um mehr über die Produktion der Teilchen zu lernen wird die Analyse für verschiedene Zentralitätsbereiche wiederholt. Für Protonen, π^- und K^+werden die Daten der 0 - 40% zentralsten Kollisionen in vier verschiedene Bereiche aufgeteilt, für die seltener produzierten Teilchen K^- und ϕ ist eine Einteilung in zwei verschiedene Klassen möglich. Die erhaltenen Multiplizitäten und effektiven Temperaturen können mit anderen Experimenten und theoretischen Modellen verglichen werden.

Die Zentralitätsabhängigkeit der Kaonen und ϕ ist auf der linken Seite von Abbildung 8.1 abgebildet. Alle Multiplizitäten steigen stärker als linear mit der Anzahl der an der Reaktion teilnehmenden Nukleonen mit $M \sim \langle A_{part} \rangle^{\alpha}$. Dieses Verhalten kann damit erklärt werden dass die Teilchen unterhalb ihrer NN-Schwelle nur über die mehrfache Interaktion der Teilchen im Medium produziert werden können. Je mehr Teilchen im kreierten System vorliegen und dichter das Medium ist, desto höher ist die Wahrscheinlichkeit für solche Wechselwirkungen und damit die Multiplizität. Erstaunlich jedoch ist, dass der Anstieg für alle Teilchen innerhalb der Fehler gleich zu sein scheint, da die K^-- und ϕ-Mesonen deutlich weiter unterhalb ihrer Schwelle produziert werden müssen als die K^+, was eine stärkere $\langle A_{part} \rangle$-Abhängigkeit vermutet hätte. Außerdem ist der erhaltene Proportionalitätsfaktor vergleichbar mit Ergebnissen der KaoS und FOPI Kollaboration von Messungen bei höheren Energien. Da das Verhältnis von K^-/K^+ konstant als Funktion der Zentralität ist, kann unser Wert direkt mit KaoS und der Messung von Ar+KCl mit HADES verglichen werden, ohne für die unterschiedlichen Zentralitätsselektionen der Experimente zu korrigieren. Der erhaltene Wert folgt dem Trend der anderen Experimente und steigt mit der Schwerpunktsenergie an (rechte Seite von Abbildung 8.1). Das gleiche Verhalten zeigen die gemessenen effektiven Temperaturen der geladenen Kaonen, wobei hier auch ein Anstieg mit der Systemgrösse beobachtet wird. Auffallend ist hierbei, dass die effektiven Temperaturen von K^- systematisch unterhalb deren von K^+ liegen.

Das ϕ/K^- Verhältnis wurde zu 0,52 $\pm$ 0,16 bestimmt, was bedeutet, dass ca. 25% aller gemessenen K^- aus ϕ-Zerfällen stammen. Das Verhältnis ist relativ konstant als Funktion der Zentralität und kann abermals mit anderen Experimenten verglichen werden. Die linke Seite von Abbildung 8.2 zeigt die Abhängigkeit des ϕ/K^- Verhältnisses von der Schwerpunktsenergie. Unser neuer Datenpunkt bei $\sqrt{s}$ = 2,4 GeV liegt etwas höher als die Ergebnisse bei $\sqrt{s}$ = 2,6 GeV. Dieses Verhalten kann

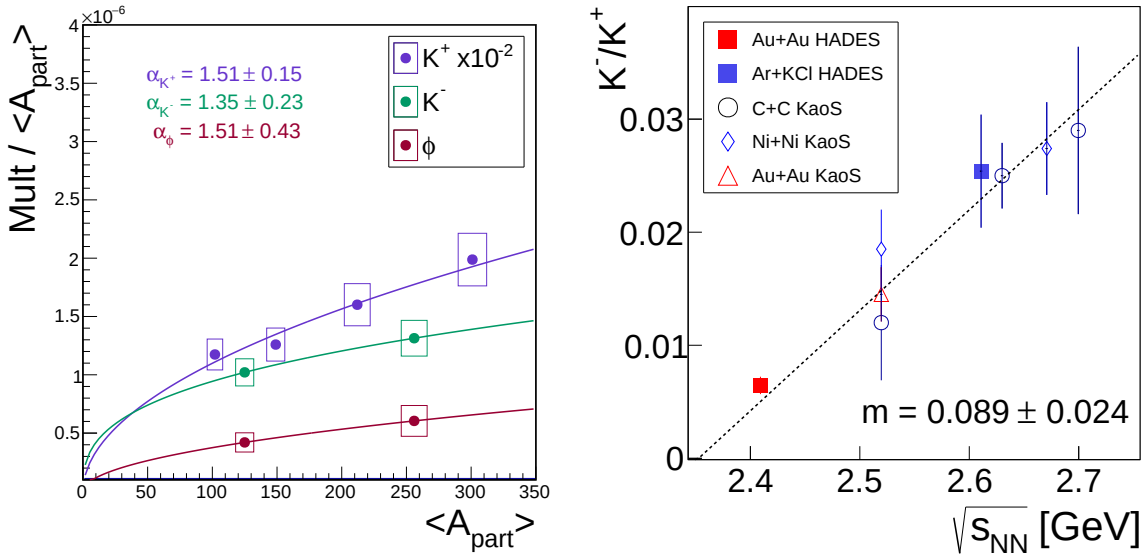

Figure 8.1: Links: Zentralitätsabhängigkeit der Multiplizitäten von K^+ (violett), K^- (grün) und ϕ (rot). Die Multiplizitäten steigen mehr als linear mit $M \sim \langle A_{part} \rangle^{\alpha}$. Rechts: Energieabhängigkeit des K^-/K^+ Verhältnisses. Der gemessene Wert für Au+Au-Kollisionen bei 1,23 AGeV (rotes Quadrat) folgt dem Anstieg mit Schwerpunktsenergie der von anderen Experimenten (Legende) beobachtet wurde.

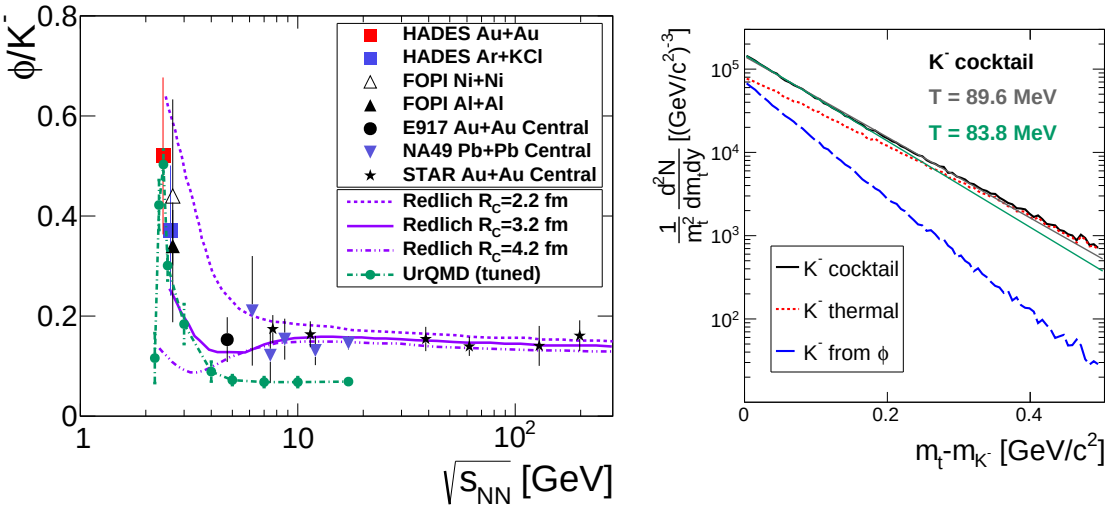

Figure 8.2: Links: Anregungsfunktion des ϕ/K^- Verhältnisses im Vergleich zu einem Statistischen Hadronisations Model für verschiedene Werte für den kanonischen Seltsamkeitsunterdrückungsradius R_C (violette gestrichelte Linien) und zu einer Transportmodell Rechnung (grün). Beide Modelle beschreiben den gemessenen Datenpunkt dieser Analyse (rotes Quadrat). Rechts: Transversales Massenspektrum bei Schwerpunktsrapidät von generierten K^- mithilfe einer zweikomponenten Cocktail Simulation (schwarze Linie) von 75% thermisch produzierten (rote gestrichelte Linie) und 25% aus ϕ-Zerfällen resultierenden K^- (blaue gestrichelte Linie). Mithilfe einer Boltzmann-Parameterisierung kann eine effektive Temperatur von 89,5 MeV im gesamten und 83,8 MeV in dem im Experiment zugänglichen transversalen Massenbereich ($m_t - m_0 < 200$ MeV/c^2) bestimmt werden.

sowohl von Statistischen Hadronisations Modellen für kanonische Seltsamkeitsunterdrückungsradien $R_C \in [2, 2, 3, 2]$ fm, als auch von Transportmodellen, in denen die Produktion von ϕ durch das Hinzufügen von schweren Baryonenresonanzen erhöht wurde, beschrieben werden. Um die Konsequenz von dem gemessenen ϕ/K^- Verhältnisses auf die beobachtete K^- Kinematik zu evaluieren, wird mit dem PLUTO-Ereignisgenerator ein einfaches Modell angenommen, in dem zwei Quellen zur K^--Produktion beitragen. 75% der produzierten K^- werden rein thermisch produziert, wobei als Temperatur die gemessene effektive Temperatur der positiven Kaonen von $T_{eff}^{K^+}$ = 104 MeV angenommen wird. Die übrigen 25% kommen aufgrund des gemessenen ϕ/K^- Verhältnisses aus ϕ-Zerfällen, wobei die ϕ-Mesonen mit der gemessenen effektiven Temperatur von T_{eff}^{ϕ} = 108 MeV produziert wurden. Der Effekt auf das transversale Massenspektrum von K^- ist auf der rechten Seite von Abbildung 8.2 zu sehen. Das Spektrum der K^- aus ϕ-Zerfällen ist deutlich steiler als das der thermisch produzierten. Das erhaltene Gesamtspektrum wird somit auch steiler, was zu einer kälteren resultierenden effektiven Temperatur von $T = 84^{+5}_{-4}$ MeV in dem im Experiment zugänglichen Akzeptanzbereich von $0 \leq m_t - m_0 \leq 200$ MeV führt. Diese Temperatur ist in perfektem Einklang mit der gemessenen effektiven Temperatur von K^- von 84 $\pm$ 6 MeV, was einem unterschiedlichen Ausfrierszenario der zwei Kaonenspezies widerspricht.

Um mehr über das kreierte System in der Schwerionenkollision, wie zum Beispiel den Grad der Thermalisierung, zu erfahren werden die gemessenen Teilchenmultipizitäten mit einem Statistischen Hadronisations Modell konfrontiert. Das Modell liefert eine gute Beschreibung aller Hadronenraten mit den Ausfrierparametern T = (68 $\pm$ 2) MeV und μ_B = (883 $\pm$ 25) MeV. Während die Temperatur vergleichbar mit den Werten von anderen Experimenten in dem gemessenen Energiebereich ist, erhalten wir eine etwas höhere Baryonendichte, welche nicht mehr mit der einfachen Parameterisierung von einer festen Energie pro Nukleon von 1 GeV zu beschreiben ist. Desweiteren ist die erhaltene chemische Ausfriertemperatur im Einklang mit der kinetischen Ausfriertemperatur von T_{kin} = (70 $\pm$ 4) MeV, die mithilfe der Siemens-Rasmussen Fits and die transversalen Massenspektren der Protonen bestimmt wurde.

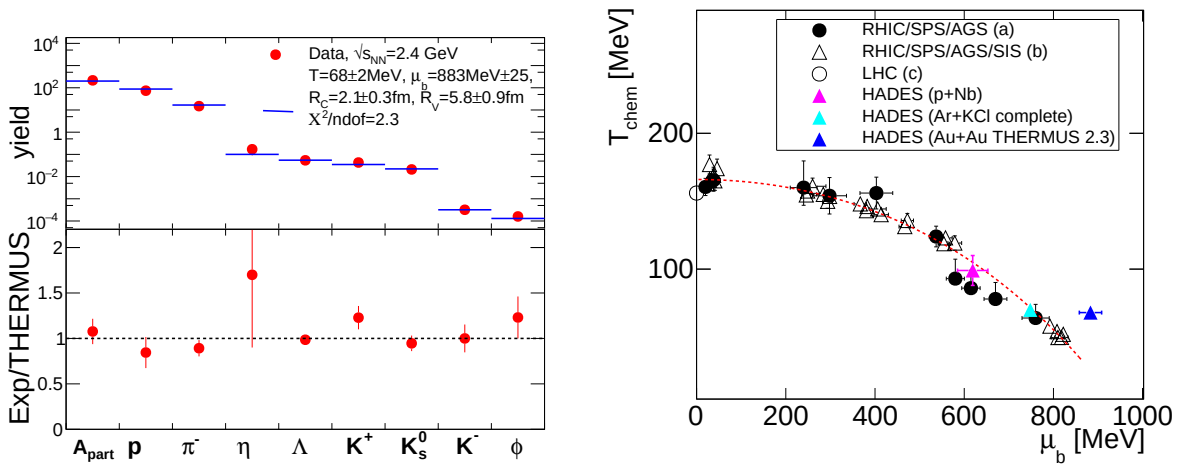

Figure 8.3: Links: Vergleich der gemessenen Teilchenmultiplizitäten (rote Kreise) dieser Analyse und aus [116] und [162] mit einem SHM-Fit mit THERMUS (v2.3) (blaue Balken). Der untere Teil zeigt das Verhältnis aus Daten zu Fit. Rechts: Zusammenstellung der erhaltenen Ausfrierparameter in der T-μ_B-Ebene von verschiedenen Experimenten [76] (a), [78] (b), [163] (c), [164] (HADES p+Nb und Ar+KCl) und dem Punkt für Au+Au bei 1,23 AGeV dieser Analyse (dunkel blaues Dreieck). Die gestrichelte Linie gehört zu einer Parameterisierung für eine feste Energie pro Nukleon von 1 GeV.

Appendix A

Supplemental Material

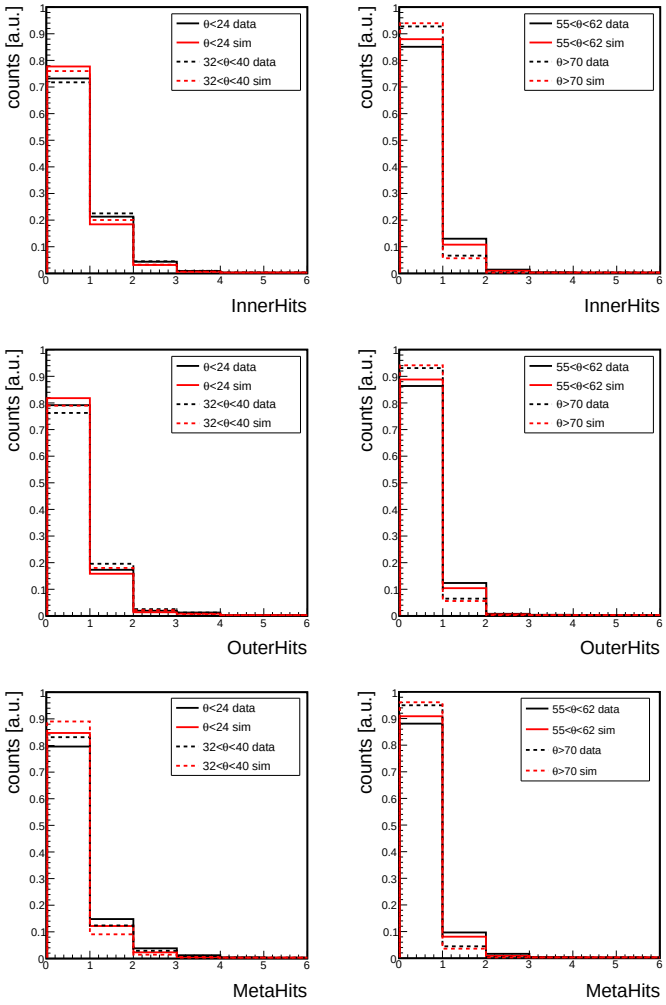

Figure A.1: Probability distribution of a particle candidate sharing an inner (top) or outer (middle) track segment or a META-hit (bottom) with other track candidates in different regions of the polar angle θ for experimental data (black) and simulation (red).

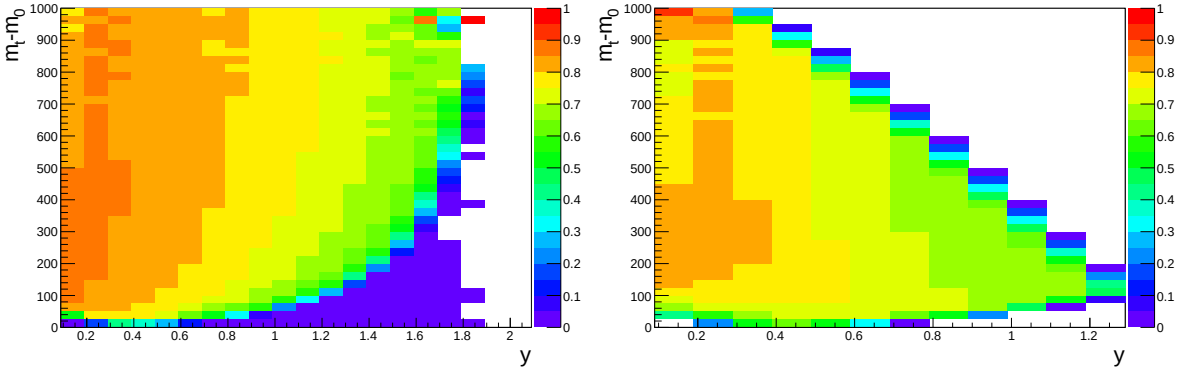

Figure A.2: Separated acceptance (left) and reconstruction efficiency (right) of protons.

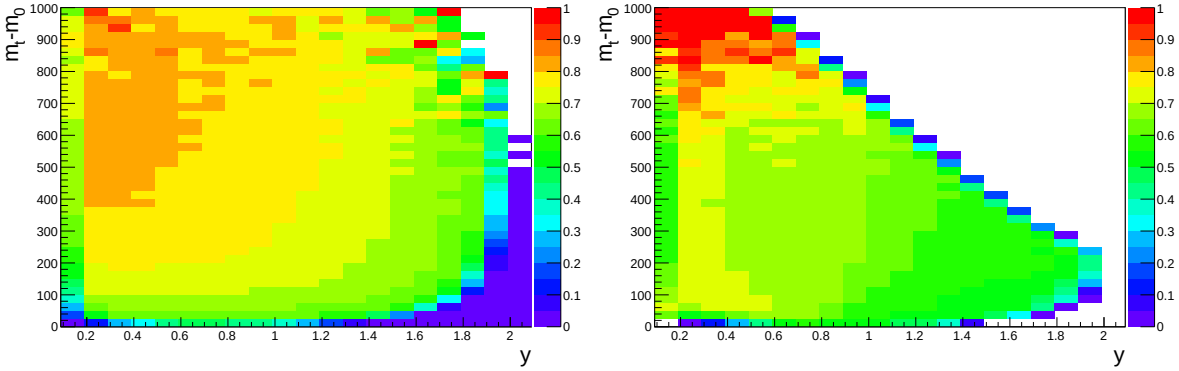

Figure A.3: Separated acceptance (left) and reconstruction efficiency (right) of π^-.

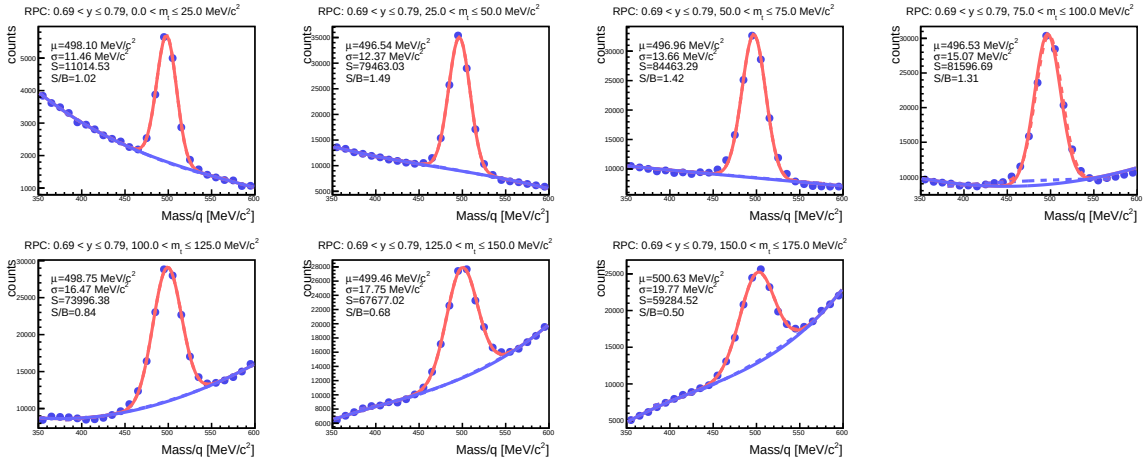

Figure A.4: Zoom into the charged particle mass spectrum in the region of K^+ in the analyzed transverse mass cells for center-of-mass rapidity for 0 - 40% most central collisions. The signal is described by a Gaussian parameterization and the residual background is subtracted using a polynomial third order (blue line).

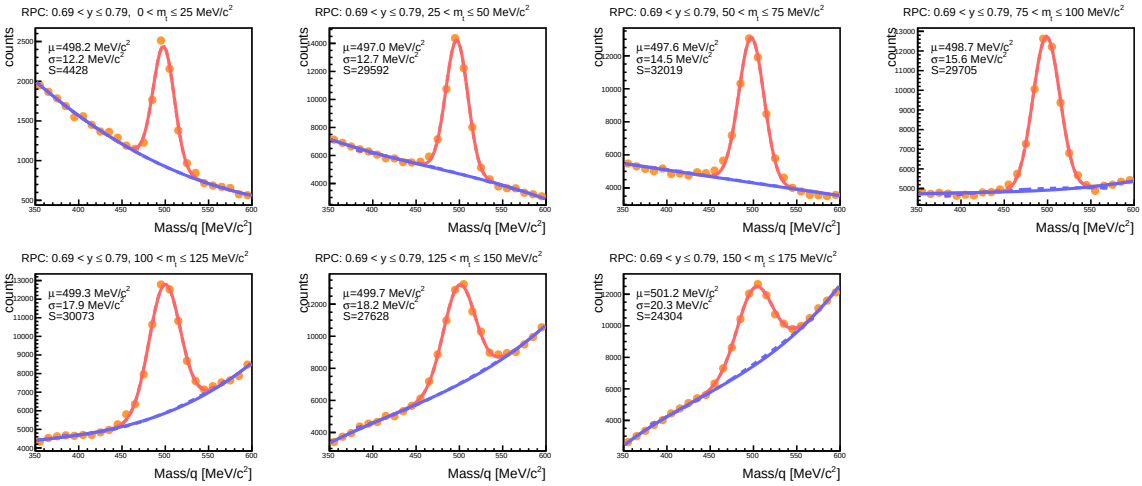

Figure A.5: Zoom into the charged particle mass spectrum in the region of K^+ in the analyzed transverse mass cells for center-of-mass rapidity for 0 - 10% most central collisions. The signal is described by a Gaussian parameterization and the residual background is subtracted using a polynomial third order (blue line).

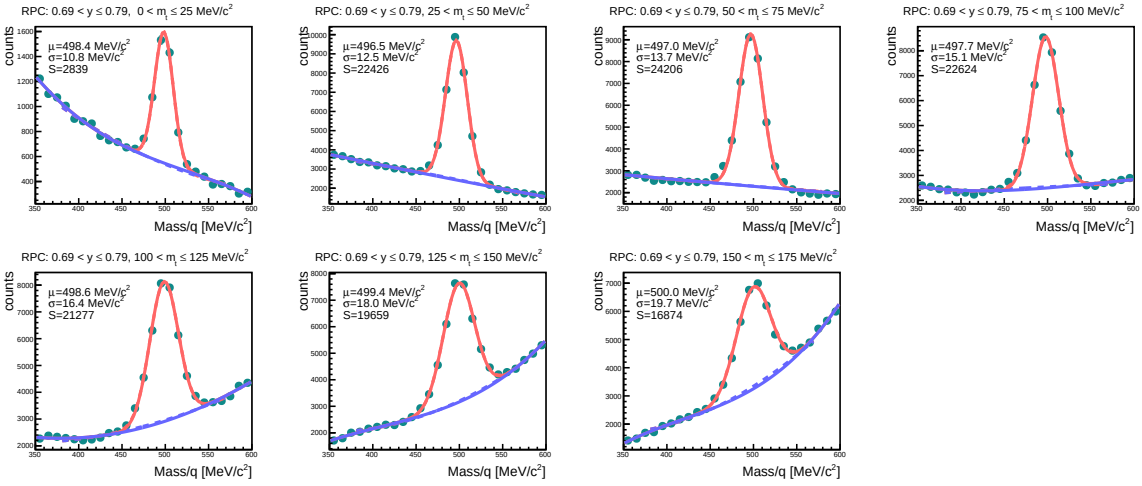

Figure A.6: Zoom into the charged particle mass spectrum in the region of K^+ in the analyzed transverse mass cells for center-of-mass rapidity for 10 - 20% most central collisions. The signal is described by a Gaussian parameterization and the residual background is subtracted using a polynomial third order (blue line).

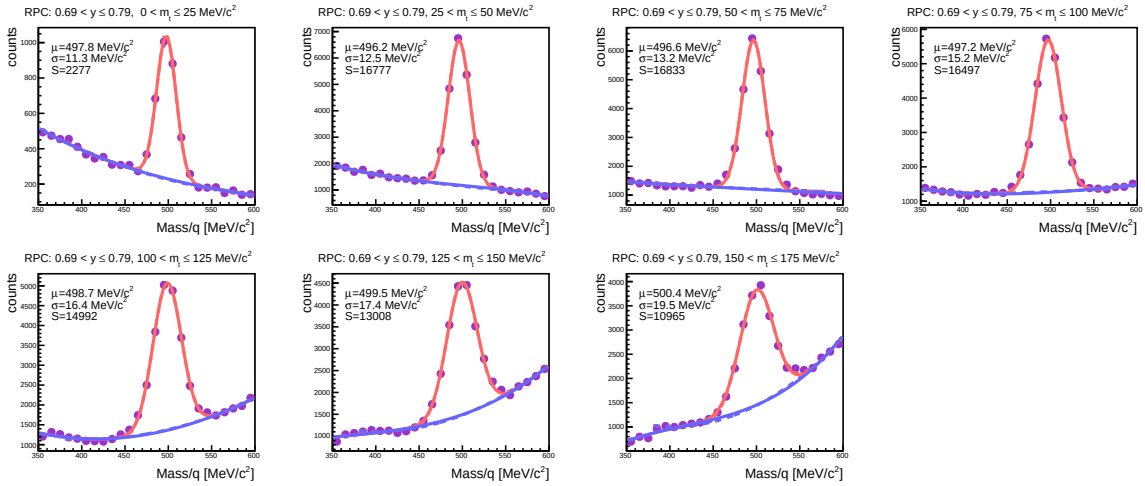

Figure A.7: Zoom into the charged particle mass spectrum in the region of K^+ in the analyzed transverse mass cells for center-of-mass rapidity for 20 - 30% most central collisions. The signal is described by a Gaussian parameterization and the residual background is subtracted using a polynomial third order (blue line).

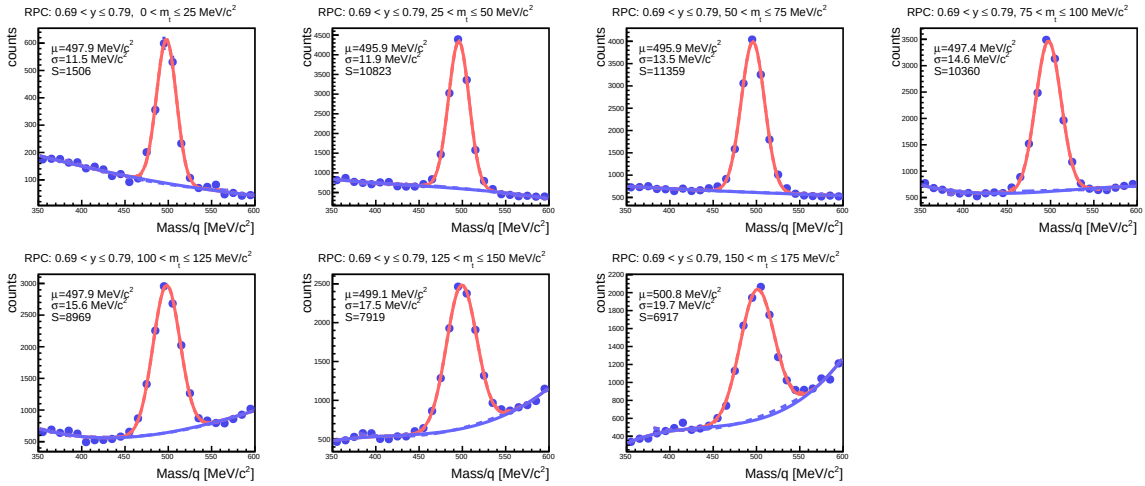

Figure A.8: Zoom into the charged particle mass spectrum in the region of K^+ in the analyzed transverse mass cells for center-of-mass rapidity for 30 - 40% most central collisions. The signal is described by a Gaussian parameterization and the residual background is subtracted using a polynomial third order (blue line).

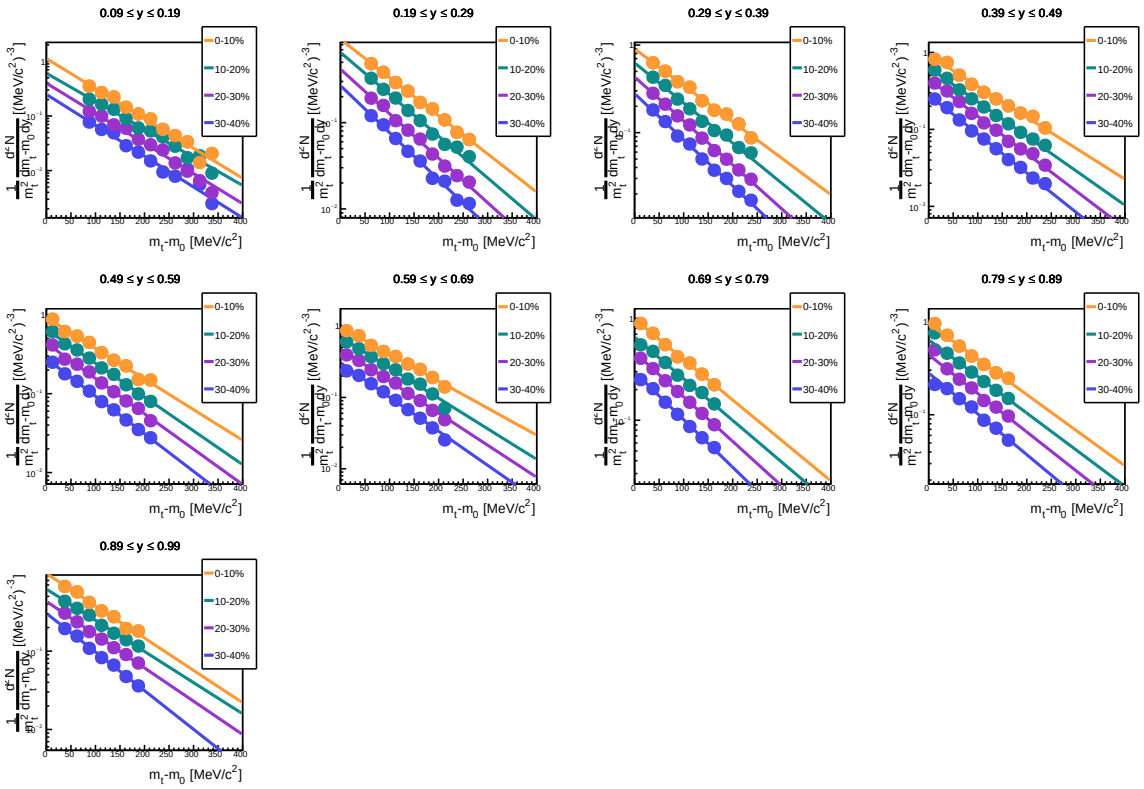

Figure A.9: Transverse mass spectra of K^+ for the analyzed rapidity slices for the different centrality classes (legend) together with Boltzmann parameterizations.

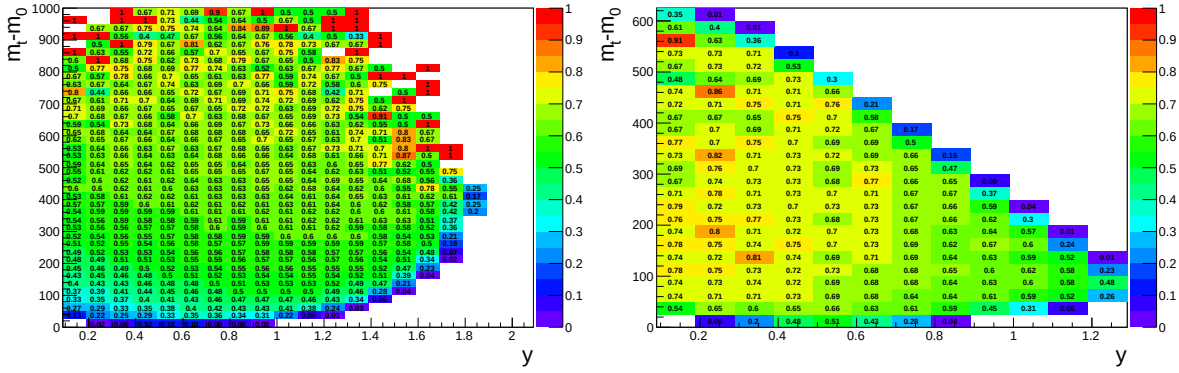

Figure A.10: Separated acceptance (left) and reconstruction efficiency (right) of K^+.

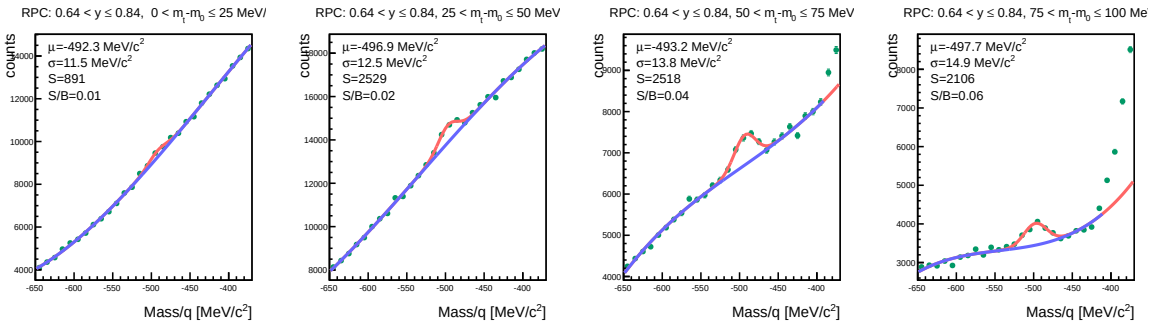

Figure A.11: Zoom into the charged particle mass spectrum in the region of K^- in the analyzed transverse mass cells for center-of-mass rapidity for 0 - 40% most central collisions. The signal is described by a Gaussian parameterization and the residual background is subtracted using a polynomial third order (blue line).

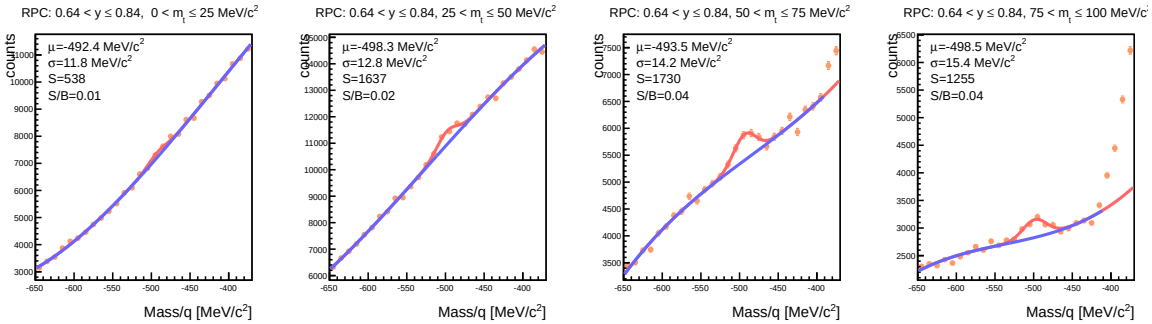

Figure A.12: Zoom into the charged particle mass spectrum in the region of K^- in the analyzed transverse mass cells for center-of-mass rapidity for 0 - 20% most central collisions. The signal is described by a Gaussian parameterization and the residual background is subtracted using a polynomial third order (blue line).

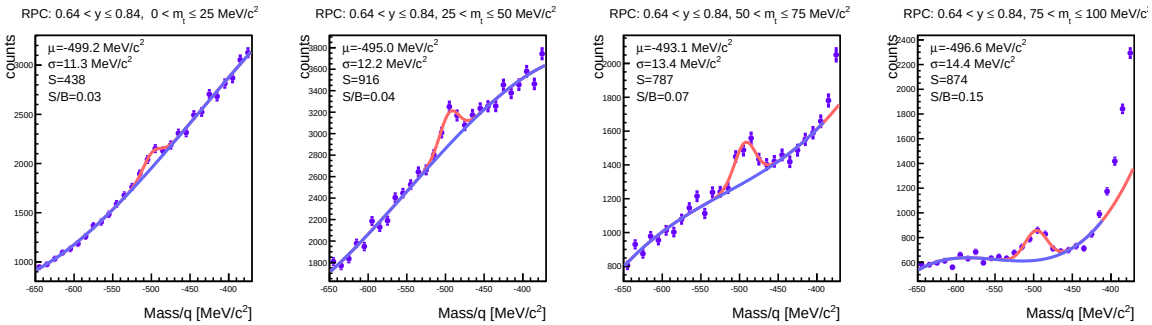

Figure A.13: Zoom into the charged particle mass spectrum in the region of K^- in the analyzed transverse mass cells for center-of-mass rapidity for 20 - 40% most central collisions. The signal is described by a Gaussian parameterization and the residual background is subtracted using a polynomial third order (blue line).

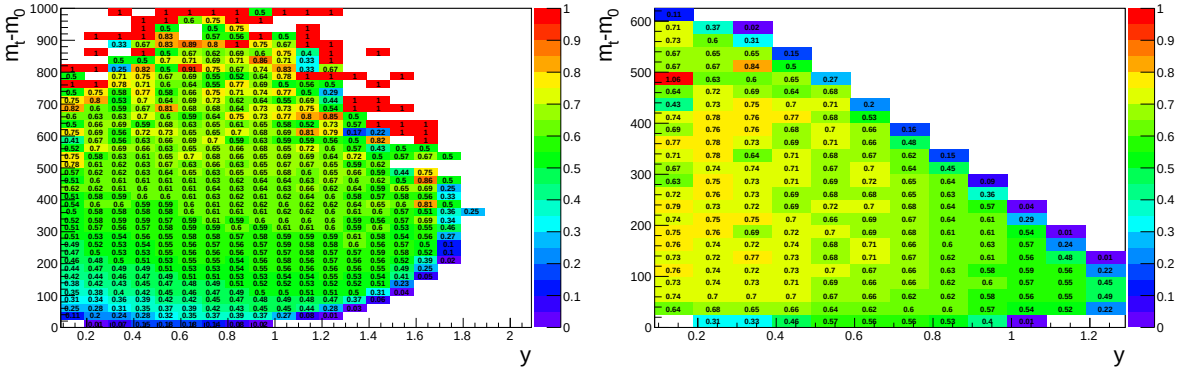

Figure A.14: Separated acceptance (left) and reconstruction efficiency (right) of K^-.

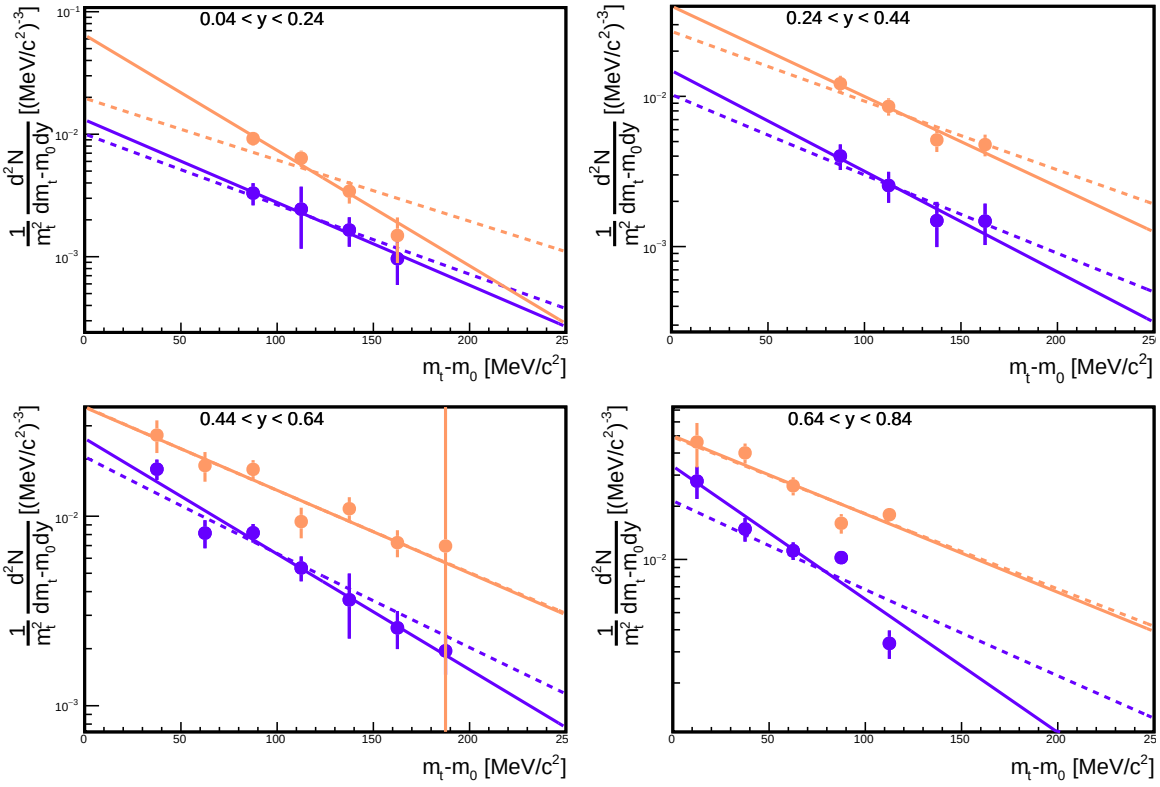

Figure A.15: Efficiency and acceptance corrected transverse mass spectra of K^- for the analyzed rapidity slices for the different centrality classes (orange: 0 - 20%, purple: 20 - 40%) together with Boltzmann (solid lines) and Siemsens-Rasmussen parameterizations (dashed lines).

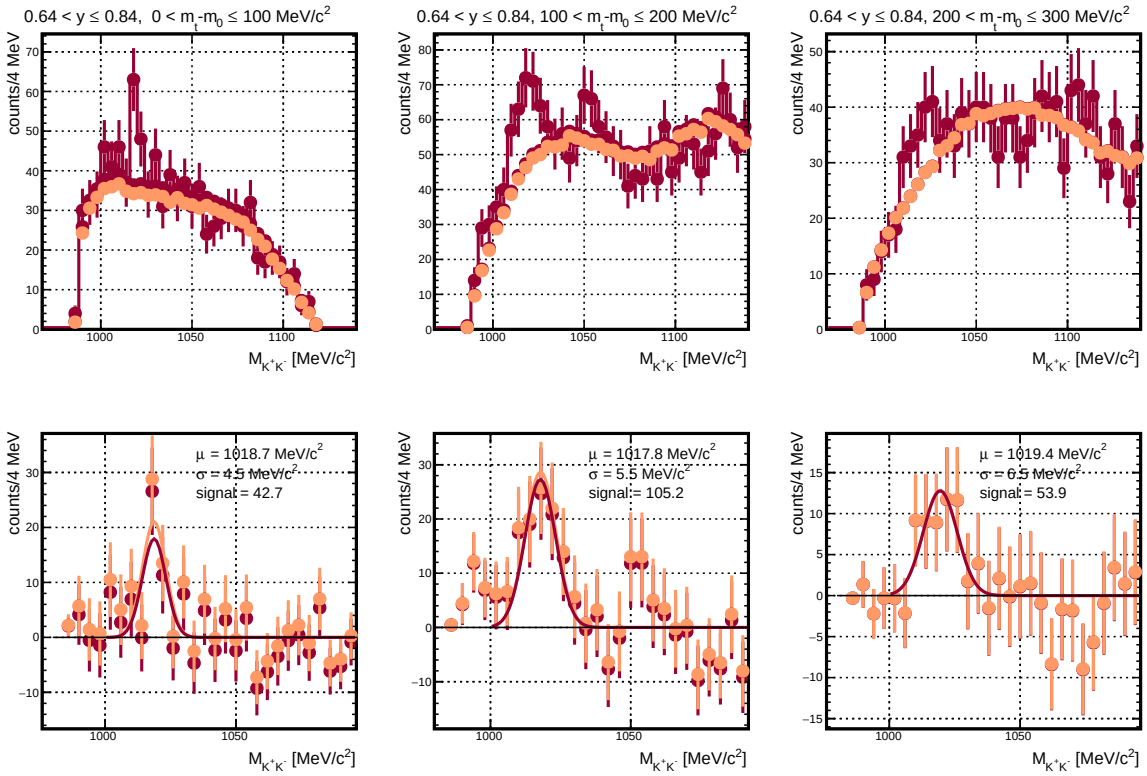

Figure A.16: Top: Invariant mass distributions as a function of m_t for the rapidity region $0.64 < y \leq 0.84$, of all K^+K^- candidates produced in 0 - 20% most central collisions with corresponding mixed-event background, normalized in the region $980 \leq M_{K^+K^-} \leq 1005$ MeV/c^2 and $1030 \leq M_{K^+K^-} \leq 1150$ MeV/c^2 simultaneously (red), respectively $1050 \leq M_{K^+K^-} \leq 1150$ MeV/c^2 (orange). Bottom: After subtraction of the mixed-event background, the ϕ meson signal can be described by a Gaussian parameterization to extract the mean μ, width σ and the differential count rate (signal).

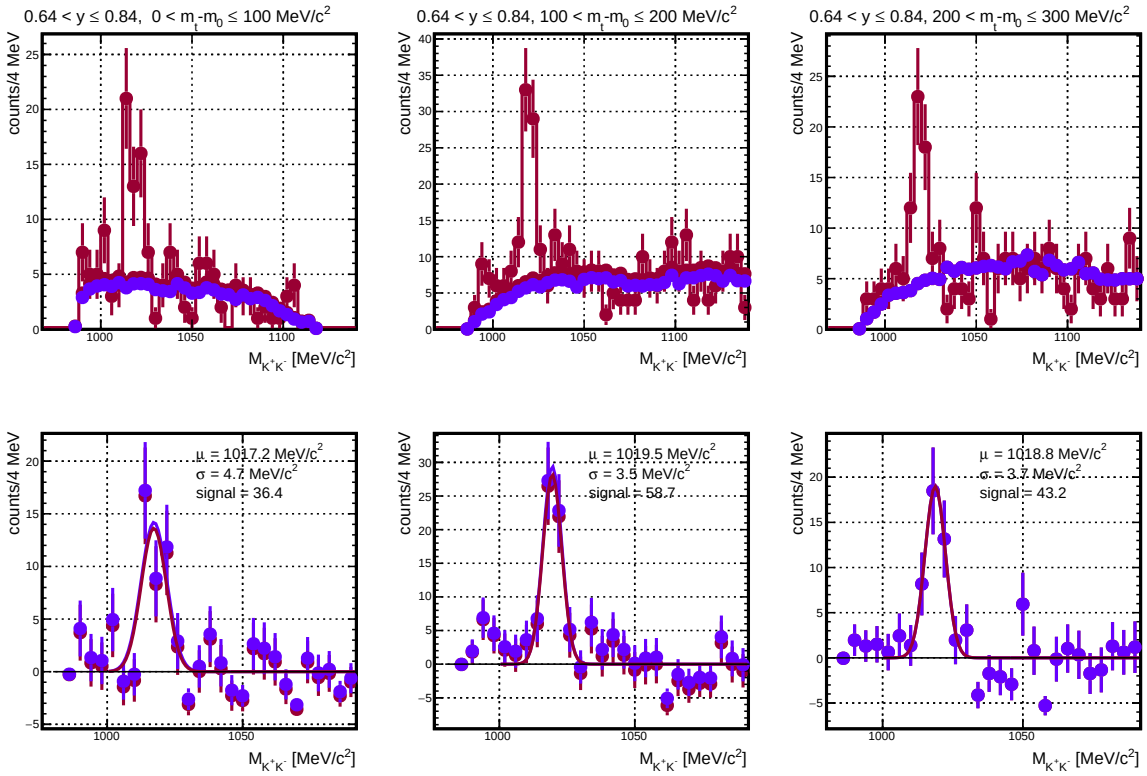

Figure A.17: Top: Invariant mass distributions as a function of m_t for the rapidity region $0.64 < y \leq 0.84$, of all K^+K^- candidates produced in 20 - 40% most central collisions with corresponding mixed-event background, normalized in the region $980 \leq M_{K^+K^-} \leq 1005$ MeV/c^2 and $1030 \leq M_{K^+K^-} \leq 1150$ MeV/c^2 simultaneously (red), respectively $1050 \leq M_{K^+K^-} \leq 1150$ MeV/c^2 (purple). Bottom: After subtraction of the mixed-event background, the ϕ meson signal can be described by a Gaussian parameterization to extract the mean μ, width σ and the differential count rate (signal).

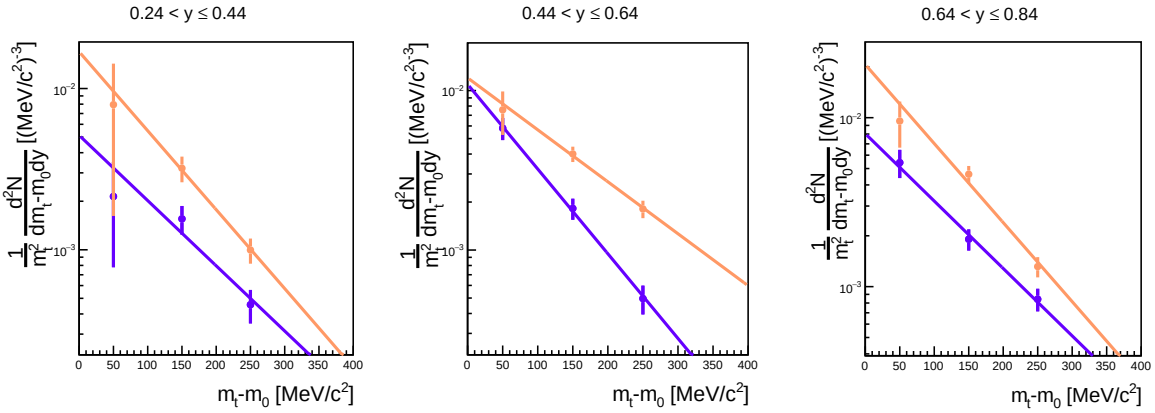

Figure A.18: Efficiency and acceptance corrected transverse mass spectra of ϕ for the analyzed rapidity slices for the different centrality classes (orange: 0 - 20%, purple: 20 - 40%) together with Boltzmann parameterizations (dashed lines).

Appendix B

Energy loss calibration of the π Beam Data

In August 2014 the HADES collaboration undertook a π beam measurement campaign. The drift gas of the second drift chamber MDC II has also been changed from Ar/isobutan to Ar/CO_2. As a consequence, the specific energy loss had to be re-calibrated in the framework of this thesis.
The procedure was basically the same as in the case of the Au+Au beam time, but as the track multiplicity is significantly lower in case of the π beam time, the event and track selection was not as strict. The effect of the calibration is shown in figure B.1. With the new parameters the measured distributions are clearly shifted onto the nominal energy loss value as expected by the Bethe-Bloch formula.

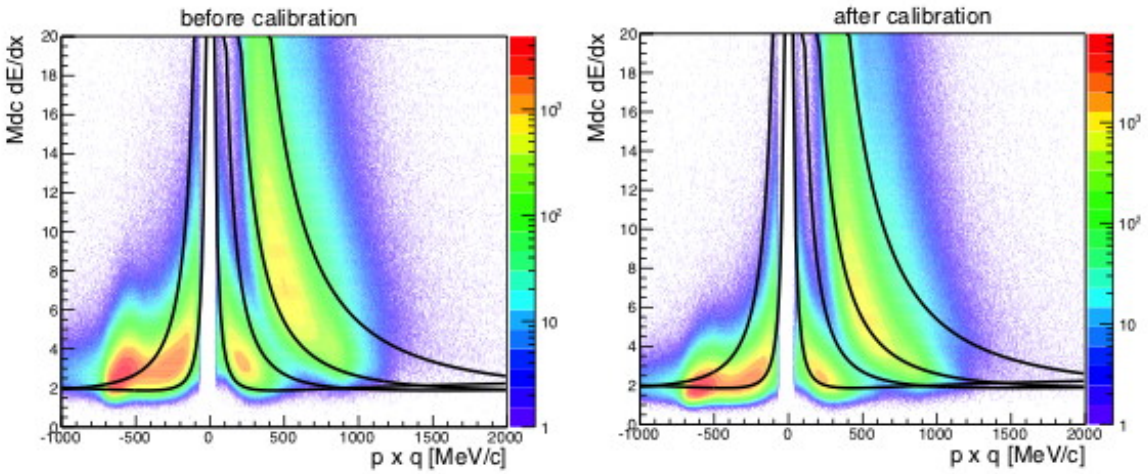

Figure B.1: Comparison of the measured energy loss in pion-induced reactions measured with the HADES-spectrometer before (left) and after (right) calibration.

List of Figures

List of Tables

Bibliography

[1] Christoph Hartnack, Helmut Oeschler, Yvonne Leifels, Elena L. Bratkovskaya, and Joerg Aichelin. Strangeness Production close to Threshold in Proton-Nucleus and Heavy-Ion Collisions. *Phys. Rept.*, 510:119–200, 2012. I, III, 112, 147, 151, 159

[2] G. Agakishiev et al. Phi decay: A Relevant source for K- production at SIS energies? *Phys.Rev.*, C80:025209, 2009. I, III, 6, 19, 24, 26, 156

[3] P. Gasik et al. Strange meson production in Al+Al collisions at 1.9A GeV. 2015. I, III, 26, 27, 156

[4] A. Forster, F. Uhlig, I. Bottcher, D. Brill, M. Debowski, et al. Production of K+ and of K- Mesons in Heavy-Ion Collisions from 0.6 to 2.0-A-GeV Incident Energy. *Phys.Rev.*, C75:024906, 2007. I, III, 23, 147, 149, 166

[5] Jan Steinheimer and Marcus Bleicher. Sub-threshold ϕ and Ξ^- production by high mass resonances with UrQMD. 2015. I, III, 18, 19, 28, 155, 156, 166

[6] Henrik Bohr and H.B. Nielsen. Hadron production from a boiling quark soup: A thermodynamical quark model predicting particle ratios in hadronic collisions. *Nuclear Physics B*, 128(2):275–293, 1977. 1

[7] `http://img.geo.de/div/image/68561/02-popup.jpg`. [Online; accessed 10-July-2016]. 1

[8] `https://upload.wikimedia.org/wikipedia/commons/thumb/0/00/Standard_Model_of_Elementary_Particles.svg/375px-Standard_Model_of_Elementary_Particles.svg.png`. [Online; accessed 21-February-2016]. 2

[9] R.P. Feynman. Forces in Molecules. *Phys.Rev.*, 56:340–343, 1939. 2

[10] William Rarita and Julian Schwinger. On a theory of particles with half integral spin. *Phys.Rev.*, 60:61, 1941. 2

[11] S. Tomonaga. On a relativistically invariant formulation of the quantum theory of wave fields. *Prog.Theor.Phys.*, 1:27–42, 1946. 2

[12] S.L. Glashow. Partial Symmetries of Weak Interactions. *Nucl.Phys.*, 22:579–588, 1961. 3

[13] A. Salam and J.C. Ward. Electromagnetic and weak interactions. *Physics Letters*, 13(2):168 – 171, 1964. 3

[14] Steven Weinberg. Charge symmetry of weak interactions. *Phys.Rev.*, 112:1375–1379, 1958. 3

[15] Georges Aad et al. Combined Measurement of the Higgs Boson Mass in pp Collisions at $\sqrt{s} = 7$ and 8 TeV with the ATLAS and CMS Experiments. 2015. 3

[16] Peter W. Higgs. Broken symmetries and the masses of gauge bosons. *Phys. Rev. Lett.*, 13(16):508–509, October 1964. 3

[17] F. Englert and R. Brout. Broken Symmetry and the Mass of Gauge Vector Mesons. *Phys. Rev. Lett.*, 13(9):321–323, August 1964. 3

[18] G. S. Guralnik, C. R. Hagen, and T. W. B. Kibble. Global Conservation Laws and Massless Particles. *Phys. Rev. Lett.*, 13(20):585–587, November 1964. 3

[19] J.W. Harris, A. Sandoval, R. Stock, H. Strobele, R.E. Renfordt, et al. Λ Production Near Threshold in Central Nucleus Nucleus Collisions. *Phys.Rev.Lett.*, 47:229–232, 1981. 3

[20] S. Schnetzer, M.C. Lemaire, R. Lombard, E. Moller, S. Nagamiya, et al. PRODUCTION OF K+ MESONS IN 2.1-GEV/NUCLEON NUCLEAR COLLISIONS. *Phys.Rev.Lett.*, 49:989–992, 1982. 3

[21] D. Miskowiec, W. Ahner, R. Barth, M. Cieslak, M. Debowski, et al. Observation of enhanced subthreshold K+ production in central collisions between heavy nuclei. *Phys.Rev.Lett.*, 72:3650–3653, 1994. 3

[22] J.L. Ritman et al. On the transverse momentum distribution of strange hadrons produced in relativistic heavy ion collisions. *Z.Phys.*, A352:355–357, 1995. 3

[23] `https://madai-public.cs.unc.edu/visualization/heavy-ion-collisions/low-energy/`. [Online; accessed 13-April-2015]. 4

[24] C. Blume and C. Markert. Strange hadron production in heavy ion collisions from SPS to RHIC. *Prog. Part. Nucl. Phys.*, 66:834–879, 2011. 5, 6

[25] C. Alt et al. Pion and kaon production in central Pb + Pb collisions at 20-A and 30-A-GeV: Evidence for the onset of deconfinement. *Phys.Rev.*, C77:024903, 2008. 6

[26] S. V. Afanasiev et al. Energy dependence of pion and kaon production in central pb+pb collisions. *Phys. Rev. C*, 66:054902, Nov 2002. 6

[27] C. Alt et al. Energy dependence of Λ and Ξ production in central $\mathrm{Pb} + \mathrm{Pb}$ collisions at $20a, 30a, 40a, 80a$, and $158a$ gev measured at the cern super proton synchrotron. *Phys. Rev. C*, 78:034918, Sep 2008. 6

[28] C. Alt et al. Energy dependence of ϕ meson production in central $\mathrm{Pb} + \mathrm{Pb}$ collisions at $\sqrt{s_{NN}} = 6$ to 17 gev. *Phys. Rev. C*, 78:044907, Oct 2008. 6

[29] C. Alt et al. Ω^- and $\overline{\Omega}^+$ production in central $\mathrm{Pb} + \mathrm{Pb}$ collisions at 40 and $158a$ GeV. *Phys. Rev. Lett.*, 94:192301, May 2005. 6

[30] J. L. Klay et al. Charged pion production in $2a$ to $8a$ GeV central Au + Au collisions. *Phys. Rev. C*, 68:054905, Nov 2003. 6

[31] L. Ahle et al. Particle production at high baryon density in central au+au reactions at $11.6a$ gev/c. *Phys. Rev. C*, 57:R466–R470, Feb 1998. 6

[32] L. Ahle et al. An Excitation function of K- and K+ production in Au + Au reactions at the AGS. *Phys.Lett.*, B490:53–60, 2000. 6

[33] L. Ahle et al. Kaon production in au+au collisions at $11.6a\mathrm{GeV}/c$. *Phys. Rev. C*, 58:3523–3538, Dec 1998. 6

[34] B. B. Back et al. Production of ϕ mesons in Au + Au collisions at $11.7a$ gev. *Phys. Rev. C*, 69:054901, May 2004. 6

[35] P. Chung et al. Near-threshold production of the multistrange Ξ^- hyperon. *Phys. Rev. Lett.*, 91:202301, Nov 2003. 6

[36] I. G. Bearden et al. Charged meson rapidity distributions in central $\mathrm{Au} + \mathrm{Au}$ collisions at $\sqrt{s_{NN}} = 200\ \mathrm{GeV}$. *Phys. Rev. Lett.*, 94:162301, Apr 2005. 6

[37] G. Agakishiev et al. In-medium effects on K^0 mesons in relativistic heavy-ion collisions. *Phys. Rev. C*, 82:044907, Oct 2010. 6, 24

[38] G. Agakishiev et al. Hyperon production in Ar+KCl collisions at 1.76A GeV. *Eur.Phys.J.*, A47:21, 2011. 6, 24, 25

[39] G. Agakishiev et al. Deep subthreshold ξ^- production in $\mathrm{Ar} + \mathrm{KCl}$ reactions at $1.76a\ \mathrm{GeV}$. *Phys. Rev. Lett.*, 103:132301, Sep 2009. 6, 24

[40] W. Reisdorf et al. Systematics of central heavy ion collisions in the 1A GeV regime. *Nucl. Phys.*, A848:366–427, 2010. 7

[41] Ekkard Schnedermann, Josef Sollfrank, and Ulrich Heinz. Thermal phenomenology of hadrons from 200 agev s+s collisions. *PHYS.REV.C*, 48:2462, 1993. 7, 110

[42] Kenneth G. Wilson. Confinement of quarks. *Phys. Rev. D*, 10:2445–2459, Oct 1974. 9

[43] K Nakamura et al. Review of particle physics. *J. Phys.*, G37:075021, 2010. 9

[44] Volker Koch. Introduction to chiral symmetry. 1995. 9, 10

[45] Y. Nambu and G. Jona-Lasinio. Dynamical Model of Elementary Particles Based on an Analogy with Superconductivity. I. *Phys. Rev.*, 122:345–358, Apr 1961. 9, 10, 12

[46] Frank Wilczek. The Recent Excitement in High-Density QCD. *Nucl.Phys. A663 (2000) 257-271*, August 1999. 9

[47] Christian Fuchs. Kaon production in heavy ion reactions at intermediate energies. *Prog.Part.Nucl.Phys.*, 56:1–103, 2006. 9, 17, 20

[48] Tetsuo Hatsuda and Su Houng Lee. Qcd sum rules for vector mesons in the nuclear medium. *Phys. Rev. C*, 46:R34–R38, Jul 1992. 11

[49] Stefan Leupold and Ulrich Mosel. On QCD sum rules for vector mesons in nuclear medium. *Phys.Rev.C58:2939-2957,1998*, May 1998. 11

[50] I. Khan. The σ-model of gell-mann and levy for a partially conserved axial vector current. *Il Nuovo Cimento A*, 53(1):18–23, 1968. 11

[51] Murray Gell-Mann, R.J. Oakes, and B. Renner. Behavior of current divergences under SU(3) x SU(3). *Phys.Rev.*, 175:2195–2199, 1968. 11

[52] H. Leutwyler. Principles of chiral perturbation theory. pages 1–46, 1994. 11

[53] D.B. Kaplan and A.E. Nelson. Strange Goings on in Dense Nucleonic Matter. *Phys.Lett.*, B175:57–63, 1986. 11

[54] Ann E. Nelson and David B. Kaplan. Strange Condensate Realignment in Relativistic Heavy Ion Collisions. *Phys.Lett.*, B192:193, 1987. 11

[55] Guo-Qiang Li and C.M. Ko. Kaon flow in heavy ion collisions. *Nucl.Phys.*, A594:460–482, 1995. 12

[56] Steven Weinberg. Nonlinear realizations of chiral symmetry. *Phys.Rev.*, 166:1568–1577, 1968. 12

[57] G.E Brown and Mannque Rho. From chiral mean field to walecka mean field and kaon condensation. *Nuclear Physics A*, 596(3–4):503 – 514, 1996. 13

[58] C.J. Batty, E. Friedman, and A. Gal. Strong interaction physics from hadronic atoms. *Physics Reports*, 287(5):385 – 445, 1997. 13

[59] Tetyana Galatyuk. *Di-electron spectroscopy in HADES and CBM: from p + p and n + p collisions at GSI to Au + Au collisions at FAIR*. PhD thesis, Goethe-Universitaet, Frankfurt am Main, 2009. 14

[60] Frank R. Brown, Frank P. Butler, Hong Chen, Norman H. Christ, Zhihua Dong, Wendy Schaffer, Leo I. Unger, and Alessandro Vaccarino. On the existence of a phase transition for QCD with three light quarks. *Phys. Rev. Lett.*, 65:2491–2494, Nov 1990. 14

[61] Z. Fodor and S. D. Katz. Critical point of QCD at finite T and mu, lattice results for physical quark masses. *JHEP*, 04:050, 2004. 14

[62] B.-J. Schaefer, J. M. Pawlowski, and J. Wambach. Phase structure of the polyakov-quark-meson model. *Phys. Rev. D*, 76:074023, Oct 2007. 14

[63] M. A. Stephanov. Non-Gaussian Fluctuations near the QCD Critical Point. *Phys. Rev. Lett.*, 102:032301, Jan 2009. 14

[64] M. A. Stephanov. Sign of Kurtosis near the QCD Critical Point. *Phys. Rev. Lett.*, 107:052301, Jul 2011. 14

[65] M. Cheng, P. Hegde, C. Jung, F. Karsch, O. Kaczmarek, et al. Baryon Number, Strangeness and Electric Charge Fluctuations in QCD at High Temperature. *Phys.Rev.*, D79:074505, 2009. 14

[66] R.V. Gavai and Sourendu Gupta. Lattice {QCD} predictions for shapes of event distributions along the freezeout curve in heavy-ion collisions. *Physics Letters B*, 696(5):459–463, 2011. 14

[67] Larry McLerran and Robert D. Pisarski. Phases of Cold, Dense Quarks at Large Nc. *Nucl. Phys.*, A796:83–100, 2007. 14

[68] Larry McLerran. Quarkyonic Matter and the Phase Diagram of QCD. pages 125–134, 2008. 14

[69] Larry McLerran, Krzystof Redlich, and Chihiro Sasaki. Quarkyonic Matter and Chiral Symmetry Breaking. *Nucl.Phys.*, A824:86–100, 2009. 14

[70] A. Bazavov, T. Bhattacharya, M. Cheng, C. DeTar, H.T. Ding, et al. The chiral and deconfinement aspects of the QCD transition. *Phys.Rev.*, D85:054503, 2012. 14

[71] Claudia Ratti et al. Recent results on QCD thermodynamics: lattice QCD versus Hadron Resonance Gas model. *Nucl.Phys.*, A855:253–256, 2011. 14

[72] `http://lhc.web.cern.ch/lhc/`. [Online; accessed 10-July-2016]. 15

[73] `http://www.bnl.gov/rhic/`. [Online; accessed 10-July-2016]. 15

[74] Adamczyk et al. Energy dependence of moments of net-proton multiplicity distributions at rhic. *Phys. Rev. Lett.*, 112:032302, Jan 2014. 15

[75] `http://www.fair-center.eu/for-users/experiments/cbm.html`. [Online; accessed 10-July-2016]. 15

[76] A. Andronic, P. Braun-Munzinger, and J. Stachel. Hadron production in central nucleus-nucleus collisions at chemical freeze-out. *Nucl.Phys.*, A772:167–199, 2006. 15, 16, 160, 161, 173

[77] J. Cleymans and K. Redlich. Chemical and thermal freeze-out parameters from $1a$ to $200a$ gev. *Phys. Rev. C*, 60:054908, Oct 1999. 15

[78] J. Cleymans, H. Oeschler, K. Redlich, and S. Wheaton. Comparison of chemical freeze-out criteria in heavy-ion collisions. *Phys.Rev.*, C73:034905, 2006. 16, 161, 173

[79] G.F. Bertsch and S. Das Gupta. A Guide to microscopic models for intermediate-energy heavy ion collisions. *Phys.Rept.*, 160:189–233, 1988. 16

[80] Che-Ming Ko and Qi Li. Relativistic Vlasov-Uehling-Uhlenbeck model for heavy-ion collisions. *Phys.Rev.*, C37:2270–2273, 1988. 16

[81] O. Buss, T. Gaitanos, K. Gallmeister, H. van Hees, M. Kaskulov, et al. Transport-theoretical Description of Nuclear Reactions. *Phys.Rept.*, 512:1–124, 2012. 16

[82] T. Skyrme. The effective nuclear potential. *Nucl.Phys.*, 9:615–634, 1959. 16

[83] Joerg Aichelin. Quantum molecular dynamics dynamical microscopic n-body approach to investigate fragment formation and the nuclear equation of state in heavy ion collisions. *Physics Reports*, 202:233 – 360, 1991. 16

[84] Heinz Sorge, Horst Stöcker, and Walter Greiner. Poincaré invariant hamiltonian dynamics: Modelling multi-hadronic interactions in a phase space approach. *Annals of Physics*, 192(2):266 – 306, 1989. 16

[85] S. A. Bass et al. Microscopic models for ultrarelativistic heavy ion collisions. *Prog. Part. Nucl. Phys.*, 41:255–369, 1998. 16, 47, 120, 152, 166

[86] C. Hartnack, Rajeev K. Puri, J. Aichelin, J. Konopka, S.A. Bass, et al. Modeling the many body dynamics of heavy ion collisions: Present status and future perspective. *Eur.Phys.J.*, A1:151–169, 1998. 16, 152, 166

[87] H. Schade, Gy. Wolf, and B. Kampfer. Role of phi decays for K- yields in relativistic heavy-ion collisions. *Phys.Rev.*, C81:034902, 2010. 18

[88] M. Lorenz. Reviewing hadron production at SIS energies featuring the new HADES $Au + Au$ data. *Nucl.Phys.*, A931:785–789, 2014. 19

[89] Burt Holzman et al. Systematic study of Au - Au collisions with AGS experiment E917. *Nucl.Phys.*, A698:643–646, 2002. 19

[90] S.V. Afanasiev et al. Production of ϕ-mesons in p+p, p+pb and central pb+pb collisions at ebeam=158 a gev. *Physics Letters B*, 491(1–2):59 – 66, 2000. 19

[91] J. Adams et al. ϕ meson production in au+au and p+p collisions at $\sqrt{s_{NN}}$=200 gev. *Physics Letters B*, 612(3–4):181 – 189, 2005. 19

[92] E.E. Kolomeitsev and B. Tomasik. Catalytic phi meson production in heavy-ion collisions. *J.Phys.*, G36:095104, 2009. 18

[93] S. Okubo. ϕ-meson and unitary symmetry model. *Physics Letters*, 5(2):165 – 168, 1963. 18

[94] G Zweig. An SU_3 model for strong interaction symmetry and its breaking; Version 2. (CERN-TH-412):80 p, Feb 1964. Version 1 is CERN preprint 8182/TH.401, Jan. 17, 1964. 18

[95] Jugoro Iizuka. Systematics and phenomenology of meson family. *Prog. Theor. Phys. Suppl.*, 37:21–34, 1966. 18

[96] J.P. Blaizot, D. Gogny, and B. Grammaticos. Nuclear Compressibility and Monopole Resonances. *Nucl.Phys.*, A265:315, 1976. 19

[97] D.H. Youngblood, C.M. Rozsa, J.M. Moss, D.R. Brown, and J.D. Bronson. Isoscalar Breathing-Mode State in Sm-144 and Pb-208. *Phys.Rev.Lett.*, 39:1188–1191, 1977. 19

[98] D.H. Youngblood, H.L. Clark, and Y.-W. Lui. Incompressibility of Nuclear Matter from the Giant Monopole Resonance. *Phys.Rev.Lett.*, 82:691–694, 1999. 19

[99] H. A. Gustafsson, H. H. Gutbrod, B. Kolb, H. Löhner, B. Ludewigt, A. M. Poskanzer, T. Renner, H. Riedesel, H. G. Ritter, A. Warwick, F. Weik, and H. Wieman. Collective flow observed in relativistic nuclear collisions. *Phys. Rev. Lett.*, 52:1590–1593, Apr 1984. 19

[100] Christian Sturm. *K^+-Produktion in Schwerionenreaktionen als Sonde für die Inkompressibilität von Kernmaterie*. PhD thesis, Technische Universität Darmstadt, 2001. 20, 21

[101] G. Buchwald, G. Graebner, J. Theis, J. Maruhn, W. Greiner, et al. KINETIC ENERGY FLOW IN NB (400-MEV/A) + NB: EVIDENCE FOR HYDRODYNAMIC COMPRESSION OF NUCLEAR MATTER. *Phys.Rev.Lett.*, 52:1594–1596, 1984. 20

[102] Horst Stöcker and Walter Greiner. High energy heavy ion collisions—probing the equation of state of highly excited hardronic matter. *Physics Reports*, 137(5–6):277 – 392, 1986. 20

[103] W. Reisdorf et al. Systematics of azimuthal asymmetries in heavy ion collisions in the 1 A GeV regime. *Nucl.Phys.*, A876:1–60, 2012. 20

[104] A. Andronic. Elliptic flow and equation of state in heavy ion collisions at {SIS} energies. *Nuclear Physics A*, 661(1–4):333 – 336, 1999. 20

[105] J. Aichelin and C.M. Ko. Subthreshold Kaon Production as a Probe of the Nuclear Equation of State. *Phys.Rev.Lett.*, 55:2661–2663, 1985. 21

[106] C. Fuchs, Amand Faessler, E. Zabrodin, and Yu-Ming Zheng. Probing the nuclear equation of state by K+ production in heavy ion collisions. *Phys.Rev.Lett.*, 86:1974–1977, 2001. 21, 151

[107] Ch. Hartnack, H. Oeschler, and Jorg Aichelin. Hadronic matter is soft. *Phys.Rev.Lett.*, 96:012302, 2006. 21

[108] Quing-feng Li, Zhu-xia Li, Sven Soff, Raj K. Gupta, Marcus Bleicher, et al. Probing the density dependence of the symmetry potential in intermediate energy heavy ion collisions. *J.Phys.*, G31:1359–1374, 2005. 22

[109] Bao-An Li and Lie-Wen Chen. Nucleon-nucleon cross sections in neutron-rich matter and isospin transport in heavy-ion reactions at intermediate energies. *Phys.Rev.*, C72:064611, 2005. 22

[110] Zhigang Xiao, Bao-An Li, Lie-Wen Chen, Gao-Chan Yong, and Ming Zhang. Circumstantial evidence for a soft nuclear symmetry energy at suprasaturation densities. *Phys. Rev. Lett.*, 102:062502, Feb 2009. 22

[111] Zhao-Qing Feng and Gen-Ming Jin. Probing high-density behavior of symmetry energy from pion emission in heavy-ion collisions. *Physics Letters B*, 683(2–3):140 – 144, 2010. 22

[112] ChenChen Guo, YongJia Wang, QingFeng Li, W. Trautmann, Ling Liu, and LiJuan Wu. Influence of the symmetry energy on the balance energy of the directed flow. *Science China Physics, Mechanics and Astronomy*, 55(2):252–259, 2012. 22

[113] G. Ferini, T. Gaitanos, M. Colonna, M. Di Toro, and H.H. Wolter. Isospin effects on subthreshold kaon production at intermediate energies. *Phys.Rev.Lett.*, 97:202301, 2006. 22

[114] William D. Myers and Wladyslaw J. Swiatecki. Nuclear masses and deformations. *Nucl.Phys.*, 81:1–60, 1966. 22

[115] Katharina Gill. Untersuchung zur produktion von geladenen und neutralen kaonen in au+au bei 1.23a gev mit hades. Master's thesis, Johann Wolfgang Goethe Universität, 2013. 22

[116] Timo Scheib. *Λ and K^0_S Reconstruction in Au+Au Collisions at 1.23 AGeV with HADES*. PhD thesis, Johann Wolfgang Goethe Universität, 2016. To be published. 22, 27, 76, 94, 145, 146, 147, 152, 154, 160, 162, 163, 166, 173

[117] S. Wheaton and J. Cleymans. THERMUS: A Thermal model package for ROOT. *Comput.Phys.Commun.*, 180:84–106, 2009. 25, 160, 166

[118] Heidi Schuldes. Produktion leichter Fragmente in Ar+KCl Kollisionen bei 1,76 AGeV. Master's thesis, Johann Wolfgang Goethe Universität, 2012. 24, 25, 112

[119] Manuel Lorenz. Investigating dense nuclear matter with rare hadronic probes. *PoS*, BORMIO2010:038, 2010. 26

[120] A. Mangiarotti et al. Sub-threshold phi-meson yield in central 58Ni+58Ni collisions. *Nucl.Phys.*, A714:89–123, 2003. 26

[121] K. Piasecki et al. Influence of ϕ mesons on negative kaons in Ni+Ni collisions at 1.91A GeV beam energy. 2014. 26, 156

[122] HADES internal reports. 29, 31, 39, 50, 51, 53, 64

[123] Jan Michel. *Development and Implementation of a New Trigger and Data Acquisition System for the HADES Detector*. PhD thesis, Johann Wolfgang Goethe Universität, 2012. 29, 34, 40

[124] Private communication T. Galatyuk. 30

[125] G. Agakishiev et al. The High-Acceptance Dielectron Spectrometer HADES. *Eur.Phys.J.*, A41:243–277, 2009. 31, 32, 33, 35, 53, 55, 56

[126] Jochen Markert. *Untersuchung Ansprechverhalten der Vieldraht-Driftkammern niedriger Massenbelegung des HADES-Experimentes*. PhD thesis, Johann Wolfgang Goethe Universität, 2005. 34, 68

[127] O. Pechenova, V. Pechenov, T. Galatyuk, T. Hennino, R. Holzmann, G. Kornakov, J. Markert, C. Muentz, P. Salabura, A. Schmah, E. Schwab, and J. Stroth. The alignment strategy of {HADES}. *Nuclear Instruments and Methods in Physics Research Section A: Accelerators, Spectrometers, Detectors and Associated Equipment*, 785(0):40 – 46, 2015. 34, 42

[128] J. Pietraszko, L. Fabbietti, and W. Koenig. Diamonds as timing detectors for MIP: The HADES proton-beam monitor and start detectors. *Nucl. Instrum. Meth.*, A618:121–123, 2010. 36, 44

[129] J. Pietraszko, T. Galatyuk, V. Grilj, W. Koenig, S. Spataro, and M. Traeger. Radiation damage in single crystal {CVD} diamond material investigated with a high current relativistic 197au beam. *Nuclear Instruments and Methods in Physics Research Section A: Accelerators, Spectrometers, Detectors and Associated Equipment*, 763:1 – 5, 2014. 36

[130] `https://indico.gsi.de/materialDisplay.py?contribId=9&sessionId=4&materialId=slides&confId=2142`. [Online; accessed 10-July-2016]. 37

[131] Behruz Kardan. Centrality determination at 1.23 agev gold-gold collision and readout-electronics for the hades electromagnetic calorimeter, 2015. 41, 46

[132] `http://web-docs.gsi.de/%7Ehalo/docs/hydra/classDocumentation/root5.28/parameter_initialization.pdf`. [Online; accessed 10-July-2016]. 42

[133] Patrick Sellheim. *Backtracking algorithm for dilelectron reconstruction with HADES*. PhD thesis, Johann Wolfgang Goethe Universität, 2017. To be published. 42, 49, 51

[134] M. Alvioli, H.J. Drescher, and M. Strikman. A monte carlo generator of nucleon configurations in complex nuclei including nucleon nucleon correlations. *Physics Letters B*, 680(3):225 – 230, 2009. 46

[135] `http://consult.cern.ch/writeup/geant`. [Online; accessed 10-July-2016]. 48

[136] Private communication G. Kornakov. 56, 57, 67

[137] Alexander Schmah. *Produktion von Seltsamkeit in Ar+KCl Reaktionen bei 1.756 AGeV mit HADES*. PhD thesis, Technische Universität Darmstadt, 2009. 60, 68

[138] H. Bethe and J. Ashkin. Passage of radiation through mass. *Experimental Nuclear Physics.*, 1:253, 1953. 66

[139] K. A. Olive et al. Review of Particle Physics. *Chin. Phys.*, C38:090001, 2014. 66, 160

[140] I. Frohlich, T. Galatyuk, R. Holzmann, J. Markert, B. Ramstein, et al. Design of the Pluto Event Generator. *J.Phys.Conf.Ser.*, 219:032039, 2010. 102, 157

[141] J. Clerk Maxwell. On the Dynamical Theory of Gases. *Philosophical Transactions of the Royal Society of London*, 157:49?88, 1867. 109

[142] Frederick Reif. *Fundamentals of Statistical and Thermal Physics*. Waveland Pr Inc;, 56946th edition, December 2008. 109

[143] P. Cerulus and E. Hagedorn. A monte-carlo method to calculate multiple phase space integrals — i. *Il Nuovo Cimento (1955-1965)*, 9(2):646–658, 1958. 109

[144] K. Piasecki et al. Centrality dependence of subthreshold ϕ meson production in Ni+Ni collisions at 1.9A GeV. 2016. 147

[145] J. Cleymans, H. Oeschler, and K. Redlich. Statistical model description of K+ and K- production between 1-GeV/A to 10-GeV/A. *Phys. Lett.*, B485:27–31, 2000. 150

[146] J.W. Harris. Results from the {STAR} experiment. *Nuclear Physics A*, 698(1–4):64 – 77, 2002. 15th Int. Conf. on Ultra-Relativistic Nucleus-Nucleus Collisions (Quark Matter 2001). 149

[147] W. Cassing and E. L. Bratkovskaya. Hadronic and electromagnetic probes of hot and dense nuclear matter. *phys rep*, 308:65–233, January 1999. 151, 152, 166

[148] Joerg Aichelin. Quantum molecular dynamics a dynamical microscopic n-body approach to investigate fragment formation and the nuclear equation of state in heavy ion collisions. *Physics Reports*, 202(5):233 – 360, 1991. 151

[149] Guo-Qiang Li, C. M. Ko, and G. E. Brown. Kaon azimuthal distributions in heavy ion collisions. *Phys. Lett.*, B381:17–22, 1996. 151, 166

[150] Y. Shin et al. Enhanced out-of-plane emission of K+ mesons observed in Au + Au collisions at 1-A/GeV. *Phys. Rev. Lett.*, 81:1576–1579, 1998. 151

[151] P. Crochet et al. Sideward flow of K+ mesons in Ru + Ru and Ni + Ni reactions near threshold. *Phys. Lett.*, B486:6–12, 2000. 151

[152] E. L. Bratkovskaya, W. Cassing, and U. Mosel. Analysis of kaon production at SIS energies. *Nucl. Phys.*, A622:593–604, 1997. 151, 166

[153] V. Zinyuk et al. Azimuthal emission patterns of K^+ and of K^- mesons in Ni+Ni collisions near the strangeness production threshold. *Phys. Rev.*, C90(2):025210, 2014. 151

[154] W. Cassing, L. Tolos, E.L. Bratkovskaya, and A. Ramos. Antikaon production in a+a collisions at sis energies within an off-shell g-matrix approach. *Nuclear Physics A*, 727(1):59 – 94, 2003. 152

[155] G. Agakishiev et al. In-Medium Effects on K^0 Mesons in Relativistic Heavy-Ion Collisions. *Phys. Rev.*, C82:044907, 2010. 152

[156] Z. Rudy, W. Cassing, Lucjan Jarczyk, B. Kamys, A. Kowalczyk, and P. Kulessa. Transport analysis of K+ production in proton-nucleus reactions. *Eur. Phys. J.*, A23:379–385, 2005. [Erratum: Eur. Phys. J.A24,159(2005)]. 152

[157] Y. Maeda et al. Kaon Pair Production in Proton–Proton Collisions. *Phys. Rev.*, C77:015204, 2008. 154

[158] Burt Holzman et al. Systematic study of Au - Au collisions with AGS experiment E917. *Nucl. Phys.*, A698:643–646, 2002. 156

[159] S.V. Afanasiev et al. Production of ϕ-mesons in p+p, p+pb and central pb+pb collisions at ebeam=158 a gev. *Physics Letters B*, 491(1?2):59 – 66, 2000. 156

[160] John Adams et al. phi meson production in Au + Au and p+p collisions at s(NN)**(1/2) = 200-GeV. *Phys. Lett.*, B612:181–189, 2005. 156

[161] J. Steinheimer and M. Bleicher. Hadron resonance production and final state hadronic interactions with UrQMD at LHC. *EPJ Web Conf.*, 97:00026, 2015. 155

[162] Claudia Behnke. *Reconstruction of neutral mesons via conversion in Au+Au Collisions at 1.23 AGeV with the HADES*. PhD thesis, Johann Wolfgang Goethe Universität, 2016. To be published. 160, 168, 173

[163] J Stachel, A Andronic, P Braun-Munzinger, and K Redlich. Confronting lhc data with the statistical hadronization model. *Journal of Physics: Conference Series*, 509(1):012019, 2014. 161, 173

[164] G. Agakishiev et al. Statistical model analysis of hadron yields in proton-nucleus and heavy-ion collisions at SIS 18 energies. 2015. 160, 161, 162, 173

[165] S. Wheaton, J. Cleymans, and M. Hauer. Thermus—a thermal model package for {ROOT}. *Computer Physics Communications*, 180(1):84 – 106, 2009. 160, 167

[166] K. Hagiwara et al. Review of particle properties. *Phys. Rev. D*, 66:010001, Jul 2002. 160

[167] `http://www.fair-center.de`. [Online; accessed 10-July-2016]. 167

[168] O. Svoboda et al. Electromagnetic calorimeter for the HADES@FAIR experiment. *JINST*, 9:C05002, 2014. 168

[169] Private communication J. Friese and HADES internal reports. 168

[170] Private communication P. Salabura and HADES internal reports. 168

[171] Private communication C. Muentz and HADES internal reports. 168

Rechtliches

Die vorliegende Druckfassung enthält kleinere, inhaltlich nicht relevante Änderungen gegenüber der dem Promotionsbüro vorgelegten Version.

Danksagung

Zunächst möchte ich meinem Doktorvater Joachim Stroth danken, dass er mich bereits zum Anfertigen meiner Bachelorarbeit in seine Arbeitsgruppe aufgenommen und es mir ermöglicht hat dieses überaus spannende Thema im Rahmen einer Doktorarbeit zu bearbeiten. Mit seinem großen Fachwissen, seiner Begeisterungsfähigkeit für das Themengebiet und Überblick hat er mich stets motiviert.

Ein großes Merci gilt Christoph Blume (Le Fleur), der mir stets mit seiner Expertise zur Seite stand und damit sehr zum Gelingen dieser Arbeit beigetragen hat und sie nicht mit einer Kettensäge zerstört hat.

Auch bei meinem externen Supervisor Dirk Rischke möchte ich mich für unsere halbjährlichen PhD-Kommittees bedanken. Es war sehr hilfreich auch mal die Meinung eines außenstehenden Theoretikers zu hören.

Ich möchte mich sehr herzlich bei Yvonne Leifels, Elena Bratkovskaya, Christoph Hartnack, Jörg Aichelin, Janus Weil und "Onkel" Jan Steinheimer für das Interesse an unseren Daten und für das Bereitstellen der verschiedenen theoretischen Modelle bedanken.

Besonderer Dank gilt selbstverständlich meinem Mentor Dr. Manuel Lorenz, that's right, Manuel Lorenz. Mit größtem physikalischen Verständnis und Leidenschaft hat er nicht nur bereits in jungen Jahren den Grundstein gelegt, sondern auch durch früchtebringende Diskussionen, seinen Fable für Occams razor und Korrekturlesen erheblich zu dieser Arbeit beigetragen. Ich konnte mich wirklich glücklich schätzen so eine super Betreuung genießen zu dürfen.

Ein riesen Dank gebührt dem schönen und schlauen Jochen Markert für das aufopferungsvolle tunen der Digitizer und dem Helfen bei jeglichen (vor allem batchfarm bezogenen) Problemen.

Dzikuje Gosia Gumberidze für die gemeinsame Leidenszeit mit der Pionenanalyse und das gegenseitige Debuggen unserer Macros.

Vielen Dank Christian Müntz für viele kritische Fragen zu Achsenbeschriftungen etc., das Korrigieren meines Detektorkapitels und für interessante Gespräche auch über Themen außerhalb der Physik.

Weiterer Dank gebührt Romain Holzmann für die große Hilfe bei allen erdenklichen mathematischen Fragen und dem Korrekturlesen meiner Einleitung.

Desweiteren danke ich allen weiteren Personen unserer GSI- und Frankfurt-HADES Gruppe Tetyana Galatyuk, Jan Michel, Ilse und Wolfgang König, Olga und Vladimir Pechenova, Georgy Kornakov, Erwin Schwab, Christian Wendisch, etc. für ihre wertvolle Arbeit auf Hard- und Software-Ebene, die die Datenauswertung meiner Doktorarbeit überhaupt erst ermöglich haben. Burki Kolb danke ich für das Angewöhnen eines regelmäßigen Essensrhythmuses und vor allem für das Vererben seines Macbooks, auf dem ich diese Arbeit geschrieben habe. Den nun CBMlern Christian Sturm und dem "faulen" Flori(an) Uhlig danke ich für die interessanten Gespräche an der Kaffeemaschine, das Einkaufen von sauren Zungen zur Nervennahrung und ihre bahnbrechenden Arbeiten über geladene

Kaonen bei KaoS, von denen ich mir einiges abschauen konnte. Großer Dank gebührt selbstverständlich Frau Frey - mein Backup vor Ort - für die super Organisation des gesamten Fachbereichs. Und in Erinnerung danke ich Lea Wunderlich, die trotz ihres Wechsels weiterhin an Geburtstagserinnerungsmails und Einladungen zum Alphabet-Supper gedacht hat.

Auch der gesamten HADES Kollaboration mit u.a. Piotr Salabura, Laura Fabietti, Pavel Tlusty, Jürgen Friese, Herbert Ströbele, um nur ein paar Namen zu nennen, möchte ich herzlich für die stets freundliche und produktive Atmosphäre bei Collaboration und Evo Meetings danken.

Ich danke dem HGS Hire Team für die wertvolle Unterstützung und dem Organisieren sehr interessanter und hilfreicher Lecture Weeks und Softskill Seminare im Rahmen des Graduierten Programms. Ich hatte eine wunderbare Zeit und habe viel gelernt.

Meinen "Leidensgenossen" Claudi, Timo Symmothy, Behruz, Patrick "der Bachelor" (Papi Sanchez), Erik, Szymon, meinen HQM Kollegen, meinen Studienfreunden, den Frankfurtern aus der ALICE Collaboration und den Münchenern HADESianern vielen Dank für die schöne und witzige Zeit im Büro, in meiner WG, an der GSI und Uni, auf Collabmeetings, auf Lecture Weeks, beim Postcolloqiumsbier, etc. und viel Glück auch euch beim baldigen Fertigstellen eurer Arbeiten.

Größter Dank und ein fröhliches "heeeey" gilt auch meinen Mädels, vor allem natürlich meiner "ABF" Caro, die mich, teilweise seit der Schulzeit, bei unseren glücklicherweise häufigen Mädelsabenden und -trips in den wichtigsten Dingen des Lebens begleiten.

Meiner Erst- und Zweitmama vielen Dank für den bedingungslosen Rückhalt und dafür, dass ihr mir nie Druck gemacht habt, sondern auch in schweren Zeiten einfach nur für mich da ward. Das Gleiche gilt auch für meinen Papa, der seit Beginn an meiner "Physikerkarriere" stets interessiert war und mich mit Kräften unterstützt hat. Es ist so unglaublich schade, dass du diesen Moment nicht mehr miterleben kannst. Ich konnte mir viel von deiner Kraft und Stärke auch in den schwersten Momenten abschauen, bewundere und vermisse dich.

Last but definitely not least danke ich meinem Freund Timo für die unglaubliche Unterstützung und die schönen letzten Jahre. Du schaffst es immer wieder mich durch deine starke Schulter(-Kuhle) runter zu holen, mir Halt zu geben und auf andere Gedanken zu bringen.

Erklärung

Ich versichere hiermit, dass ich die vorliegende Arbeit selbständig verfasst, keine anderen als die angegebenen Hilfsmittel verwendet und sämtliche Stellen, die den benutzten Werke im Wortlaut oder dem Sinne nach entnommen sind, mit Quellen- bzw. Herkunftsangaben kenntlich gemacht habe.

Frankfurt Main, d. 15.08.2016

Heidi Schuldes